

RUHR
UNIVERSITÄT
BOCHUM

RUB

Role of oxides and nano structure
of Cu catalysts for the
electrochemical reduction of CO₂

Dissertation

zur Erlangung des Grades eines
Doktors der Naturwissenschaften

in der Fakultät für Physik und Astronomie
der Ruhr-Universität Bochum

vorgelegt von

Fabian Scholten

aus Schwelm

Fritz Haber Institut der Max Planck Gesellschaft
Abteilung für Grenzflächenwissenschaft

Berlin, September 2021

1. Gutachterin: Prof. Dr. Beatriz Roldán Cuenya
2. Gutachter: Prof. Dr. Achim von Keudell

Datum der Disputation: 06.09.2021

Disputationskomitee:

Prof. Dr. Heiko Krabbe (Vorsitzender)
Prof. Dr. Beatriz Roldán Cuenya
Prof. Dr. Achim von Keudell
Prof. Dr. Ilya Eremin
Prof. Dr. Ulrich Wiedner

Acknowledgements

First of all I want to express my appreciation and thanks to my supervisor Prof. Dr. Beatriz Roldán Cuenya. She has been supporting my work since my Master Thesis and enabled me to grow as a scientist as well as a person. Whenever I needed her feedback, help or was looking for a partner for scientific discussions she had an open door at her office for me throughout the four years of my doctoral research. I always appreciated it a lot. I also want to express my thanks for the chance of moving together with her to the Fritz-Haber Institute of the Max Planck Society which changed my scientific and personal life for the better. I am very thankful for the great work environment and financial support she provided me, enabling me to conduct the research presented in this work.

My thanks also goes to Prof. Dr. Achim von Keudell for his supervision during the time of my Ph.D. research. I enjoyed the scientific exchange with him a lot and want to say thanks for his critical view and valuable feedback on research projects.

I also want to express my thanks to the Engineers and Technicians I had the chance to work with, especially Dr. Bernd Steinhauer and Dr. Nikolai Berdunov who supported me in maintaining and building up the experimental infrastructure needed.

I am very thankful that I was able to work together with so many great scientists from all over the world on different projects and research topics which not only opened up my scientific but also personal view. I want to especially thank Dr. Dunfeng Gao, Dr. Hyo Sang Jeon, Dr. Hemma Mistry, Dr. Yong Wook-Choi, Dr. Miguel Bernal, Dr. Jared Bruce, Dr. Rubén Rizo and Dr. Rosa M. Arán-Ais for the chance of working together with them and the numerous scientific discussions.

Special thanks and my deepest appreciation for time we shared goes to Dr. Rosa M. Arán-Ais and Dr. Rubén Rizo who became close friends during the course of my Ph.D. research. Thank you very much!

Der wohl größte Dank gilt meinen Eltern, ohne deren selbstlose und liebevolle Unterstützung ich niemals so weit gekommen wäre. Ihr wart und seid mir noch immer ein Vorbild, eine Stütze und eine Orientierungshilfe im Leben.
Ich bin euch über alle Maßen dankbar!

Abstract

The need for clean, energy efficient and environmental friendly technologies to close the resource cycle and help building a sustainable economy is higher than ever. A promising approach to achieve this goal is the utilization of atmospheric CO₂ by its electro-catalytic reduction towards non-fossil fuels and chemical resources.

Despite numerous dedicated studies carried out in the past decades, detailed understanding of the reaction mechanism and the reaction's dependence on specific parameters such as the surface orientation and structure on an atomic scale, the chemical environment under which the reaction is carried out, the oxidation state of the employed catalysts or quantum size effects possibly becoming relevant at small length scales, is missing.

The scientific work presented here is addressing many of these issues focusing on examining the influence of oxides when running the reaction as well as on the selectivity-structure correlations on an atomic scale. Utilizing various existing ultra high vacuum based techniques together with operando, synchrotron-based, electro-chemical experiments and developing new techniques, this work demonstrated for the first time that oxide species are particularly important for the reaction pathway towards multi-carbon chain oxygenate products. Surprisingly, unlike thought, the selectivity towards especially ethylene is independent on the presence of those species. Employing well defined single crystal surfaces it is revealed that structural properties are the key parameter determining the reduction reaction selectivity towards non-oxygenate products. By controlling and characterising such surfaces on the atomic scale this work significantly contributes to the field by further pointing out that the pristine undisturbed crystal orientation of the surface is, unlike believed on the basis of the existing theoretical predictions and experimental data, not as important as the presence of defects in the atomic lattice and high index facets on the surface. Furthermore, those results are put to use and into perspective when analysing the behaviour of high surface area nano-structured catalysts that are also considered for large scale up industrial applications. Using a combination of spectroscopic and electrochemical techniques the work provides detailed information about the importance of the chemical environment in the catalytic performance and points out new directions to further improve existing catalysts. For instance synergistic effects in bi-metallic nano structured systems are utilized, and the crucial role of the support in determining the reaction outcome explained. Similarly the effects of the electrolyte are explored, showcasing that the performance of already existing highly selective catalysts can be further improved due to an enhanced stability of crucial reaction intermediates on the surface as a consequence of the exposure to certain halides and alkaline cations.

These results clearly indicate that structural and morphological properties of catalysts are the key factors in determining the reaction selectivity towards specific products while only the oxygenate selectivity is found to be significantly affected by the chemical state and environment.

List of Publications

1. Scholten, F.; Nguyen, K.-L. C.; Bruce, J.P.; Heyde, M.; Roldan Cuenya, B. **Identifying structure-selectivity correlations in the electrochemical reduction of CO₂: a comparison of well-ordered atomically-clean and chemically-etched Cu single crystal surfaces.** *Angewandte Chemie* **2021**, Submitted (Under Review)
2. Bruce, P. J.; Nguyen, K.; Arán-Ais, R. M.; Scholten, F.; Navarro, J.J.; Hartmann, J.; Heyde, M.; Roldan Cuenya, B. **Development of a Single Crystal Sample Holder for Interfacing Ultra-High Vacuum and Electrochemical Experimentation** In Preparation, to be submitted to *Rev. Sci. Instr.* **2021**
3. Kunze, S.; Tănasea, L. C.; Prietoa, M. J.; Grosse, P.; Scholten, F.; Caldas, L.S.; Van Vörden, D; Schmidt, T.; Roldan Cuenya, B. **Plasma-assisted oxidation of Cu(100) and Cu(111) surfaces** In Preparation, to be submitted to *Chemical Sciences* **2021**
4. Rizo, R.; Bergmann, A.; Timoshenko, J.; Scholten, F.; Rettenmaier, C.; Jeon, H.; Chen, Y.-T.; Yoon, A.; Bagger, A.; Rossmeisl, J.; **Pt-Sn-Co nanocubes as highly active catalysts for ethanol electro-oxidation.** *Journal of Catalysis* **2021**, 393, 247-258.
5. Puring, K.; Evers, O.; Prokein, M.; Siegmund, D.; Scholten, F.; Mölders, N.; Renner, M.; Roldan Cuenya, B.; Petermann, M.; Weidner, E. Apfel, U.-P. **Assessing the influence of supercritical carbon dioxide on the electrochemical reduction to formic acid using carbon-supported copper catalysts.** *ACS Catalysis* **2020**, 10, 12783–12789.
6. Arán-Ais, R. M.; Scholten, F.; Kunze, S.; Rizo, R.; Cuenya, B. R. **The role of in situ generated morphological motifs and Cu (i) species in C₂₊ product selectivity during CO₂ pulsed electroreduction.** *Nature Energy* **2020**, 5, 317– 325.
7. Möller, T.; Scholten, F.; Thanh, T.N.; Sinev, I.; Timoshenko, J.; Wang, X.; Jovanov, Z.; Gliech, M.; Roldan Cuenya, B.; Varela, A.S.; Strasser, P. **Electrocatalytic CO₂ Reduction on CuO_x Nanocubes Tracking the Evolution of Chemical State, Geometric Structure, and Catalytic Selectivity using Operando Spectroscopy.** *Angewandte Chemie International Edition* **2020**, 59, 17974–17983.
8. Scholten, F.; Sinev, I.; Bernal, M.; Roldan Cuenya, B. **Plasma-modified dendritic Cu catalyst for CO₂ electroreduction.** *ACS catalysis* **2019**, 9, 5496– 5502.

9. Jeon, H. S.; Timoshenko, J.; Scholten, F.; Sinev, I.; Herzog, A.; Haase, F. T.; Roldan Cuenya, B. **Operando Insight into the Correlation between the Structure and Composition of CuZn Nanoparticles and their Selectivity for the Electrochemical CO₂ Reduction.** *Journal of the American Chemical Society* **2019**, *141*, 19879–19887.
10. Choi, Y.-W.; Scholten, F.; Sinev, I.; Roldan Cuenya, B. **Enhanced Stability and CO/Formate Selectivity of Plasma-Treated SnO_x/AgO_x Catalysts during CO₂ Electroreduction.** *Journal of the American Chemical Society* **2019**, *141*, 5261–5266.
11. Gao, D.; Sinev, I.; Scholten, F.; Arán-Ais, R. M.; Divins, N. J.; Kvashnina, K.; Timoshenko, J.; Roldan Cuenya, B. **Selective CO₂ Electroreduction to Ethylene and Multicarbon Alcohols via Electrolyte-Driven Nanostructuring.** *Angewandte Chemie International Edition* **2019**, *58*, 17047–17053.
12. Klingan, K.; Kottakkat, T.; Jovanov, Z. P.; Jiang, S.; Pasquini, C.; Scholten, F.; Kubella, P.; Bergmann, A.; Cuenya, B. R.; Roth, C., et al. **Reactivity determinants in electrodeposited Cu foams for electrochemical CO₂ reduction.** *ChemSusChem* **2018**, *11*, 3449–3459.
13. Jeon, H. S.; Sinev, I.; Scholten, F.; Divins, N. J.; Zegkinoglou, I.; Pielsticker, L.; Cuenya, B. R. **Operando evolution of the structure and oxidation state of size-controlled Zn nanoparticles during CO₂ electroreduction.** *Journal of the American Chemical Society* **2018**, *140*, 9383–9386.
14. Grosse, P.; Gao, D.; Scholten, F.; Sinev, I.; Mistry, H.; Roldan Cuenya, B. **Dynamic changes in the structure, chemical state and catalytic selectivity of Cu nanocubes during CO₂ electroreduction: size and support effects.** *Angewandte Chemie International Edition* **2018**, *57*, 6192–6197.
15. Bernal, M.; Bagger, A.; Scholten, F.; Sinev, I.; Bergmann, A.; Ahmadi, M.; Rossmeisl, J.; Cuenya, B. R. **CO₂ electroreduction on copper-cobalt nanoparticles: Size and composition effect.** *Nano Energy* **2018**, *53*, 27–36.
16. Gao, D.; McCrum, I. T.; Deo, S.; Choi, Y.-W.; Scholten, F.; Wan, W.; Chen, J. G.; Janik, M. J.; Roldan Cuenya, B. **Activity and Selectivity Control in CO₂ Electroreduction to Multicarbon Products over Cu_xO Catalysts via Electrolyte Design.** *Acs catalysis* **2018**, *8*, 10012–10020.
17. Jeon, H.S.; Kunze, S.; Scholten, F.; Roldan Cuenya, B. **Prism-Shaped Cu Nanocatalysts for Electrochemical CO₂ Reduction to Ethylene.** *ACS Catalysis* **2018**, *8*, 531–535.

18. Mistry, H.; Choi, Y.-W.; Bagger, A.; Scholten, F.; Bonifacio, C. S.; Sinev, I.; Divins, N. J.; Zegkinoglou, I.; Jeon, H. S.; Kisslinger, K., et al. **Enhanced carbon dioxide electroreduction to carbon monoxide over defect-rich plasma-activated silver catalysts.** *Angewandte Chemie* **2017**, *129*, 11552–11556.
19. Gao, D.; Scholten, F.; Roldan Cuenya, B. **Improved CO₂ electroreduction performance on plasma-activated Cu catalysts via electrolyte design: halide effect.** *ACS Catalysis* **2017**, *7*, 5112–5120.
20. Gao, D.; Zegkinoglou, I.; Divins, N. J.; Scholten, F.; Sinev, I.; Grosse, P.; Roldan Cuenya, B. **Plasma-activated copper nanocube catalysts for efficient carbon dioxide electroreduction to hydrocarbons and alcohols.** *ACS nano* **2017**, *11*, 4825–4831.

Contents

1	Introduction	1
2	Experimental Setups	9
2.1	Electrochemistry	9
2.1.1	Electrochemical Cell Design	10
2.1.2	Gas Chromatography	12
2.1.3	Electrolyte Cleansing	15
2.1.4	Electrochemical Techniques	16
2.1.5	Setup Benchmarking	21
2.2	Scanning Probe and Electron Microscopy	23
2.2.1	Atomic Force Microscopy	23
2.2.2	Scanning Tunneling Microscopy	26
2.2.3	Scanning Electron Microscopy	27
2.3	X-ray Photoelectron Spectroscopy	28
2.3.1	Chemical shifts and energy level splitting	29
2.3.2	Experimental realisation	33
2.3.3	Copper Reference Spectra	34
2.4	<i>Operando</i> and <i>In Situ</i> Techniques	36
2.4.1	Quasi <i>In Situ</i> XPS	36
2.4.2	X-ray Absorption Fine Structure: XAFS	39
2.4.3	Fundamentals of XAFS	39
2.4.4	<i>Operando</i> XAFS setup	43
2.5	Temperature Programmed Desorption	45
2.5.1	Quadropole Mass Spectrometer	48
3	Synthesis	49
3.1	Electropolishing	49
3.2	Dendritic Cu Catalysts	50
3.3	UHV preparation of Cu	52
3.4	Plasma treatment	53
3.5	Nanoparticle Synthesis	54
4	Role of the Catalysts Oxidation State in CO₂RR	55
4.1	Polycrystalline Cu	57
4.2	Copper Dendrites	61
4.3	Pulsed electrolysis on single crystal surfaces	81

5	Structure and Selectivity Correlations: Cu(100) and Cu(111)	95
6	Role of the Electrolyte on CO₂RR	109
6.1	Chemical Effect of the electrolyte	110
6.1.1	Halides	110
6.1.2	Cations	119
6.2	Electrolyte Driven Nanostructuring	127
6.3	Summary: Electrolyte Effects	134
7	Role of the Nanoparticle Size	137
7.1	Zn Particles: Size and Oxidation State Effect	139
7.2	Role of the Nanoparticle Composition	143
8	Outlook and Conclusion	151
8.1	Conclusion	151
8.2	Outlook	152

List of Figures

1.1	Elements for CO ₂ RR	3
1.2	Schematic reaction pathway for CO ₂ RR on Cu	5
2.1	Two Electrode Cell Setup	10
2.2	Schematic Electrochemical Cell	11
2.3	Electrochemical Cell	12
2.4	Schematic of a Gas Chromatograph	13
2.5	Example Chromatogram	15
2.6	Schematic of Helmholtz-Double Layer	17
2.7	Cyclic Voltammetry on Cu(100)	19
2.8	Chronoamperometric data obtained during a CO ₂ RR experiment	20
2.9	Example of an Electrochemical Surface Area measurement	21
2.10	Benchmarking of the electrochemical setup: Cu Foil Faradaic Efficiency	22
2.11	Atomic Force Microscopy measurement principle	23
2.12	Example Atomic Force Microscopy images	24
2.13	Bruker Atomic Force Microscope	25
2.14	Energy Diagram of Scanning Tunneling Microscopy	26
2.15	X-Ray Photoelectron Spectroscopy survey scan of clean Cu	28
2.16	XPS of Copper oxide Cu 2p	31
2.17	Energy Diagram of auger electron processes	32
2.18	Cu XPS reference spectra	35
2.19	Quasi In Situ XPS EC Cell	37
2.20	EXAFS spectrum of Cu	40
2.21	k-space and R-space spectrum of Cu	42
2.22	Operando EXAFS Cell	44
2.23	CO TPD ramp on Cu(111)	45
2.24	UHV TPD setup	46
3.1	Large scale SEM images of Cu dendrites on Ag	50
3.2	Current over time curve for the electrochemical grown of Cu dendrites	51
3.3	Image of the plasma chamber	53
3.4	Schematic of Nano-Particle Synthesis	54
4.1	SEM analysis of plasma oxidized Cu	57
4.2	XPS analysis of electropolished and plasma oxidized Cu foils before CO ₂ RR	58

4.3	XPS analysis of electropolished and plasma oxidized Cu foils after 1h of CO ₂ RR	59
4.4	XPS Cu LMM and O1s spectra of plasma oxidized Cu foils after different times of CO ₂ RR	60
4.5	XPS Cu 2p spectra of plasma oxidized Cu foils after different times of CO ₂ RR	60
4.6	Large scale SEM images of Cu dendrites on Pt and Ag Substrates .	62
4.7	One minute oxygen plasma treated Cu dendrites on Ag before and after EC	62
4.8	SEM images of Cu Dendrites	63
4.9	SEM of Ag and Pt substrate	64
4.10	SEM of plamsa treated Cu dendrites supported on Ag	65
4.11	Capacitance measurements on Cu dendrite samples	65
4.12	Faradaic efficiency data for Cu dendrites	66
4.13	Total and partial current density Cu dendrites supported on Ag and Pt	67
4.14	Faradaic efficiencies for the pristine and plasma treated Ag and Pt substrates	68
4.15	Ag MNN Auger and 3 d Data on Ag substrate	70
4.16	XPS O1s data on Cu dendrites before and after EC	71
4.17	XPS Auger data on Cu dendrites	72
4.18	XPS Auger data on Cu dendrites	73
4.19	Cu LMM and Cu 2p spectra of Cu dendrites grown on a carbon based Gas-Diffusion-Electrodes	74
4.20	Dendrite operando EXAFS data	75
4.21	k-Space representation of operando EXAFS data acquired on Cu dendrite systems	76
4.22	Wavelet transformed EXAFS data of Ag-supported Cu dendrites . .	77
4.23	Wavelet transformed EXAFS data of Pt-supported Cu dendrites . .	77
4.24	Summary plot of oxide derived Cu dendrites on different substrates	79
4.25	Cyclic Voltammetry on polycrystalline and Cu (100)	82
4.26	XPS analysis of electropolished Cu(100) surfaces exposed to employed anodic potentials for 5 minutes	83
4.27	Cu LMM spectra acquired after 1s pulsed electrolysis	85
4.28	O 1s and C 1s spectra acquired after 1s pulsed electrolysis	86
4.29	Cyclic Voltammetry on Cu (hkl) electrodes in 0.1M NaOH and 0.1M KHCO ₃	87
4.30	Faradaic selectivity of Cu (100) under pulsed conditions	89
4.31	Cu LMM auger data acquired for Cu(100) single crystals after different anodic pulse length	91
4.32	O 1s and C 1s data acquired for Cu(100) after different anodic pulse length	92

5.1	XPS Survey of UHV prepared Cu	96
5.2	UHV prepared Cu(100) and Cu (111) LEED pattern	97
5.3	STM images of UHV prepared Cu(100) and Cu (111) surfaces . . .	97
5.4	Ex situ AFM imaging of differently treated Cu(100) surfaces before and after EC	98
5.5	Ex situ AFM imaging of differently treated Cu(111) surfaces before and after EC	99
5.6	Cu LMM XPS spectra acquired on differently treated Cu single crys- tals before and after EC	100
5.7	O1s and C1s XPS spectra acquired on differently treated Cu single crystals before and after EC	101
5.8	O1s and C1s XPS spectra acquired on differently treated Cu single crystals before and after EC	102
5.9	CO TPD data acquired on differently prepared Cu single crystals .	103
5.10	CO binding strength for different dosing	104
5.11	Faradaic efficiency of differently pre-treated Cu single crystal surfaces	105
5.12	Electrochemical surface area measurements of differently pre-treated Cu single crystals after 1h of CO ₂ RR	106
6.1	SEM analysis of plasma oxidized Cu Foils run in halide containing electrolytes	110
6.2	XPS Cu 2p spectra of halide exposed samples before and after EC .	111
6.3	Cu LMM spectra of halide exposed samples before and after EC . .	112
6.4	XPS O1s spectra of halide exposed samples after EC	113
6.5	Activity and Selectivity of halide exposed oxide-derived Cu Foils un- der CO ₂ RR	114
6.6	Production rates for halide and consequent non-halide exposed samples	116
6.7	Current density and production rate vs theoretical halide absorption potential	117
6.8	SEM images on cation exposed Cu _x O foils	120
6.9	XPS data acquired on cation exposed Cu _x O foils	121
6.10	Supporting XPS data acquired on cation exposed Cu _x O foils	121
6.11	Current densities and combined C ₂₊ Faradaic efficiency of cation ex- posed Cu _x O foils	122
6.12	Surface normal dipole moment generated by cations on Cu(100) and adsorption potential of cations with and without the presence of sub- surface oxygen	124
6.13	SEM analysis of nanostructured Cu via cycling in different electrolytes	128
6.14	Cu LMM Auger data of the halide and carbonate cycled Cu foils before and after EC	129
6.15	Halide XPS regions of halide cycled Cu foils	130
6.16	Cu 2p XPS data of the halide and carbonate cycled Cu foils before and after EC	130

6.17	Geometric current density and Faradaic efficiency for the joint C ₂₊ products and ethanol of the halide and carbonate cycled electropolished foils in 0.1M KHCO ₃	132
7.1	AFM Images of differently sized Zn Nps	139
7.2	Activity and Faradaic efficiency for differently Sized Zn Nano-Particles	140
7.3	Quasi <i>in situ</i> XPS on Zn Nano-Particles	141
7.4	AFM images of differently composed CuZn Nano-Particles	143
7.5	Quasi in situ XPS spectra of differently composed CuZn Nano-Particles	144
7.6	Extracted CuZn Nano-Particle surface composition from XPS	145
7.7	Fitting of Cu 2p and Zn 2p Nano-Particle XPS data	146
7.8	Electrochemical performance of CuZn Nano-Particles	147

List of Tables

2.1	XPS energy values for the Cu reference spectra	35
3.1	Sputtering conditions	52
4.1	EDX analysis of Cu dendrites supported on Ag and Pt	64
4.2	Binding energy and modified Auger parameter of the Ag MNN and Ag 3d spectra	71
4.3	Linear combination analysis results of XANES spectra acquired on Cu dendrites supported on Ag and Pt	76
4.4	EXAFS fitting results for Cu dendrites supported on Ag and Pt . .	78
4.5	Linear combination analysis of the Cu LMM spectra of electropolished Cu(100) single crystals exposed to different potentials for 5 minutes	84
4.6	ECSA measurements of Cu(100) single crystal after pulsed conditions	85
5.1	Cu _x O distributions extracted from linear combination fitting of Cu LMM data on differently treated Cu single crystals	102
6.1	Cycling parameters	127
7.1	Nano-Particle synthesis parameters and extracted height values . .	139
7.2	XPS energy values obtained and reference values for different Zn species	141
7.3	CuZn Nano-Particle synthesis parameters and extracted height values	143

1 Introduction

The rapid advance in technology which was accompanied by a drastic increase in the overall world population has led to numerous new challenges over the course of the last century. Among them, feeding the all time high demand for energy and resources is of general societal interest [1–4]. Up to now the conventional industry is mainly based on fossil fuels, whether it is for energy production by burning them, or fossil cracking for carbon based chemicals and other goods. This approach, however, has led to a drastic increase in the carbon dioxide concentration which is on an all time high since 800 thousand years [5, 6]. As CO₂ is a green house gas, this causes changes in the global climate and offsets the thermodynamic equilibrium state of many processes on the planet, thus changing the global ecosystem. Furthermore the conventional industrial processes led to a great deal of pollution across the planet, which is threatening ecosystems and animal life.

As the aforementioned mentioned economy is not sustainable on a long time scale, new ways and technologies have to be found and implemented into the existing industry to be able to close the resource cycle. Of special importance is hereby the carbon cycle, since the released CO₂ is endangering the planet's climate.

A promising concept is to recover carbon dioxide from the air, or take it concentrated from industrial sites and make use of it as a source for carbon based chemicals. If such a process is only powered by energy from renewable sources such as wind and solar, a sustainable artificial closing of the carbon resource cycle could be achieved. A possible technology in this framework, that could be used to transform carbon dioxide into useful chemicals is the so called electrochemical catalytic reduction of CO₂. While within the field of electrochemistry the conversion of chemicals into electrical energy has been studied to an extend since almost 250 years [7], including reactions such as hydrogen- (HER) or oxygen evolution reaction (OER) from water splitting, CO₂ reduction reaction (CO₂RR) remained relatively unexplored until three decades ago. It was the work of Hori and his co-workers that sparked interest in the field when they reported that it was possible to transform carbon dioxide into valuable hydrocarbons such as ethylene and ethanol when the right catalyst is employed [8, 9]. Developing this and similar technologies on an industrial scale has since then been a goal within developed countries and regions, whose achievement remained elusive until now. Nevertheless, since Hori's discovery over three decades ago, dedicated research within the field has led to more fundamental knowledge [4, 9–13], allowing rational design of new catalysts not only for the generation of hydrocarbons from CO₂ but also carbon monoxide (CO). The latter is an important synthetic gas for common industrial processes such as the

synthesis of methanol [14–16] or simply as a reducing agent within chemical synthesis [4, 17, 18]. Additionally, energy storage technologies, especially independent ones, have become more important due to a shift into a more sustainable economy.

The present work is motivated by the aforementioned problems and research. It is dedicated not only to fundamental research but also to finding practical solutions with respect to the catalyst design to be able to contribute to CO₂RR becoming viable.

It is clear that in order to incorporate this technology on a large scale within future industry it has to be as efficient as possible. The key is hereby to get as close as possible to an energy conversion rate of 100 % to the targeted products. For achieving this, the right choice of catalysts and its design is crucial. Demands for these are for instance a high stability in operation over a long time while being active, so that high amounts can be converted per given time. Also economy related needs such as price, abundance and availability play an important role. Furthermore, since CO₂ is a very stable molecule, the energy barrier of reducing it has to be lowered by the catalyst as much as possible, at best meeting the thermodynamically needed minimum energy.

There are various CO₂RR catalysts [9, 19] which are mainly metals, however, possible industrial candidates among them are very few. For instance copper, is the only metal capable of catalysing the pathway towards hydrocarbons such as methane, ethane, ethylene, ethanol and n-propanol [8]. Especially ethylene and ethanol are of great interest due to their widespread usage and the high economic value. The first is a fundamental basis chemical needed as a precursor for the polymere industry and for the synthesis of carbon based chemicals [20, 21] and the second is a common and easy-to-use fuel to power machines [22, 23], which is also reflected by the relatively high market prices [4]. Other materials are only able to generate formic acid which is mostly considered as a low value product or carbon monoxide from CO₂. As mentioned, CO is widely employed and needed in industrial processes, which also makes the usage of other metal catalysts than copper interesting.

A summary of the elements that have been tested by researchers over the last years [19, 24, 25] and their capabilities are given in Figure 1.1.

What can be seen immediately is that most of the considered elements are only capable of producing hydrogen under CO₂RR conditions, which requires fairly high negative potentials due to the high stability of the CO₂ molecule. Moreover, a common need among all catalysts, is to suppress the parasitic HER from water which competes for active sites on the used catalysts surfaces. Metals that have been considered for CO generation are Au, Ag and Zn. Not all of them are attractive for usage though, as for example gold is very expensive due to its low availability on the planet and therefore, large scale industrial applications on its basis are elusive.

CO vs hydrogen adsorption properties has been a topic of research. Key parameters that are linked to the CO binding strength are the catalyst structure, especially on a microscopic scale, its shape, surface orientation and the total surface area available. The latter is of importance since higher surface area catalyst facilitate the increase the overall CO surface coverage, which is believed to enhance the coupling of CO molecules with each other and consequently result in a higher amount of C₂ hydrocarbon products [37]. Another commonly used approach to alter the CO binding strength and thus, the selectivity is the use of bimetallic systems [38–40]. Within these the electronic structure of the surface is changed, many times due to alloying, with respect to the mono-metallic analogue and thereby the binding strength of CO on the surface of is altered [39]. Additionally, some of these bimetallic systems also show a synergistic effect just by being next to each other, without any alloying. For instance, in the case of combining Cu and Ag, a more selective formation of CO₂RR products as a result of a higher CO coverage and spill over effect has been reported [27, 41, 42].

Regarding the surface properties of Cu catalysts and especially those determining the surface binding strength of CO is the crystalline orientation. Therefore, already early on studies on single crystal surfaces have been conducted to gain insight into their influence on the catalytic selectivity. And indeed, using mechanically and chemically polished Cu(hkl) single crystal surfaces, significant differences have been observed [37, 43, 44]. For instance, Cu(111) has been found to exhibit a high selectivity for unwanted methane, while Cu(100) surfaces are selective for the much desired ethylene and Cu(310) and (911) surfaces have displayed a higher selectivity for ethanol [37, 44, 45]. The reasons for this behaviour are up to this point not fully clear. Theoretical and experimental studies supposed it to be linked to the different binding properties of the pristine surfaces [46, 47], but also defect sites and steps are believed to play a crucial role [48]. For instance, the superior selectivity of Cu(100) surfaces for C₂ hydrocarbons was predicted to be linked to a higher dimerization probability due to the binding properties of CO on the surface leading to a higher overall coverage and thus, a higher probability of forming the C-C bond [37, 49]. Precise knowledge on how the reduction pathway towards a specific product proceeds remains elusive, especially when going beyond single crystal model systems, that are easier to model in theory than polycrystalline surfaces.

Nevertheless, dedicated theoretical and experimental efforts conducted during past years have led to a consensus on possible pathways, even though the details are under a lot of debate up to date [25, 31, 46, 50–55]. Parameters considered are hereby not necessarily linked to CO binding only, but also chemical state, catalyst composition, pre-functionalization, the electrolyte composition, the pH and thermodynamic parameters such as temperature and pressure which are also able to influence the reaction pathway.

Summarizing these complex dependencies has been attempted in the past [4, 10–12], but remained elusive, as a consistent theoretical concept has not been provided. Here only the fundamental ideas and pathway dependencies having the most agree-

ment shall be discussed. Figure 1.2 shows a simplified schematic of possible reaction pathways.

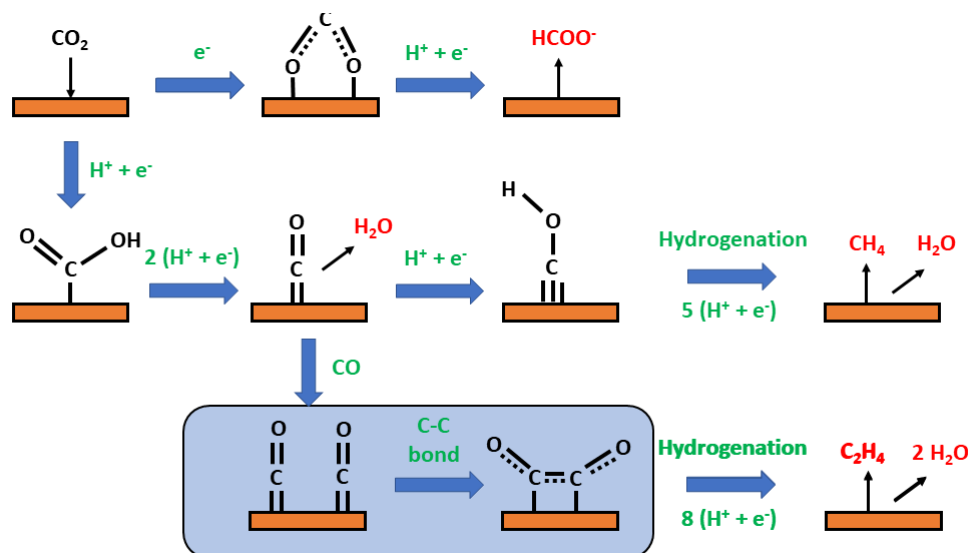


Figure 1.2: Schematic reaction pathway for CO₂RR. C-C coupling step is highlighted light blue.

The underlying idea in this simplified picture as well as within detailed studies that rely on numerical and analytical theoretical calculations is that the pathway chosen should be the one which is energetically most favourable. Besides the first step which is the binding and activation of CO₂ on the surface, the whole reduction reaction is energetically downhill with slight differences within the different possible pathways. This makes it difficult to determine which of all possible routes is chosen. Considering only the first step which is the binding of CO₂ on the surface, two different possibilities are taken into account. The first is that the carbon dioxide is bound to the surface by means of the oxygen atoms.

This leads to the hydrogenation of carbon and thus to the first product which is formic acid. This pathway is therefore mostly considered to be a dead end. If, however, the carbon atom within the molecule is the one interacting with the surface, there is the possibility of hydrogenating one of the oxygen atoms leading to carbon monoxide on the surface (see fig. 1.2). This also illustrates why CO and its binding strength to the surface is considered to be one of the most important parameters in determining a catalysts CO₂RR behaviour, as it is a common intermediate for all consequent reduction products.

From this crucial step of having CO on the surface there is either a further hydrogenation of CO leading to methane or the C-C bond is formed leading to higher chain hydrocarbons such as ethylene or alcohols such as ethanol.

An important macroscopic parameter affecting the choice of reaction pathway is the electrolyte pH, which can be locally different from the bulk pH in the vicin-

ity of the working electrode due to kinetic limitations [53, 56, 57]. Studies that changed the bulk pH, as well as those employing electrolytes with different buffer capacity, revealed that a lower pH, and thus a higher concentration of hydrogen, favours methane generation [57, 58]. This is understood by means of the probability of hydrogenating the oxygen atom of carbon monoxide over forming the C-C bond. A higher hydrogen concentration increases this probability and thus leads to more methane yield at lower pH [57, 59]. On the contrary with a high pH, C₂ products are favoured since the dimerization and formation of the C-C bond is happening before the hydrogenation occurs.

This effect and explanation has also been considered and supported within other studies that changed kinetic limitation parameters other than the employed electrolyte. For instance, studies on nano- and micro-structured high surface area copper based dendrite catalysts also showed that the selectivity for methane is decreasing drastically once the reaction is proceeding fast enough so that the local pH is changing to higher values [27, 60]. Mostly these studies have been carried out in H-type cell configurations (see chapter 2), which limits the carbon dioxide transport towards the catalyst by their intrinsic design. They rely on the dissolution and consequently the transport of CO₂ within the electrolyte and thus are kinetically limited. As this can lead to the depletion of the available carbon dioxide in the electrode vicinity due to the high surface area catalyst consuming it faster than it can be kinetically redelivered. Consequently, parts of the catalyst surface which could be doing CO₂RR are instead free for performing HER, artificially increasing the selectivity of the catalyst for HER vs CO₂RR. As per H₂ molecule two OH molecules are generated, the local pH in the vicinity of the electrode is increasing in these type of systems [60]. Regarding only the CO₂RR products disregarding the competing HER from the total amount yield, this increase in the local pH is believed to suppress the methane generation in favour of higher chain hydrocarbons which is what is experimentally observed [27, 61]. Therefore, balancing these two effects out to generate the optimal C₂ hydrocarbon yield is crucial for high surface area catalysts who are especially important for possible large scale industrial applications, since they are also the ones capable of being operated at high current densities. This idea has also been supported by studies carried out on the same catalyst in flow cell setups that manage to overcome kinetic limitations to an extent. These experiments showed that the amount of ethylene generated with respect to hydrogen can be further increased, while still suppressing methane generation, by delivering enough carbon dioxide to the active sites of the surface area dendrite catalysts [61].

Another macroscopic parameter that has shown to be important when it comes down to engineering and affecting the selectivity is the electrolyte employed. Hereby, different cations and anions within the electrode vicinity are believed to affect the binding strength, structure of CO₂RR intermediates on the surface as well the transport of hydrogen and OH⁻ ions across the electrodes vicinity interface [58, 62–64]. By changing the content of alkaline and halide ions in different experiments, an in-

crease in the selectivity for ethylene was achieved [63, 65], together with an increase of the overall activity [62, 66, 67]. These changes are again understood as a change in the overall CO binding strength on the copper surface, but also bigger alkaline ions are believed to affect the hydrogen transport across the electrolyte/electrode interface due to the differently sized hydration shell around the ions [63]. Furthermore, halides especially iodine have been found to significantly alter the overall mesoscopic structure and the chemical state of the catalyst leading to a higher overall surface area and samples with Cu(I) being present either as Cu_2O or CuI [62, 66]. Especially those two parameters the overall roughness and surface oxidation affect the selectivity and have gained a lot of attention recently since studies on oxygen-plasma treated polycrystalline Cu surfaces reported an up to 45 % higher ethylene selectivity as compared to non plasma treated samples [68].

First speaking about the higher surface area and its effect on the catalytic selectivity, the idea behind it is linked to the previously discussed local pH effect as well as the CO surface coverage that has been suggested as a reason for the superior ethylene selectivity over Cu (100) surfaces [37]. A higher surface area would naturally lead to a higher amount of active sites, thus a higher activity. Therefore, similar to dendritic catalysts who exhibit a high surface area, the depletion of reactants would lead to a higher local pH and consequently a higher selectivity for ethylene on pre-oxidized so called "oxide derived (OD)" systems. At the same time, a higher surface area also means that more active sites might be present, which could serve as a binding partner for CO, thus increasing the overall surface coverage with CO during the reduction reaction.

Remarkably, the authors who pointed out the superior catalytic performance of pre-oxidized Cu systems have, at the same time, being able to prove that the overall roughness cannot solely explain the observed catalytic trends as the sample exhibiting the highest roughness had significantly worse selective (20%) for ethylene, likely due to mass transport limitations [68]. This has led to numerous assumptions and studies focusing on the presence of residual oxides during CO_2RR [27, 45, 69–76] since the surfaces are supposed to be mostly metallic under CO_2RR conditions and the presence of specific active sites or structures on the nano scale [66, 77–80]. Since the first is difficult to investigate due to the poor stability of oxides and the need of combining operando techniques with electrochemical setups, their role and effect on the CO_2RR pathways is still under debate. Similarly, the precise effect of special active sites and/or nano-scaled structures that are only selective towards a given product remains under debate even though dedicated research efforts on model systems managed to narrow down their role. For instance, it has been shown on model nano-sized Cu based particles that the smaller those particles are, the higher is their selectivity towards hydrogen due to an increased amount of under-coordinated sites [29, 38, 81]. Thus, the superior C_2 chain hydrocarbon selectivity of oxide- derived catalysts cannot be attributed to the presence of such structures on the surface.

These insights and ideas have led to numerous attempts to facilitate and increase the catalytic performance through surface engineering. Common approaches based on the previously discussed ideas are related to tuning the catalysts morphology either by pre-functionalization [27, 66, 82, 83] and/or exposure to specific chemical environments [62, 67, 84, 85]. Also the use of bimetallic and/or nanostructured systems is a commonly applied strategy [38–40, 84, 86].

With all these developments in recent years it was possible to increase the Faradaic efficiency for the generation of ethylene from 23 % as first reported by Hori [8] to up to 60 % when using oxide-derived catalysts [68, 72] and to go even beyond 80 % by employing nanostructured catalysts and additionally optimizing kinetic aspects of the reaction which was done recently [87, 88].

The presented work connects to the previous literature discussing many of the mentioned aspects within different research efforts towards understanding and improving the electroreduction of CO₂ towards valuable hydrocarbons and alcohols. Special emphasis is given to the role of the chemical state of copper and its relation to morphological and structural aspects of copper-based catalysts, providing new insights into the role of residual oxides and their overall stability, as well as narrowing down the nature of the active sites on the catalytic surfaces employed. The work not only contributes to the fundamental understanding of the reaction but also gives perspectives and new approaches to support the technical advance in the research field by working out new experimental procedures and setups allowing to study CO₂RR in new ways.

2 Experimental Setups

The goal of this chapter is to give a detailed description of the employed experimental setups, as well as brief overview of the underlying fundamental techniques used within the presented studies. The latter is of importance when considering the design of experiments and especially when it comes down to combining techniques that traditionally are not designed to work together, such as for example electrochemical methods and UHV based techniques.

2.1 Electrochemistry

Electrochemistry, being the branch of chemistry dedicated to studying the interplay of chemical reactions and electrical currents has led to numerous industrial processes as well as devices such as for instance electroplating of surfaces, batteries and accumulators. While the latter are mainly used to turn chemical energy into electricity and vice-versa, it is also of great interest to convert chemicals into one another such as for instance converting CO_2 into hydrocarbons. Most of the time this field is referred to as the electrocatalytic conversion of chemicals.

What all these devices and techniques share in common is that they are at least based on a so-called two electrode setup consisting of a working electrode (WE), where the catalytic conversion is happening and a counter electrode (CE), where the counter reaction happens.

The downside of these simple two electrode setups is that they are not sufficient for scientific investigation of the underlying processes as the potential at the working electrode remains unknown in two electrode setups and only the cell voltage, which is the voltage across the whole device including the electrolyte and counter electrode, can be measured. Therefore, most commonly a third electrode, the so-called reference electrode (RE) is introduced to be able to define the potential at the working electrode. The standard electrode referred to is the so-called reversible hydrogen electrode (RHE) or the so-called silver-silver chloride (Ag/AgCl) electrode. To understand the idea of this third electrode it is helpful to recall that even in an unconnected electrochemical cell, where two electrodes are conductively connected throughout the electrolyte interfacing them, chemical reactions happen. These lead to a transport of ions across the electrolyte interface resulting in an electric current across the electrodes. The potential in between two different electrode materials driving the current is hereby dependent on the given reaction and the reaction enthalpy of a given reaction with respect to another one. This is also known as the

electrochemical voltage series and discussed into detail elsewhere [56]. The key point of a reference electrode is to be able to know and control the rate and the potential that is building up due to these thermodynamic equilibrium reactions happening at the electrode/electrolyte interface of the reference electrode. Knowing the potential building up there it is possible to use it as a reference to measure and define the potential at a given working electrode. RHE electrodes are based on Pt wires resting within a hydrogen-saturated aqueous solution, while in Ag/AgCl electrodes Ag is used in a saturated aqueous chloride solution. The electrodes employed for all studies conducted within this work are commercially available ones (RHE: HydroFlex, Gaskatel ; Ag/AgCl: LF-1, Innovative Instruments).

2.1.1 Electrochemical Cell Design

Two Electrode Cell

The two electrode setup is only used for tasks that do not necessarily require a well defined control of the voltage applied at the working electrode. Those are operated by applying a voltage across the cell at the two electrodes. The setup is very simple and shown in Figure 2.1.

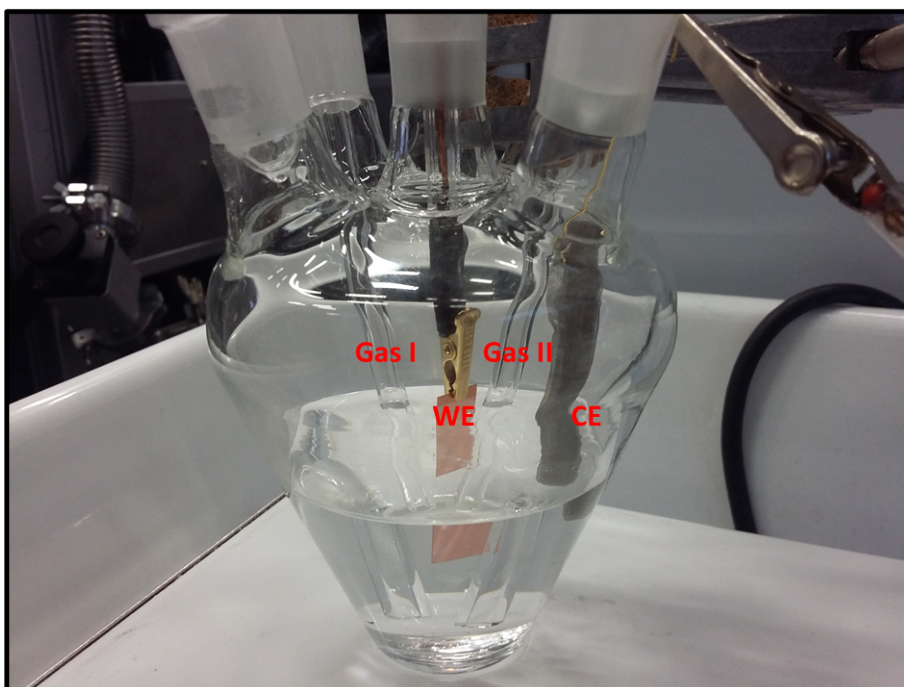


Figure 2.1: Two electrode setup. The working electrode is hung using a gold-coated crocodile clamp and the exchangeable counter electrode (a Pt mesh here) is connected via a gold wire that is not in contact with the electrode. The whole setup is leak-tight. Additionally, two gas inlets are connected via glass tubes for purging or saturating the solution with a specific gas.

As it can be seen it consists of a single glass compartment cell that can be sealed with respect to the environmental air to be able to work in a well defined gas atmosphere. This is for instance used and of importance when the employed solution needs to be purged of oxygen or saturated with CO_2 . The two glass tube inlets are used for these purposes. The working electrode is fixated with the help of a gold-coated crocodile clamp, while the counter is connected via a gold wire that is not in touch with the employed solution at all.

The two electrode setup is mainly employed for either electropolishing/etching surfaces or to electrochemically grow nanostructured catalyst from a precursor solution (see also chapter 3.1 and 3.2).

Three Electrode Cell

The three electrode setup is used within most of the conducted scientific studies as it has the advantage of being able to know and control the potential at the working electrode with respect to a given reference electrode. A schematic design of the cell is shown in Figure 2.2. The actual setup used is shown in Figure 2.3.

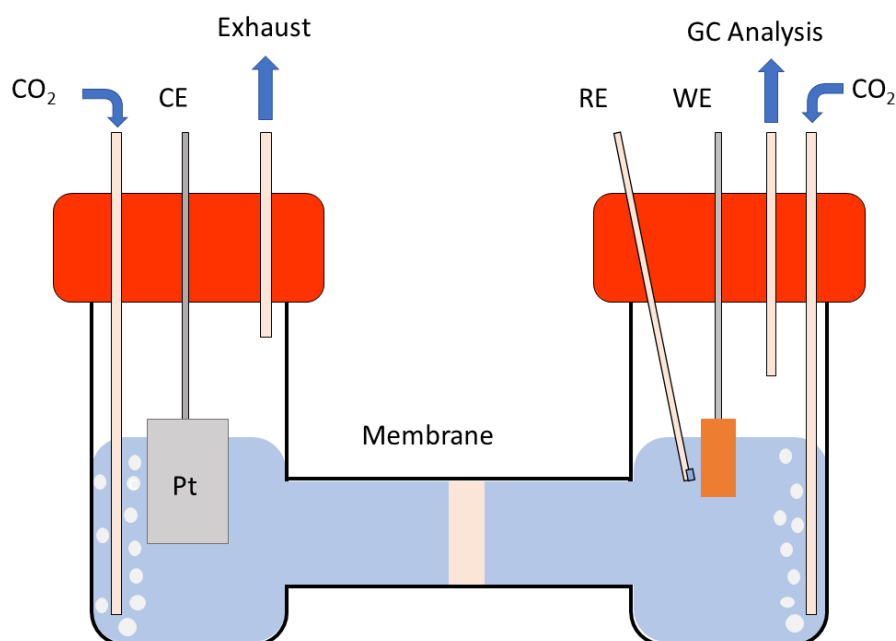


Figure 2.2: Schematic of an electrochemical H-type cell as used within the present work.

From the electrochemical point of view the investigation of the electrochemical reduction of CO_2 , especially on copper based catalysts comes with some additional challenges that need to be addressed within the framework of the experimental setup and procedures. An obvious, yet important, example is the fact that unlike other reactions such as for example hydrogen (HER) or oxygen (OER) evolution reaction there, is more than just one reaction product for CO_2RR . This demands several

things on the electrochemical setup. For instance the detection of the gas products by gas chromatography to quantify the amount of the different products.

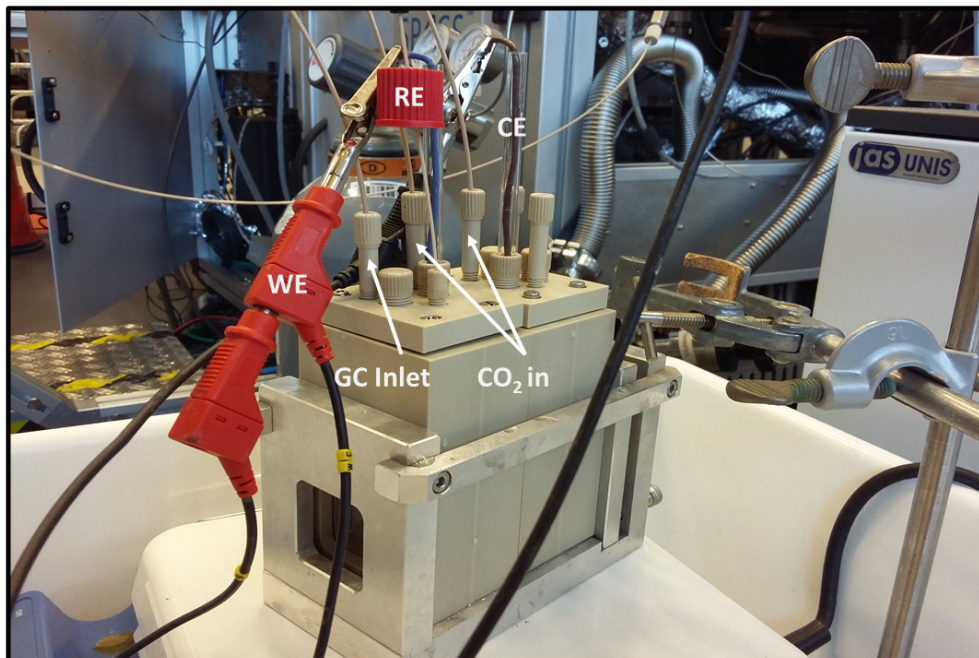


Figure 2.3: Electrochemical H-type cell made out of PEEK used in this thesis.

Our H-type cell is made out of Poly-ether-ketone (PEEK). Both compartments are separated from each other by an anion exchange membrane (Selemion AMV) so that reaction products from neither the cathodic nor the anodic side are able to migrate towards their respective counter electrode and be oxidized/reduced again, which would affect the quantification of the gaseous products. The caps are gas-leak tight sealed by the use of standard viton rings and screwed against the body of the cell. This way the only outlet for the gases are the exhaust for the counter compartment and the gas chromatography detection line for the working electrode compartment. The counter electrode employed is a high surface area Pt gauze mesh (MaTeck, $3,600 \text{ mesh cm}^{-2}$) so that the counter reaction which is OER for the case of CO_2RR is not limited by the active surface area which could lead to a limitation of the CO_2RR on the working electrode. Pt is chosen since it is known to be active for OER and is addition chemically very stable. The employed reference electrodes for all CO_2RR experiments are commercial leak-free Ag/AgCl (LF-1, Innovative Instruments, Inc.).

2.1.2 Gas Chromatography

The detection of the products and their quantification is crucial for CO_2RR to evaluate whether a given catalyst is selective for a specific product.

To achieve a reliable detection, a gas chromatograph (GC, Agilent 7890B) is directly connected to the electrochemical cell. This is also denoted as the online detection of gas products. The used chromatograph is equipped with a thermal conductivity detector and a flame ionization detector to be able to detect the gaseous products resulting from CO₂RR (H₂, CO, CH₄, C₂H₄, C₂H₆). The idea and underlying principle is schematically represented in Figure 2.4 (a), and (b) shows an image of the work station including the GC.

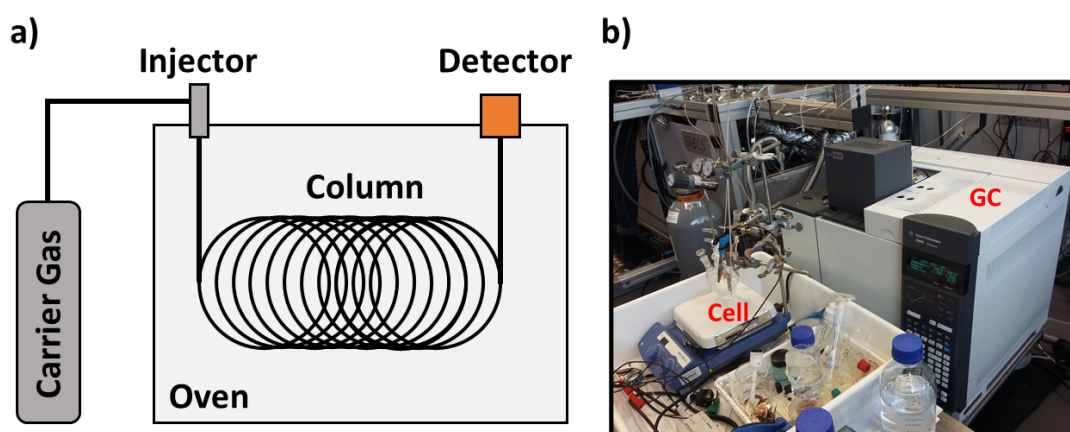


Figure 2.4: (a) Schematic of a gas chromatograph. (b) Experimental work station.

Every 16 minutes, gas from the Cell is injected into the GC column within which it is adsorbed on a porous material. By increasing the temperature from $T = 60^{\circ}\text{C}$ to $T = 200^{\circ}\text{C}$ using a linear ramp, the separation of the different gases is achieved, since they have a different desorption temperature and diffusivity within the column. At the end of the column line, the exhaust gases are constantly directed towards the two detectors where they are combusted. The FID (flame ionization detector) is based on measuring the resulting CO₂ from the combustion, whereas the TCD (thermal conductivity detector) measures the thermal conductivity. Naturally, the TCD detector is also able to detect non flammable gases such as Ar or N₂. To be able to quantify and interpret the resulting chromatograms, the GC has to be calibrated, meaning that the peak intensity and area obtained from the detector signal has to be normalized to a given known amount of the respective gas species. This is done by employing a known calibrated gas mixture containing a well defined mixture of the gases of interest of which the concentration is known. The mixture used here contains all CO₂RR products (H₂, CO, CH₄, C₂H₄, C₂H₆) in a known concentration (Westfalen, 99,995% purity for each).

Once this is done, the concentrations of each product produced in a given experiment can be quantified and measured by the GC. Consequently, it is possible to calculate the so-called faradaic efficiency (FE), that is commonly referred to within the field of electrochemistry. Assuming that the current measured is always used up to drive the reaction process within the electrochemical cell, the faradaic efficiency

is simply balancing the total charge consumed with the charge consumed to produce a given product. The resulting equation reads:

$$F_{gas,i} = \frac{5}{3} \frac{f_{CO_2} c_{gas} n_i F}{V_m I} \quad (2.1)$$

with:

f_{CO_2} - The carrier flow of CO₂ into the cell that goes throughout the GC

c_{gas} - The measured gas concentration by the GC

n_i - The amount of electrons used to generate a specific gas species

F - Faraday constant

v_m - molar volume of an ideal gas

I - Average current during the electrolysis time

For the liquid products the concentration of a given species is measured with the help of a liquid GC (Shimadzu 2010 plus) and similarly normalized over the total charge consumed during the electrolysis time. Note that the amount of liquid products is not measured online as the gaseous ones, but after electrochemistry. Therefore, the obtained values are the integral of all liquid products that have been produced over the full electrolysis. The equation used to calculate the concentration of liquid products used reads:

$$F_{liquid} = \frac{c_{liquid} V n F}{Q_{Total}} \quad (2.2)$$

with:

c_{liquid} - Measured liquid concentration

V - Total electrolyte volume

Q_{total} - Total charge consumed

An example chromatogram obtained during a run injecting the calibration gas mix is shown in figure 2.5. As seen the mixture contains all of the major CO₂RR gas products and does not show any oxygen or nitrogen peaks, supporting the leak tightness of the employed system. Since the relative concentration of the gases with respect to each other within the calibration mixture is known from the obtained peak area in the chromatogram, one can normalize by these values. This is then used to quantify the amounts measured in a given CO₂RR experiment.

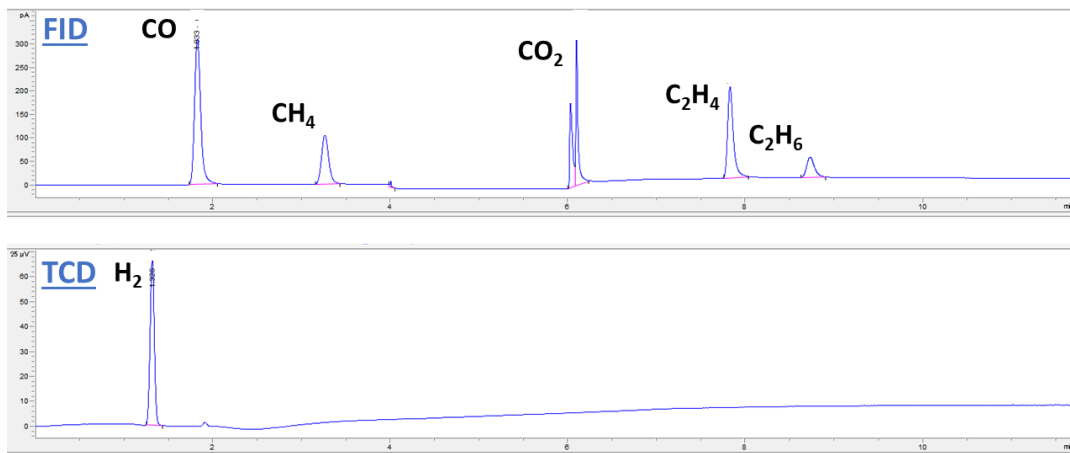


Figure 2.5: Example chromatogram obtained when injecting the calibrated gas mixture.

2.1.3 Electrolyte Cleansing

Another important topic to address, especially for CO₂RR, is to work in a very clean environment. Keeping the used solutions, i.e. the electrolyte, free of metallic and other impurities such as iron for example, which has shown to be poisonous for CO₂RR on copper, is crucial [89]. Due to this issue, all used glassware and parts have been cleaned by the following procedure and afterwards have not been exposed to any contaminants or solutions except the ones they are intended for:

1. Initial rinsing by MilliQ water ($R = 18.2M\Omega \text{ cm}$) and immersion into a KMnO₄ solution for 24h.
2. Rinsing 5 times by boiling MilliQ water within the vessel.
3. Immersion into a 1M HNO₃ solution for 24h.
4. Rinsing 5 times by boiling MilliQ water within the vessel.
5. Since the glassware is dissolved by the KOH solution, only the non-glass parts of the setup such as Teflon, Viton, Pt Mesh etc. have been cleaned by immersion into 1.5M KOH solution for 24h at $T = 60^\circ\text{C}$. This step is crucial when removing Silicon that can be introduced by dust or dirt particles easily.

In addition, the electrolyte usually contains a salt, like KHCO₃ in most CO₂RR applications, which was priorly purged off metal contaminations that are commonly present. The treatment is based on a polymer called Chelex Resin (Bio-Rad Laboratories Inc.) which is able to capture small (ppm) amounts of metal impurities [90, 91]. To achieve cleanness, the Chelex is purged itself by the following procedure prior to usage:

1. Per 1 L of MilliQ Water, 60g of the Chelex Resin is used and cleaned by adding HCL so that a 1M HCl solution is obtained. The solution is stirred for at least 12h.
2. The Chelex is rinsed with MilliQ Water using a filter to capture the Chelex at least with 5 L of water that is poured through the filter.
3. The Chelex is introduced in a 1M KOH solution and stirr it for at least 24h at $T = 60^{\circ}C$.
4. The Chelex is rinsed with MilliQ Water using a filter and at least 5L of water.
5. The last step is to clean the electrolyte for instance in a 0.1M $KHCO_3$ solution by introducing the chelex and stirring for at least 12h. By filtering out the Chelex, a clean metal impurity-free electrolyte can be obtained.

All samples measured within the present work have been evaluated in electrolytes pre-cleansed using the previously described chelex resin procedure.

2.1.4 Electrochemical Techniques

This section intends to shortly summarize the electrochemical techniques and procedures used. All electrochemical measurements are done by using a commercial potentiostat (Autolab, PGSTAT 302 N).

Compensation of Resistances

The compensation of resistances is mentioned first since it is a general concern for all electrochemical experiments and has to be taken into account for all electrochemical experiments, especially those showing high currents.

Generally the applied potential which is defined by using a reference electrode suffers from ohmic losses across the electrolyte. Since the potential is defined by the use of a reference electrode, only the ohmic loss in between the working and the reference electrode has to be taken into account. From the experimental point of view this immediately constraints the position of the reference electrode with respect to the working electrode. Since the ohmic loss is proportional to the thickness of the electrolyte layer that has to be crossed, or the distance of the two electrodes, the reference should be mounted as close as possible to the working electrode within the electrochemical cell. Nevertheless, losses will occur and have to be compensated by increasing the applied voltage to counteract the offset. Since the voltage loss is proportional to the resistance and the current, the target voltage can be calculated as follows:

$$E_{WE} = E_{applied} - E_{IR} = E_{applied} - IR \quad (2.3)$$

Usually this correction is denoted as the IR-correction. Since the current is the standard response function measured in electrochemical experiments, the problem is to obtain the resistance. Most commonly there are two ways of determining the solution resistance in between the reference and the working electrode. Both are based on the fact that the electrochemical cell can be understood in the form of a circuit diagram as a capacitor parallel to a resistor.

This property originates from the solid liquid boundary interface of the electrolyte and a given electrode. Since information about the working electrode is most commonly to be investigated it is the one looked at the most. The interface is sketched in Figure 2.6.

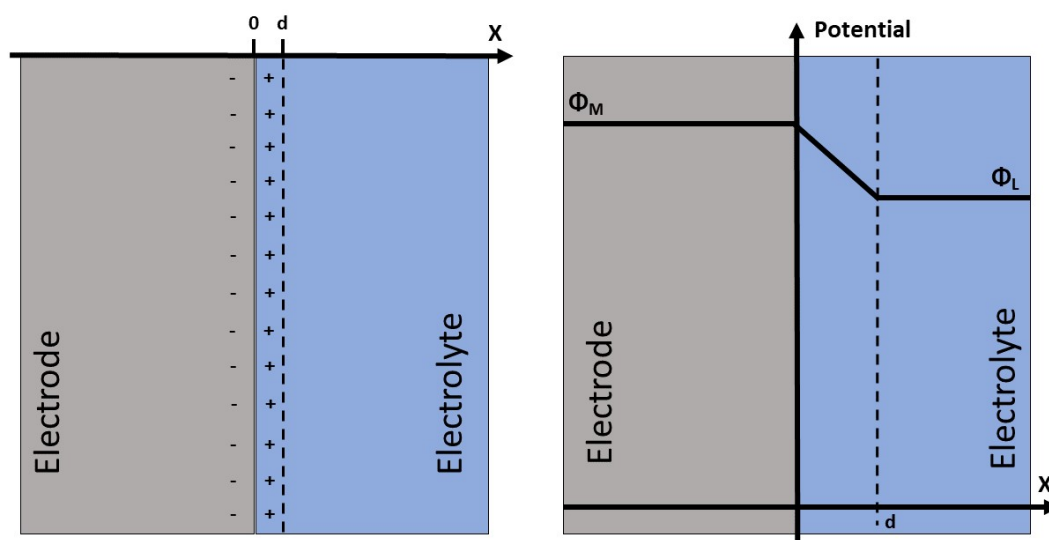


Figure 2.6: Schematic of the Helmholtz layer building up at the electrode/liquid interface and the corresponding change in the surface potential.

Due to the applied voltage at the working electrode, ions of the opposite charge are attracted towards the electrode surface and within its vicinity, the accumulation of an opposite charged layer takes place. This layer is also known as the Helmholtz Double Layer [56]. This layer is also considered as being dominated by diffusive and electric field transport rather than convective due to its behaviour being dominated by the electric field and the concentration difference of species across the double layer interface. This results in a potential drop across the interface and thus there is a different potential, commonly also denoted as the surface potential to refer to solid state interfaces. This potential difference and the separation of charge across the interface is from a physical perspective nothing but capacitor, which is why it can be understood in the framework as such. More precise and detailed models are not discussed here can be found in the related literature[56].

As a consequence, the capacitive behaviour of the cell can be used as a characteristic

fingerprint to extract information from the electrolyte solid interface such as the resistance. One possibility to do this is the frequency modulation while tracking the interface response to it which is commonly denoted as impedance spectroscopy. Another, approach that is used for the experiments conducted in this work is the so called I-interrupt method. It is based on applying a voltage for a short time (commonly 1s) that is used to charge the capacitor of the cell. In the following step the voltage is turned off and the discharge of the cell is measured by monitoring the resulting decreasing voltage over time. Since the discharge is proportional to the time constant $\tau = RC$, the resistance can be estimated from the extrapolation of the measured voltage drop.

Electrochemical Procedures

With the previous discussion in mind the electrochemical procedures and protocols used to run experiments can be briefly explained and highlighted in short which is the goal of this subsection.

Cyclic Voltammetry: Cyclic Voltammetry (CV) is one of the most important and powerful tools of electrochemical analysis. The experiment is based on changing the potential from a defined bottom cathodic potential (U_c) to an upper anodic value (U_a) with a given scan rate. By observing the systems response in the form of monitoring the current, several conclusions can be drawn. Fig. 2.7 shows an example CV acquired on a Cu(100) single crystal in a 0.1M KHCO_3 solution. The peaks linked to a change in the oxidation state are marked and can be seen very well choosing a scan rate that is low enough to resolve them and high enough to get a decent peak intensity.

The information contained in the CVs goes beyond this simple application of measuring the changes in the oxidation state and defining the respective potential needed to drive the changes. Generally, the peaks can also be linked to the adsorption and desorption of specific molecules on different parts of the surface, as the adsorption energy will depend on the surface energy which is linked to the underlying structure of the surface. A common application for instance is CO stripping which is a standard technique on Pt-based materials since Pt manages to adsorb CO strongly. Hereby CO is adsorbed on and stripped off the surface by cycling the potential.

Since the adsorption strength is dependent on the surface orientation as well as on the presence of defects and impurities in the atomic lattice, those can be identified [92, 93]. Furthermore, not only the identification but also the quantification is possible since the obtained peak area and magnitude is highly dependent on the amount of adsorption sites present. Additionally, the technique provides insight into which processes are fully reversible. For these the amount of charge transferred during the adsorption and desorption should be equal to each other, thus the obtained peak area for the respective peaks should be the same.

Looking at the case of Cu which is the most discussed one in CO₂RR, CO stripping is not possible due to its weak binding onto the surface. Instead, OH⁻ is used to probe the presence of specific active sites, defects and binding sites on the surface [45, 94].

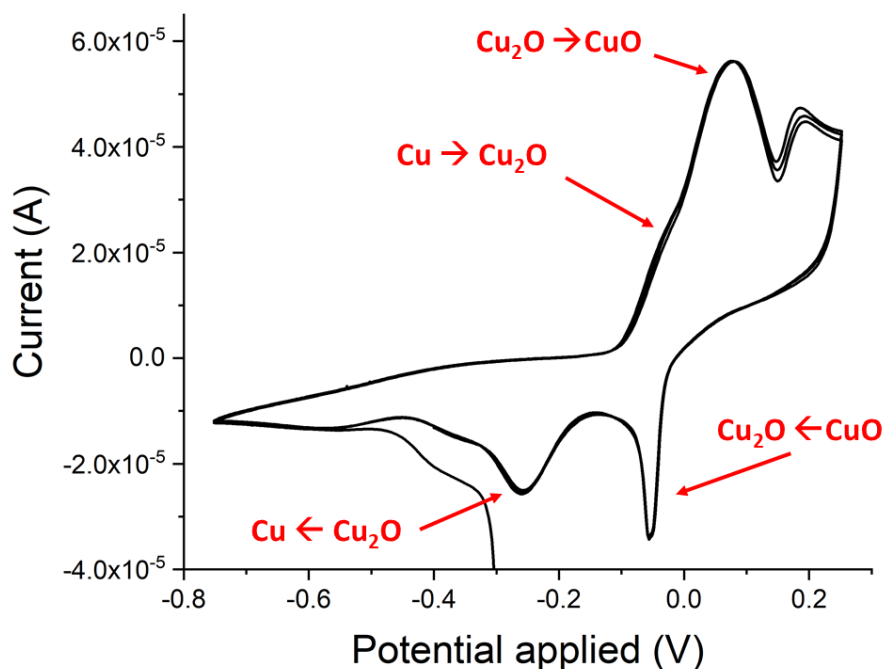


Figure 2.7: Example cyclic voltammety obtained on a UHV prepared Cu(100) single crystal in 0.1M KHCO₃ solution. Reported potential values vs Ag/AgCl.

Chronoamperometry: Chronoamperometry (CA) is a standard technique in which a given constant potential is applied and the response in current is measured. This is usually done to study the long term behaviour and activity of a given catalyst for a given reaction. In the framework of CO₂RR it is commonly used to study the faradaic selectivity of a given catalyst by additionally employing a GC to quantify the evolving gas products. An example chronoamperometry obtained during a CO₂RR experiment is shown in Figure 2.8. The initial decrease of the current magnitude is linked to the initial reduction of native oxides as well as the system converging into its stable kinetic conditions. The abrupt increases in the current magnitude seen throughout the run are related to the gaseous products accumulating at the electrodes surface and being released at once in the form of a bubble which rapidly frees up additional active surface area.

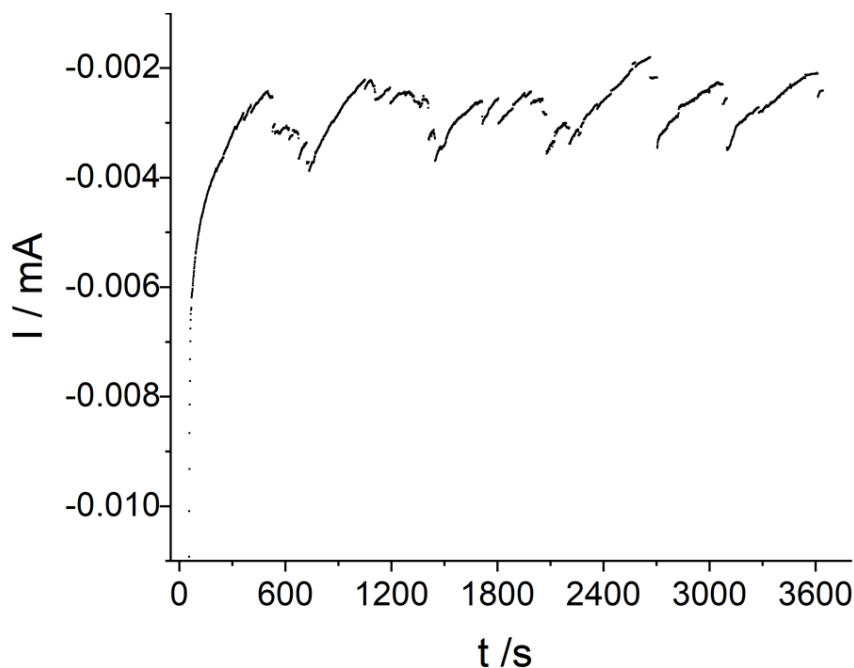


Figure 2.8: Current over time dataset acquired during a chronoamperometric CO₂RR experiment on an electropolished Cu foil at -0.9V vs RHE.

Pulsed electrolysis: Pulsed electrolysis means to apply a series of alternating potentials for a well defined period of time t_p . Usually the technique is used to study the dynamic response of a system which is why short times are most commonly used. Similar to CA, the response of the system is observed by measuring the current. The only difference is that the applied potential is a function of the time and changes accordingly. The advantage over CA is that the technique can be used to dynamically change the chemical environment and/or state of a given catalyst and thereby take influence in its behaviour or study effects related to such. For instance, it is possible to oxidized a catalyst in between a series of two reductive potentials to investigate the influence of the oxides on the reaction. Another application would be the cleaning or refreshing of a given catalyst, for instance if the catalysts gets poisoned during electrolysis by one of the reaction intermediates or products, applying a high enough opposite biased voltage usually results in the desorption of those products.

Capacitance measurements: Electrochemical surface area measurements (ECSA) are also based on the previously discussed capacitance of the Helmholtz double layer. The technique is used to define the surface area of a given catalyst with respect to a reference sample. The most commonly used reference in the field of CO₂ electroreduction is an electropolished Cu foil as it is also the benchmark sample for the gas product selectivity. The technique is based on the assumption that the capacitance

is proportional to the electrochemical surface area:

$$C = \frac{dQ}{dU} = \frac{I dt}{dU} = \frac{I}{dU dt^{-1}} = \frac{I}{S} \quad (2.4)$$

with:

S - scan rate

Using the above definition of the capacitance it can be estimated by looking at the slope obtained from the difference in current at the upward and downward sweep for different scan rates (see Fig. 2.9 (b)). The current difference is hereby to be considered since it arises from the capacitive current being biased opposite to each other at the two sweep directions. When increasing the voltage at an overall negative potential, the double layer gets charged and discharged when decreasing. Since the obtained signals are usually in the μA range and the differences are not to be affected by chemical processes going on, the potential window chosen is usually small and within the range where no chemical reactions occur. An example data set obtained on an electropolished Cu (100) single crystal surface is shown in Figure 2.9. Commonly, unlike here, the current is reported in the form of the geometric current density which is important when comparing surfaces to one another.

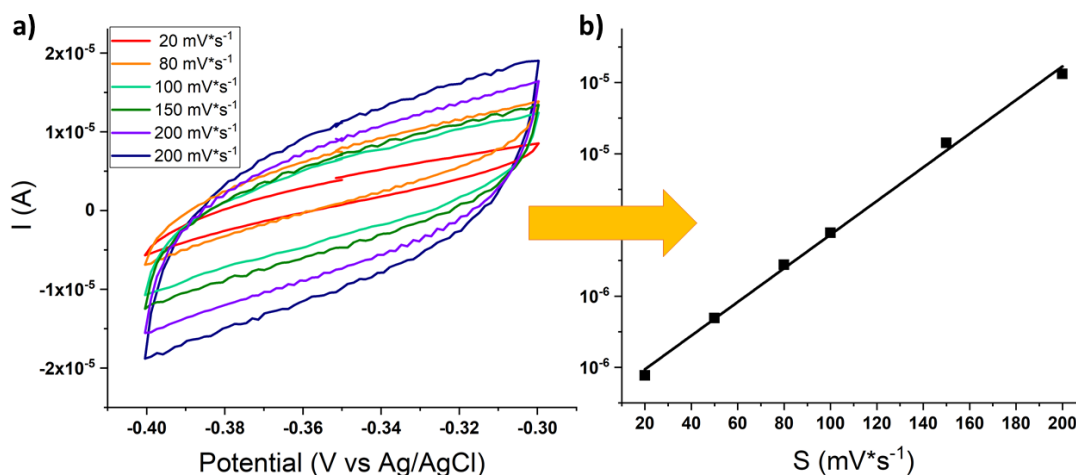


Figure 2.9: (a) CVs acquired at different scan rates and (b) the resulting current difference in between the upper and lower sweep current.

2.1.5 Setup Benchmarking

As mentioned before electropolished Cu foils have become the benchmarking samples among the field of CO_2RR since the pioneering work of Hori et. al [8]. The previously described setups including the electrochemical cell, as well as the potentiostat and the GC are also checked and benchmarked using these type of samples.

Several Cu foils (Advent Research Materials, 99,995 %) have therefore been electropolished (see also chapter 3.1) for 3 minutes each. Consequently they have been measured under CO₂RR conditions at different potentials. The resulting faradaic efficiencies for the gaseous products obtained are presented in Figure 2.10 together with the values reported in the literature extracted from [9].

As it can be seen below, the values obtained with the setup used to study CO₂RR within this work are in agreement with the literature values. This check supports the validity of the calibration as well as the functionality of the setup employed here. Usually this test is repeated after each recalibration of the GC or if any parts of the electrochemical cell have been exchanged like for instance the reference electrode.

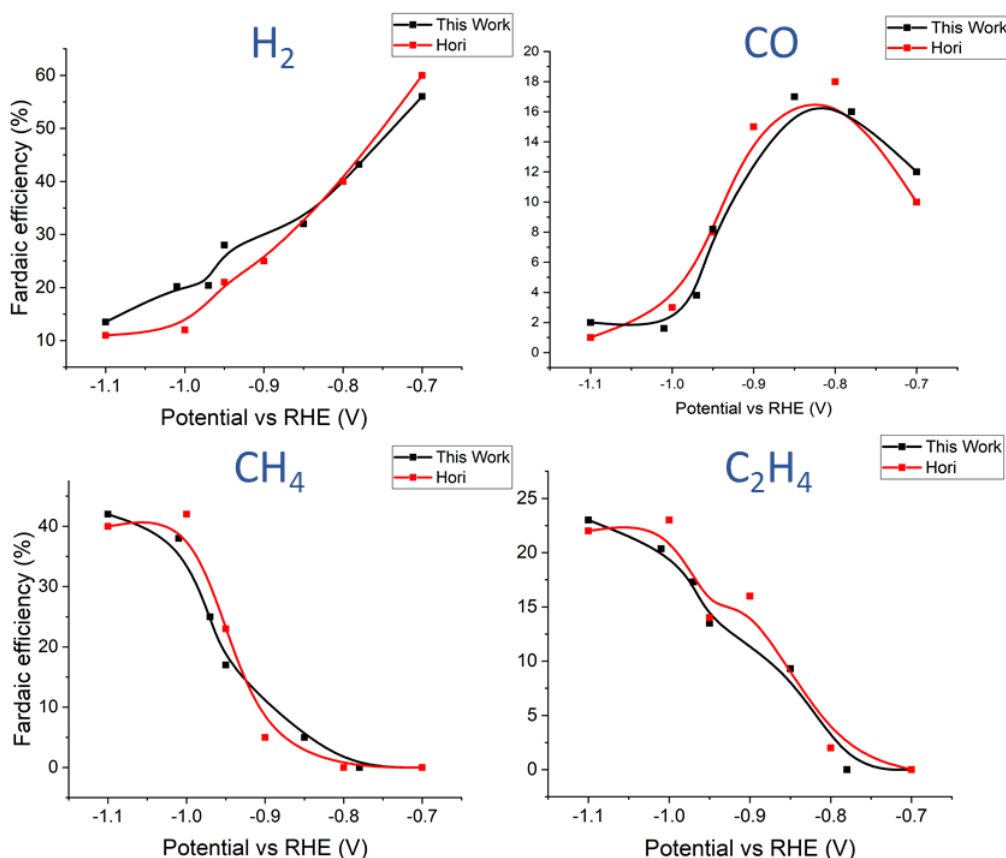


Figure 2.10: Faradaic efficiency for the main gaseous products of an electropolished Cu foil at different potentials. **Black curve:** Measured with the experimental setup used to study CO₂ electroreduction within this work. **Red curve:** Literature values extracted from [9].

2.2 Scanning Probe and Electron Microscopy

Scanning probe microscopy (SPM) covers the physical interaction of a given sample surface and a probe. The probe usually consists of a sharp tip. By probing the interaction strength in between the tip and a given surface when scanning across the surface this techniques can be used to obtain very highly resolved ($< 1\text{nm}$) images of the height and structure of surfaces. The origin of these techniques goes back to scanning tunneling microscopy (STM), which uses the quantum mechanical tunneling effect. Hereby the current obtained due to electrons tunneling across a potential barrier when a small voltage (0-2V) is applied is proportional to the distance of the tip to the sample. Thus, by monitoring and controlling the current, the distance from tip to sample can be obtained. Another similar and commonly used technique is the so-called atomic force microscopy (AFM). Instead of monitoring the current obtained, the forces in between the tip and the surface are monitored. Since those are dependent on the distance of tip and surface to each other, the distance can be obtained. Both techniques are only shortly summarized and sketched within this section to motivate and describe why they are of use to study the electrochemical reduction of CO_2 . Detailed discussions can be found across the literature [95, 96].

2.2.1 Atomic Force Microscopy

Atomic force microscopy (AFM) is based on the interaction and the resulting forces between the employed tip and the sample surface. The magnitude of the force is hereby probed employing a tip at the end of a cantilever that is bended due to the repulsive forces originating form the surface and tip interaction. The experimental setup is schematically presented in Figure 2.11.

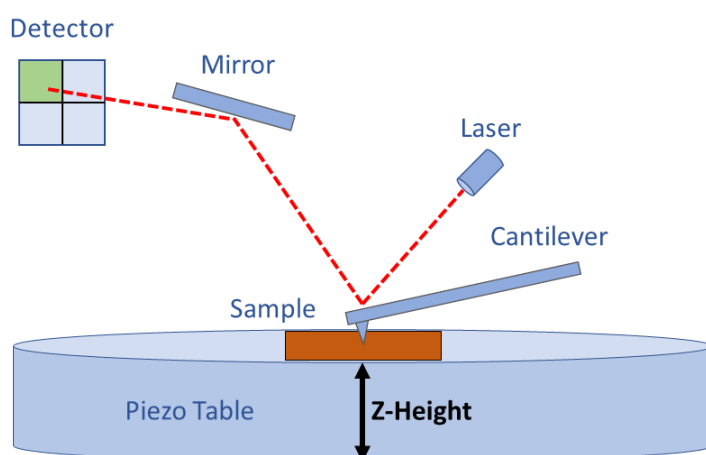


Figure 2.11: AFM set-up.

As can be seen in Fig. 2.12, the cantilever bending results in the movement of the laser movement across the position-sensitive detector by redirecting the laser from the reflective cantilever coating on its back to the detector. This way the detector is able to sense small movements and thus using a feedback loop, the tip to sample distance can be obtained and controlled. By scanning across the surface, the sample topography can be re-constructed. An example of a UHV prepared Cu(111) single crystal model nanoparticle system is shown in Fig. 2.12 (a) and (b). As it can be seen, the height of the nanoparticles is well resolved by AFM. Important is hereby that the lateral size of the objects can not be trusted in AFM measurements due to tip convolution effects making objects appear bigger than they actually are. The tip convolution originates from the fact that the tip has a finite size and a given object is therefore a combination of its own lateral size and the tip size.

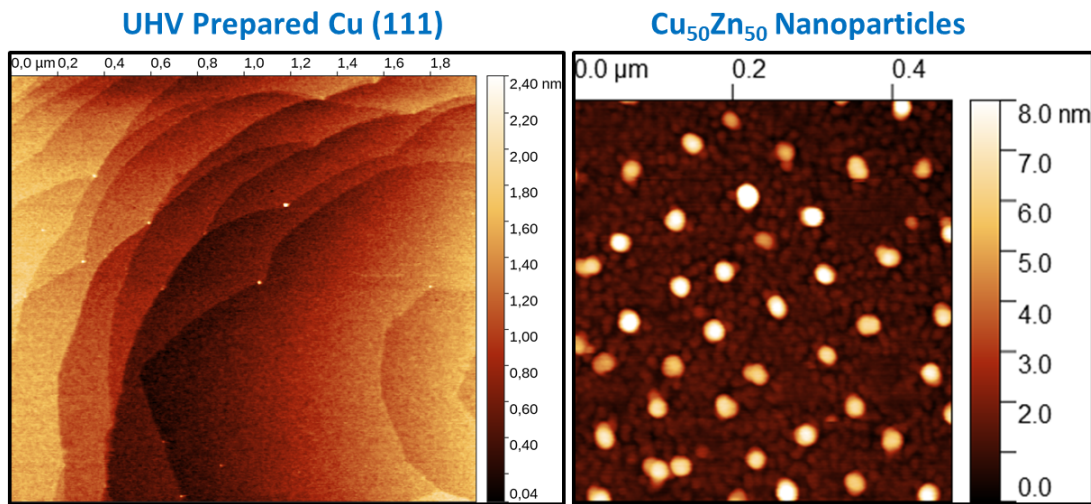


Figure 2.12: Example AFM images taken throughout studies conducted on a clean UHV prepared (see also section 3.3) Cu (111) single crystal and bimetallic nanoparticles consisting of a 1:1 mixture of Cu and Zn supported on a Si wafer.

Briefly talking about the underlying models and forces used in AFM the most important one is the modelling of the cantilever by means of second order differential equation including damping and an external force. During a given measurement, the homogeneous part of the differential equation is used by setting the tip to be moving in its resonance frequency with the help of a piezo motor. The damping term is mostly reflecting simple damping due to the surrounding air or liquid, but also energy dissipation due to the interaction with the surface forces. The external forces who alter the oscillation frequency of the tip are the atomic forces that can generally be attractive and repulsive.

This way of measurement is particularly important since it enables to measure without the tip being in contact with the sample, which can cause damage to the surface. This so-called tapping mode is the preferential one used and also the one

employed for this work. Regarding the surface forces, the repulsive ones are mainly resulting from the Pauli repulsion while the attractive ones originate from dipole moment interactions, so basically Van-der-Waals forces.

The AFM used within this work is a commercial one (Bruker Multi Mode). An image of the setup is presented in Fig. 2.13 (a), also highlighting the laser pathway.

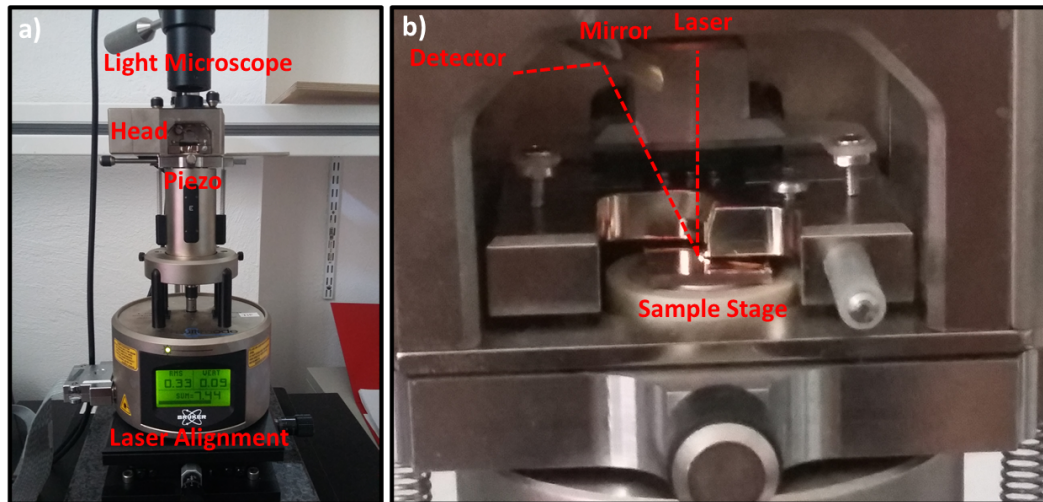


Figure 2.13: (a) Commercial AFM setup used and (b) close-up shot of the sample stage showing parts also mentioned in Fig. 2.11.

Scanning Modes

As mentioned AFM measurements can be carried out in different ways using different scanning modes. The information about the samples surface topology can be extracted from the up and down movement of the tip that is realized by a piezo crystal. The main difference in scanning modes is hereby if the tip is in contact with the sample. Tapping made imaging is the most frequently used mode, as it is less likely to damage the samples surface:

1. **Contact Mode:** As the name suggests the sample is in very close distance to the tip during the whole time of measurement. Usually this mode is employed for very hard and stiff surfaces that give a good and well defined response at all times and are at the same time less likely to be changed by the tip. The benefit of this mode is that due to the strong interaction of tip and sample due to their close distance to each other atomic resolution can be achieved using this mode.
2. **Tapping Mode:** The tapping mode is the most commonly used made as it does not require a direct contact between the sample and the tip but rather

the tip is driven into oscillations near its resonance frequency in the vicinity of the surface. When interacting with the forces originating from the sample, this frequency is changed due to the external force. The shift in the oscillation frequency as well as the accompanied change in the tip oscillating amplitude can be measured and contains the information about the strength of the interaction, which is proportional to the tip to sample distance. Since there is no direct physical contact between the tip and the sample, this mode does not damage the sample surface. Furthermore, this mode provides additional information about the sample, as the phase shift in between two oscillations can be measured, which is proportional to the energy dissipation out of the cantilever system [95, 96]. This dissipation corresponds to the stiffness of the sample and thus the information about the stiffness of different sample regions can be obtained.

2.2.2 Scanning Tunneling Microscopy

STM is based on controlling the distance of the sample to tip by means of the quantum mechanical tunnel current obtained when bringing both closely together while applying a voltage. The tunnel current results from the quantum mechanical properties of electrons being able to jump across a potential barrier due to their wave function existing outside of the barrier, thus them having a likelihood to reside there [96, 97]. The situation is schematically drawn in the form of an energy level diagram in Fig. 2.14 to illustrate the basic working principle of STM. Details about the technique can be found in the literature [98, 99] and are not discussed in detail here since the employed commercial STM (SPECS GmbH) has not been modified.

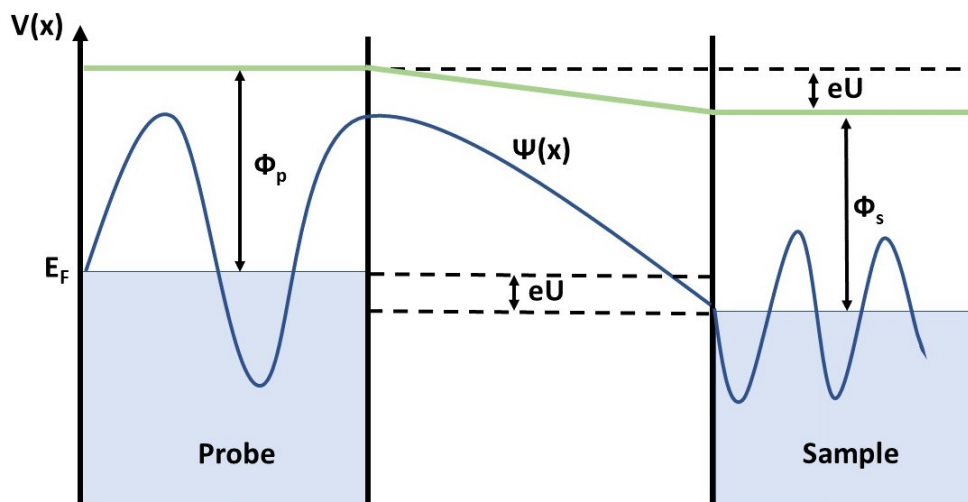


Figure 2.14: Energy level diagram of STM.

In short, the applied voltage offsets the Fermi level of tip and sample with respect

to each other, so that electrons can tunnel throughout the potential barrier into free states on the site with the lower Fermi level. Only electronic states near the Fermi level are mapped and only those accessed depending on the value of the extend potential bias applied. Since the overlap integral of the states within the tip and sample is dependent on the distance of each other this results in a current proportional to their distance. This tunnel current is then used within feedback loop electronics to control the distance with the help of piezo elements. Since STM measurements are usually carried out under UHV environments using the tunnel effect the techniques yields very high precision (atomically resolved) surface topographic images.

The STM used within this work is a commercial one (SPECS GmbH) implemented in the UHV system employed. The tip piezo movement is controlled with the help of the Nanonis (SPECS GmbH) electronics.

2.2.3 Scanning Electron Microscopy

Scanning electron microscopy (SEM) is used to generate highly resolved (nm range) contrast images of a given surface by monitoring the interaction of electrons with a given surface. Additionally so called energy dispersive X-ray (EDX) measurements can be used where the photons originating from the sample, due to exposure to X-rays, are probed. Since their energy depends on the characteristic atomic states it is possible to quantify the elemental composition with the technique. Both techniques are frequently used to study catalysts with respect to their morphology and composition which is also done in the present work. Since no modifications on the commercial SEM setup have been done and the technique is widely spread and discussed into detail in the literature this is not done here (see [100]).

The experimental setup used is the Quanta 200 FEG microscope from FEI with a field emitter as electron source (10 kV). To acquire the images, a secondary electron detector (Everhart Thornley) was employed. The EDX measurements were performed with a separate liquid-N₂-cooled detector (10 kV).

2.3 X-ray Photoelectron Spectroscopy

X-Ray Photoelectron spectroscopy has over the past century since its discovery and understanding of the photoelectric effect made its way into everyday modern surface science. It is a powerful tool as it does not only provide information about the elemental composition of a given surface, but also about the chemical state of those elements.

Fig. 2.15 shows an example spectrum acquired on a clean Cu(100) single crystal without any contamination such as carbon or oxygen for instance.

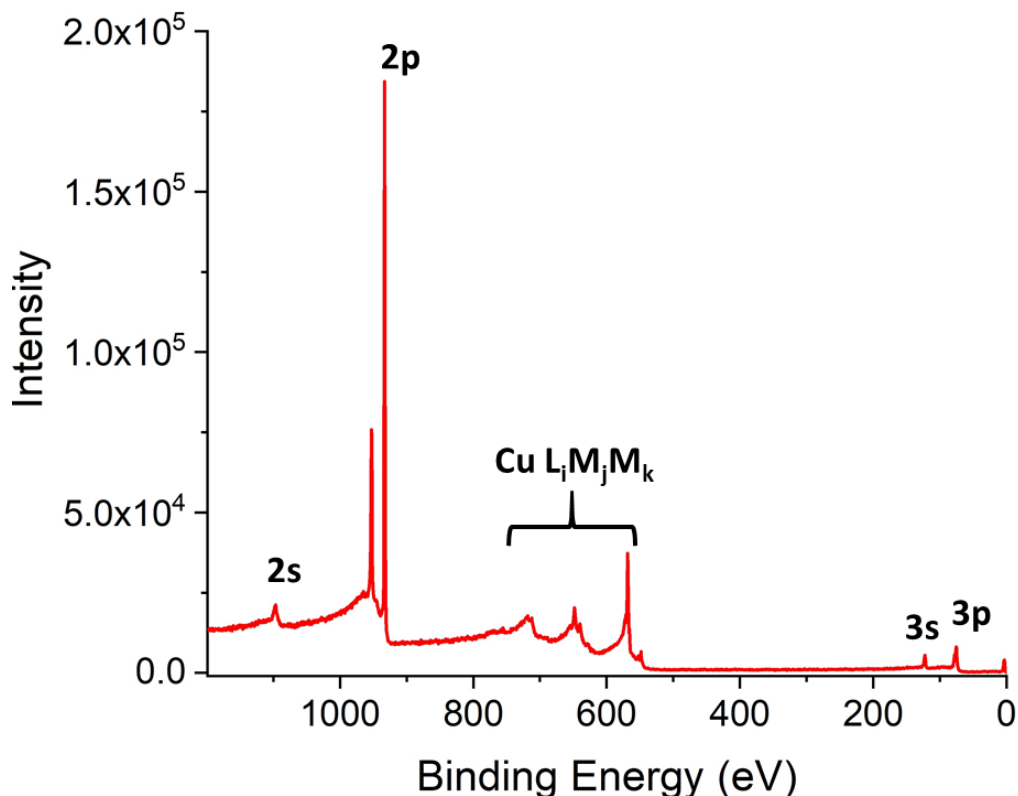


Figure 2.15: UHV-cleaned (see section 3.3) Cu (100) single crystal XPS survey scan. The sample does not contain any oxygen or carbon as judged from the respective XPS scans. Cu peaks are labeled, including Auger peaks Cu-LMM.

The XPS intensity is a function $N(E)$, where E denotes the kinetic or binding energy and N is the number of electrons detected with that given energy. It is common to represent spectra in terms of binding energy even though the kinetic energy of the electrons is measured.

Within the following sections the fundamentals and key features of XPS are discussed briefly focusing on the parts that are important for the present work, as detailed discussion and information on the fundamentals of the technique is also available elsewhere [101].

The basis idea of XPS is to use the fact that the maximum energy available to photoelectrons is the one of the initial photon. By balancing out the equation knowing the initial X-ray energy and measuring the photoelectrons kinetic energy it is possible to determine the binding energy of a given state within an atom the electron originates from. As these energy states are characteristic for each specific element it is therefore possible to identify them (Fig. 2.15). The equation used reads:

$$h\nu = E_{kin} + E_b + \phi \quad (2.5)$$

ϕ is hereby the so called work function. It is the energy difference of the fermi level (highest occupied state) within an atom or compound and the vacuum state (unbound/free electron state).

As mentioned the technique also yields information beyond just the binding energy of electrons within atoms and therefore the identification of elements which is the chemical state of those atoms.

2.3.1 Chemical shifts and energy level splitting

Assuming a constant work function ϕ and a constant initial photon energy the electrons kinetic energy measured only depends on the binding strength of the electron in its quantum mechanical state within the atom. Thanks to the effort directed towards understanding these energy levels during past century it is well known, that these quantum mechanical energy states obey Schrödinger's equation (SE), even when considering multiple atoms bound to each other:

$$H\Psi = E\Psi \quad (2.6)$$

The Hamiltonian H is the operator that thereby contains the information on how the physical properties such as angular momentum, spin, external electric- and/or magnetic fields and so forth (see. [97] for further details) act on the wave function Ψ . When just considering the easy case of a hydrogen atom SE reproduces Bohr's famous values for the energy levels within the hydrogen atom [97], however, when considering the more realistic and complicated case of atoms bound to each other within a solid or liquid solving SE gets far more challenging. Sometimes beyond the scope of our up to date knowledge and capabilities. As detailed mathematical and physical discussions about this topic are available elsewhere [97] again only the general idea and results are presented here to be able understand why photoelectrons are sensitive to the chemical state of molecules and atoms.

When considering multi body quantum mechanics the Hamiltonian accounts for those additional bodies by multiple terms:

$$H = \sum_{i=1}^N H_i + \sum_{i,j}^N H_{ij} \quad (2.7)$$

where the second terms accounts for the cross interaction between atoms and the first for interaction within a single atom. Similar to the Hamiltonians the Wave function will be a linear combination of single atom wave functions:

$$\Psi_{tot} = \sum_{i=1}^N \alpha_i \Psi_i \quad (2.8)$$

Usually these states within molecules represented by Ψ_{tot} are referred to as molecular orbitals. The corresponding SE can be solved using multiple approaches from which numerical methods such as the self consistent Hartree Fock Theory [102] for instance are a very convenient way for many cases. Important here is only that the solution of these equations leads to the so-called initial (n electrons) and final (n-1 electrons) state of the atoms involved. The binding energy of the emitted electron can then be defined as the difference between those states:

$$E_b = E_{final}^{(n-1)} - E_{initial}^{(n)} \quad (2.9)$$

Thus, the energy measured in the experiment depends on the state of the atom before and after emitting the electron due to the photoelectric effect. Generally it is possible to split the obtained energy into different contributions. Here, only the two most important ones for XPS shall be mentioned:

$$E_b = \Delta E_{chem} + \Delta E_{B-element} \quad (2.10)$$

where:

$E_{B-element}$ is the term representing the energy levels of the stand alone atom not bound to any other atom via molecular orbitals (sharing of electrons/states within two or more atoms).

E_{chem} is the energy difference invoked by local changes of the electronic density within a given molecule or in other words atoms bound to each other. Within the molecular orbitals the probability of an electron to be close to one of the atoms can be higher than for the others, resulting in a local effective separation of charge and an electric potential. Therefore the core potential of the atoms can be more or less shielded. This stronger or weaker shielding is consequently affecting the energy of electrons escaping the atoms. Thus, this change in energy contains information about the local separation of charge within molecules and compounds and their binding structure and thereby their chemical state.

A common example for this change in the measured energy are metal oxides. Looking at copper oxides for instance the higher positive charge due to the weaker shielding of the copper atom core results in a lower kinetic energy of photoelectrons and thereby, in a higher binding energy. For the electrons escaping the oxygen atoms the trend is the opposite as there is a higher negative charge. An example of the

Cu 2p XPS line spectra for copper and copper oxide is given in Fig. 2.16. As seen here there is a clear shift in the binding energy of the oxide species with respect to the metallic peak. In addition there are two peaks for CuO, the so called shake-up peaks. Those can only be seen for CuO and other compounds where copper is in the 2+ state (Cu^{2+}).

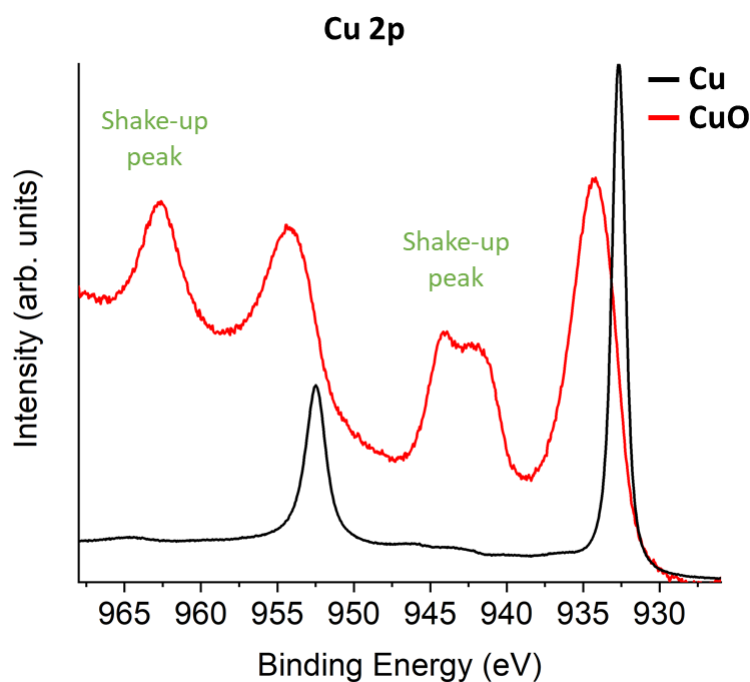


Figure 2.16: Cu 2p XPS spectra of a copper (black) and a copper oxide sample (red). Acquired on UHV cleaned polycrystalline Cu Foil and 10 min oxygen plasma treated Cu foil.

These arise from the fact that the emitted photoelectrons can scatter with and impart energy from another electron within the atom final state. If the electron scattered with is lifted into a higher unoccupied state within the atom it is called shake-up and when even set free into a vacuum state the process is called shake-off. Nevertheless the initial electron will lose parts of its kinetic energy resulting in a well defined peak at higher binding energies within the XPS spectrum. Why this peak only shows up for CuO or other 2+ states in Cu is due to the amount of electrons being used to bind within then the molecules. In the case of CuO the electrons used to bind have a higher probability within the molecular orbitals of being close to the oxygen atom resulting in effective free states in the Cu band structure. This increases the cross section of scattering processes significantly that involve the occupation of free valence states and thus shale up electrons are likely to be pushed into these states by emitted electrons from the core levels due to the photoelectric effect.

As discussed it is usually possible to distinguish the oxidation states by shifts in binding energies of even additional peaks arising but not for all. For instance to be able to identify Cu_2O in which copper is in its one plus state (Cu^+) using only the core level spectra is not sufficient. Fortunately, there are additional processes that lead to so-called Auger electrons that are even more sensitive to the chemical state of a given atom. Auger electrons are different from photoelectrons in the sense that they are produced by secondary processes after the photoelectric effect has taken place and left an unoccupied core level behind. These core levels can be refilled by electrons from higher shells having a lower binding energy as compared to the one within the core level. The energy difference between those two states results in the creation of a photon with exactly that energy. This photon can then again be annihilated and invoke another photoelectric effect, ejecting an electron with a lower binding energy than the aforementioned electrons. The process is sketched in terms of an energy diagram in Fig. 2.17.

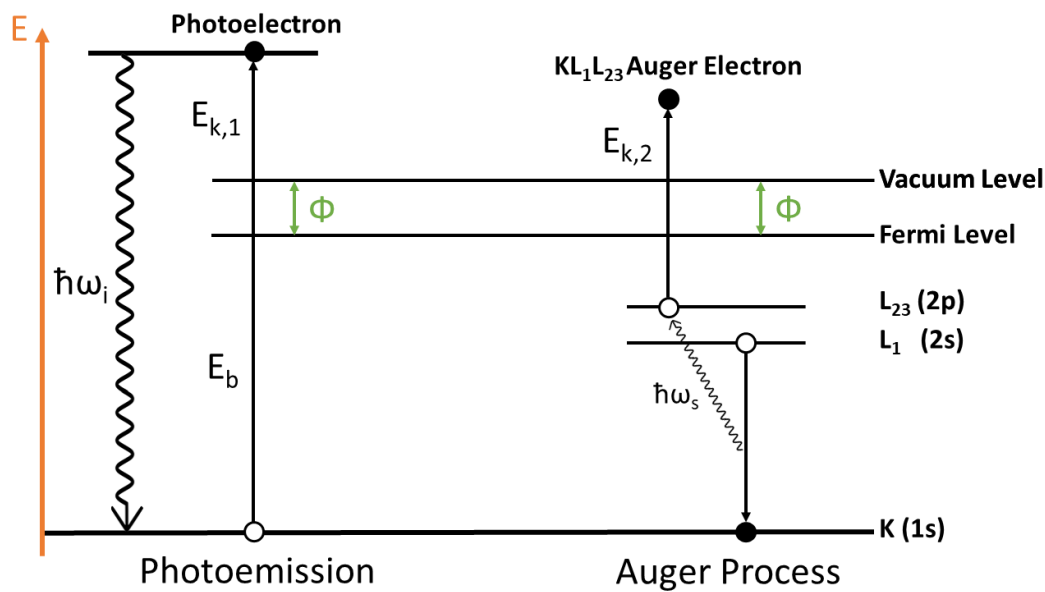


Figure 2.17: Energy diagram of the photoelectric effect (left) and secondary auger electron processes (right).

Usually the resulting Auger electrons originate from the outer shells of the atoms involved due to their nature of having a higher energy state than the core level ones. Since especially those electrons within or close to the valence states are involved into molecular binding, they contain more information about the chemical state and binding environment than the core level atoms who are only shifted in energy due to feeling an altered core potential when escaping the atom.

Sampling depth

Since electrons are used to extract the information in XPS the technique is mainly surface sensitive, as the interaction probability of electrons with surrounding matter is very high. Once the energy of the electrons used is altered the information is lost. Thus, the obtained spectra will reflect the first atomic layers depending on the scattering cross section the involved electrons. Generally this cross section is different for each material and depends on the energy the electrons have. It is sufficient to summarize these scattering processes in a more or less macroscopic approach by only looking at the absorption in dependence of the travel distance of the electrons. This absorption law is described by means of a first order differential equation that assumes a constant average length, which electrons can travel without scattering to occur. This length is the so called mean free path λ . The underlying then equation reads:

$$I(d) = I_0 e^{-\frac{d}{\lambda}} \quad (2.11)$$

By knowing λ it is therefore possible to estimate the sampling depth d from which electrons originate. Since this issue has been explored to an extent in the past the values used within this work are based on the available literature. A good summary of these empirical data is the so called universal curve [103].

2.3.2 Experimental realisation

The first experimental realisation of the XPS setup employed in this work is a commercial product as sold by SPECS GmbH. The setup consisting of a X-ray source (XR50 SPECS GmbH) with Al ($E_{k_\alpha} = 1486.3eV$) and Mg ($E_{k_\alpha} = 1253.6eV$) as anode material. The energy filtering of the electrons is done with the help of the Phoibus 100/150 Analyser (SPECS GmbH, 5 CCD Detector) which is mounted into a standard type UHV chamber (base pressure $p = 1.3 * 10^{-9}mbar$).

The second used XPS setup is also a commercially available one (SPECS GmbH). It is equipped with the XR50X-ray source (Al anode) and the Phoibus 150 analyser with a 5 CCD Detector. Additionally the setup is equipped with a monochromator. The base pressure of the UHV chamber is $p = 3.6 * 10^{-10}mbar$.

Sample charging

A common problem of XPS is charging of the sample which mostly occurs for samples with high resistance where compensating the positive build up charge due to electrons leaving the sample via the photoelectric effect is not sufficiently fast enough. Usually when operating the used X-ray sources at 300W the current of electrons leaving the sample is within the nA range and therefore easy to be compensated for. This compensation is done by using a so called flood gun (SPECS

GmbH, FG22/35) which sends electrons towards the sample so that the positive charge is compensated. This compensation current and the power of the gun have to be calibrated and adjusted for all of the given samples and is usually done by increasing the gun current until charging effects vanish from the measured spectra. These effects are visible by either an increased asymmetry of the peaks as electrons lose part of their kinetic energy when escaping the material and therefore appear to be at higher binding energies, or by overall altered and shifted peaks that completely lose their shape. For copper a common approach that is also followed within this work is simply to compare the obtained data on samples susceptible to charging with those from clean non charging reference spectra.

The effect of charging can be very dominant for samples and catalysts that are not-bulk like but not bigger than several nanometers. For those due to a possible bad contact with the sample support or a general low amount of free charge carriers within the material, charging effects can occur quite fast. In fact it has been reported for samples consisting of small nanoparticles that the peak shifts due to charging observed in XPS spectra can be proportional to the size of those particles [38].

2.3.3 Copper Reference Spectra

To be able to judge in what chemical state a given sample is, it is crucial to analyse the mentioned parameters, such as the position, width and shape of specific peaks originating from core level or Auger electrons. This creates the need for well defined references to compare with. Since the scientific section focuses on copper and also its compounds, those references have been measured and compared with the literature to gain insight into their quality. The Cu 2p and Cu LMM Auger spectra used as reference spectra throughout this work are shown in Figure 2.18.

All spectra but the metallic are aligned to the carbon C 1s line using $E_B=284.8\text{eV}$. The metallic was aligned to the Cu 2p peak energy using $E_B=932.67\text{eV}$ ([104]) since it does not have any carbon on the surface due to being UHV cleaned. Table 2.1 summarized the obtained binding energies for the Cu 2p peak maximum, the kinetic energy for the Auger peak maximum and the corresponding modified Auger parameters. Hereby, the Cu sample has been *in situ* UHV-cleaned (see also section 3.3), the CuO was made by oxygen plasma treating a Cu foil for 5 minutes (see section 3.4) and the other compounds have been measured on commercially available powders (Sigma Aldrich, 99,995% purity).

The obtained values are in good agreement with the ones reported in the literature proving the functionality of the employed system [104, 105].

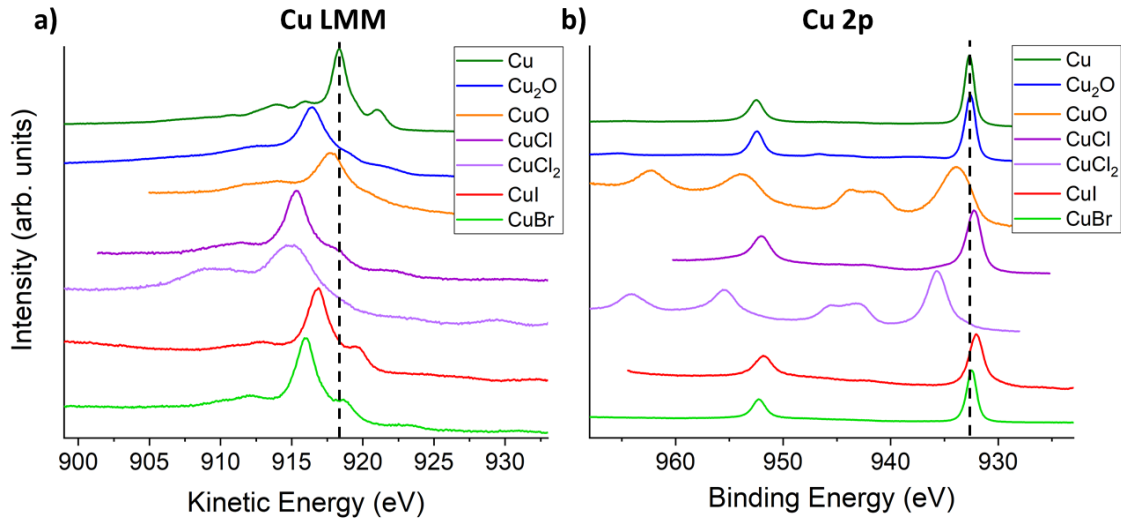


Figure 2.18: (a) Cu LMM and (b) Cu 2p reference spectra of different Cu compounds relevant for the analysis of the investigated catalysts within this work. Dashed line marks the main peak of metallic Cu.

Species	Cu 2p E_B (eV)	Cu LMM E_k (eV)	Auger Parameter (eV)
Cu	932.67	918.2	1850.87
Cu ₂ O	932.58	916.4	1848.98
CuO	933.8	917.71	1851.51
CuCl	932.25	915.38	1847.63
CuCl ₂	935.73	914.8	1850.53
CuI	935.73	917.2	1848.8
CuBr	932.46	915.89	1848.35

Table 2.1: Cu 2p binding, Cu LMM kinetic and the corresponding modified auger parameters energy values for the references used within this work.

2.4 *Operando* and *In Situ* Techniques

As atomic structure, order and chemical state are important parameters when it comes to understanding the underlying processes to a catalytic reaction on the atomic scale, it is important to use and further develop experimental techniques that provide insight on these. While *ex situ* studies are not able to provide detailed information about the state of samples during the electrochemical reaction due to the sample subsequent exposure to air which can significantly alter the sample state, *in situ* and *operando* techniques are closer to the real conditions. In fact, the *operando* term designs measurements carried out while the reaction is running and while measuring the reaction conversion and products. *In situ* measurements are conducted while protecting the sample from changes after the reaction by keeping it in a protective gas atmosphere or under UHV conditions but without the catalytic turn-over.

Generally the noble metals such as Au or Pt who do not undergo a big change when exposed to air or mild electrolytes conditions such as 0.1M KHCO₃ or 0.1M KOH solutions at room temperature are able to be examined on *ex situ* based experiments. Naturally this does only hold true if the reactions studied do not require high potentials, so that the oxidation state during the reaction would be different from the thermodynamically stable state under normal conditions. For metals such Zn, Sn or the most interesting within this work copper, it is not sufficient to use *ex situ* based experiments, as exposure to air alters the chemical state with respect to the one during CO₂RR conditions, when the catalytic processes occur.

Therefore, it is necessary to develop new techniques and approaches to be able to monitor structure and chemical state of the catalysts as close as possible to the real conditions. The following chapter gives an overview over two of these approaches, where the first has been developed and improved within the framework of the present work and the second is a well known *operando* technique within the field of catalysis.

2.4.1 Quasi *In Situ* XPS

Even though *operando* X-ray absorption fine structure (XAFS) measurements (see next section) provide valuable information about the sample composition and structure during the catalytic reaction it is mainly a bulk sensitive technique. Also these measurements require a lot of effort and cannot be conducted on a daily basis as a synchrotron is required to provide high energy and intensity X-rays. These reasons motivated the efforts to construct a lab based experimental setup that employs a standard XPS setup, so that experiments can also be conducted on lab based X-ray sources. The choice to use XPS as a spectroscopic technique was made due to the fact that XAFS is mainly bulk sensitive and XPS is very surface sensitive, so that the combination of both provide a detailed view on the samples studied.

To overcome the mentioned problems of *ex situ* based studies that expose the sample to air which leads to contaminations and changes in the chemical state, an experi-

mental setup that would be as close to an *in situ* characterization as possible was planned.

When wanting to combine these ideas with electrochemistry, the problem is that electrochemistry requires an electrolyte mostly based on water in the liquid phase. Having water in liquid phase under UHV conditions is, however, not possible. Even near ambient pressure (NAP) based approaches that are used to mimic environments for gas phase based reactions and studies are not enough as the technical limit in most NAP-XPS based system is within the mbar range, as the X-ray source compartment has to be separated and kept under UHV conditions while acquiring gas phase XPS data. This is usually done by a silicon nitrate window allowing X-rays to pass and to resist pressure differences up to almost 25 mbar. Furthermore, the inelastic mean free path of electrons is very low, leading to low signals due to inelastic collisions of photoelectrons with atoms and other electrons within the escape depth if the pressure is too high.

Thus the samples have to be introduced to normal conditions in order to do electrochemical measurements and treatments before they are reintroduced to UHV conditions to do the XPS analysis. This is the main idea of the presented and developed setup which is shown in Figure 2.19.

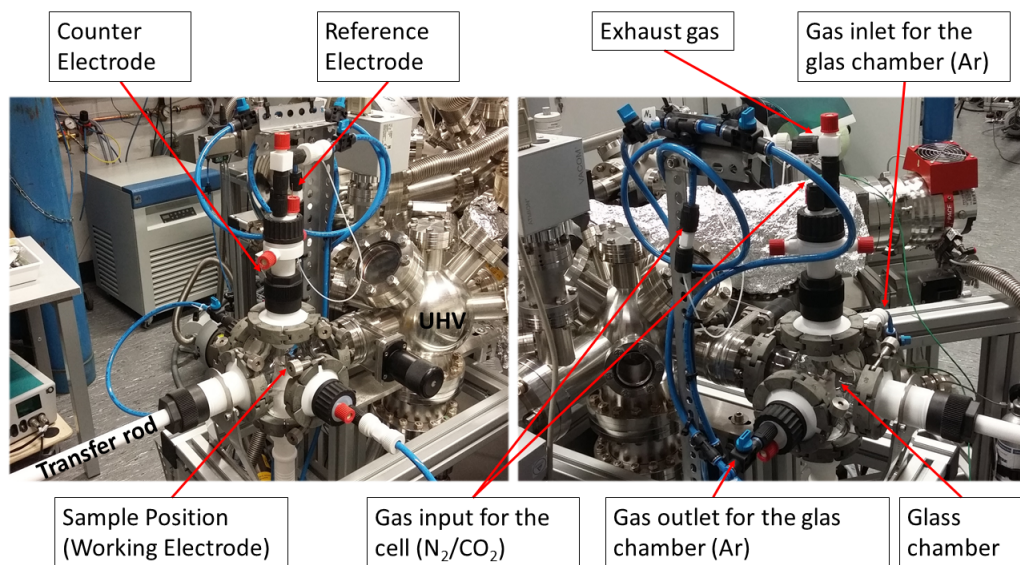


Figure 2.19: Electrochemical cell directly attached to an UHV setup.

The samples are kept in UHV until they are to be transferred to an electrochemical cell that is directly attached to the UHV system. The UHV part is hereby vented by nitrogen (N_2 , 99,9999%, Air Liquide) while the glass compartment part (glass cross) is kept under a protective pressurized Argon ($p_{Ar} = 1.1$ bar, 99,999%, Air Liquide) atmosphere. Argon was hereby chosen as the mass of Argon is higher than nitrogen with respect to oxygen and therefore keeping oxygen from the surrounding

air out of the transfer compartment is easier. This constant overpressure results in a flow of argon out of the cell throughout the exhaust line of the glass volume part. Therefore, the cell and the glass part are constantly flushed with clean pressurized argon during the sample transfer, protecting it from contaminants and oxygen.

Once the sample is transferred into a stamp stage, the stamp with the sample on top can be pressed against the electrochemical cell made out of PTFE (Teflon), leading to a sealing of the cell compartment with respect to the Argon atmosphere. In the following step the cell is filled throughout a septum with the electrolyte which has been previously saturated with CO₂ for 30 min for CO₂RR based experiments. The gas volume making space for the electrolyte is able to escape the cell compartment through an exhaust which is sealed against air, preventing back stream into the cell. This exhaust line is also used for the gas products as well as the CO₂ (99,9999%, Air Liquide), which is constantly introduced into the cell with a flow rate of $f = 20 \frac{mL}{min}$ through a 0.5mm thick Teflon tube. The tube is installed in a way so that once the electrolyte is filled in it is constantly bubbled with the CO₂ gas, keeping the electrolyte saturated during the whole experiment. The amount of electrolyte used is usually 25 mL, however, the cell allows for a total volume of 63 mL. As reference electrode a leak-free Ag/AgCl electrode (LF-1, Innovative Instruments, Inc.) is used which sits directly in front of the sample ($d < 0.2mm$) so that the resulting resistance that has to be compensated is minimal. As counter electrode a Pt mesh (99,9999%, Sigma Aldrich) is employed and the electrical contact is fitted through a septum out of the cell using a 1 mm thick Pt wire (99,9999%, Sigma Aldrich). The downside of this cell setup is that the whole cell is a one compartment cell not allowing to quantise the gas products online, as the counter reaction is also taking place in the same volume.

After the electrochemical treatment has been conducted the cell is reopened and reconnected to the pressurized argon volume by removing the stamp from the cell on which the working electrode rests. The electrical connection for the working electrode is made by a Pt wire spot welded to a metal plate and a standard BNC pin on the other side.

Once the sample is removed it is rinsed from the residual electrolyte by 10 mL of deionized Water ($R = 18.2 M\Omega$), that was bubbled with Argon (99,999%, Air Liquide) for 30 minutes to purge it of oxygen. Note that during this time there is no electrical connection and thus no control of the potential throughout the circuit used during electrochemistry, which can lead to changes in the sample composition depending on the material used. Once the sample has been transferred back into the UHV compartment, it is sealed again by a valve and pumped down to a base pressure of $p = 2.1 * 10^{-8}$ mbar. The residual water resting on top of the sample is thereby vaporized and pumped out of the compartment. As known in UHV technology, water is a common residue sticking on the walls of steel-based chambers, which explains why once the cell is used on a daily basis only a base pressure within the 10^{-8} and not 10^{-10} mbar regime is achieved. The whole transfer from the EC cell to the UHV part and backwards does not usually take more than 1 minute. If the user

is experienced, the transfer can be carried out within 20 seconds. All measurements with this cell are done using an Autolab potentiostat (PGSTAT 302N).

2.4.2 X-ray Absorption Fine Structure: XAFS

X-ray absorption fine structure (XAFS) or extended X-ray absorption fine structure (EXAFS) is a technique that was developed during last century in the framework of synchrotron-based applications. It was first used to study the collisions and therefore the nature of fundamental particles and matter itself, however, quickly enough its use has been expanded to different fields. Charged particles, who can be confined within a synchrotron by usage of magnetic fields, emit radiation when being accelerated, whose energy is proportional to the strength of the acceleration and the energy of the charged particle and can be used as a source to generate well defined X-ray radiation. Depending on the size of the synchrotron ring and therefore the maximum energy to which electrons and positrons which are most commonly used can be accelerated to, the obtained X-rays can have energies up to several keV even MeV. The most common technical realisation of generating these x-rays is to use undulators (see also [106]) which are accelerating the used particles originating from the synchrotron ring by employing strong alternating magnetic fields. Since high energy X-rays are able to penetrate matter if there are no sufficient energy states within the atoms of the material to absorb them, light elements can be penetrated easily. This is of great use when considering combining electrochemistry and XAFS together as the water based electrolyte does not absorb much of the used X-rays. Before explaining these *operando* XAFS experiments in detail, first the fundamentals of XAFS are shortly summarized.

2.4.3 Fundamentals of XAFS

XAFS is a technique that is based on the absorption of X-rays within a given material. The amount absorbed depends on the energy of the X-rays with respect to the energy levels of the electrons bound to the atoms of a given material. The absorption process can be described by means of a first order differential equation leading to Lambert's Law:

$$I_{transmitted} = I_{initial}e^{-\mu(E)d} \quad (2.12)$$

where:

$I_{transmitted}$ - is the transmitted signal intensity

$I_{initial}$ - is the initial signal intensity

$\mu(E)$ - is a linear absorption coefficient

d - the thickness the photons travel through

As electrons can only be freed up by the photoelectric effect once the energy of the incoming photon is high enough there is no absorption below that threshold

energy and a significant jump in the absorption of X-rays within a material once their energy is high enough. This energy is usually referred to as the edge energy E_{edge} since the corresponding absorption coefficient $\mu(E)$ shows a strong increase in its intensity around this energy which is therefore also called the edge jump. To illustrate this behaviour an example K-edge EXAFS spectrum measured on a clean metallic copper sample at the synchrotron facility DESY Hamburg is shown in Fig. 2.20.

The so called X-ray absorption near edge structure region (XANES) is marked blue and consists of the previously discussed edge jump and features which are characteristic for the material as well as its chemical state which is often invoking a shift in the edge position. The green marked part is the EXAFS part which provides information about the structure such as for instance the coordination number of atoms and thus also about the chemical state of a given material. Understanding these type of spectra, especially the oscillations within the EXAFS part is possible by keeping the wave nature of electrons in mind. As two or more electrons are ejected from an atom and its neighbours these electron waves interact with the surrounding atoms.

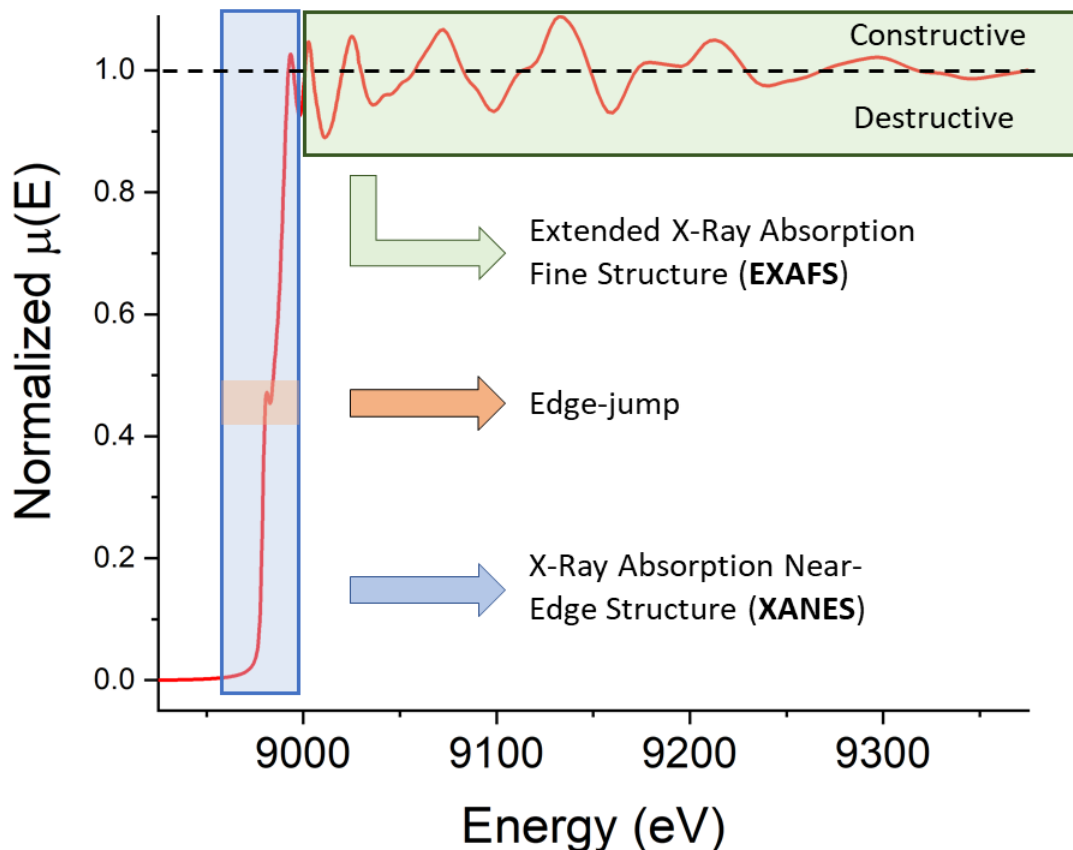


Figure 2.20: Normalized absorption coefficient as a function of the energy, measured from a bulk metallic copper sample for the K-shell.

Representing them as spherical waves their wave number and therefore wavelength ($\lambda = \frac{2\pi}{k}$) is linked to their energy via :

$$k = \sqrt{\left(\frac{8\pi^2 m}{h^2}\right) (h\nu - E_B)} \quad (2.13)$$

where $h\nu$ is the photon energy and E_B is the binding energy which can also be expressed in terms of the edge energy ($E_B = E_{edge} - E_0$) if E_0 is defined to be the kinetic energy of the photoelectron at the absorption edge.

The absorption coefficient $\mu(E)$ is (within a dipole approximation, see also [106]) proportional to the transition probability of the photoelectric event which can be described by means of Fermi's Golden Rule [97]:

$$\mu(E) = A |\langle \Psi_f | \hat{V} | \Psi_i \rangle|^2 \delta(E_f - E_i - h\nu) \quad (2.14)$$

Where \hat{V} is the electric field polarisation energy that pertubates the inital state electrons. It is convenient to split the final state wave function into two components reflecting the non-scattered and the scattered part:

$$\Psi_f = \Psi_{outgoing} + \Psi_{backscattered} \quad (2.15)$$

These outgoing and backscattered spherical electron waves are able to interfere with one another which is also reflected by equation 2.14, since the square will invoke cross terms to emerge when inserting the final state wave function into it. The resulting interference will be either constructive or destructive depending, on their wavelength and phase. As the phases of these two wave components depend on their path length the interference pattern is affected by the distance of neighbouring atoms at which the scattering occurs. Thus, information about the lattice structure with respect to bonding distance and coordination number can be extracted from the EXAFS signal.

With this in mind it is also helpful to split the absorption coefficient in two components due to its proportionality to the matrix element in eq. 2.14, since there are two components arising when using 2.15 as final state wave function:

$$\mu(E) = \mu_0(1 + \chi) \quad (2.16)$$

with μ_0 representing the atomic single background signal and χ accounting for the scattered oscillating part of the signal. Knowing and modelling the function χ constitutes the EXAFS analysis. From the experimental point of view it can be determined using the measured signal by:

$$\chi = \frac{\mu_{total} - \mu_{atomic}}{\mu_{atomic}} \quad (2.17)$$

The theoretical modelling of χ is well studied. As other authors have already given a detailed derivation of the function, here only the final result shall be given [106, 107]:

$$\chi(k) = \sum_{i=1}^{shells} A_i(k) \sin \Phi_i(k) \quad (2.18)$$

where $A(k)$ is the amplitude factor for the corresponding shell and the \sin function models the oscillations. The amplitude function is hereby given by [106, 107]:

$$A_i(k) = \frac{N_i}{kR_i^2} S_0^2 F_i(k) e^{-2k^2\sigma_i^2} e^{-2R_i\lambda^{-1}k^{-1}} \quad (2.19)$$

where:

$F(k)$ - is the backscattering amplitude.

S_0^2 - is the amplitude reduction factor accounting for many body effects such as shake-up and shake-off.

λ - is the inelastic mean free path.

R - is the radial distance.

N - is the coordination number.

σ - is the disorder factor.

Modelling the obtained data using this theoretical function makes possible to extract information about the coordination number, the disorder and the distance of atoms to each other from the EXAFS part of the obtained signal. Most commonly it is convenient to interpret the data in K-space, whose spectrum can be easily obtained from the energy-dependent spectrum by using eq. 2.13. For the case of the previously shown data on a bulk metallic copper sample (see fig. 2.20) the K-space spectrum obtained is shown in fig. 2.21

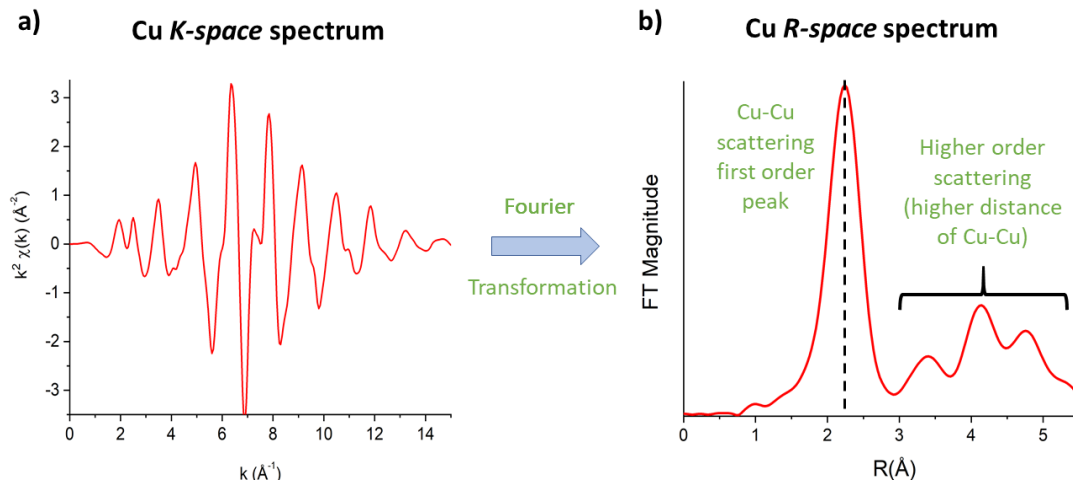


Figure 2.21: a) K-space spectrum of copper for the data shown in fig. 2.20. b) R-space representation as obtained from K-space spectrum by Fourier transformation.

The advantage of representing the data in R-space, obtained by Fourier transformation of the K-space signal (see fig. 2.21. b), is that the distance of neighbouring atoms can be directly seen. Thus, the first main peak at 2.2 Å reflects the scattering of the spherical outgoing wave with the first neighbouring atom, while peaks at higher distances corresponding to second, third and higher order scattering processes. As these distances are also characteristic for different chemical states of elements, this information can also be extracted from the R-space representation of the EXAFS signal.

Further analysis leads to modelling the obtained spectra by means of the above mentioned equations (2.18, 2.4.3). Usually this is done with the help of computational software to speed up the calculation process significantly as well as the data handling. Within this work the software used is the one most commonly employed within the field of XAFS measurements. It is the software package Athena [108, 109] which can be used to process the XANES data and to do linear combination fitting of it, and the Artemis software using the FEFF6 code [108] to conduct the analysis of the EXAFS data.

2.4.4 Operando XAFS setup

The experimental setup used to conduct *operando* XAFS measurements is shown in Fig. 2.22. The three electrodes are marked up as well as the sample position and CO₂ input line. For all data acquired within this work the used CO₂ flow rate was equal to the one used in the gas chromatograph based experiments ($f = 20 \frac{ml}{min}$). The reference electrode was a commercial leak-free Ag/AgCl electrode (LF-1, Innovative Instruments, Inc.). The data is acquired in a fluorescence setup, meaning that the transmitted amount of X-rays is not being measured, but the one being absorbed is used to determine the absorption coefficient $\mu(E)$. This is possible since the absorption of X-rays within the sample would naturally lead to electrons filling vacant core level states within the atoms from which electrons have been freed up by means of the photoelectric effect.

The resulting photons from this process can be detected and make up the fluorescence signal intensity which is thus proportional to the amount of absorbed X-rays within the sample. The detector used is a passivated implanted planar silicon (PIPS) detector. This mode of measurement has the advantage that even for very thick samples data, acquisition is possible. Since the transmitted signal has to cross not only the sample but also the electrolyte and the cell walls, the signal obtainable is very low, especially for nanosized catalysts where not much material is present. Therefore, it is more convenient to acquire *operando* electrochemistry datasets in fluorescence. The downside is that the obtained intensity of the signal is altered by so-called self-absorption. As the name suggests, this means that the secondary photons are able to be reabsorbed and scattered within the material itself. Fortunately this scattering and re-absorption processes can be modelled, allowing the correction of the obtained signal for self absorption. This is usually done by

computational algorithms provided within the Athena software package that have been developed and improved in the past [109].

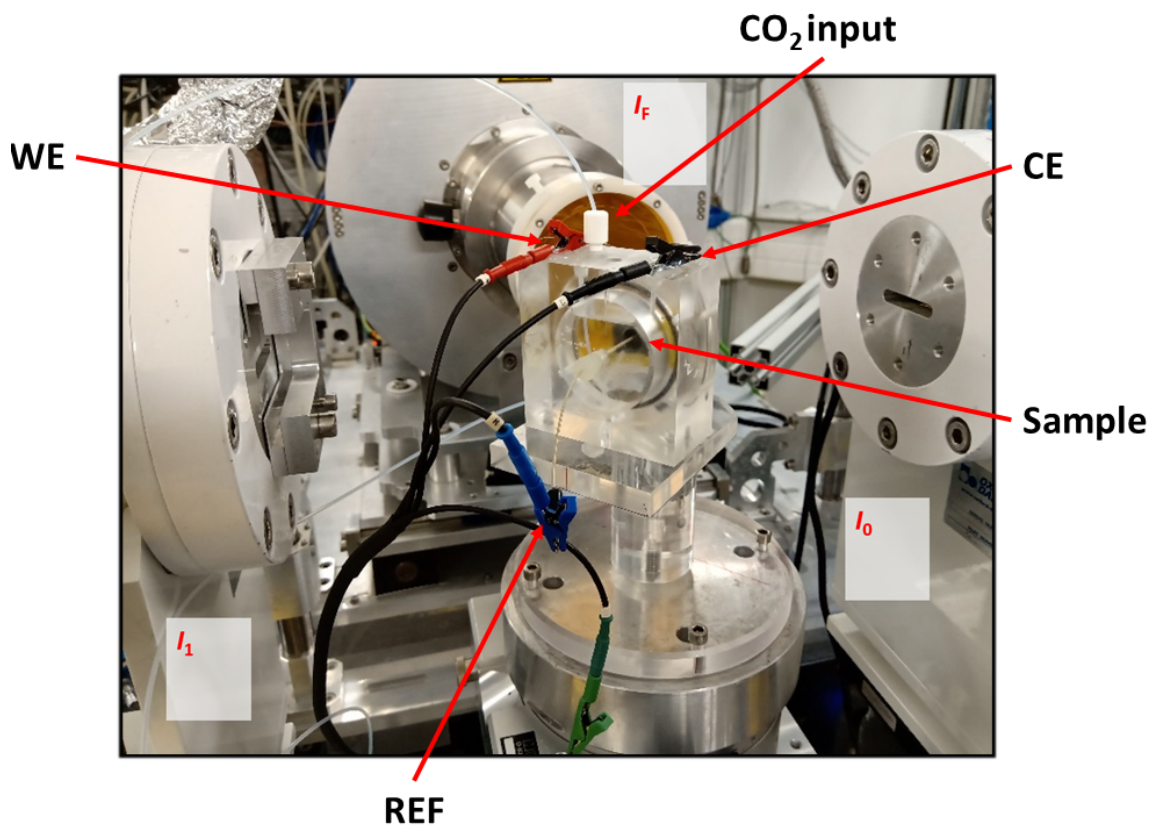


Figure 2.22: Electrochemical *operando* cell for XAFS measurements. Initial (I_0) and transmitted (I_1) ionization chamber detectors are marked as well as the passivated implanted planar silicon (PIPS) detector used to acquire the fluorescence signal (I_F).

Furthermore, it is important to note that due to the cell design it is only possible to measure the obtained signal with an incident angle of the incoming beam of 12° with respect to the sample surface. Therefore the obtained signals will not only reflect the very surface as it would be the case under grazing incidence but also the bulk of the samples.

2.5 Temperature Programmed Desorption

Temperature Programmed Desorption (TPD) is a UHV-based technique used to probe the binding specific molecules on a given surface. The basic idea is to control the temperature of a given sample by cooling, to adsorb a given molecule of interest on the sample surface and then increase the temperature while observing the desorption of the molecules of interest. By ramping up the temperature with a given speed, the desorption of molecules can be followed with the help of a mass spectrometer. This is of particular importance in gas phase reactions and the corresponding employed catalyst. Nevertheless, the technique has recently also been used to study electrocatalysts with respect to their binding properties of reactants and intermediates, as the technique does not only provide valuable informations about the binding strength of adsorbates under UHV conditions, but also about the surface structure and surface area, as different facets exhibit different binding strengths [110–112]. In addition, the obtained signals are proportional to the coverage of the molecule dosed on the surface, and thus to the surface area which is of interest for electrocatalysis. To be able to compare and estimate the surface area by means of the signal intensity using a fixed geometry within the experiments is crucial. Within the conducted experiments, this is achieved by keeping a nozzle serving as the entrance to the mass spectrometer at a constant distance of 0.5 mm at an angle of 90° in front of the sample (see also Figure 2.24). Furthermore, the mass spectrometer itself is differentially pumped to avoid accumulation of the molecules detected from the desorption at lower temperatures.

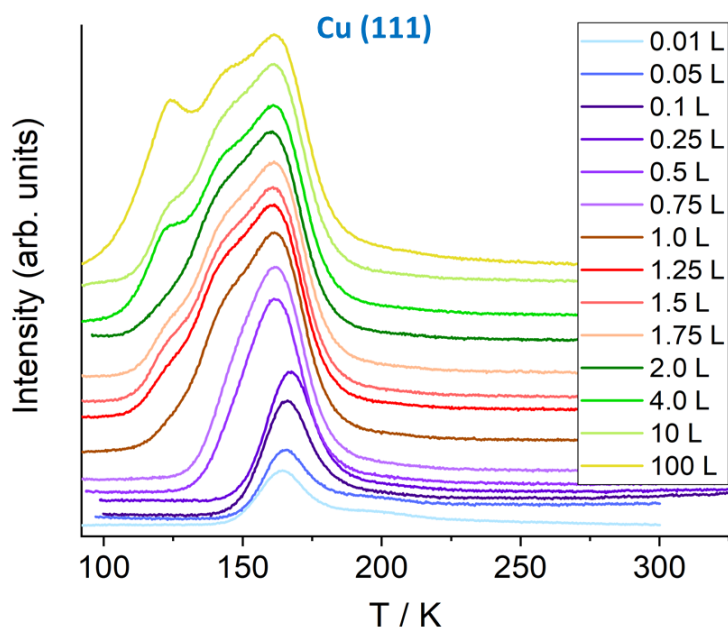


Figure 2.23: CO TPD experiment run on a clean Cu (111) single crystalline surface increasing the dosing gradually.

Experimental Setups

The TPD experiments of interest for Cu are based on CO TPD. As mentioned, CO is considered to be the most important intermediate and its binding strength believed to be crucial in determining the reduction pathway towards hydrocarbons after the CO₂ activation step has been achieved on the Cu surface, which is why these measurements are of interest.

An example spectrum obtained on a clean (no other elements detected in XPS) is shown in Figure 2.23.

The CO dosing is done using a leak valve, background dosing CO in different amounts into a background pressure of 4.2×10^{-10} mbar. As it can be seen with increasing dosing the highest binding energy sites are populated at first until a so-called monolayer is achieved, which is known to result in almost $\frac{3}{4}$ of the surface covered by CO [113]. Those are known to be related to the desorption of CO from the Cu (111) step sites [111]. Afterwards the terraces are populated as reflected by an additional intermediate peak followed by a low temperature desorption peak reflecting multilayer adsorption of CO on CO which is also seen by the scalability of the peak intensity with increasing dosing [111].

The cooling to liquid nitrogen temperature which is necessary to conduct these experiments is done by flowing nitrogen throughout the sample manipulator on which the sample rests within the UHV system after a stream of nitrogen gas passed through a coil immersed in liquid nitrogen. The setup is shown in Figure 2.24.

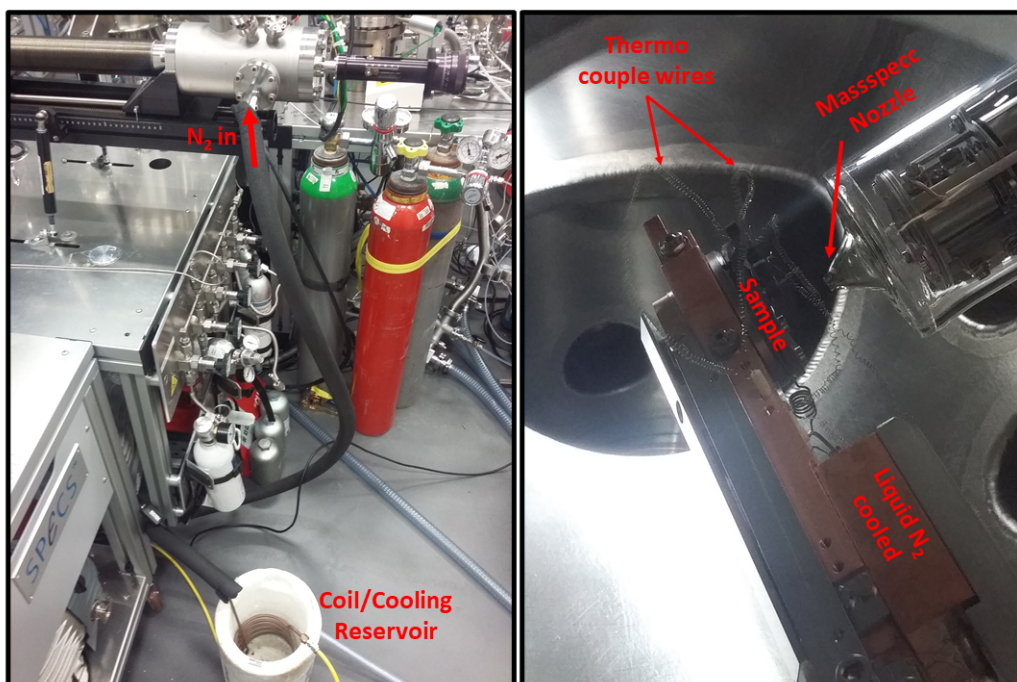


Figure 2.24: TPD setup implemented within the UHV chamber used to conduct TPD based studies.

An estimation of the binding energies for the different peaks obtained is done

by using theoretical models. Those are depending on the assumptions made and differ in their complexity and consequently accuracy [114–116]. What most of those models have in common is that they describe the desorption of the gases with help of a first order differential equation, resulting in an Arrhenius equation since the desorption is also dependent on an activation energy to start the process:

$$r(\sigma) = \frac{d\sigma}{dt} = A(\sigma)\sigma^n \exp\left(-\frac{E_a(\sigma)}{RT}\right) \quad (2.20)$$

with:

$r(\sigma)$ - the desorption rate as a function of the coverage

σ - the surface coverage

$v(\sigma)$ - a pre exponential factor. [v]= Hz

n - the desorption order

$E_a(\sigma)$ - the activation energy

R - gas constant

T - the temperature

As seen extracting the activation energy which is the desorption energy from this equation is very complicated, since most of the parameters are a function of the surface coverage. A commonly applied simplification of this model is known as the so-called Redhead-model which assumes there is no interaction of the adsorbed molecules on the surface with each other, which leads to the pre exponential factor and activation energy being independent on the surface coverage [114, 117]. Since this model is the one used to analyse the data obtained within this work it is the only one discussed to detail. Others such as for instance the so-called "leading edge method" or the "complete analysis method" are discussed in detail in the existing literature [118, 119].

With the previously mentioned assumptions, equation 2.20 can be rewritten also assuming a linear heating ramp $T(t) = T_0 + \beta t$, where T_0 is the starting temperature, β is the heating rate and t the time passed since starting the heating ramp:

$$r(\sigma, t) = \frac{d\sigma}{dt} = A\sigma^n \exp\left(-\frac{E_a}{R(T_0 + \beta t)}\right) \quad (2.21)$$

Assuming a first order desorption ($n=1$) which reflects the lack of interaction of the molecules on the surface and thus no recombinative desorption (chemical reaction followed by desorption of the product for instance $2 \text{CO} + \text{O}_2 \rightarrow 2 \text{CO}_2$) should occur. This also demands that the peak position should be independent on the surface coverage. As seen in Figure 2.23 this only holds true for the higher coverages, as there is a clear shift towards lower binding energies/temperatures up to a dosing of 0.5 L for Cu(111). For other surfaces, such as for instance Cu(100)

this shift related to the coverage is not as dominant due to a higher distance of CO to each other on the surface, resulting in a weaker interaction. Nevertheless, due to this effect only the high dosing peaks are taken into account for determining the corresponding peak Temperature T_p .

Using the fact that the desorption rate equals zero at the peak temperature it is possible to obtain an equation from which E_a can be extracted by carrying out the derivative of $r(t = t_p)$:

$$\frac{dr}{dt}|_{t=t_p} = \frac{d}{dt}|_{t=t_p} \left(A\sigma \exp\left(-\frac{E_a}{R(T_0 + \beta t)}\right) \right) \quad (2.22)$$

$$(2.23)$$

$$\Leftrightarrow 0 = \frac{d\sigma}{dt} A \exp\left(\frac{-E_a}{R(T_0 + \beta t_{t_p})}\right) + A\sigma \frac{\beta E_a}{R^2(T_0 + \beta t_{t_p})^2} \exp\left(\frac{-E_a}{R(T_0 + \beta t_{t_p})}\right) \quad (2.24)$$

$$(2.25)$$

Inserting equation 2.21 into 2.24 then yields:

$$A \exp\left(-\frac{E_a}{R(T_0 + \beta t_{t_p})}\right) = -\frac{\beta E_a}{R^2(T_0 + \beta t_{t_p})^2} \quad (2.26)$$

Since $T(t_p) = T_p$ the maximum temperature equation 2.26 can be simplified to:

$$A \exp\left(-\frac{E_a}{RT_p}\right) = -\frac{\beta E_a}{R^2 T_p^2} \quad (2.27)$$

Equation 2.27 can be solved iterative for a peak temperature obtained from the conducted experiments. The proportionality constant A is used is usually estimated to be $A \approx 10^{13}$, which is based on already existing analysis present in the literature and also employed in the analysis conducted on the data acquired within this work [114–116, 118].

2.5.1 Quadropole Mass Spectrometer

The mass spectrometer employed to extract the rate of desorption within the presented work is a commercial HAL RC 301 from HIDEN analytical. The instrument is based on an ionisation chamber that is used to ionize the incoming gases via inelastic scattering. The obtained ions are filtered with respect to their mass to charge ratio by using an electric quadropole. Within the electric field obtained from the quadropole geometry only a specific mass to charge ratio atom/molecule has a stable trajectory at a given time, resulting in only those reaching the detector being consequently counted. The fundamental differential equations used to describe the stable trajectory conditions are also known as Mathieu equations and are discussed in detail in prior literature [120, 121]. Since the mass spectrometry instrumentation is commonly used in UHV approaches and has not been modified in the present work these topics are hereby not discussed.

3 Synthesis

3.1 Electropolishing

The so-called electropolishing (EP) has become a standard sample preparation technique within the field of CO₂RR since Hori et al. published their benchmark work on electropolished Cu electrodes for CO₂RR [24]. Mainly for comparative reasons other scientific studies directed towards CO₂RR have adapted this method. It is based on electrochemically etching the surface of a given electrode/catalyst by employing acidic solutions in combination with strong oxidizing potentials. While first chemically etches the surface cleaning it, the applied potential causes the etching process to be directed and supports a smooth etching across the whole surface.

Within this work, electropolished samples serve as a defined starting point from which onwards the samples are changed and altered to be able to address the scientific questions raised. Furthermore, electropolished polycrystalline Cu foils serve as benchmark samples to double check the calibration of the employed electrochemical equipment. If the electrochemical cell and gas chromatograph are properly calibrated and set up it must be possible with their help to reproduce the reported values within the literature [24, 122].

Additionally, the treatment provides an efficient and fast cleaning procedure from contaminations on a given surface enabling the recovery of samples used for prior experiments, which is especially important for the Cu single crystal studies carried out, as those are expensive and laborious to clean when started from scratch.

The solutions used to do the electropolishing treatment are always phosphoric acid based (H₃PO₄, VWR 99,95 %), sometimes (see chapter 4.3) adding sulfuric acid (H₂SO₄, VWR 95 %) and water. The sulfuric acid is hereby added to prevent the oxygen evolution reaction from occurring even though high anodic potentials are employed. This is of special importance for single crystalline electrodes, since OER is known to produce etch pits on these type of samples [37].

The counter electrode used consists of a Ti foil (Advent Research Materials, 99,995 %) at which a potential of 3V is applied with respect to the working electrode in a two electrode setup. Although the time may vary from sample to sample (only 10s for single crystals), the most commonly used etch times are around 3 minutes (Cu foils).

3.2 Dendritic Cu Catalysts

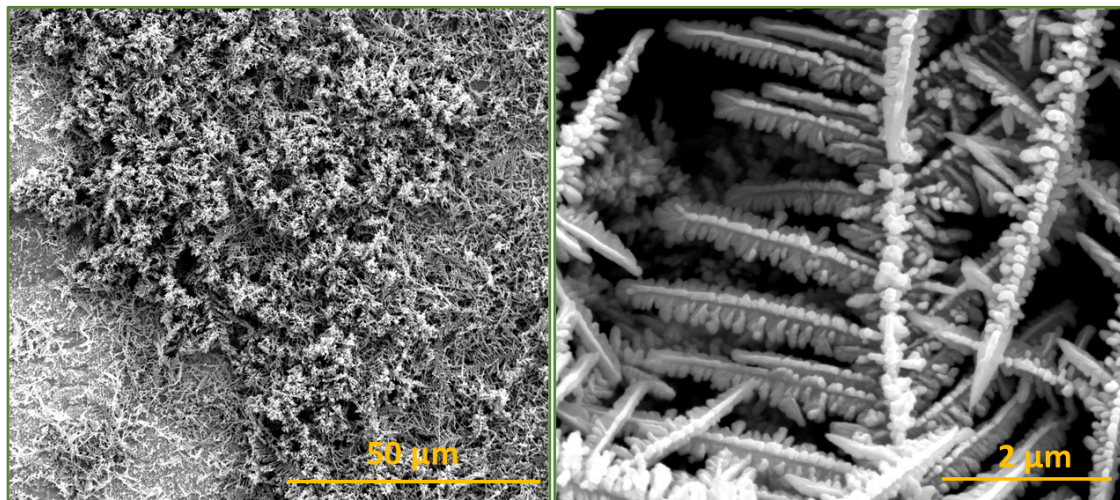


Figure 3.1: Large and small magnification SEM images of Cu dendrites deposited on an Ag substrate using the above described method.

Figure 3.1 shows an example SEM image of Cu dendrites, resulting from electrodepositing Cu using a negative potential to reduce a solvated precursor Cu species present in the electrolyte at the electrode surface (see below). The scientific questions studied with the help of these type of samples are presented in chapter 4.2.

The synthesis of these dendritic Cu samples was based on electrochemically depositing Cu on Ag and Pt foils (99.9999 %, Advent Research Materials)) from an aqueous solution containing a small amount of CuSO_4 (0.05M CuSO_4 , 99.9995 %, Sigma-Aldrich). The deposition was carried out at a constant potential of $U_{\text{applied}} = -1.25\text{V}$ vs RHE in a two electrode setup using a Pt mesh as counter (Advent Research Materials, 99,995 %) for the Ag substrate and a Ti foil (Advent Research Materials, 99,995 %) for the Pt substrate. The potential has been chosen to be high due to the fact that the growth process of dendritic copper is based on the concentration of solvated Cu species within the vicinity of the electrode to be mass transport-limited. This is achieved by keeping the bulk concentration of Cu low and the electric field-mediated transport high [123].

By keeping the available Cu species in the electrode surface low, those who are present are preferentially transported alongside the electric field gradient, which is pointing towards already existing Cu agglomerations on the surface. This inhomogeneous transport then gives rise to the dendritic morphology [124, 125]. The whole deposition process is carried out for 10 minutes. Furthermore, the generation of a highly porous material can be achieved by enhancing the amount of hydrogen bubbles being produced by HER during the deposition process in acidic media. The solution pH was therefore defined to be within 2-3 by adding sulfuric acid H_2SO_4 . This process is known as hydrogen templating [123, 125, 126] and was adapted from

Ref. [61]. After deposition, the samples are washed with clean water ($18.2 \text{ M}\Omega\text{cm}$) to rinse residual sulfur from them. Prior to depositing the Cu dendrites on top of the substrate, the Pt was cleaned by immersing it for 2 minutes in a $1 \text{ M H}_2\text{SO}_4$ solution and the Ag one was immersed for 2 minutes into a 0.5M HNO_3 solution.

Figure 3.2 highlights the resulting current over time curve obtained during the growth of the Cu dendrites. The increase of the current over time is attributed to the increase in the overall active surface area as the dendrites grow. Since the deposition is carried out in acidic media and no CO_2 is bubbled within the solution used, the resulting product is mainly hydrogen. The noise seen within the current over time curve is attributed to hydrogen gas bubbles in agreement with literature reports [60, 123, 126].

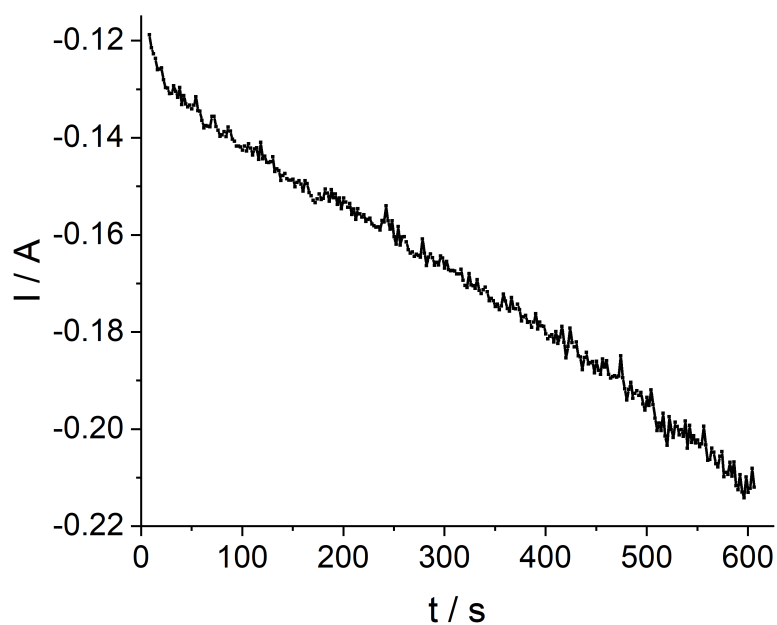


Figure 3.2: Current over time curve for the electrochemical growth of Cu dendrites on an Ag substrate.

3.3 UHV preparation of Cu

Ultra high vacuum (UHV)-based studies allow for controlling the environmental conditions of samples on a very precise level. Prior to any studies conducted within UHV chamber the employed samples also have to be prepared and characterised, so that they are in a well-known and defined state. The standard technique to achieve this goal which is commonly used to provide well-defined initial surfaces prior to any further preparation is to sputter/anneal the samples. Sputtering hereby denotes the acceleration of ions towards a given surface using a high electric field. The ions themselves are most commonly produced from a chemical inert gas (Argon) by means of a magnetron (see also [127]). Upon hitting the surface of a given sample, adsorbate atoms are removed and consequently the surface is cleaned. Since this process does not leave behind a smooth and flat surface which is most commonly wanted, the samples are annealed (heated) in a subsequent step. This procedure is repeated several times until the surfaces are in the desired state (clean, flat, well ordered).

Within this work, UHV based samples are used to clean metallic surfaces prior to the XPS measurements to obtain reference spectra for the clean metallic surfaces but most importantly, they are also employed to prepare Cu-based single crystalline surfaces that are used to study their electrochemical behaviour under CO₂RR conditions (see chapter 5).

The gas used to sputter is Ar (99,9999 % Westfalen) and the ion gun is a commercial one (SPECS GmbH IQE-11 Ion source). The heating is based on electron bombardment of the sample holder. The electrons are accelerated towards the bottom of the holder by using a voltage of U=900V. Depending on the sample and the sample state, different parameters are employed and the corresponding cleaning is denoted as strong and mild within this work. All samples used are Cu-based and the annealing temperature in all cases is 970K. Furthermore, the samples were cooled down slowly with every last cycle of a given cleaning run using a cooling ramp of 25K/min until a temperature of 500K was reached. By then the heating is turned off completely. Especially for single crystalline surfaces this supports the generation of a flat surface, as the strain may be released by the movement of the atoms. The used sputtering parameters are summarized in table 3.1:

Treatment	p (Ar) / mbar	I _{sample} / μ A	time / min	E _{Ion} / keV
Strong	3.2×10^{-5}	28-31	15	2.5
Mild	1.5×10^{-5}	8-11	5	1.5

Table 3.1: Sputter conditions employed to clean and prepare Cu based samples.

3.4 Plasma treatment

The plasma treatments done to prepare and clean samples for different projects within this work are based on a low pressure plasma chamber system that is commercially available (SPI Supplies). The setup is equipped with a roughing membrane pump used to create a rough vacuum (25 mTorr range). Figure 3.3 shows an image of the plasma setup. The plasma itself is capacitively generated and powered by two half cylindrical metal plates around the glass chamber.

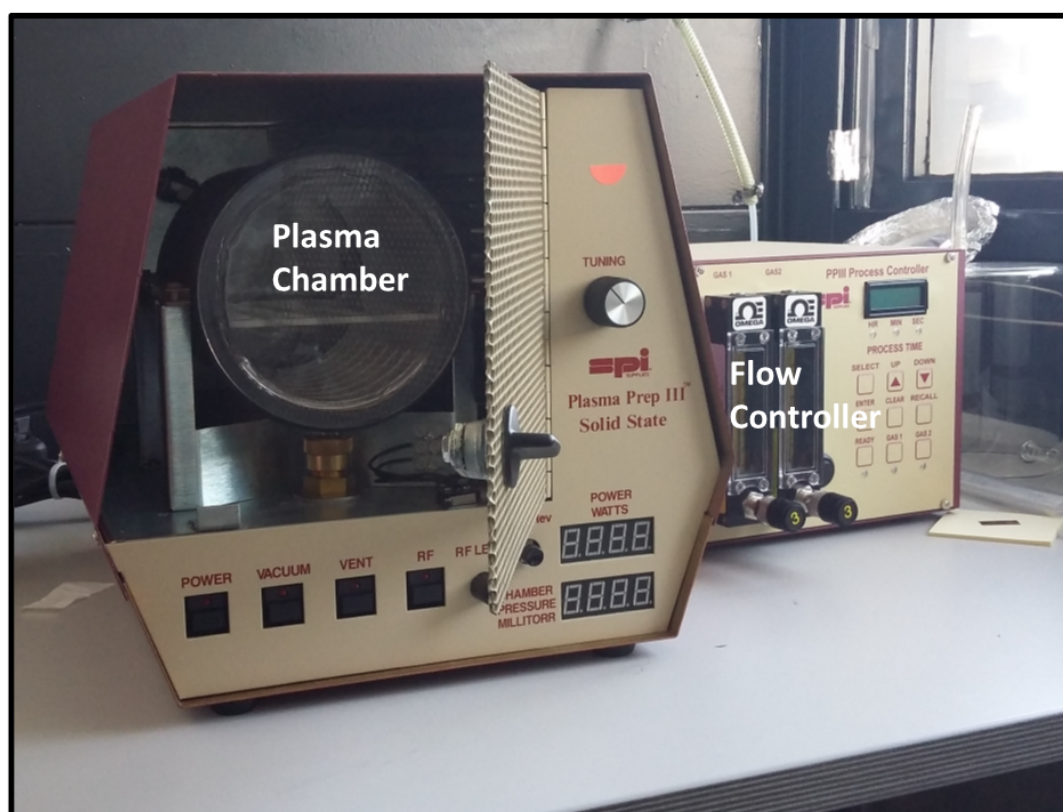


Figure 3.3: Image of the experimental plasma chamber.

The treatments done mostly are oxygen (Air liquide, 99,95 %) and hydrogen (Air liquide, 99,95 % plasma treatments with respect to the copper based samples). The main purpose is to change the chemical state of a given sample towards its oxidized or reduced state while at the same time roughening the sample, increasing the total surface area which has proven to be crucial for CO₂RR [68].

Furthermore, the setup has been used for the synthesis of nanoparticle which is discussed in the next section in detail.

3.5 Nanoparticle Synthesis

A field of catalysis offering a promising approach to facilitate and control a given reaction outcome is the use of nano sized catalysts. Their exploration is still ongoing and consequently there is a demand for methods of producing such catalysts in a reliable way. Especially when studying effects on the nano-scale linked to the size, shape and composition, well defined model catalysts are important.

The method used within the present work to produce and study such nano-sized catalysts is based on a colloidal chemistry approach utilizing a polymer to encapsulate metals within. By controlling the polymer features and the ratio of the dissolved metals in solution, the composition and size of small nano-sized metal particles can be controlled. Figure 3.4 shows the schematic representation of the process. The chain polymer consists of a so-called tail and core part. The core part is polar while the tail part is not, which results on the accumulation of metals at the polar polymer core if both are added into solution. When using polar solvents such as toluene (used within the present work) or tetrahydrofuran (THF), the polymer cores align as shown in Fig. 3.4 due to the interaction with the solvent. The metal nano-particle is consequently formed within the polymer core. By controlling the size of the polymer's core and tail, the size of the particles and their distance with respect to each other can be tuned.

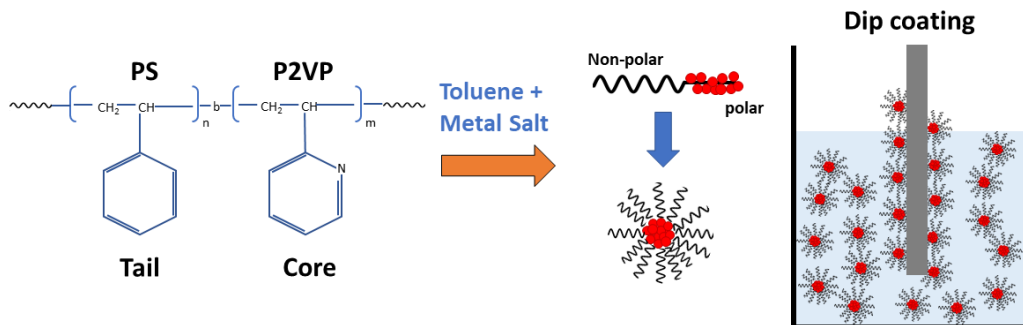


Figure 3.4: Schematic representation of the micellar polymer based nano-particle synthesis.

Once a solution containing the dissolved polymer with the particles with the polymer core is made, the particles can be deposited on a substrate by dip coating, drop casting or spin coating. The substrates used within this work are Si wafers and glassy carbon supports which are dip-coated into the solution. Post dip-coating and drying, the polymer that is still protecting the particle has to be removed. An easy way to do this is with the help of the previously described plasma etcher. Using a low pressure (250-400mTorr) oxygen plasma, the carbon based polymer can be removed. The cleanliness of the particles is then checked with XPS, looking out for the N and C signal since both elements make up the polymer.

4 Role of the Catalysts Oxidation State in CO₂RR

Across the field of CO₂ electroreduction, oxide derived (OD) Cu catalyst are of special interest due to their ability to outperform metallic Cu catalysts by a large margin with respect to their selectivity for C₂₊ products. The fact that especially the ethylene selectivity is enhanced by up to 42 % [68] also makes them attractive for industrial considerations as discussed previously.

Scientific effort carried out is mainly directed towards understanding the underlying properties of OD Cu catalysts, as the origin of their superior catalytic behaviour remains unknown.

The experimental work, highlighting the mentioned increase employing oxygen plasma treated polycrystalline Cu foils as catalyst, was also able to demonstrate that the observed changes cannot be solely attributed to the overall surface area [68]. Several other possible reasons have been subject to dedicated studies since then. For instance the presence of sub-surface oxygen species or oxides present during CO₂RR [68–72, 128], changes in the local pH [84], an enhanced coverage of reaction intermediates due to specific facets being predominantly present [37] and the presence of special active sites and defects [68, 72, 79, 129] has been considered. While theoretical effort based on density functional theory (DFT) studies supports and suggests that the crucial CO dimerization and overall stability of reaction intermediates on the surface is facilitated due to oxides and other Cu(I) species being present [11, 65, 71, 75–77], their stabilization has proven to be very difficult [73, 75, 76, 130] and only been demonstrated for nanosized catalysts [72, 131] as well as upon introducing modifier elements [62, 65, 132]. Due to the lack of stability depending on the catalysts morphology [60, 133], composition [38, 39, 131, 134], pretreatment [38, 76], support [63, 89] and the electrolyte employed [11, 62], the influence of Cu⁺ species remains controversial.

In addition, the influence of adsorbed oxygen species on the formation of oxygenates has been reported recently [135] pointing out further the complexity of understanding the role of copper oxides within the framework of CO₂RR.

The studies presented within this chapter focus on this topic and contribute to the overall literature by significantly narrowing down the possible influence of oxides. Employing spectroscopic tools it was possible to show that the stabilization of oxides on the surface of well performing oxide-derived catalysts is rather difficult, thus suggesting that the improved selectivity towards ethylene seen is independent on the catalysts oxidation state during CO₂RR. Furthermore, by employing and

plasma-modifying a high surface area catalyst known to be selective for ethylene due to a local pH effect it was possible to demonstrate that the effect of OD catalysts cannot solely be explained by means of an increased local pH in the surface vicinity.

With these results in mind the question on what is facilitating the important CO dimerization on the surface is addressed in the second part of this chapter. By employing single crystalline surfaces who have shown to be selective towards specific products [37, 43, 46, 52] it was possible to show that the selectivity towards oxygenates linked to the presence of Cu⁺ at the surface while the ethylene selectivity of oxide derived catalysts has to be attributed to the crystal orientation and the presence of defects on the surface.

The last part of the chapter builds up on these results and employs differently oriented single crystalline Cu surfaces to further investigate the importance structural parameters and their influence on the selectivity towards specific products. Especially the binding strength and surface roughness as well as the presence of defective sites is considered and investigated hereby.

4.1 Polycrystalline Cu

The original experimental work demonstrating the impact of pre-oxidizing polycrystalline copper on CO₂RR activity and selectivity employ oxygen plasma-treated samples that have been electropolished beforehand [68]. To be able to follow the presence of oxides during CO₂RR, *operando* XAS measurements were used in a grazing incidence configuration. Directly after the plasma treatment, all but the hydrogen plasma treated samples have been oxidized towards CuO due to the exposure to the oxygen plasma. Upon running the samples under CO₂RR conditions at -0.9V vs RHE the reported XANES and EXAFS data reflect a decrease of the oxide species up until a reaction time of 15 minutes, where the corresponding fingerprint within the EXAFS spectra completely vanished [68]. The downside of these type of measurements is that they are dominated by the bulk signal, due to the nature of the X-rays employed having a high energy (9keV), being able to penetrate into deep layers of the material. To be able to complement the discussed XAS data with more surface sensitive XPS data, the XPS system described in chapter 2.4.1 in combination with an electrochemical cell was employed. The first sample investigated has been an electropolished Cu foil since it is a common benchmark sample within the literature [9, 19, 122] and the plasma treated was the most selective towards ethylene (20W, 250mTorr, 2 minutes oxygen plasma) [68].

Figure 4.1 shows SEM data obtained on the plasma treated sample. The observed morphology is similar to what has been reported for the same treatment [68], supporting the reproducibility of the plasma treatment.

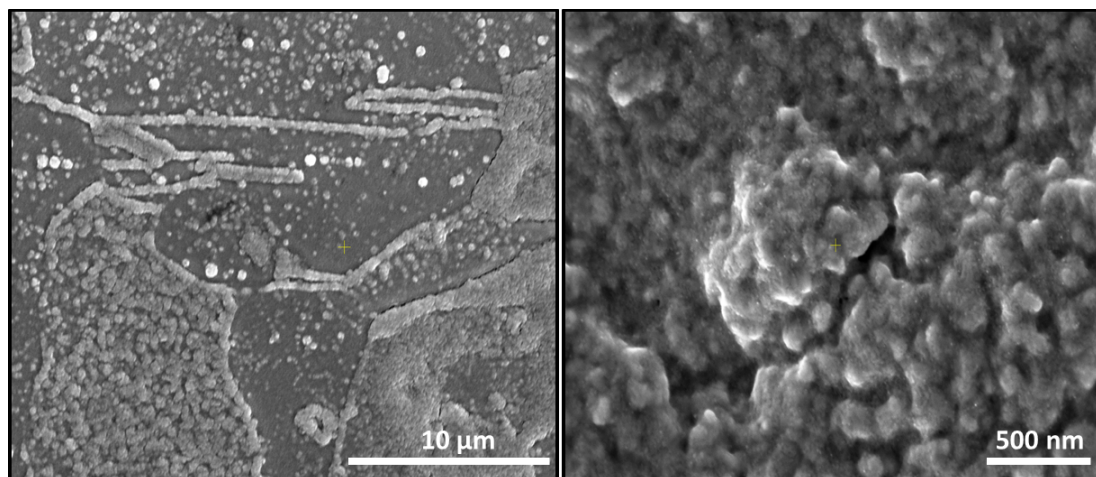


Figure 4.1: SEM image of an electropolished Cu foil after oxygen plasma treatment (20W, 250mTorr) for 2 min.

The obtained Cu LMM Auger, Cu 2p and O 1s XPS spectra on an electropolished Cu foil before as well as after exposure to the low pressure oxygen plasma are shown in Figure 4.2. Linear combination fitting of the Cu Auger spectra with the

corresponding references reflects a strong oxidation towards CuO for the plasma treated sample. In agreement with this finding, the presence of the characteristic shake up features in the Cu 2p is seen, and a high intensity peak in the O 1s spectra deconvolution at $E_B=529.8$ eV can be seen, which fits the existing literature [104, 105]. In the case of the electropolished foil a mixture of Cu, Cu₂O and CuO is found to be present whereas metallic (36.4 at %) and Cu(I) (61.5 at %) species are dominantly present. Even though linear combination fitting only suggests a small amount of CuO (2 at %), its presence is supported by the O 1s spectra and the presence of small shake up features in the Cu 2p region. It is important to note at this point that the assigned species (see fig. 4.2) within the O 1s spectra denoted as adventitious and organic compounds are difficult to assign, since metal carbonates and hydroxides, as well as C-O-H, C-O and COOH compounds are difficult to distinguish within the O 1s spectra without a complementary technique [104]. The presence of water is most likely originating from the rinsing step with ultraure water.

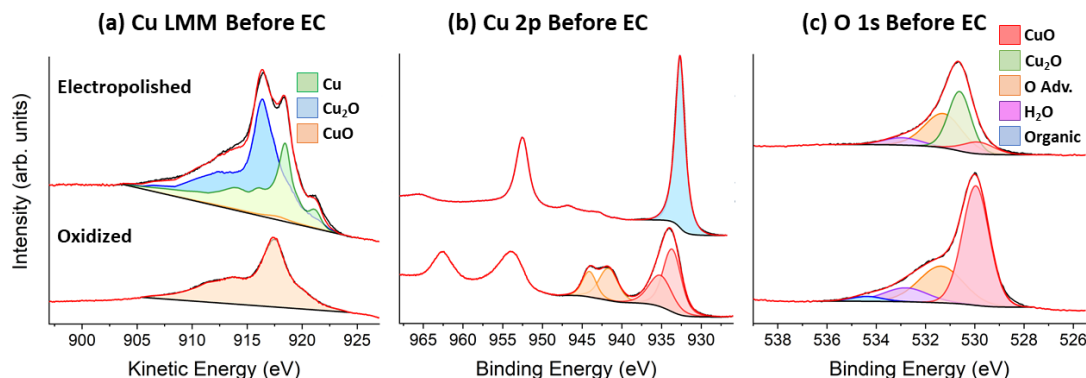


Figure 4.2: Quasi *in situ* (a) Cu LMM spectra, (b) the corresponding Cu 2p spectra and (c) the O 1s spectra for the electropolished and plasma oxidized Cu foil before EC.

After 1h of electrochemistry under CO₂RR conditions within 0.1M KHCO₃ holding a constant applied potential of -1.0V vs RHE, the situation changes completely. The respective Cu LMM and the O 1s XPS data is shown in Figure 4.3. Both Cu LMM Auger spectra match the acquired reference for metallic Cu. At the same time, the O 1s XPS spectrum does not reflect the presence of any oxides. Thus, by means of XPS, there are no oxides stable within the employed catalyst since none could be detected after electrochemistry.

As previously mentioned, the complementary EXAFS data present in the literature reported oxides to be present within the sample up until 15 minutes CO₂RR [68]. Therefore the plasma oxidized Cu foils have also been investigated by means of the employed XPS setup after 15 minutes of CO₂RR up to times as short as 5 seconds. The obtained data are shown in Figures 4.4 and 4.5. Again linear combination fitting with the respective references suggests that the samples are in its metallic state which is consistent with the fact that the acquired O 1s spectra do not reflect the presence of oxides. In combination with the mentioned *operando* EXAFS

experiments this leads to the conclusion that the oxides seen must be present within the samples bulk or subsurface region, as XPS is a surface sensitive technique and EXAFS is bulk sensitive.

Even though these results suggest that the observed catalytic trends towards ethylene are mostly independent from the presence of surface oxides during the catalytic reaction it is not enough to generalize these ideas on the basis of the conducted XPS study. On the one hand the presence of oxides could be beyond the detection limit, as the employed X-ray energy ($E_{Al} = 1486.71\text{eV}$) is high as compared to the binding energies for oxygen leading to a lower differential cross section for the photoemission process and consequently a lower signal. On the other hand the insufficient stability of oxides could only hold true for polycrystalline Cu foils and the stability of oxides could be higher within other type of materials such as alloyed, nanostructured and single crystalline catalysts that have also been reported to be more selective for C_{2+} products [61, 62, 72, 129].

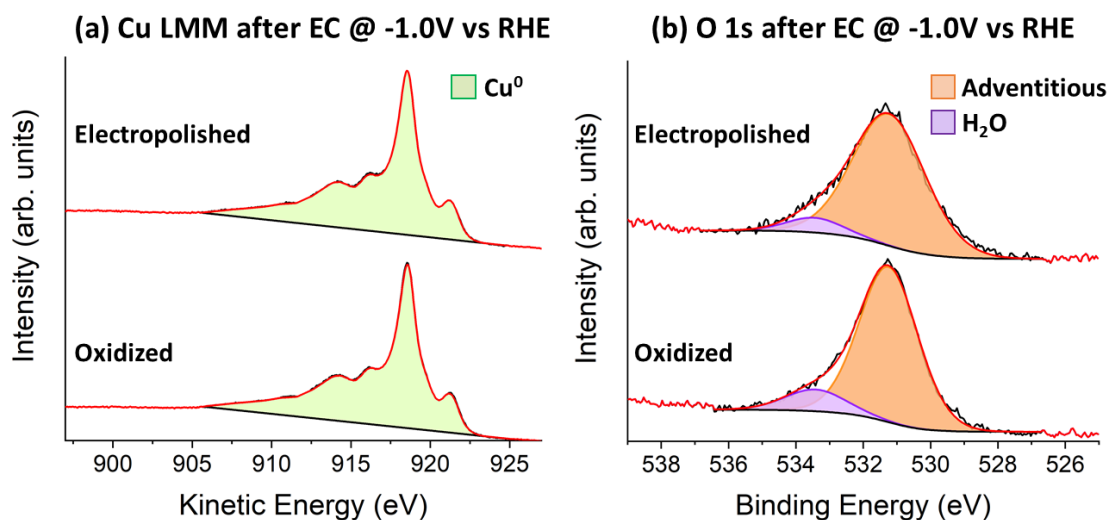


Figure 4.3: Quasi *in situ* (a) Cu LMM spectra and (b) the corresponding O1s spectra for the electropolished and plasma oxidized Cu foils after 1 h of electrochemistry in 0.1M $KHCO_3$ at -1.0V vs RHE. The oxidized data are published in [62].

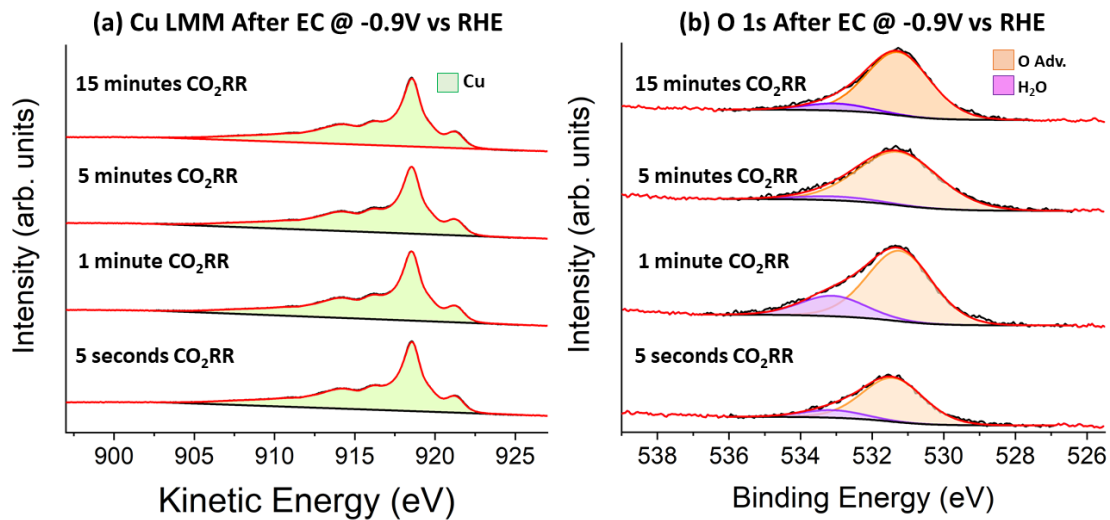


Figure 4.4: Quasi *in situ* (a) Cu LMM spectra and (b) the corresponding O1s spectra for the plasma oxidized Cu foil after different times of electrochemistry in 0.1M KHCO₃ at -0.9V vs RHE.

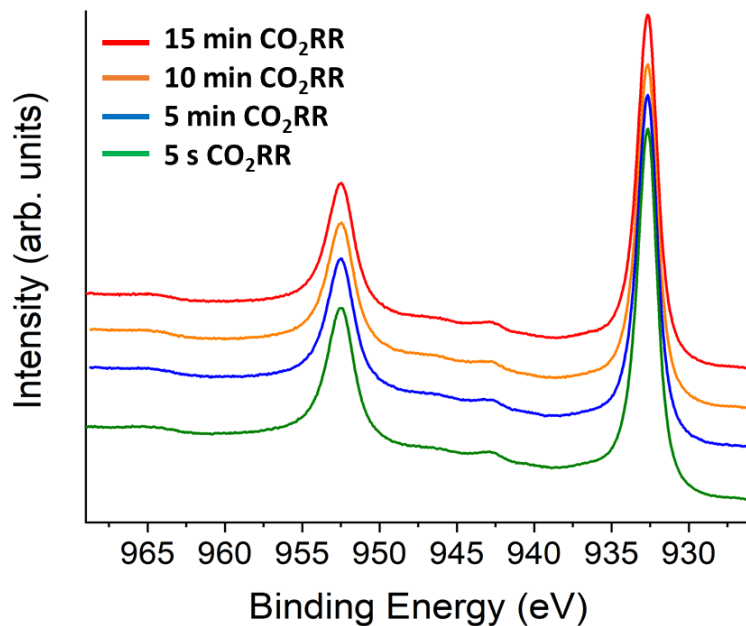


Figure 4.5: Quasi *in situ* Cu 2p data after different times of CO₂RR in 0.1M KHCO₃ at -0.9V vs RHE.

4.2 Copper Dendrites

Of special importance among the various catalysts studied [4, 10, 11, 19, 24, 37, 122] are nanostructured materials, since they have proven to outperform bulk materials in several aspects of CO₂ electroreduction [61, 62, 66, 72, 84, 131]. For instance, they display a higher selectivity towards a given reduction reaction product [52, 72, 84, 131] or a higher overall activity [62, 66]. Engineering those type of systems with respect their properties on a nanoscale is hereby key. For example nanosized Cu cubes exhibiting the beneficial Cu(100) facets have shown a superior selectivity towards ethylene [37, 43]. In addition, kinetic transport limitations present in low surface area catalysts and H-type cell setups can be overcome by employing highly porous catalysts that can be operated at high current densities in a three-phase (gas/solid/liquid) flow cell setup [61, 136]. Especially dendritic shaped catalysts have been demonstrated to be very selective towards ethylene (63 %) at current densities as high as $750\text{mA} \cdot \text{cm}^2$ [136]. Their intrinsic high selectivity for ethylene was mainly understood in the framework of a high local pH due to their high surface area and their porous structure resulting in a high hydrophobicity, which leads to readsorption and further reduction of reaction intermediates like carbon monoxide towards hydrocarbons [60, 61, 125, 137].

The latter is also the reason why within the study of dendritic Cu presented here, Ag and Pt have been chosen as a substrate. Ag is known to selectively produce CO at lower overpotentials, especially when being oxygen plasma treated due to the higher resulting roughness [26]. Pt has been chosen to be able to compare the results obtained on Ag with a substrate that is only selective for HER due to its high CO binding strength [24].

Since the exceptional selectivity towards ethylene for dendritic catalysts is also shared by oxide derived catalyst who also display the suppression of methane in favour of ethylene production [68, 78, 134] the combination of both type of systems is a promising approach to study if the selectivity towards ethylene of oxide-derived catalysts is linked to the local pH. If both effects are independent of each other, oxide-derived dendritic Cu catalysts should not show any significant further suppression of methane and no higher amount of ethylene than normal metallic dendritic catalysts. The fact that the observed selectivity trends of Cu dendrites and oxide derived catalyst are similar to each other has also lead to the suggestion that dendritic Cu systems might contain some residual oxides even when grown *in situ* which could be a possible reason for their selectivity trends [61].

The studies presented within this section focus on answering open questions on Cu dendritic systems, since they are considered promising catalyst for CO₂RR.

The used samples have been synthesized as described previously 3.2. Afterwards the obtained dendritic Cu catalysts have been exposed to a low pressure oxygen plasma (250mTorr, 20W) for 1 and 5 minutes, respectively. The dendrites were grown on Ag and Pt substrates which were cleaned by etching and washing them (see chapter 3.2).

Figure 4.6 shows a large area SEM image of the resulting samples on the respective Ag and Pt substrates. The respective high resolution SEM images of the sample before and after the oxygen plasma treatment as well as after electrochemistry at -1.0V vs RHE are shown in Figure 4.8 and 4.7. The acquired images on the substrates are presented in Figure 4.9.

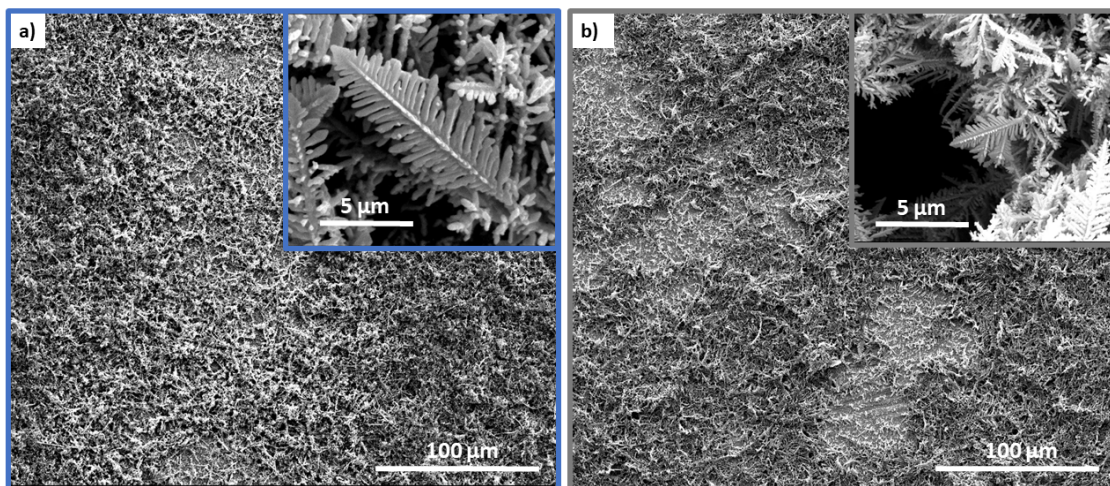


Figure 4.6: SEM images of Cu dendrites on (a) Ag and (b) Pt substrate. Large scale images were published in [27]. Reprinted with permission from [27]. Copyright 2019 American Chemical Society.

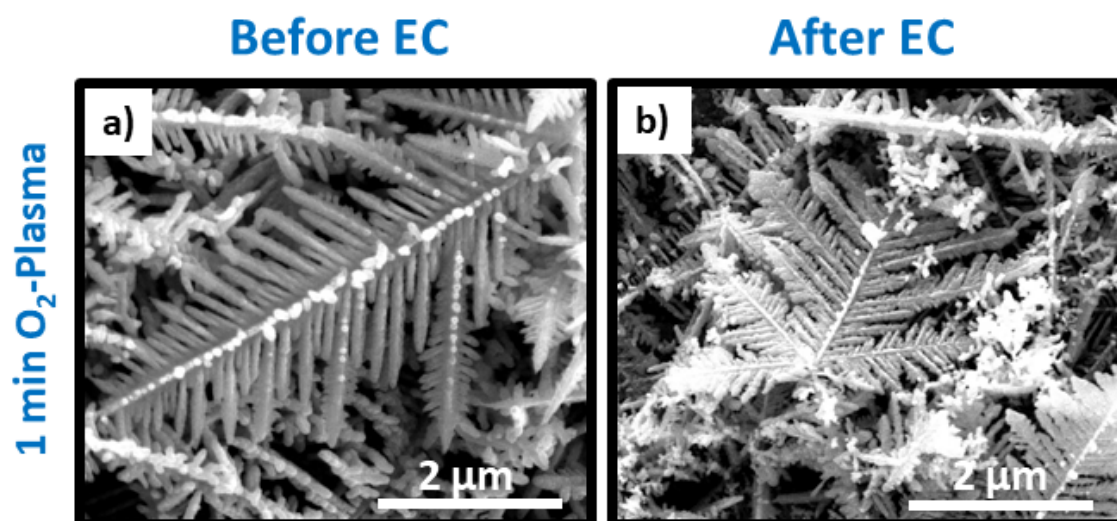


Figure 4.7: SEM images of Cu dendrites deposited on an Ag substrate after (a) being exposed to a low pressure oxygen plasma treatment for 1 minute and (b) subsequently running CO₂RR for 1h at -0.9V vs RHE in 0.1M KHCO₃ electrolyte. Published in [27]. Reprinted with permission from [27]. Copyright 2019 American Chemical Society.

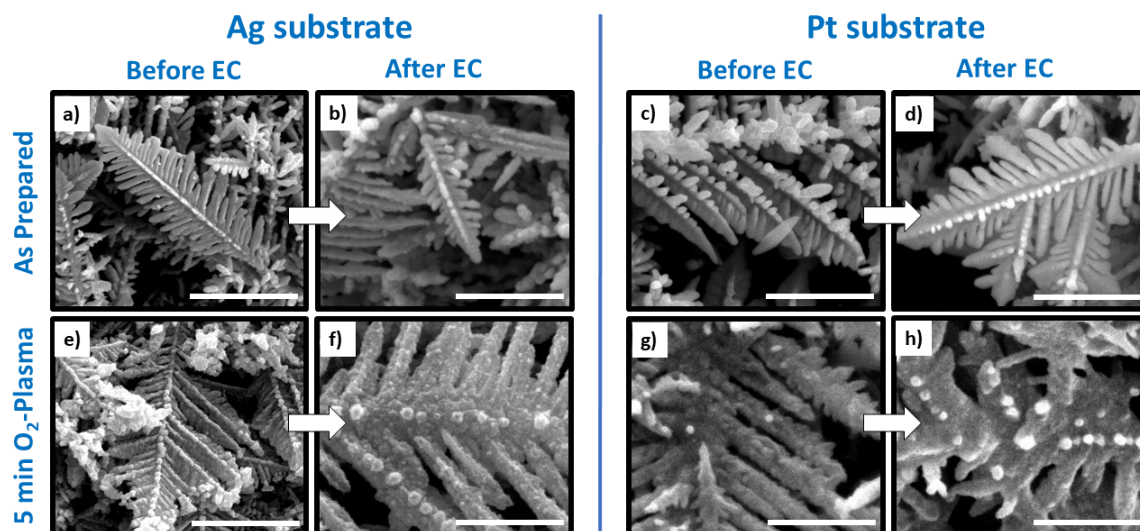


Figure 4.8: SEM images of Cu dendrites deposited on Ag (a, b, e, f) and Pt (c, d, g, h) acquired before and after CO₂RR at -1.0V vs RHE for the untreated (a-d) and 5 min O₂-plasma treated (e-h) samples. The scale bars correspond to 2 μ m. Published in [27]. Reprinted with permission from [27]. Copyright 2019 American Chemical Society.

As it can be seen, the Ag substrate changes significantly under the influence of the low pressure oxygen plasma treatment towards agglomerated structures. This change is already visible for treatments as short as 1 minute and becomes more dominant for the 5 minutes treated samples (fig. 4.9 (a-f) and 4.7). The Pt surface remains mainly unaffected (fig. 4.9 (g-i)). Looking at the dendrites grown on top they are unaltered with respect to their morphology after the short 1 minute oxygen plasma treatment and subsequent exposure to reaction conditions at -0.9V vs RHE (fig. 4.7). The changes occur upon treating them for 5 minutes with the oxygen plasma and consequently running them under CO₂RR conditions (fig. 4.8 (e-h)). After the plasma treatment, a loss of the sharpness of the dendrite tips is observed, which is most likely linked to the formation of copper oxides that make up the observed agglomerations at the edges of the dendrites, as also indicated by the obtained EDX results (tab. 4.1).

Once the samples are exposed to electrochemical conditions for 1 hour, an increase in the roughness of the dendrites is observed for both employed substrates. At the same time, the presence of small particles (100-200nm) can be seen that are also present in small amounts on the Ag substrate as confirmed by EDX (see Figure 4.8 and 4.10). As far as it can be judged from the SEM images, especially the high magnification ones (fig. 4.10), these crystals do not have a preferential crystalline orientation or surface structure. Most likely they originate from the backbones of the dendritic branches as they are aligned alongside these. Regarding the Ag substrate, a porous network like structure is present after electrochemistry (fig. 4.10 (b)).

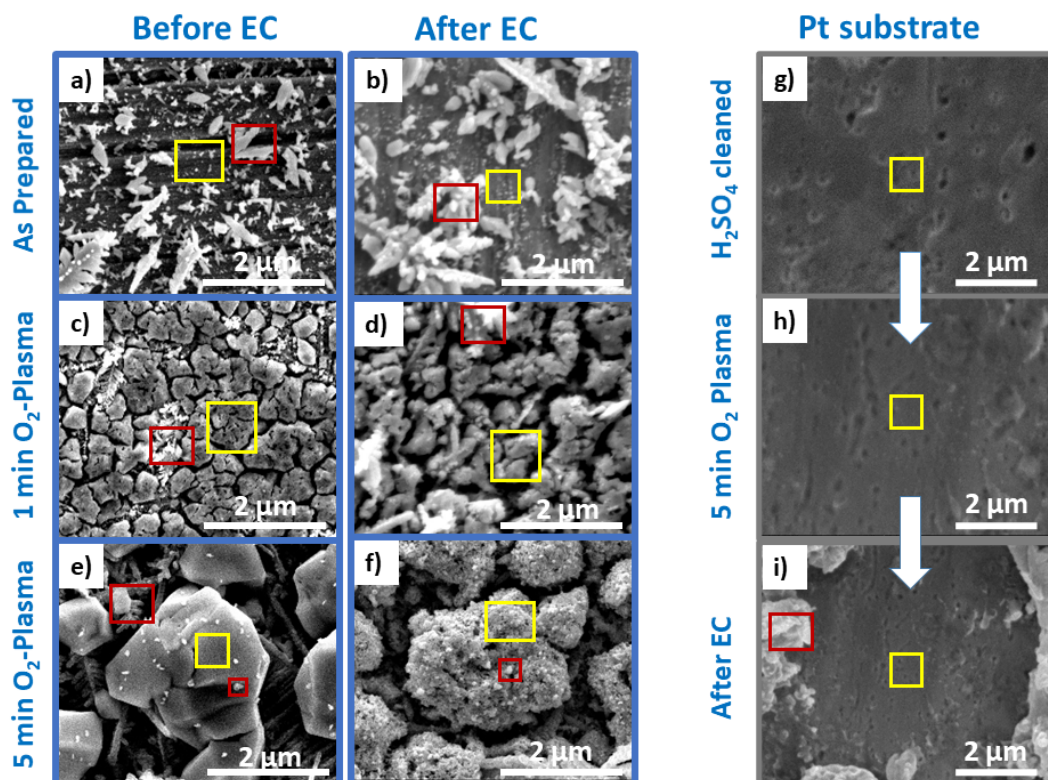


Figure 4.9: SEM of Ag substrate with dendrites deposited before (a,c,e) and after CO₂RR at -1.0V vs RHE (b,d,f) for the untreated (a,b) and plasma-treated cases (c,d). Right panel (g-i) shows the Pt supported samples. Yellow squares mark Ag/Pt-rich regions and red ones Cu rich regions, as probed by EDX. Published in [27]. Reprinted with permission from [27]. Copyright 2019 American Chemical Society.

Sample	Part	Before EC	After EC
On Ag -	Dendrites	87% Cu, 13% O	95% Cu, 5% O
As prep	Substrate	79% Ag, 16% Cu, 5% O	86% Ag, 12% Cu, 2% O
On Ag -	Dendrites	51% Cu, 49% O	93% Cu, 7% O
O ₂ Plasma	Substrate	55% Ag, 40% O, 5% Cu	67% Ag, 21% Cu, 12% O
On Pt -	Dendrites	86% Cu, 14% O	95% Cu, 5% O
As prep	Substrate	61% Pt, 39% Cu	59% Pt, 41% Cu,
On Pt -	Dendrites	54% Cu, 46% O	83% Cu, 17% O
O ₂ Plasma	Substrate	48% O, 28% Pt, 24% Cu	64% Pt, 35% Cu

Table 4.1: EDX analysis of Cu dendrites supported on Ag and Pt. The values given are the relative amount of Cu, O, Ag and Pt detected. Plasma treatments refer to the 5 min treated samples. Published in [27].

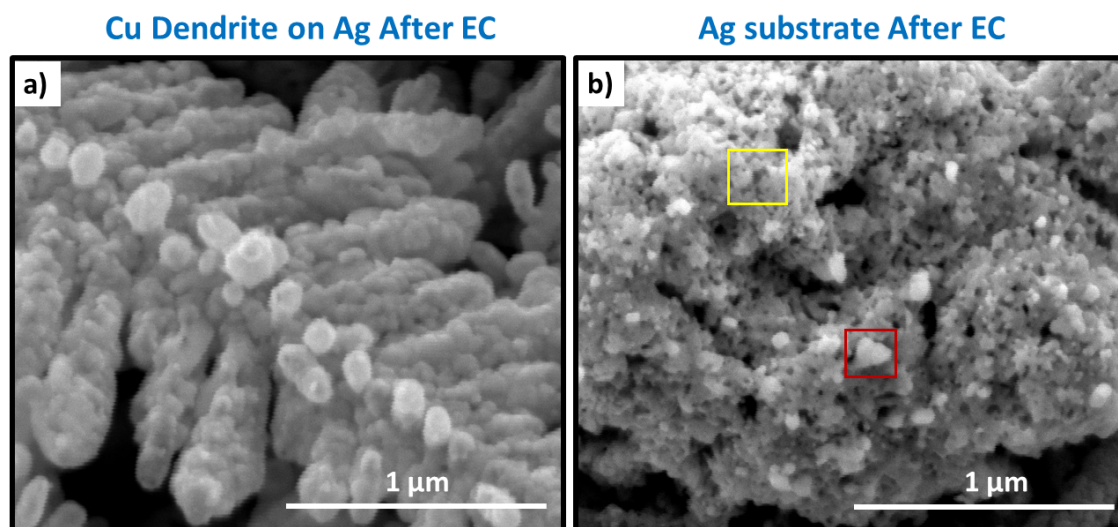


Figure 4.10: High magnification SEM images of 5 min O₂ plasma treated (a) Cu dendrites on Ag and (b) the underlying Ag substrate. Both images are taken after 1h of CO₂RR at -1.0V vs RHE in 0.1M KHCO₃. The yellow box marks Ag-rich areas and the red one Cu rich areas on the substrate as probed by EDX.

In order to estimate the relative increase of the overall roughness by another method to complement the SEM results electrochemical surface area measurements based on the Helmholtz-double layer capacitance have been conducted. The acquired data are summarized in Figure 4.11.

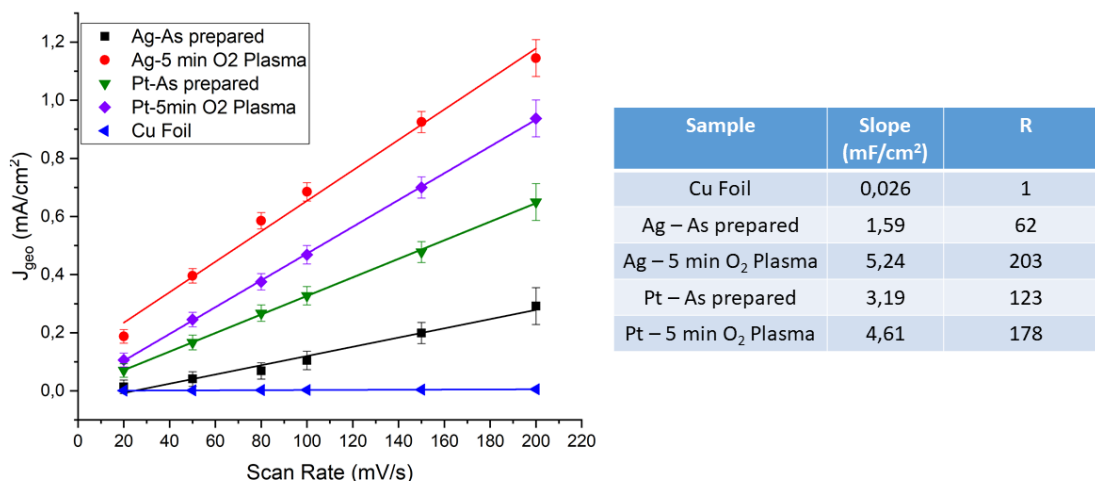


Figure 4.11: Capacitance measurements and the corresponding roughness factors with respect to an electropolished polycrystalline Cu foil. Published in [27]. Reprinted with permission from [27]. Copyright 2019 American Chemical Society.

The obtained results are consistent with the observations based on the SEM images. The plasma treated samples are significantly rougher as compared to the

non plasma treated samples independent on the substrate used. Nevertheless, the increase in the roughness of the Ag-supported samples is two times higher than for the ones supported on Pt. This difference is attributed to the large changes of the Ag substrate upon exposure to the oxygen plasma (fig. 4.9 (c-f)).

To be able to judge whether or not these changes in the morphology have an impact on the catalytic selectivity, the faradaic efficiency for gas product distribution of the considered samples has been measured as a function of the applied potential. Each sample was measured under CO₂RR conditions for 1 hour. The joint Faradaic efficiency for the C₂₊ products as well as the other obtained products is presented in fig. 4.12. The total and partial current densities are shown in fig. 4.13.

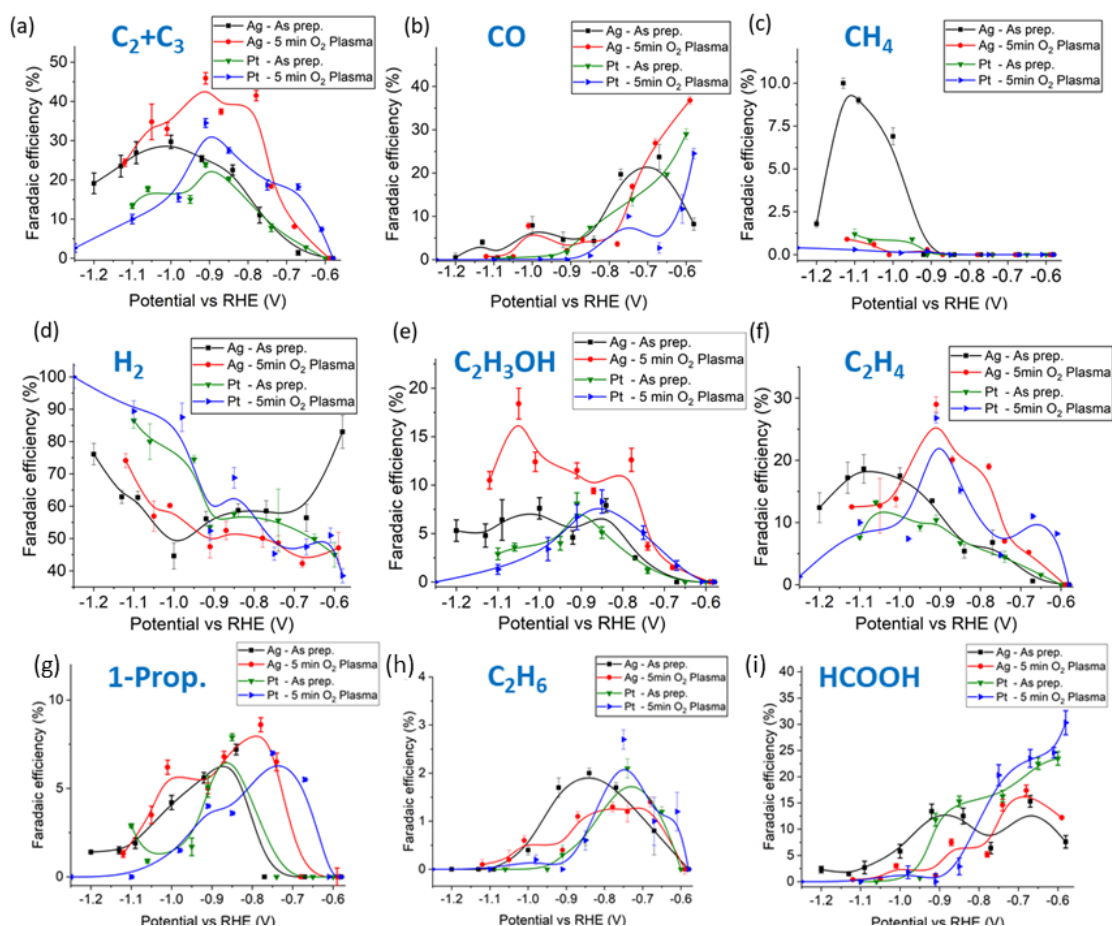


Figure 4.12: (a) combined CO₂RR faradaic efficiency for C₂ + C₃ products and individual faradaic efficiencies for (b) CO, (c) CH₄, (d) H₂, (e) ethanol, (f) C₂H₄, (g) 1-prop., (h) C₂H₆ and (i) HCOOH from Cu dendrites grown on Ag (black and red curves) and Pt (green and blue curves) substrates as a function of the potential in 0.1M KHCO₃. Data from the as prepared (untreated) and 5 min O₂-plasma treated samples are shown. Solid lines are a guide for the eye. Published in [27]. Reprinted with permission from [27]. Copyright 2019 American Chemical Society.

Clearly, the oxygen plasma treated samples show a superior catalytic selectivity towards C_2 and C_3 products as their Faradaic efficiency increases by almost 20 % at a potential as low as $-0.9V$ vs RHE. At the same time the parasitic HER and formation of methane are further suppressed within the potential window here most hydrocarbons are seen ($-0.8V$ to $-1.0V$). The latter, in agreement with the literature [60, 61, 125], is already low on the as prepared samples and only seen for the Ag-supported dendrites which displayed a lower overall average roughness than the Pt-supported ones. This behaviour supports the idea that the methane suppression in favour of ethylene seen on dendritic Cu systems is linked to the overall surface area being high, resulting in a high local pH at the working electrode interface which blocks the methane pathway kinetically [57, 59–61, 125, 131]. The fact that HER is increasing at higher potentials ($>-1.0V$ vs RHE) is attributed to mass transport limitations of CO_2 towards the electrode within the H-type cell setup. Thus, the partial current density of hydrogen is almost equal to the total current density at those potentials (Figure. 4.13 (a), (i)).

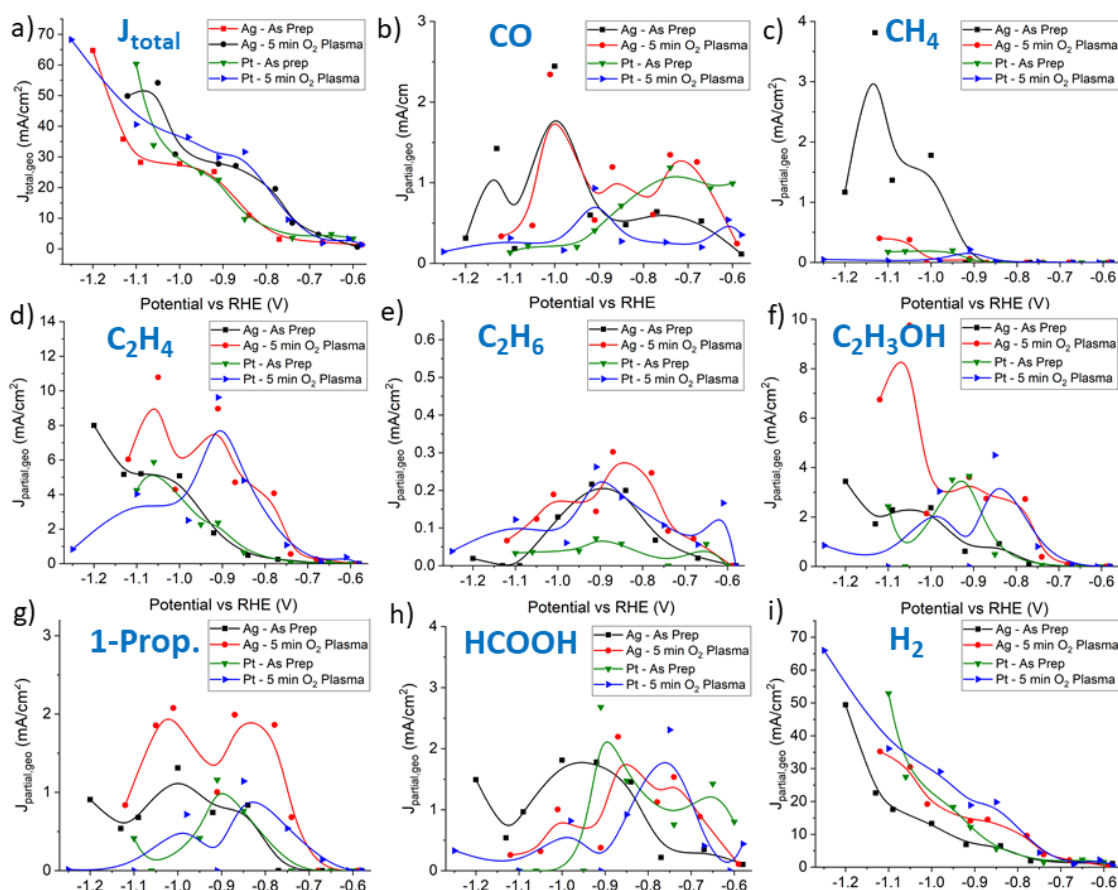


Figure 4.13: (a) Total current density and (b)-(i) partial current density of the reduction reaction products. Solid lines are a guide for the eye. Published in [27]. Reprinted with permission from [27]. Copyright 2019 American Chemical Society.

In addition to the samples showing a superior performance due to the fact that they are oxide-derived, a promoting effect on the selectivity depending on if the employed substrate can be observed. Regardless of the plasma treatment, an increase towards C₂₊ products is present for the Ag-supported dendrites when comparing to the ones supported on Pt, even though the overall roughness was found to be smaller for the as prepared samples on Ag (Fig. 4.11). The reason that Ag is able to reduce CO₂ towards CO, while Pt is inert for CO₂RR and only produces hydrogen due to its strong binding energy for CO that leads to poisoning of the active sites [9]. The promoting effect of Ag is even more dominant on the oxygen-plasma treated Ag substrates.

To be able to understand the interplay of the Cu dendrites and their respective substrate the substrates have been considered without the dendrites on top. The resulting Faradaic efficiencies and current densities are shown in Fig. 4.14. The plasma treated Ag substrate clearly shows a high selectivity towards CO over HER for the whole potential range investigated, while the non plasma treated one only exhibits a high selectivity towards CO at higher potentials (> -1.0V vs RHE), which is in agreement with literature [26]. The obtained SEM images after EC hereby show to be similar to the cases when Cu dendrites have been on top during CO₂RR (fig. 4.8). Regarding the Pt sample, there is as expected only HER observable for the whole potential range investigated (fig. 4.14).

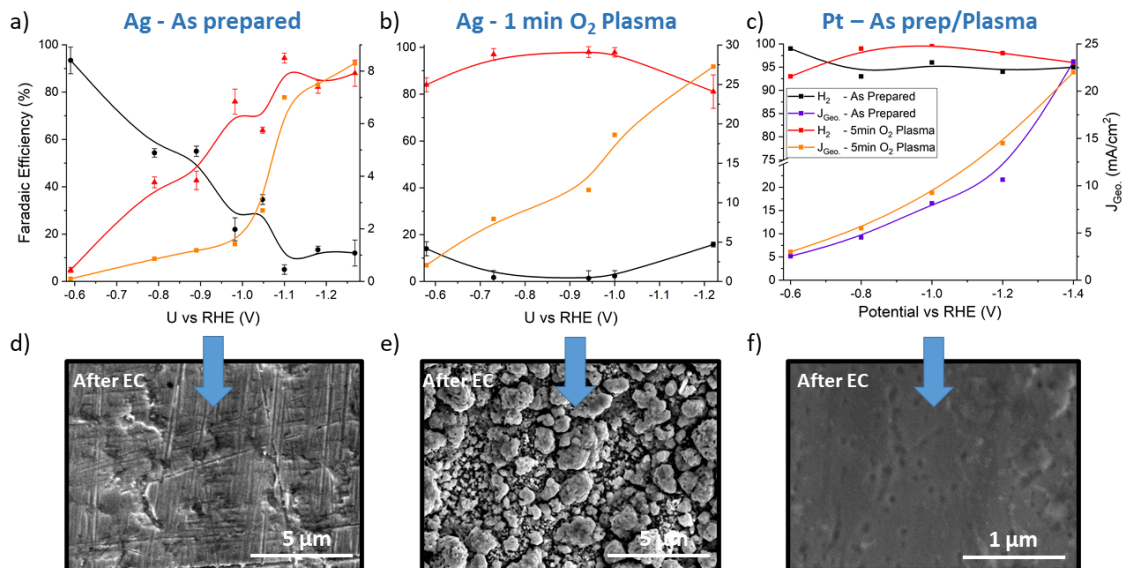


Figure 4.14: Faradaic efficiencies for the pristine and plasma-treated Ag (a), (b) and Pt (c) substrates as a function of the applied potential. SEM images show the corresponding surfaces after 1h of CO₂RR at -0.9V vs RHE in 0.1M KHCO₃. Data published in [27]. Reprinted with permission from [27]. Copyright 2019 American Chemical Society.

Looking at the combined system of Cu/Ag (Cu on Ag) there is a small amount of CO (5-10 %) detected at high potentials ($> -0.95\text{V}$ vs RHE) while none is found on the Cu/Pt system. Combining these observations with the recently discussed selectivity trends for the substrates leads to the conclusion that the CO originates from the Ag substrate rather than from the Cu dendrites on top. Similarly, the higher amount of hydrogen detected on the Cu/Pt systems for potentials higher than -0.9V vs RHE is most likely originates from the exposed Pt areas on the sample.

Furthermore, the high amount of CO at low overpotentials (-0.6V vs RHE) seen for the plasma-treated Cu/Ag system also has to be assigned to the superior performance of the pre-oxidized Ag support, which shows up to 70 % higher Faradaic efficiency for CO as compared to the untreated Ag substrate (Fig. 4.14). The mentioned improved C_2 selectivity of the dendrites supported on Ag as compared to the ones supported on Pt is likely linked to the substrate's ability to participate in CO_2RR . The CO generated can be recaptured by the high surface area dendritic Cu on top and get further reduced in a coupled mechanism. The difficult activation step of the CO_2 is hereby done by the substrate which manages to do it at a lower overpotential in the case of Ag.

As mentioned in the case of the Pt substrate, the detected CO can only originate from the Cu dendrites. The decrease in the selectivity towards CO at lower potentials (18 % less as compared to the non plasma-treated sample at -0.7V vs RHE) seen for the plasma treated dendrites on Pt therefore suggests a change in the preferred reduction pathway. Possibly the binding strength for CO and other intermediates such as COOH and COH is increased on the oxide-derived catalysts, resulting in an increased selectivity towards higher chain hydrocarbons at higher potentials ($> -0.9\text{V}$ vs RHE). This idea would also go in line with changes in the selectivity seen for halide-exposed samples, where the COOH facilitating step was most likely enhanced and TPD measurements suggested a simultaneous increase in the CO binding strength on oxidized surfaces, which is likely to persist upon reduction [62, 65, 110]. In addition, the plasma treatment manages to further reduce the generated CH_4 in favour of ethylene and ethanol for potentials higher than -0.9V vs RHE. Even though this additional methane suppression is proportional to the roughness (fig. 4.12, 4.8 and 4.11) and can be explained by means of the local pH [60, 125] it is not enough to explain the overall increase of C_{2+} hydrocarbons detected.

The increase of almost 20 % of the C_{2+} products on the oxide derived samples is already observable at potentials where the methane generation is not observable for the as prepared non-plasma treated dendrites on Ag and Pt, namely lower than -0.9V vs RHE. Consequently, the increased performance towards higher chain hydrocarbons due to being Cu oxide-derived can not solely be explained by an increase in the local pH, but must be linked to different parameters which is an important conclusion that can be drawn from this study.

To address the open question if oxides are stabilized and present for the Cu dendrites either in the as prepared or oxide-derived samples and consequently to investigate and understand the possible impact of those species, a combination of quasi *in situ* XPS and *operando* XAFS measurements have been employed. The XAFS measurements were carried out at the undulator beamline P65 of the PETRA III storage ring in Hamburg DESY. A passivated implanted planar silicon (PIPS) detector was at an incidence angle of 45° to obtain the fluorescence yield at energies around the Cu-K edge (8989 eV). The employed setup and data analysis tools have been described previously (see. chapter 2.4.4).

Figure 4.15 shows the obtained Ag MNN Auger spectra obtained on the samples supported on Ag which has been the only substrate proven to undergo a chemical change (see Tab. 4.1). The obtained binding energies after alignment to the C 1s line ($E_B=284.8\text{eV}$) for the Ag 3d and the corresponding modified Auger parameters are summarized in Tab. 4.2. As it can be seen, the values obtained reflect the ones reported in the literature [138, 139] providing information about the chemical state. The O 1s, Cu LMM and Cu 2p data on the Ag supported samples, as well as on the Pt supported samples are summarized in Figure 4.16, 4.17 and 4.18.

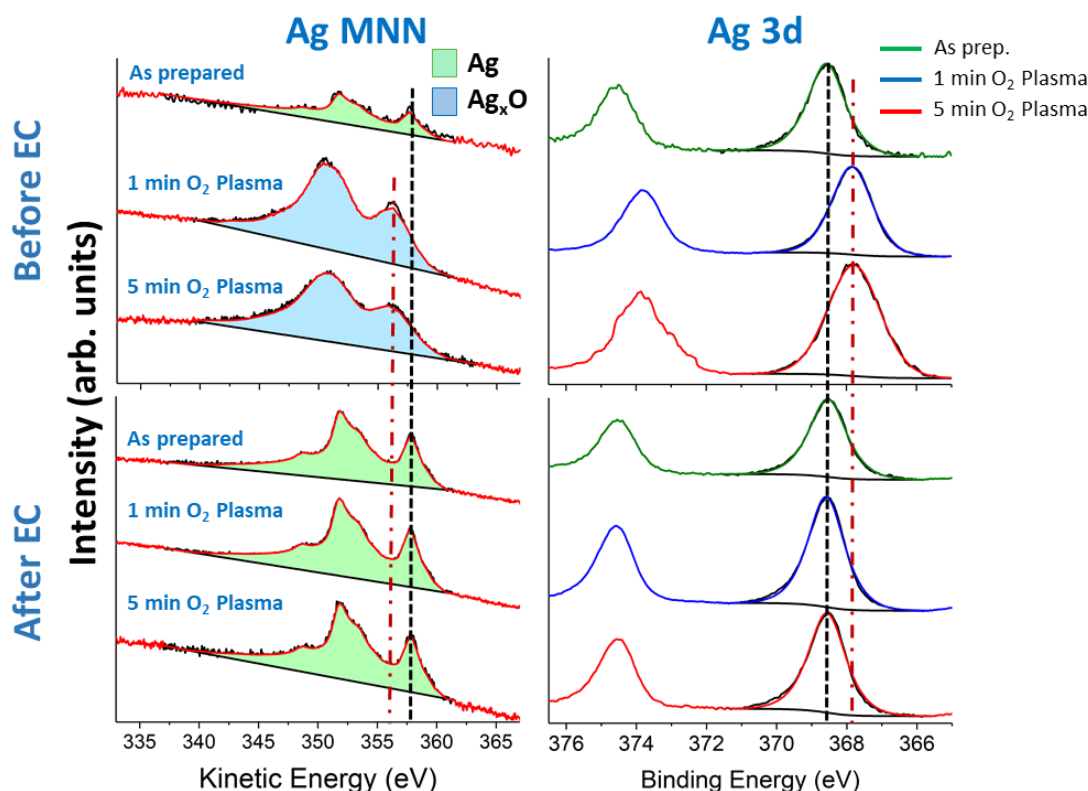


Figure 4.15: Ag MNN Auger-(left) and Ag 3d (right) XPS data for the pristine and plasma treated Ag before and after electrochemistry at -0.9V vs RHE. Published in [27]. Reprinted with permission from [27]. Copyright 2019 American Chemical Society.

Region	As fitted / eV	Lit. [138] / eV.	Lit. [139] / eV
Ag $M_5N_{45}N_{45}$ parameter	720.2	-	720.5
AgO $M_5N_{45}N_{45}$ parameter	718.3	-	718.3
Ag 3d	368.4	368.3	368.2
AgO 3d	367.8	367.3	367.6

Table 4.2: Binding energy and modified Auger parameter of the Ag MNN and Ag 3d spectra. Literature values extracted from Ferrara et al. [138] and Wagner et al. [139]. Published in [27].

The obtained result by linear combination fitting with the corresponding Ag MNN Auger reference spectra is that the underlying Ag substrate is metallic during CO_2RR , even though being strongly oxidized by the initial plasma treatments [26]. In agreement, the O 1s spectra for the dendrites supported on Ag only show a distinct peak at a binding energy of $E_B=528.9$ eV (Fig. 4.16), that can be assigned to the presence of silver oxide species [140] for the plasma treated sample before electrochemistry. Note that at the same time the binding energy of the "adventitious" oxygen on the plasma treated Ag substrate is shifted towards lower binding energies as compared to the same peak on the other samples. This shift is believed to be due to the interaction of oxygen species with the oxidized Ag substrate.

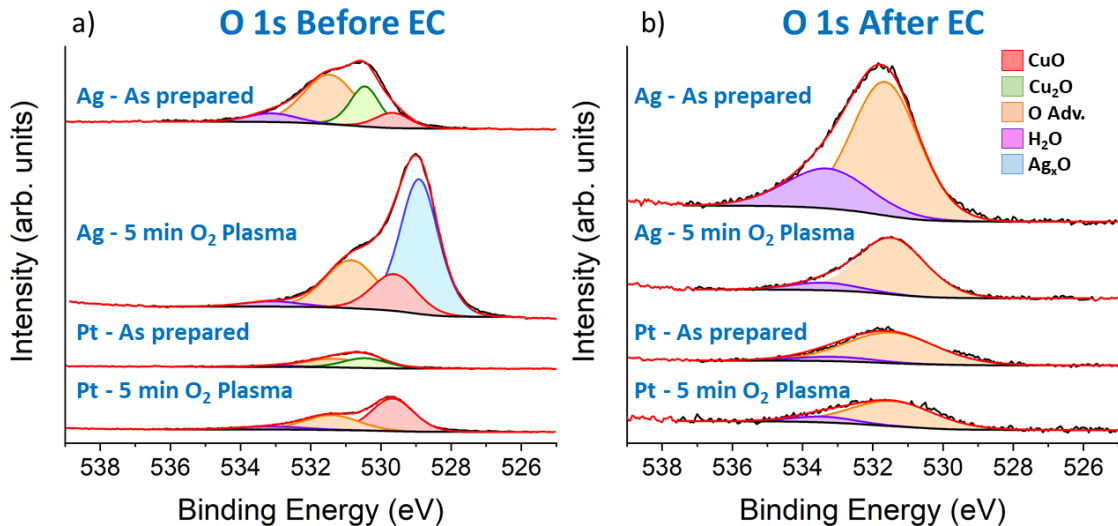


Figure 4.16: Quasi *in situ* O 1s XPS spectra of Cu dendrites (a) before and (b) after EC supported on Ag and Pt. CO_2RR run at $-0.9V$ vs RHE for 1 h in $0.1M$ $KHCO_3$.

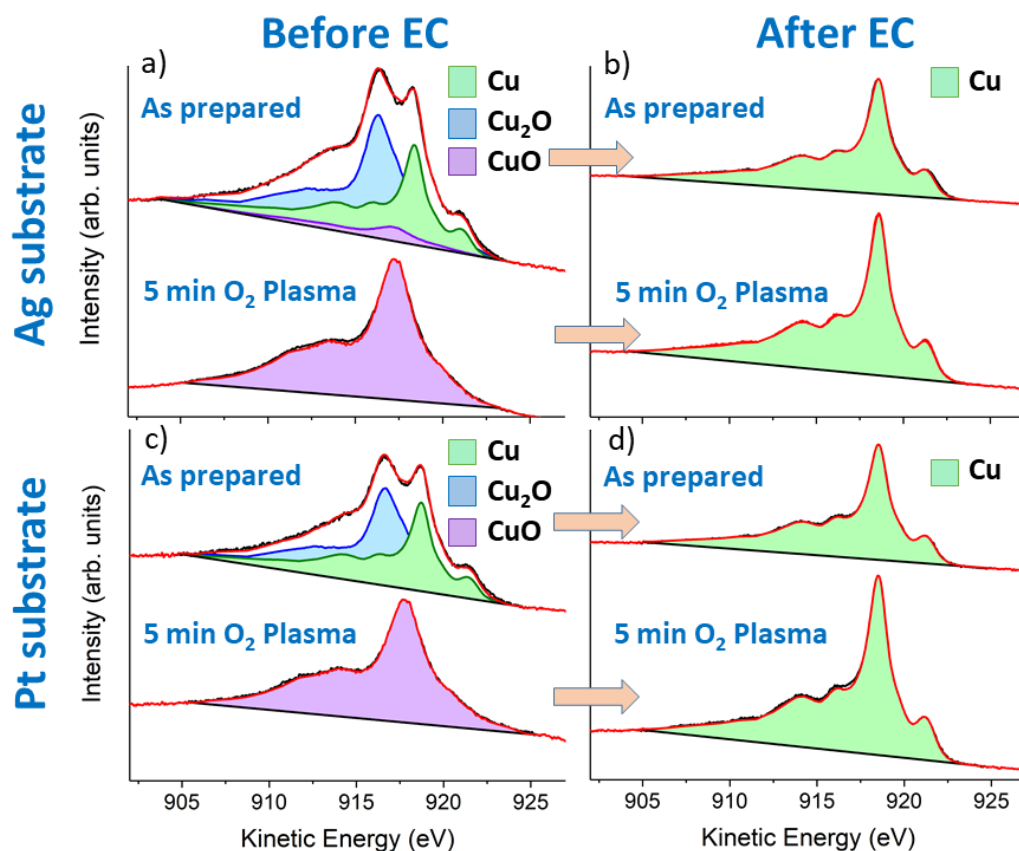


Figure 4.17: Quasi *in situ* Cu LMM XPS spectra acquired on Ag- and Pt-supported Cu dendrites before (a, c) and after 1h of CO₂RR at an applied potential of -0.9V vs RHE (b, d). The spectra are fitted with a linear combination of the corresponding Cu, Cu₂O and CuO reference spectra. Published in [27]. Reprinted with permission from [27]. Copyright 2019 American Chemical Society.

The obtained Cu LMM data which reflect the chemical state of the Cu dendrites shows that all samples contained Cu_xO species before reaction either due to being plasma treated or exposed to air. The plasma-treated samples were fully oxidized towards CuO, while the others are composed of a mixture of Cu and Cu₂O. The Cu 2p core level spectra (Fig. 4.18) show the characteristic shake-up features of CuO for the plasma-treated samples before EC. The quasi *in situ* XPS measurements after EC reveal that all samples were reduced to the metallic state, irrespective of the pretreatment, (Fig. 4.17) since neither the Cu LMM nor the Cu 2p or O 1s spectra reflect the presence of Cu oxide. The potential chosen was hereby the peak potential for ethylene. Consequently, there are also no oxides present at higher reduction potentials such as -1.0V or -1.1V vs RHE at which a high amount of ethanol and 1-propanol was detected. The improved selectivity towards C₂₊ hydrocarbons seen on Cu dendritic systems is therefore not linked to the presence of Cu⁺ species during the reaction as far as it can be told by XPS.

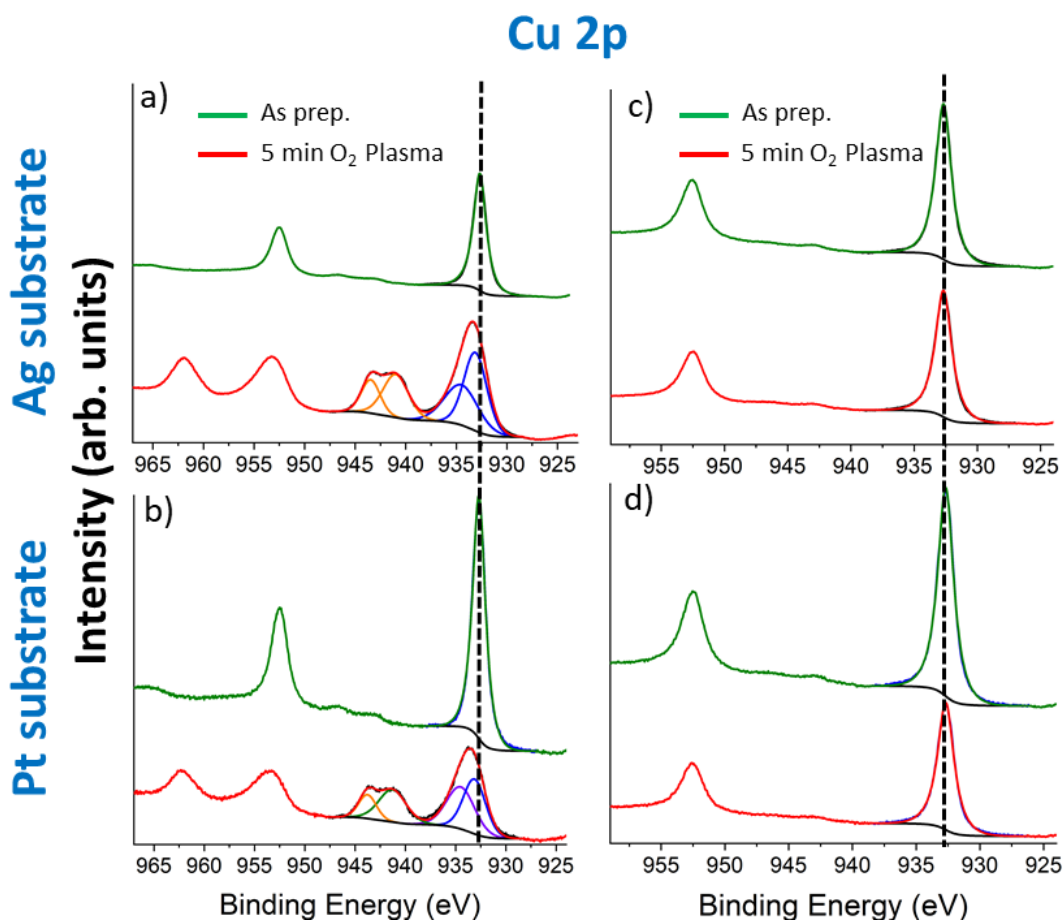


Figure 4.18: Quasi *in situ* Cu 2p spectra acquired on Ag- and Pt-supported Cu dendrites before (a, b) and after 1h of CO₂RR at an applied potential of -0.9V vs RHE (c, d). The dashed line indicates the Cu/Cu₂O peak position at $E_B=932.67\text{eV}$. Published in [27]. Reprinted with permission from [27]. Copyright 2019 American Chemical Society.

Additionally, it was checked if the Cu dendrites contain any oxides directly after the deposition process. As mentioned, it was suggested that the selectivity trends for Cu dendrite systems could be due to the presence of oxides after the deposition process and consequently being reduced [61]. The high intrinsic selectivity seen would therefore be linked to the catalyst being oxide derived.

The dendrites have therefore been grown on a commercial (Freudenberg C2 GDL gas diffusion electrode (GDE) which is the type of system used within the literature for CO₂RR [61]. The acquired Cu LMM and Cu 2p spectra directly after growing the Cu dendrites on GDEs are shown in Fig. 4.19.

Clearly, Cu is in its metallic state, supporting the interpretation that the observed catalytic behaviour of dendritic Cu is linked to its morphology and not to the presence of Cu⁺ species. The result also supports the previous interpretation that the dendrites grown on Ag and Pt are metallic in their as prepared state and

that the previously reported oxides for the as prepared samples before EC are indeed originating from the exposure of the samples to air and/or the oxygen plasma treatment.

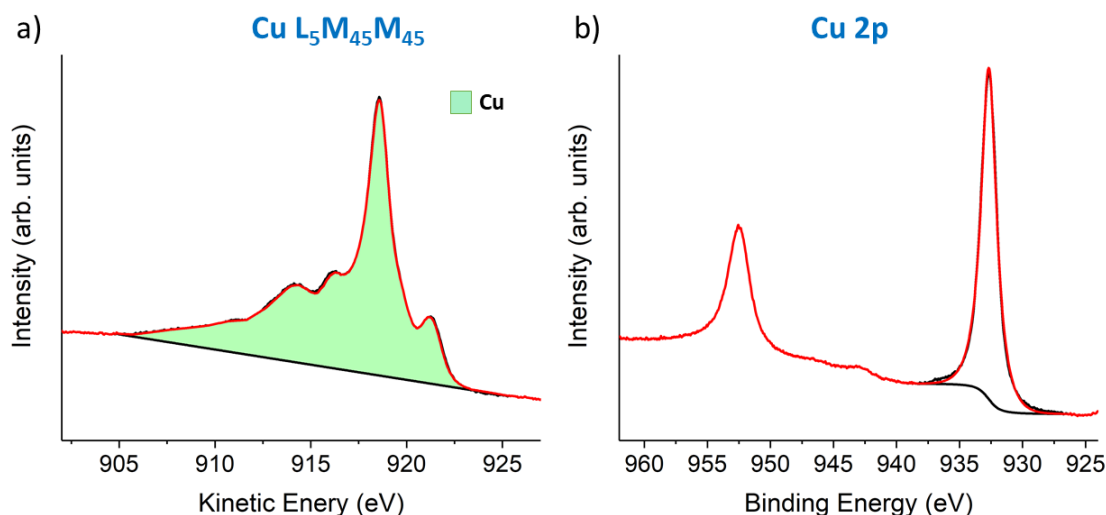


Figure 4.19: (a) Cu LMM and (b) Cu 2p spectra of Cu dendrites grown on a carbon based GDE. Published in [27]. Reprinted with permission from [27]. Copyright 2019 American Chemical Society.

As mentioned, these results suggest that the superior catalytic performance of oxide derived Cu dendrites as well as for the pristine samples is not linked to the presence of copper oxide species, but has to be explained by means of the local pH and the morphology. Complementary to the hereby discussed data and results, Reller et. al. reported a drop in the faradaic efficiency for ethylene once the needle like structure of the dendritic tips coarsens [61]. Furthermore, *operando* Raman experiments carried out by Klingan et. al. managed to show that indeed the local pH in the vicinity of the electrode is increased with respect to the bulk pH on dendritic shaped Cu catalysts [60]. Examining samples prepared by Klingan et. al. with the help of the quasi *in situ* XPS setup also showed them to be in their metallic state [60].

To back these findings up and to complement the surface sensitive XPS spectroscopic analysis, *operando* XAFS measurements have been conducted in addition. These provide information about the bulk state of the sample and thus, the presence of subsurface oxide species which have been considered to play a role by migrating to the surface and consequently getting reduced, maintaining a special defective undercoordinated surface as well as changing the electronic structure of the surface atoms [69, 74]. The obtained XANES spectra and their respective Fourier transformed R-space as well as the k-space representation is shown in Fig 4.20 and 4.21. Additionally, the data has been Wavelet-transformed [141] to further visualize the sample chemical state (fig. 4.22 and 4.23).

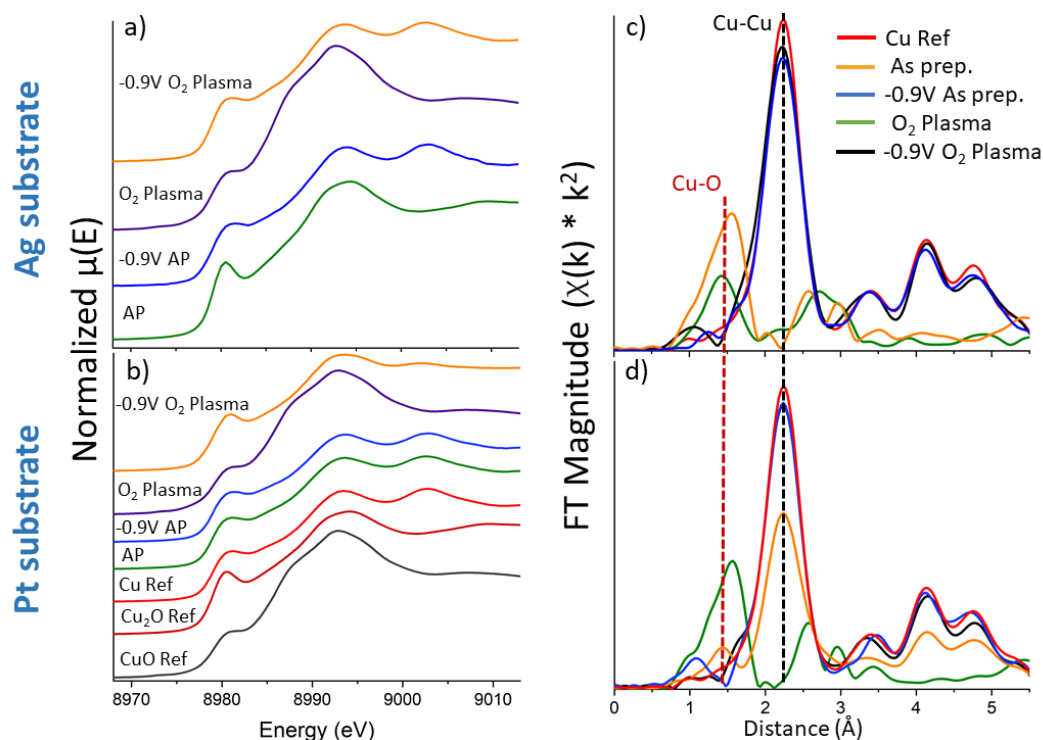


Figure 4.20: XANES spectra of the as prepared and 5 min O_2 -plasma treated Cu dendrite samples supported on (a) Ag and (b) Pt. The measurements were conducted on the differently pretreated samples before and during CO_2RR at $-0.9V$ vs RHE. Panels (c) and (d) show the corresponding FT signals in r-space for the Cu/Ag and Cu/Pt. Dashed lines indicate the position of the characteristic peaks for Cu-Cu and Cu-O coordination. Published in [27]. Reprinted with permission from [27]. Copyright 2019 American Chemical Society.

A comparison of the k-space representations of the acquired data before electrochemistry (fig. 4.21 (a) and (c)) with the respective references (fig. 4.21 (b) and dashed lines in (a) and (c)) shows the as prepared samples consist of a mixture of Cu and Cu_2O whereas the Ag-supported sample is more oxidized than the Pt-supported one. Regarding the sample states after plasma oxidation, both closely follow the line shape for the obtained CuO reference. Similarly, there are distinct features at 1.45 \AA and 1.55 \AA in the R-space representation of the samples before EC which are marking the copper to oxygen bond interaction in Cu_2O and CuO.

Upon applying a potential of $-0.9V$ vs RHE, all spectra closely follow the reference for Cu in the k-space representation (fig. 4.21 (d)). At the same time, the characteristic features for Cu_2O and CuO marking the Cu-O interaction vanish completely in the R-space representation of the data, and a distinct peak at 2.2 \AA marking the Cu-Cu interaction in Cu appears. The change in the oxidation state towards metallic Cu is also clearly visible in the wavelet transformed data representation [141–143] as all samples during CO_2RR reproduce the acquired spectra on metallic Cu (fig. 4.22 and 4.23).

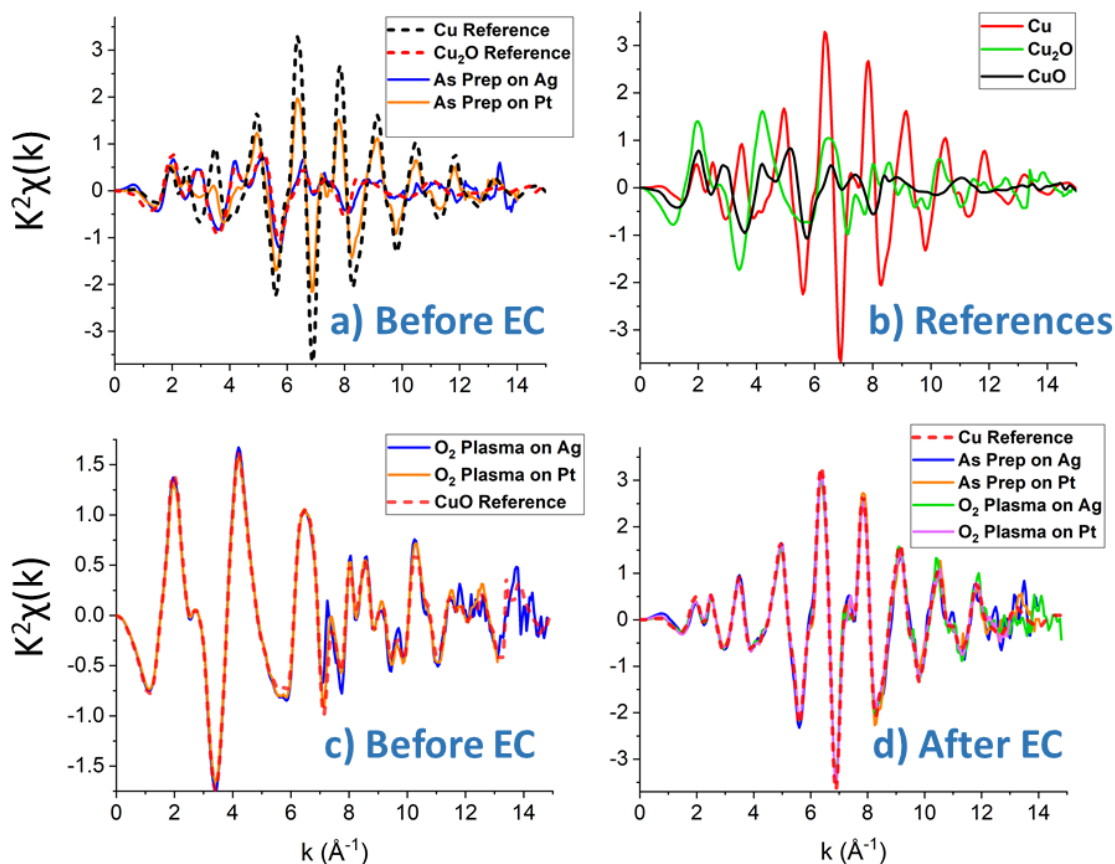


Figure 4.21: K-Space representation of *operando* EXAFS data acquired on (a) the as prepared and (c) the plasma treated samples before EC and (d) the samples at -0.9V vs RHE in 0.1M KHCO_3 . Panel (b) shows the acquired reference datasets for copper.

To also quantify the recently discussed results, the XANES spectra have been linear combination fitted with the respective references. The results are summarized in tab. 4.3.

Sample	Cu (%)	Cu ₂ O (%)	CuO (%)
Before EC As prep on Pt	53	46	1
During EC As prep on Pt	100	-	-
Before EC O ₂ Plasma on Pt	-	5	95
During EC O ₂ Plasma on Pt	100	-	-
Before EC As prep on Ag	7	86	7
During EC As prep on Ag	100	-	-
Before EC O ₂ Plasma on Ag	-	3	97
During EC O ₂ Plasma on Ag	100	-	-

Table 4.3: Linear combination analysis of the acquired XANES spectra with the respective reference data sets. Published in [27].

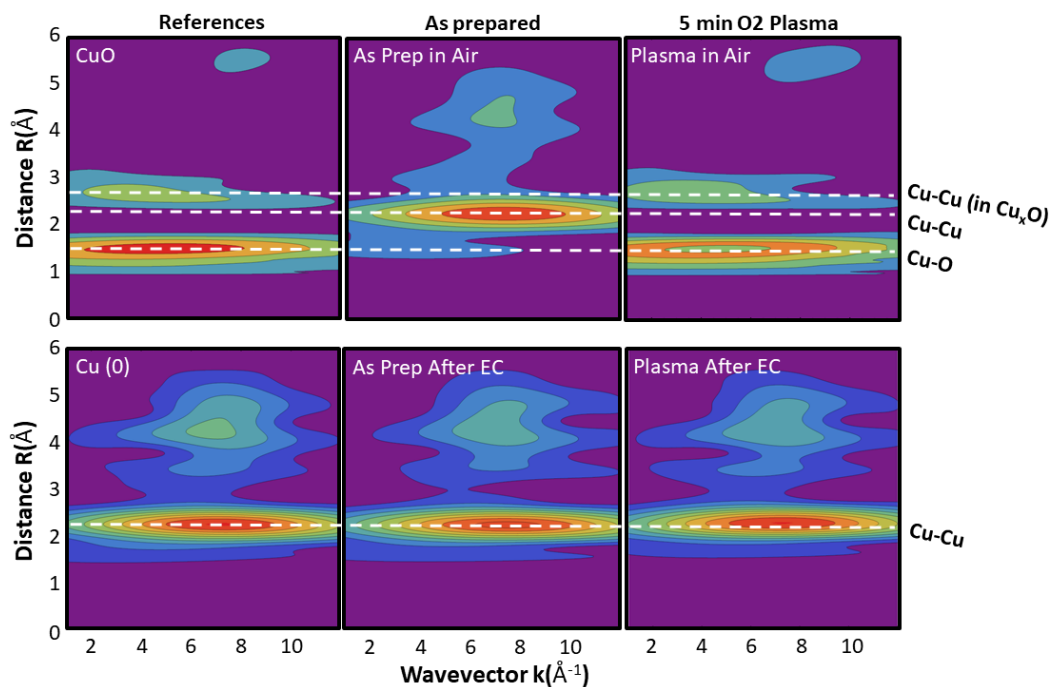


Figure 4.22: Wavelet transform of Ag supported Cu dendrite EXAFS data. Published in [27]. Reprinted with permission from [27]. Copyright 2019 American Chemical Society.

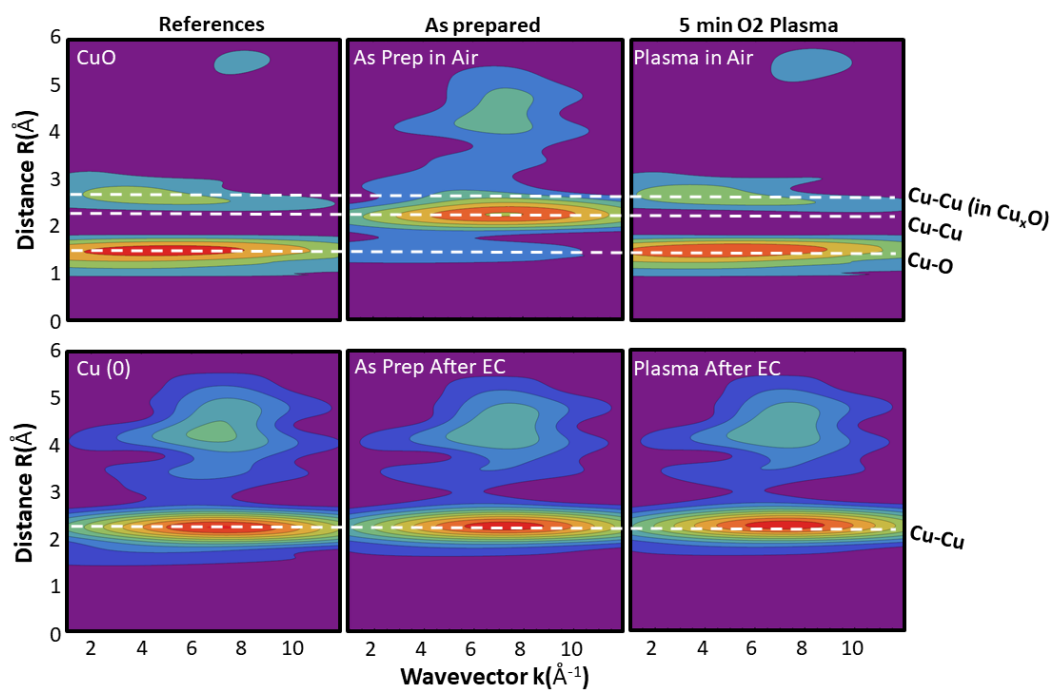


Figure 4.23: Wavelet transform of Pt supported Cu dendrite EXAFS data. Published in [27]. Reprinted with permission from [27]. Copyright 2019 American Chemical Society.

The analysis also shows the main species to be present before electrochemistry to be Cu and Cu₂O for the as prepared samples and CuO for the plasma treated samples. While for the Pt supported samples there is a nearly one to one mixture of Cu and Cu₂O species the Ag supported samples are almost fully oxidized towards Cu₂O. Nevertheless, the most important result hereby is that the quasi *in situ* XPS data of all samples demonstrate that they are fully metallic during electrochemistry once a potential of -0.9V is applied.

Additionally modelling the EXAFS spectra by means of the model discussed in section 2.4.3 to extract the coordination numbers further supports the results obtained from linear combination fitting. These results and fitting parameters are summarized in Tab. 4.4. The analysis yields a coordination number for the Cu-Cu interaction in Cu on the Pt-supported Cu dendrites of $N_{Pt} = 10.8-11.3 \pm 1.0$ and $N_{Ag} = 11.8 \pm 1.5$ for the Ag supported dendrites. Taking into account that the measurements have been conducted not in transition but fluorescence mode there is the possibility of error margins due to self-absorption within the material. Thus, here the conclusion is that the surface as well as the bulk of the sample is metallic Cu since the obtained coordination numbers fit the one for metallic Cu ($N_{Cu-Cu} = 12$). At the same time, the mean displacement σ obtained from the fits is very low and positive, supporting that the applied model is working out properly. Regarding the amount of undercoordinated atoms, it has to be emphasized that since the acquired data is dominated by the bulk, their presence at the surface can not be probed with high enough accuracy to be able to judge if the near surface atoms participating in the reaction are undercoordinated (>8) or not.

Sample	Path	N	R (Å)	σ (Å ²)
Pt-As prep.	Cu-Cu (Cu)	6.8 ± 1.2	2.55 ± 0.01	0.01 ± 0.001
	Cu-O (Cu ₂ O)	1.5 ± 0.5	1.84 ± 0.04	0.001 ± 0.001
Pt-As prep. EC	Cu-Cu (Cu)	10.8 ± 1.0	2.55 ± 0.01	0.01 ± 0.001
Pt-O ₂ Plasma	Cu-O (CuO)	3.7 ± 0.6	1.95 ± 0.02	0.0029 ± 0.001
Pt-O ₂ Plasma EC	Cu-Cu (Cu)	11.3 ± 1.0	2.55 ± 0.004	0.008 ± 0.001
Ag-As prep.	Cu-O (Cu ₂ O)	3.7 ± 0.9	1.84 ± 0.02	0.0019 ± 0.0003
Ag-As prep. EC	Cu-Cu (Cu)	11.8 ± 1.5	2.55 ± 0.02	0.01 ± 0.001
Ag-O ₂ Plasma	Cu-O (CuO)	4.0 ± 0.7	1.95 ± 0.10	0.004 ± 0.002
Ag-O ₂ Plasma EC	Cu-Cu (Cu)	11.8 ± 1.5	2.55 ± 0.012	0.008 ± 0.001

Table 4.4: EXAFS fitting results for the Cu dendrite samples supported on Ag and Pt. Before EC denotes that the sample was not in contact with any electrolyte. During EC denotes the measurements done under *operando* CO₂RR conditions at -0.9V vs RHE in 0.1 M KHCO₃ solution. Published in [27].

Summary: Oxide derived dendrites

Figure 4.24 represents a summary of the obtained results on oxide derived Cu dendrites supported on different secondary metals.

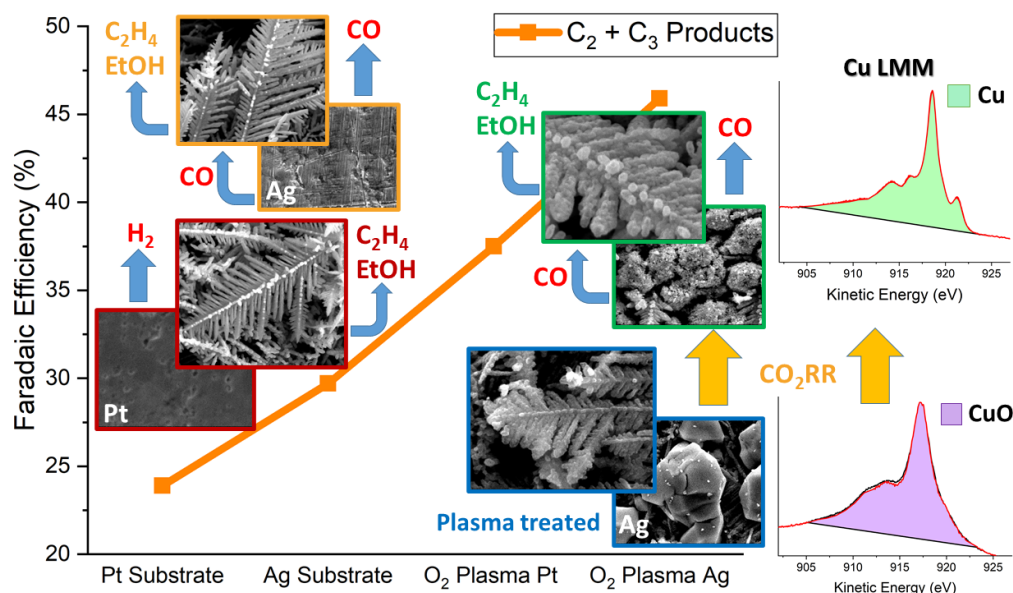


Figure 4.24: Description of the performance of oxide-derived Cu dendrites supported on Ag and Pt featuring their Faradaic efficiency for C₂₊ products and the correlated SEM (insets) and XPS results.

The obtained results for Cu dendrites support the idea that the presence of Cu⁺ species during electrochemistry plays an inferior role within the framework of CO₂RR as the modified morphology. At least for Cu dendrites, Cu_xO species cannot be stabilized and thus cannot participate in the reaction mechanism responsible for the observed increase in the C₂₊ product selectivity. Furthermore, the effect of an altered local pH cannot solely explain the observed changes in the selectivity trends either. Thus, the superior selectivity towards C₂₊ products is mainly emerging from structural and morphological properties of oxide-derived catalysts that emerge upon their reduction under reaction conditions. Nevertheless, the possible beneficial influence of Cu⁺ species cannot be discarded completely at this point, since the obtained selectivity trends for Cu dendrites are inferior to what has been reported on other oxide derived catalysts [72, 86, 131]. This discrepancy could still be due to the fact that other catalysts might be able to stabilize those oxidic species, contrary to the hereby investigated Cu dendrite systems. Taking into account the previously presented results, their influence should be minor and mainly be directed towards oxygenates such as ethanol rather than ethylene.

Regarding Cu dendrites specifically, it was possible to demonstrate that their selectivity towards higher chain hydrocarbons is tunable by low pressure oxygen plasma treating them (Fig. 4.24). This is only possible as their intrinsic selectivity

and the selectivity of oxide-derived catalysts are both not solely explainable by the evolving local pH during reaction. Furthermore, by using different substrates it was possible to further improve their selectivity while maintaining the intrinsic high current densities which is specially important for technological applications. The obtained results also point out the importance of synergistic effects when combining several metals in order to improve the CO₂RR selectivity.

4.3 Pulsed electrolysis on single crystal surfaces

Superior performing oxide-derived catalysts, as compared to their metallic counterparts are not likely able to stabilize copper oxide species during CO₂RR. Thus, the improved selectivity is supposedly independent on their presence during EC. Nevertheless, since there are even better performing catalysts reported within the literature that have also been proven retain Cu⁺ species [69, 71, 72, 74, 131] the question whether or not there is an effect related to their presence remains open. Additionally, their beneficial influence on the CO dimerization by partially differently charged CO molecules due to sitting on top of Cu and Cu₂O species next to each other has been predicted recently, thus pointing towards a possible influence on the reaction [71].

The downside that all these recently investigated catalysts have in common is that they are of polycrystalline nature. Since theoretical [46, 47, 54, 144] and experimental [37, 43, 44, 49, 52, 135] studies pointed out the importance of specific crystalline facets being present and especially the influence of (100) Cu facets on the selectivity towards ethylene understanding the precise effect of oxides present on these type of systems is very difficult. Furthermore, other factors such as the positive effect of oxygenates being present on the surface for the amount of ethanol generated has been pointed out recently, and it was showcased that their absorption is also very much dependent on the crystal orientation of the employed catalyst [135]. Consequently, the control of the surface structure is of importance when investigating the possible role of copper oxide species on the catalytic reaction.

To overcome these issues a Cu(100) single crystalline surface, whose oxidation state is controlled by electrochemically pulsing the applied potential has been employed. By applying an anodic pulse that is able to oxidize the surface followed by a cathodic pulse at a potential sufficiently low to have CO₂RR occur, the generated oxide species are present during CO₂RR. Thus, instead of stabilizing oxides for a long time during CO₂RR, they are dynamically generated. Even though several other studies carried out have employed this method in the past and highlighted its potential for controlling and altering the obtained product selectivities for methane or for synthetic gas (H₂, CO), they have not been able to directly provide experimental evidence on the parameters leading to the observed trends [145–147]. Mostly because either the product analysis with respect to liquid products such as ethanol has not been carried out in detail, due to the fact that polycrystalline samples have been employed, or a restrictive range of anodic potentials selected, making it difficult to unravel the specific contributions of the different parameters.

By carefully analysing the obtained selectivities in chronoamperometric experiments and by comparison to pulsed potential experiments, while at the same time monitoring the structural evolution, the study conducted hereby is able to close this gap and provide direct evidence of the role of Cu_xO species on CO₂ electroreduction.

The first task is hereby to determine the potentials at which the oxidation towards the different oxidation states occurs on Cu (100) in 0.1M KHCO₃, which is the employed electrolyte. The fastest and easiest approach is to perform cyclic voltammetry experiments.

Prior to usage, all electrodes have been electropolished (see also chapter 3.1) for 10s at a potential of 3 V vs a Ti counter in a H₃PO₄(130ml, VWR 85 % wt) + H₂SO₄ (20ml, VWR 95%) solution adding 60ml ultrapure water (Elga. 10,2 MΩcm). The employed Cu (100) electrodes (MaTeck) have a diameter of 1cm. The Cu foils (Advent Research Materials 99,995%) used for comparison have been polished for 3 minutes as it was the case in the previously highlighted cases. After polishing, all electrodes have been rinsed immediately with ultra pure water and dried with nitrogen. The cyclic voltammograms acquired within 0.1M KHCO₃ are shown in Figure 4.25 (a). Panel (b) showcases the potential scheme applied during pulsed electrolysis which is alternating in between an oxidizing anodic potential pulse E_a and a reductive cathodic potential pulse E_c at which CO₂RR occurs.

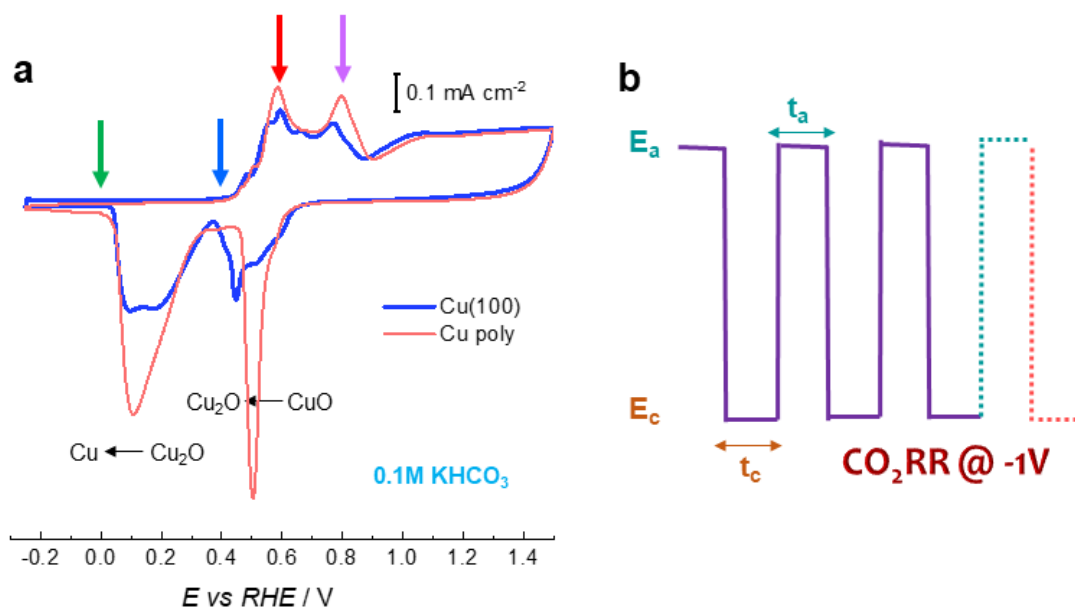


Figure 4.25: (a) Cyclic voltammetry profiles of polycrystalline (red) and Cu(100) (blue) in Ar-saturated 0.1M KHCO₃ solution at a scan rate of 50 $\frac{mV}{s}$. Arrows mark the different anodic potentials E_a employed within this study to alter the surface oxidation state. (b) Potential sequence scheme that is applied during pulsed electrolysis to change from an oxidized surface at the anodic pulse potential E_a to a mostly reduced surface during CO₂RR at the cathodic pulse potential E_c. Data acquired by Dr. Rosa M. Arán-Ais. Published in [45].

The potentials chosen for E_a are marked with arrows in Figure 4.25 (a). The first being E_{a1} = 0.0V vs RHE has been chosen since there are according to the CVs no oxides are stable at this potential as it lies lower than the peak marking the

reductive potential at which Cu_2O is reduced towards Cu. Therefore this potential is used to be able to compare how pulsed electrolysis acts on the electrode when no oxides are generated. The second one being $E_{a_2}=0.4\text{V}$ vs RHE was chosen as an intermediate state where some Cu_2O will be present but not a high amount since, it lies on the onset of the first oxidation peak (blue arrow in Fig. 4.25) in the CV. The third one, $E_{a_3}=0.6\text{V}$ vs RHE, lies on top of the first oxidation peak and should produce Cu_2O . The fourth one, $E_{a_4}=0.8\text{V}$, vs RHE should additionally be able to create CuO species as it lies at the second oxidation peak in the CV. The last two potentials have been chosen to be able to compare the influence of the different Cu oxidations states on the CO_2RR selectivity [76, 145].

To be able to judge if the chosen potentials are meaningful and if the obtained oxidation states by applying these potentials are the ones expected from the analysis of the CV curves [146], quasi *in situ* XPS measurements have been carried out on freshly electropolished Cu (100) single crystals. The potential was hereby kept constant for 5 minutes to be able to clearly observe the evolving oxidation state and exclude the influence of errors. The results obtained are summarized in Figure 4.26.

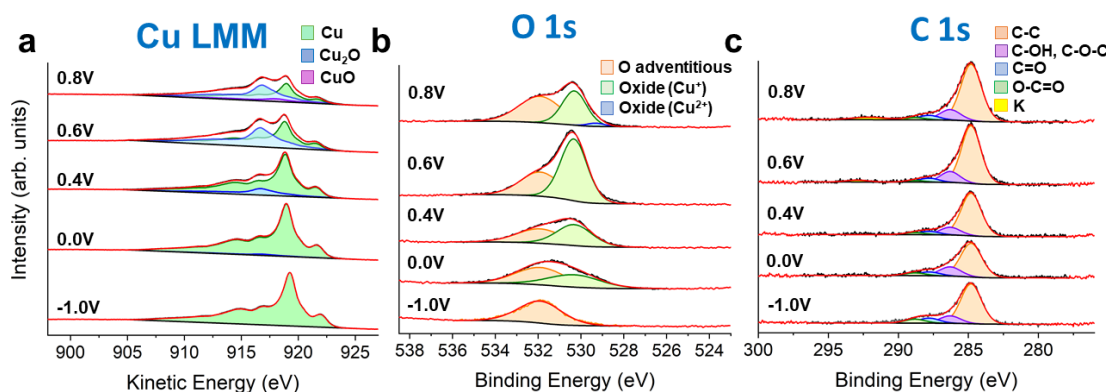


Figure 4.26: (a) Cu LMM Auger, (b) O 1s and (c) C 1s data for the electropolished Cu(100) single crystals exposed to a constant anodic potential for 5 minutes in 0.1M KHCO_3 saturated with CO_2 . All spectra have been aligned to the carbon C-C bond feature $E_B=284.8\text{eV}$ [148]. Published in [45].

Looking at the acquired Cu LMM Auger spectra (Fig. 4.26 (a)) and the corresponding O 1s data (b), the sample kept at -1.0V vs RHE for 5 minutes does not show any oxides, which is in line with what has been observed for polycrystalline Cu and Cu dendrites. The spectra for the sample kept at 0.0V vs RHE do show a little amount (2 % judging from the integrated area of the linear combination fitting of the Cu LMM spectra with the corresponding references) of Cu_2O being present as there is also a shoulder in the O 1s spectrum at $E_B=530.2\text{eV}$ that is assigned to Cu_2O , consistent with what is reported in the literature [104, 148]. Due to its low magnitude and to the fact that there is no potential applied while rinsing the sample with ultrapure water after electrochemistry, these oxides most likely originate from the exposure to water rather than due to the applied potential. The same

shoulder peak is also present for all samples exposed to a higher anodic potential, while the highest one also reflects the presence of CuO (9 %) as it is expected. The one showing the most Cu₂O is the one at 0.6 V vs RHE which is meaningful as it is the potential supposed to generate this species. The amount of oxides found within the sample exposed to a constant potential of 0.4 V vs RHE is in between the 0.6V vs RHE and the 0.0V vs RHE cases. This fits the general picture of a Cu sample not being completely reduced at 0.4V vs RHE. Therefore, the observed oxides are considered to originate from the sample's interaction with the electrolyte during the 5 minutes it is kept within. The C 1s spectra is additionally showcased to support the consistence of the obtained spectra, as the alignment here was done using the C 1s C-C interaction peak rather than the Cu 2p spectra as it had to be done previously since especially the UHV-cleaned samples have no carbon present on the surface that could be used for the alignment. The precise amounts for the obtained Cu_xO compositions are summarized in tab. 4.5.

E vs RHE / V	Cu (atomic %)	Cu ₂ O (atomic %)	CuO (atomic %)
0.8	45	46	9
0.6	54	46	–
0.4	85	15	–
0.0	98	2	–
-1.0	100	–	–

Table 4.5: Linear combination analysis of the Cu LMM spectra (see fig. 4.26 (a)) with the corresponding reference spectra. Published in [45].

Knowing that the chosen potentials indeed generate the desired chemical states on the Cu (100) electrode surfaces pulsed experiments have been conducted setting the anodic- (t_a) and cathodic (t_c) pulse time to 1 second and alternating in between $E_c = -1.0V$ vs RHE and $E_a = 0, 0.4, 0.6, 0.8$ V vs RHE. To investigate if copper oxides are also present on the electrode surface during the pulsed electrolysis quasi *in situ* XPS measurements were again conducted after stopping the potential sequence either at the upper or lower potential after running the CO₂RR for 1h. The obtained Cu LMM Auger spectra and the corresponding O 1s and C 1s spectra are shown in Figure 4.27 and 4.28.

As expected, the total amount of Cu₂O found is lower as compared to when the exposure time to the corresponding potentials was 5 minutes. Nevertheless, for all E_a cases supposed to produce copper oxides there is a high amount present (14-24 % after stopping at the upper and 4-11 % at the lower pulse). The fact that a large fraction of the oxides is generated and reduced already within pulses as short as 1 second also reflects the exponential behaviour of their generation as a large amount of the metallic surface/oxides is available at the start of the corresponding pulse. For the case of $E_a = 0.8V$ a small amount (4 %) of CuO was also found to be present at the upper pulse, which is consistent with the long time exposure case (fig. 4.5).

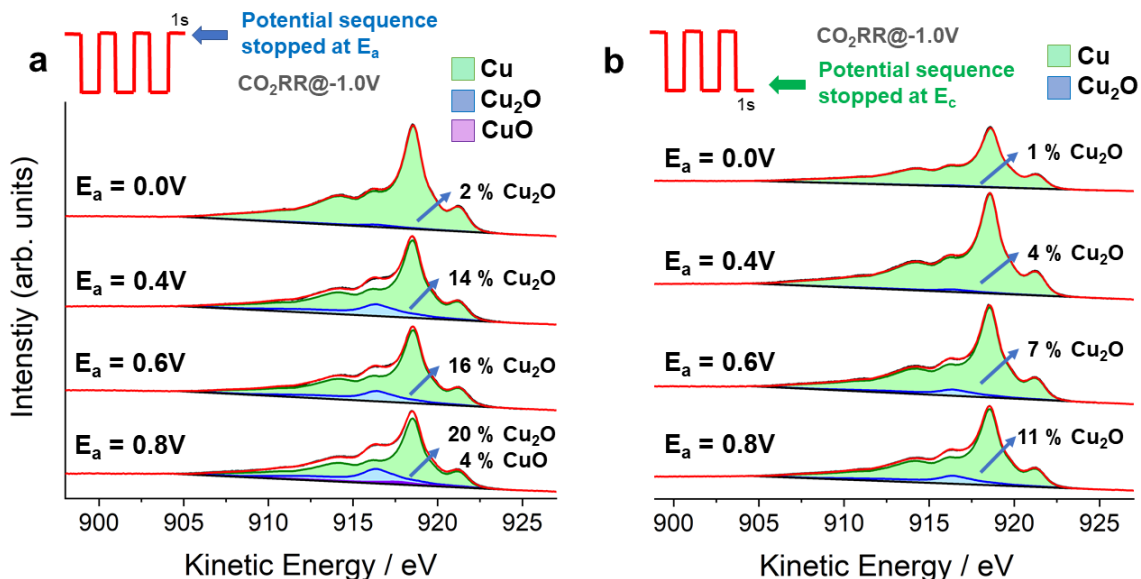


Figure 4.27: (a) Cu LMM spectra stopping the pulse sequence at the upper potential E_a and (b) the corresponding spectra stopping at the lower pulse E_c . Total pulsed CO_2RR electrolysis run time is 1h within the 0.1M $KHCO_3$ solution using a pulse length of $t_c=t_a=1s$. $E_c=-1.0V$ vs RHE for all samples. Published in [45].

As these results suggest that the generated oxides at the upper pulses are not fully reduced during the lower pulses, Cu_2O is present during the lower pulse when CO_2RR is taking place. Looking at the obtained O 1s data (Figure 4.28), similar conclusions can be drawn as the presence of the oxides during the pulsed experiments is also indicated by a peak towards lower binding energies ($E_B=530.2eV$), as expected for Cu_2O . The alignment was again done using the obtained C-C bond feature within the C 1s region ($E_B=284.8eV$).

Sample	Capacitance (mF)	Roughness Factor
Electropolished	0.004	1.0
$E_a=0.0V$	0.005	1.1
$E_a=0.4V$	0.004	1.0
$E_a=0.6V$	0.004	1.0
$E_a=0.8V$	0.005	1.1

Table 4.6: ECSA measurements of Cu (100) single crystal surfaces after 1h pulsed CO_2RR at different anodic potentials E_a in 0.1M $KHCO_3$. All potentials are reported vs RHE. Cathodic potential $E_c=-1.0V$ vs RHE for all cases. Pulse length of 1s. The "electropolished" sample has been run under potentiostatic conditions at the cathodic potential. Data acquired by Dr. Rosa M. Arán-Ais. Published in [45].

Since the selectivity of CO₂RR is highly dependent on structural and morphological properties of the employed catalysts such as the crystal orientation [43, 44, 46] and overall surface area [27], the evolution of these features has to be followed in order to be able to understand the influence of the oxides present during CO₂RR. The overall roughness of the employed samples was kept track of by means of electrochemical surface area measurements based on the double layer capacitance. The data are summarized in Table 4.6. As it can be seen the obtained capacitances are almost similar to each other, reflecting that the overall surface area remains constant under pulsed conditions despite oxidizing and reducing the samples to and from different oxidation states. Nevertheless, the influence of structural changes happening on the microscopic scale can not be discarded on the basis of these experiments alone.

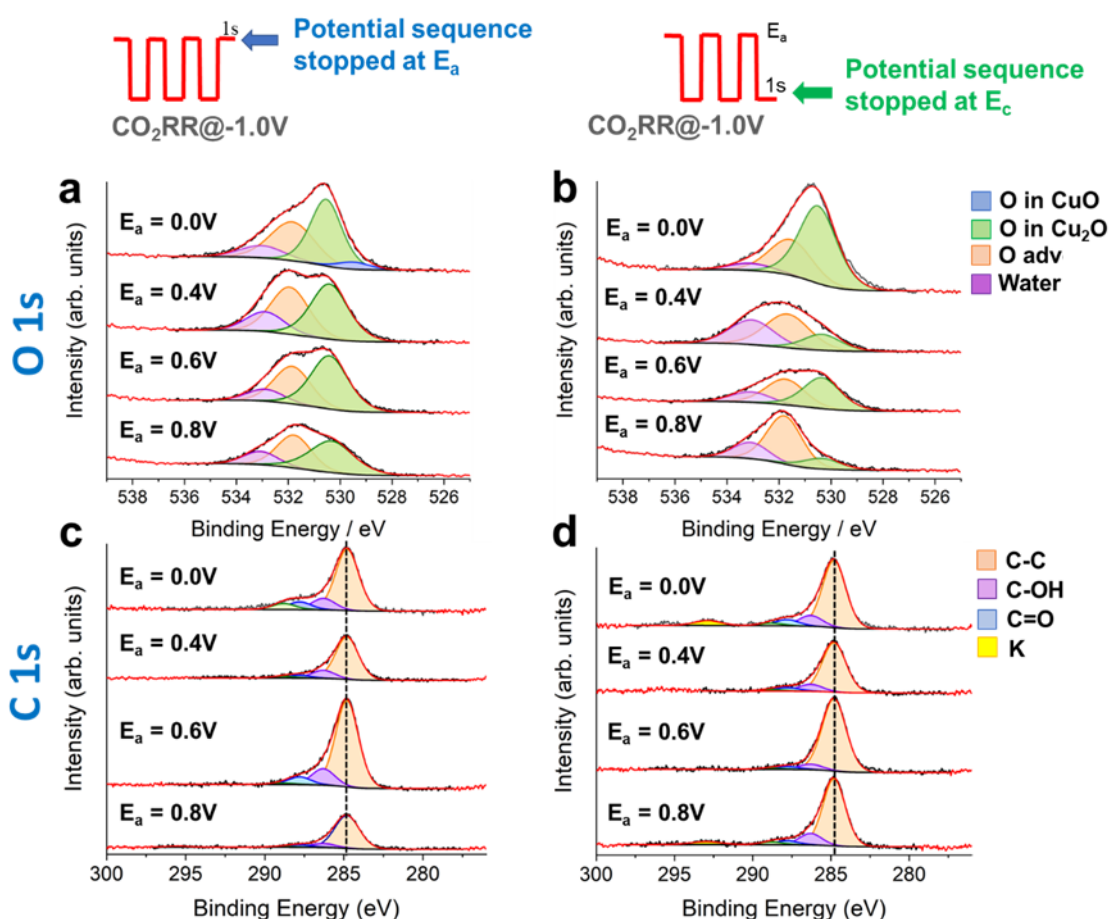


Figure 4.28: (a) O 1s and (c) C 1s spectra stopping the pulse sequence at the upper potential E_a and (b) the O 1s and (d) C 1s spectra stopping at the lower pulse E_c . Total pulsed electrolysis run time is 1h within the 0.1M KHCO₃ solution using a pulse length of $t_c=t_a=1s$. $E_c=-1.0V$ vs RHE for all samples. Published in [45].

To investigate this topic, cyclic voltammetry (CV) experiments have been carried out, using the fact that different crystalline sites and surface structures generally have different adsorption properties with respect to molecules [37, 94, 149, 150]. The electrolyte chosen was a 0.1M NaOH (ACS Reagent Materials, 99.995 %) aqueous solution. Figure 4.29 shows the obtained CVs of the electropolished Cu (100) and an electropolished polycrystalline Cu foil in 0.1M NaOH and 0.1M KHCO₃ solution for comparison. Both serve as a reference to later on understand the obtained CVs on the pulsed surfaces.

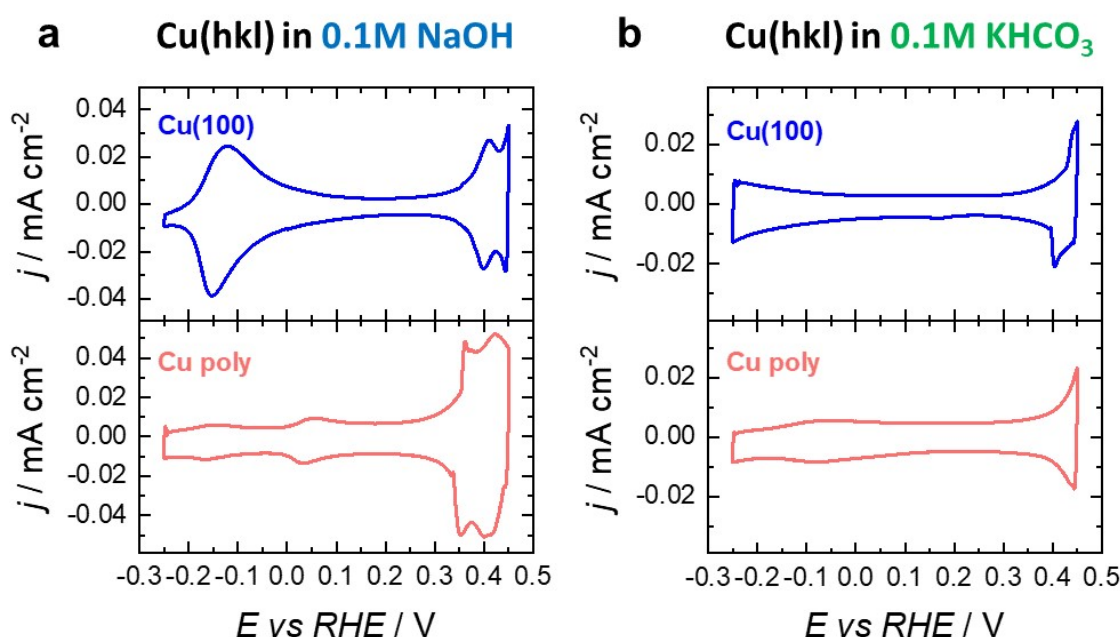


Figure 4.29: CVs of an electropolished Cu(100) and polycrystalline Cu electrode in (a) Argon saturated 0.1M NaOH and (b) Argon saturated 0.1M KHCO₃ solution. Data acquired by Dr. Rosa M. Arán-Ais. Data published in [45].

The obtained CVs within the Argon-saturated 0.1M KHCO₃ solution do not reflect the presence of specific adsorption and desorption peaks (Figure 4.29 (b)) unlike the samples cycled in 0.1M NaOH solution, where distinct features are visible. By this comparison, the reversible (same peak area and short distance to each other; see also [56]) process reflected by the two peaks at around -0.15V vs RHE can be assigned to the adsorption and desorption of OH⁻ ions on the Cu (100) terraces, in agreement with what has been reported in the literature [94, 150]. Regarding the polycrystalline Cu foil, the peak at 0.06V vs RHE is known to represent the adsorption/desorption of OH⁻ on Cu (111) sites [94, 150]. The onset of Cu₂O species takes place for potentials higher than 0.3V vs RHE. Nevertheless, the obtained features are clearly different from each other in the 0.1M NaOH solution for the single and polycrystalline surfaces, reflecting a different behaviour with respect to their electrochemical oxidation as well as a sensitivity for structural properties. In

agreement to what is expected the obtained signal for the polycrystalline Cu foil can be explained by means of the linear combination contribution of the three different basal planes [151].

Having in mind this access to structural properties of the employed surfaces together with the knowledge from XPS about which pulse conditions are able to generate Cu₂O species that are present during CO₂RR the connection towards the catalytic behaviour can be done. Gas- and liquid chromatography are used to investigate the resulting product distribution dependent on the applied electrochemical protocol. An important thing to note is hereby that all distributions acquired under pulsed conditions are reported in selectivity, not Faradaic efficiency. This is due to the fact that with the ongoing reduction and oxidation during the pulsed electrolysis, a significant amount of the obtained current is non-faradaic (no electrocatalytic conversion) and used to produce and reduce the oxides on the surface.

Figure 4.30 shows the product selectivities for each electrolysis protocol, together with the obtained post mortem CVs in 0.1M NaOH solution acquired immediately after the pulsed electrolysis experiments and subsequent rinsing of the bicarbonate electrolyte on the surface with ultra pure water.

Although the overall voltammetric profile for the chronoamperometric case (no pulse) does not show a strong change after electrochemistry for 1 h at -1.0V vs RHE, small changes due to reconstruction cannot be excluded as ratio for the peaks above 0.3V vs RHE with respect to each other changes slightly (compare Fig. 4.29 (a) and Fig. 4.30 (b)). As indicated by quasi *in situ* XPS (Fig. 4.26), the surface remains metallic under these conditions. In agreement to what is expected from the literature, the obtained product distribution clearly shows the characteristic high ethylene selectivity for Cu(100) and reflects the distributions reported in Refs.[43, 44]. Upon measuring the Cu(100) single crystal surfaces under pulsed conditions, the selectivity trends clearly change towards a preferential production of ethanol. For the lowest anodic pulse potential $E_a=0.0V$ this increase is minor, and the overall product distribution is close to the one obtained during the potentiostatic runs. Consistently, the acquired voltammograms only deviate slightly from each other when looking at the features above 0.3V vs RHE, pointing out a similar surface structure to be present in both cases (fig. 4.30 (c)). In agreement, the obtained quasi *in situ* XPS results also showed the sample to be mostly metallic under these pulsed conditions as well. Thus, in short the surfaces show similar catalytic behaviour due to being similar to each other. Nevertheless, the observed modest increase in the ethanol selectivity is in good agreement with a previous study that ascribed the increase to a higher OH coverage at the surface [135].

This picture changes significantly once an anodic potential is employed that has proven to produce oxides which persist during the negative CO₂RR pulse for 1 s at -1.0V vs RHE (fig. 4.27). Even though the resulting product distributions for these potentials are different from each other, they all have a higher ethanol selectivity in common. For instance, for $E_a=0.4V$ up to 24 % ethanol has been detected, while around 4 % Cu₂O was shown to coexists with metallic Cu at the surface.

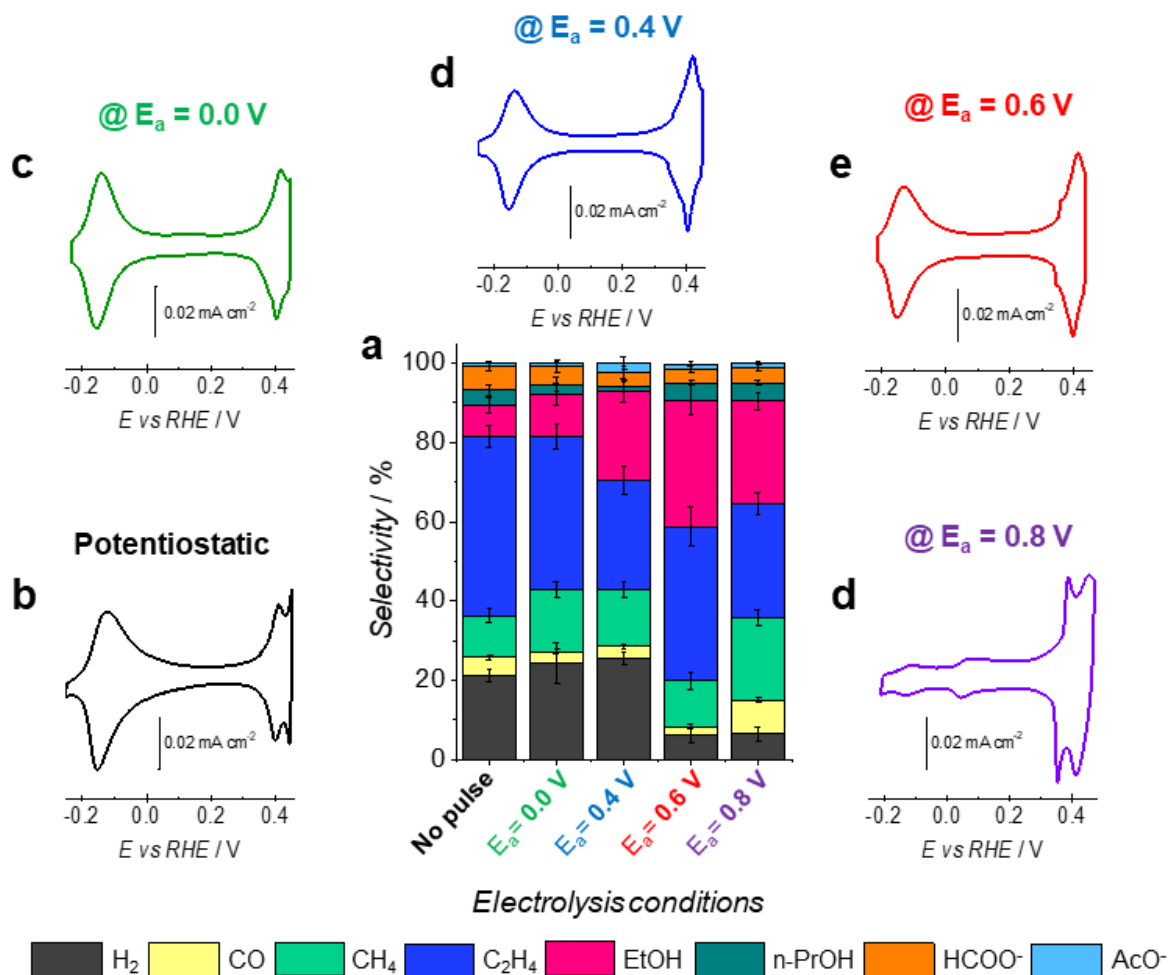


Figure 4.30: (a) Product selectivity obtained on electropolished Cu(100) single crystals in 0.1M KHCO₃ solution when applying potentiostatic and pulsed conditions. (b)-(d) corresponding cyclic voltammograms acquired in 0.1M NaOH solution immediately after running the electrolysis experiments for 1h and subsequently rinsing with ultra pure water. Data acquired by Dr. Rosa M. Arán-Ais. Data published in [45].

This even increased up to 32 % ethanol when employing $E_a=0.6V$, where 7 % Cu₂O has been detected at -1.0V vs RHE. Surprisingly, when comparing to the potentiostatic case where only 8 % ethanol and 45 % ethylene is found, it can be seen that the increased ethanol selectivity for oxidizing anodic potentials is at the expense of ethylene (27 %) when using $E_a=0.4V$, and mostly hydrogen when employing $E_a=0.6V$ and $0.8V$ (< 10 %). Since the positive polarization during the anodic pulse is known to lower the hydrogen coverage, if it is sufficiently high, this results in a lower hydrogen selectivity [152]. Also, a higher OH coverage is expected at these potentials favouring the ethanol formation.

Nevertheless, these observations, especially the increase in ethanol selectivity at the expense of ethylene, point out that a change in the preferential reduction pathway on Cu(100) towards either ethylene or ethanol is invoked by the pulses.

Looking first into detail to the highest anodic potential, the decreased HER observed is not transferred into a single CO₂RR product but rather all of the main CO₂RR products. While the ethylene selectivity even decreased as compared to the potentiostatic case, the amount of CO and methane increased. Comparing the obtained CV (Fig. 4.30 (d)) with the one for the pristine (Fig. 4.29 (a)) and potentiostatic case (Fig. 4.30 (b)), clear differences are visible. The loss of the ethylene favouring Cu(100) structure is indicated by the loss of the related OH adsorption/desorption features at -0.15V. Instead, the one suggested to be related to the adsorption/desorption on Cu(111) sites [94] appear. Overall, the obtained CV compares very well to the one of the polycrystalline Cu foil (Fig. 4.29 (a)), especially when including the profile features above 0.3V. Thus, the higher selectivity for methane and lower selectivity for ethylene can be ascribed to the sample becoming more polycrystalline as a result of the strong oxidizing anodic pulses.

Regarding the CVs recorded at $E_a=0.4V$ and $0.6V$, both reflect the presence of the Cu(100) structure, as indicated by the peaks at -0.15V. Nevertheless, both show different profiles from the pristine (Fig. 4.29 (a)) and potentiostatic (Fig. 4.30 (b)) samples when looking at the peaks above 0.3V. These features have been previously associated with the presence of (111) steps and defects on the Cu(100) surface, thus the CVs also reflect changes in the surface structure, crystal orientation and/or quality of the Cu(100) surface as a result of the pulses [45, 94].

Although the oxides are present for the cases showing the highest ethanol selectivity, and surface area changes as proven by the ESCA measurements are negligible, the CVs clearly indicate that the surface structure is changing upon applying the pulsed protocol. Especially since the presence of steps on the Cu (100) surface is known to lower the CO₂ activation barrier [48], the observed catalytic trends with respect to the C₂₊ selectivity must at least be partially linked to the changes that the surface undergoes [153]. Thus, understanding the role of these changes is of fundamental importance to be able to separate it from the role of the oxides present.

To achieve this goal, additional control experiments were conducted, with freshly electropolished samples being measured in a pulsed experiment and subsequently immediately measured after operation under constant potential conditions for 1 h each. The CV of the pristine Cu (100) crystal clearly deviates from the sample exposed to the pulses Ref. [45]. At the same time, the selectivity shows the previously discussed change towards ethanol at the expense of ethylene and hydrogen. Employing this restructured sample within a consecutive constant potential run reveals a different selectivity. Overall, the obtained selectivity is similar to the one of the just electropolished sample that has not been exposed to the pulses. The only difference being that a higher amount of hydrogen at the expense of ethylene is observed. This might be attributed to the partial degradation of the beneficial (100) facets as indi-

cated by a decrease in the characteristic OH adsorption/desorption peak at -0.15V (lower peak area). Furthermore, the obtained CVs for the sample after the pulses and after pulses + chronoamperometry are almost identical. Thus, the defects and changes in the surface structure, as invoked by the pulses, remain stable under potentiostatic conditions. Yet, although having a similar surface structure as far as it can be told from the CV analysis, the obtained product distributions under pulsed and potentiostatic conditions are different from each other. This indicates that the effect of the surface orientation and structural changes, as well as the presence of defects and step sites due to the pulses play a minor role when it comes down to the changes in selectivity trends towards ethanol. It is rather likely that the surface chemical composition, especially the presence of the oxides facilitates the pathway towards ethanol, as well as the existence of a chemical environment in which more OH is supposed to be present at the surface due to the positive pulse [135].

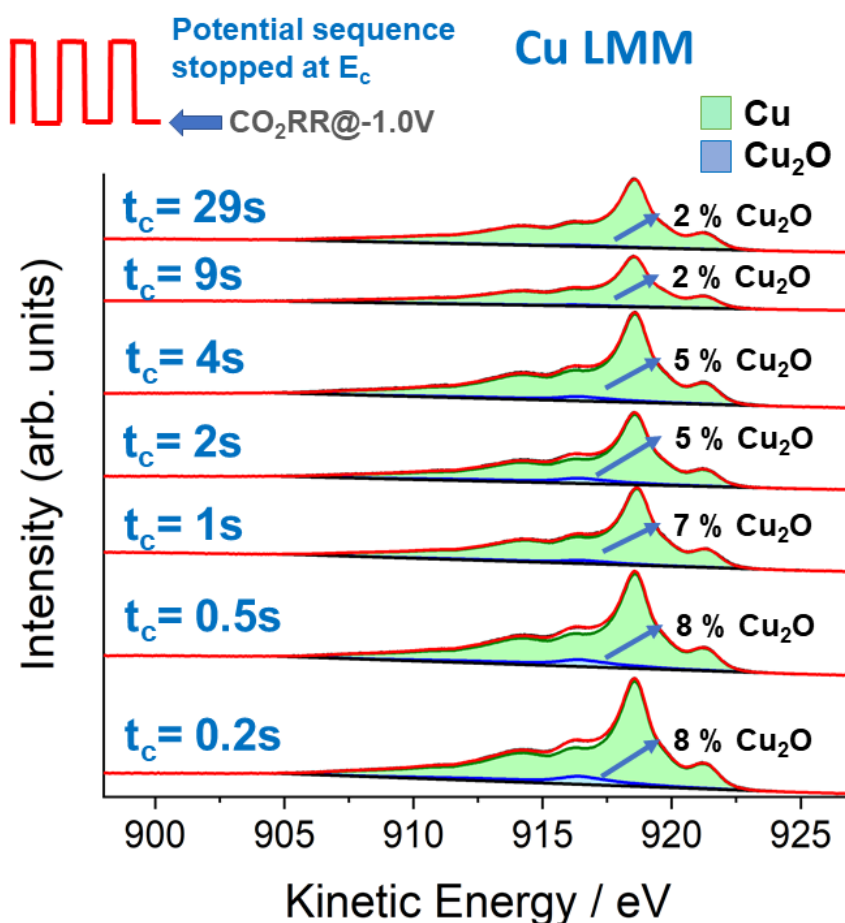


Figure 4.31: Cu LMM auger data acquired on Cu(100) after different anodic pulse lengths in 0.1M KHCO_2 solution. The cathodic pulse length $t_c=1\text{s}$ is kept constant. $E_c=-1.0\text{V}$ vs RHE, $E_a=0.6\text{V}$ vs RHE. Data published in [45].

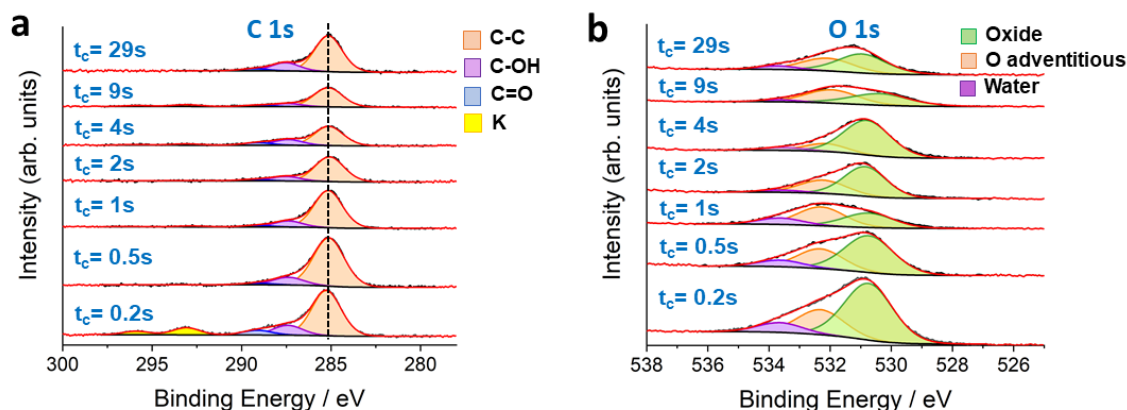


Figure 4.32: O 1s and C 1s data acquired for Cu(100) single crystals after different anodic pulse length in a 0.1M KHCO₂ solution. The cathodic pulse length $t_c=1s$ is kept constant. $E_c=-1.0V$ vs RHE, $E_a=0.6V$ vs RHE. Published in [45].

To investigate this topic different cathodic pulse lengths have been employed. The idea behind this is that lowering the cathodic pulse length, the surface is exposed to a shorter reductive pulse. Consequently, more of the oxides should remain present during the CO₂RR pulse when keeping the anodic pulse length constant and higher. In the same way, increasing the cathodic pulse length should lower the amount of oxides present. If the ethanol selectivity is indeed linked to the presence of oxides on the surface the selectivity should show a correlation to the pulse length.

Looking at the acquired quasi *in situ* XPS data for different cathodic pulse lengths while keeping the anodic one constant, the amount of oxides found indeed varies as expected (Fig. 4.31). Unfortunately, due to the exponential generation and reduction of the oxides, a major part is reduced right away and the remaining values are close to each other. Even though minor oxide contributions (2 %) are found for the long time cathodic pulses ($t_c=9s$ and $t_c=29s$) these are considered to be within the experimental error of the technique as discussed into detail previously (chapter 2.4.1). Thus, these surfaces are mostly metallic under CO₂RR conditions and the short time (2s) of oxides being present at the start of the pulse is getting less important for the 9s and negligible for the 29s pulse experiment.

For the longest cathodic pulse length the amount of ethanol (Ref. [45]) is again lower than for the shorter pulse length (Ref. [45]). Also the obtained overall distribution is becoming similar to the ones for the constant potential run without any pulses. Although the differences are rather small a trend can be seen for the oxide containing samples. The more oxides are found to be present during the CO₂RR pulse the more ethanol is detected.

In conclusion the pulsed experiments conducted on electropolished Cu (100) single crystalline surfaces provide a surface populated with oxides present during CO₂RR. The results presented in this sections further highlight and narrow down the role those oxides play within the framework of CO₂RR towards higher chain hydrocar-

bons. While the formation of ethylene and the corresponding reduction path shows, in agreement to the literature, to be independent on the presence of oxides during CO₂RR, the amount of ethanol seen correlates with the amount of oxides present. Furthermore, the control experiments conducted with and without pulses support this conclusion, as the amount of ethanol seen immediately drops down when running CO₂RR without pulses, even though the surface structure as probed by cyclic voltammetry shows to be similar in both cases. The changes seen in the reaction pathway from ethylene towards ethanol are therefore not solely explainable by the presence of specific surface defects or structures that have proven to persist throughout several consecutive experiments but have to be understood in the framework of the chemical environment in the vicinity of the electrode that is altered as a consequence of the anodic pulses. While the presence of OH⁻ species should also be enhanced by the positive anodic pulse the influence of oxides cannot be discarded and Cu/Cu⁺ interfaces appear to favour ethanol production.

5 Structure and Selectivity

Correlations: Cu(100) and Cu(111)

Knowing from previous results on electro-polished Cu(100) single crystals under pulsed conditions that the selectivity for ethylene versus the one for C_1 products is independent of the presence of oxides, studying the correlation between selectivity and structure on a fundamental level is crucial. Despite significant theoretical efforts and the advances in the engineering part of the field, pushing the faradaic efficiency for C_2 products higher than 80 %, fundamental knowledge about the active sites for specific products remain elusive and is still up to debate [51, 144, 154, 155].

Partially due to insufficient data on well-ordered, clean and atomically flat surfaces but also because of the general complexity of CO_2RR , whose selectivity is dependent on various factors such as the pH [27, 57, 144], electrolyte composition [62, 63], surface coverage [37, 152] and binding strength of reaction intermediates on the surface [110]. Experimental work on single crystalline surfaces reporting facet dependent selectivities [43, 94] helped to theoretically classify facets and active sites with respect to their theoretically predicted selectivity for specific CO_2RR products [46–48]. Among those, especially Cu(100) and Cu(111) surfaces have gained interest because of their significant difference in the selective for C_2 and C_1 products, with C_2 begin favoured on the Cu(100) surface [37, 43]. This has led to the understanding of the obtained selectivities on polycrystalline and/or oxide-derived systems as a function of the presence of specific active sites [48, 79] which also motivated the use of faceted nano-sized catalysts in the past [72, 156]. Much of the work on this topic is based on the work of Hori et. al. [43, 44] that used a combination of mechanical- and electrochemical polishing to prepare the employed Cu(hkl) surfaces. Theoretical calculations on the other side, focus on pristine atomically-ordered and flat surfaces to determine the most energetically downhill reaction pathway on differently oriented surfaces [31, 46, 47]. Those descriptions might, however, not be suitable to model the behaviour of experimentally employed samples who are structurally different. For instance, *in situ* and *operando* AFM measurements highlighted that faceted surfaces change significantly under CO_2RR conditions [45, 157]. Thus, theoretical studies still have numerous challenges to overcome in order to mimic realistic electrochemical reaction conditions. At the same time, experimental work approaching the up to now theoretical considered pristine and atomically ordered surfaces is missing.

The goal of the work presented in this section is to close this gap and to help understand the nature and structure of active sites for specific products. A combination of UHV-based preparation, microscopy and spectroscopy techniques is utilized together with online gas chromatography, to characterize the surface of well-ordered atomically flat Cu(100) and Cu(111) single crystals with respect to their binding sites for CO, the most important intermediate, and their catalytic selectivity.

The used Cu(100) and Cu(111) single crystals have been UHV-prepared and cleaned (see section 3.3) till the samples showed to be clean in XPS, and a low energy electron diffraction (LEED) pattern reflecting the respective expected crystal structure was observable [158]. The acquired spectra and images are shown in Fig. 5.1 and Fig. 5.2. Furthermore, STM images have been acquired on the pristine UHV-prepared surfaces, Fig. 5.3. The surface of both samples is flat over several hundred of nanometers. Scanning with high resolution also yields atomically resolved images showing that the surface is pristine and well-ordered, containing only few defects. Thus, the overall sample surface of the UHV-prepared samples is dominated by large pristine atomically well-ordered terraces.

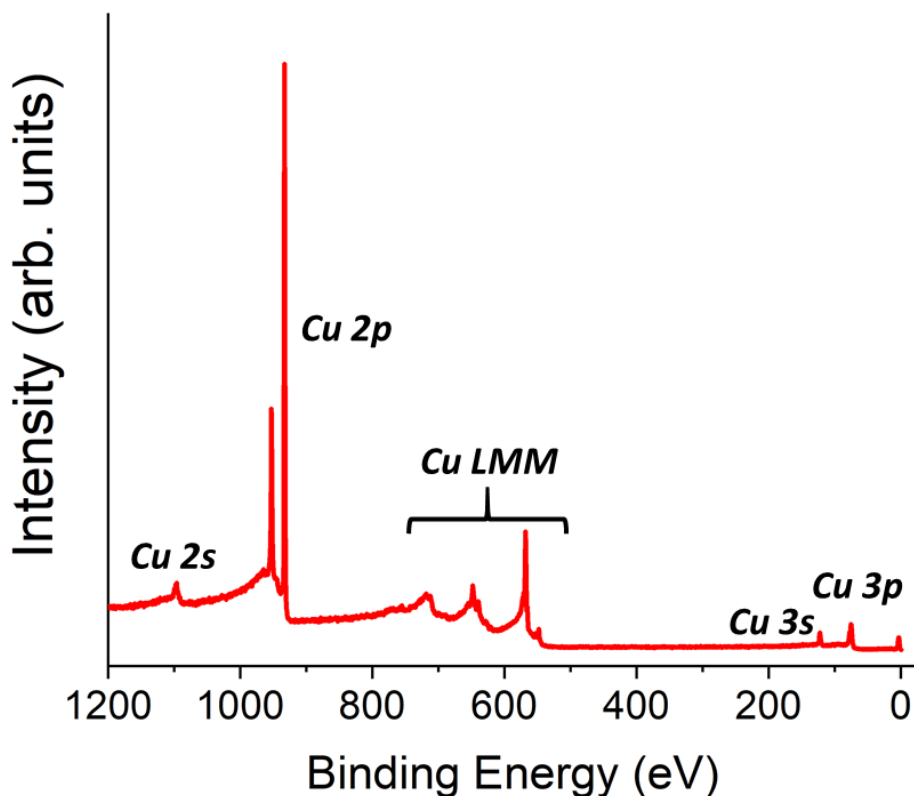


Figure 5.1: Example XPS Survey spectrum of a Cu(111) single crystal after UHV preparation only showing Cu related peaks.

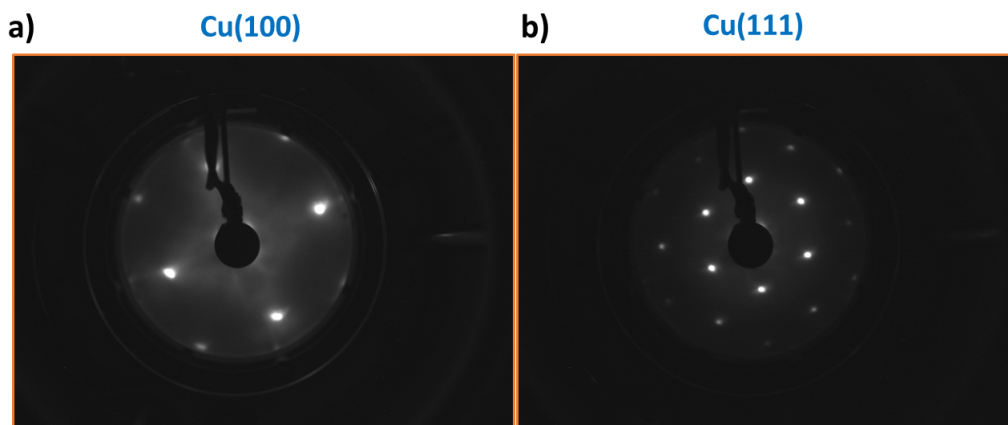


Figure 5.2: LEED images acquired using an electron energy of $E_e = 78.6$ eV at an angle of 90° on (a) UHV-prepared Cu(100) and (b) UHV-prepared Cu(111).

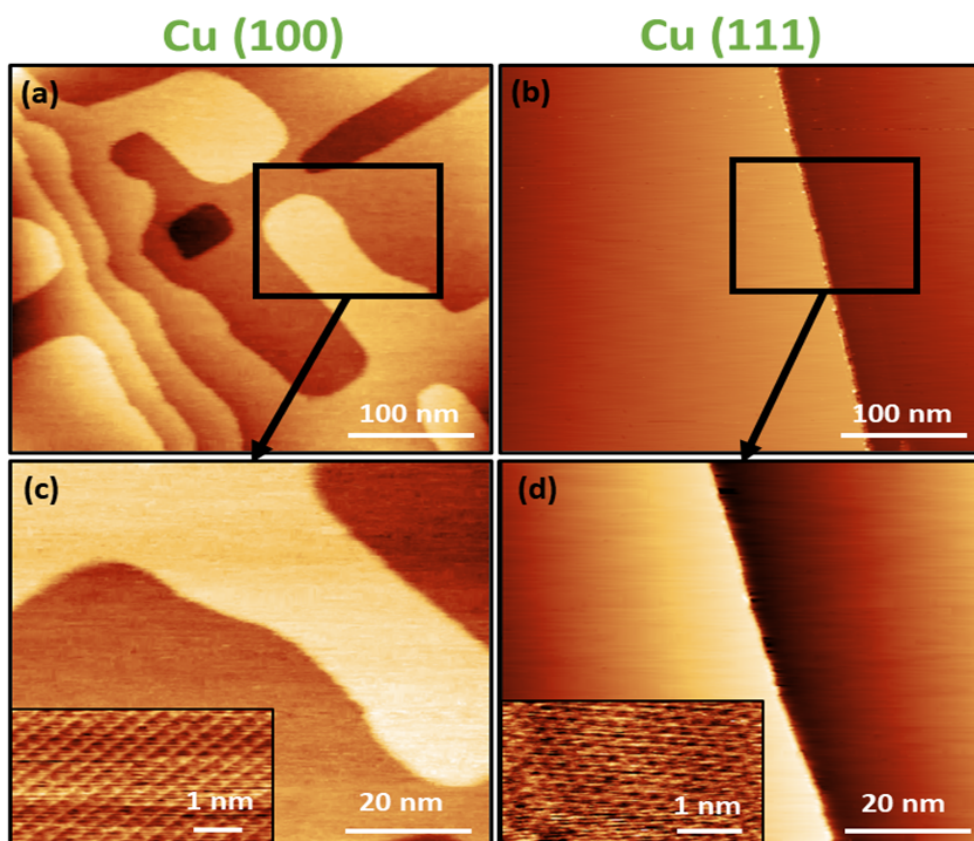


Figure 5.3: Large scan range (420 nm) STM images of (a) Cu(100) and (b) Cu(111) single crystal surfaces acquired at $T=292$ K using a bias voltage of $U=125$ - 250 mV and a tunnel current of $I=150$ - 250 pA. Panels (c) and (d) depict higher magnification images of the areas indicated by the black box. Inset shows atomically-resolved images acquired at $T=292$ K using a bias voltage of $U=250$ mV and a tunnel current of $I=1.5$ nA.

From this starting point the samples have been additionally treated following the following procedures:

1. **Sputter:** Additional sputtering with Ar-ions using an energy of $E_{Ion}=2.5$ keV while adjusting the pressure for 2 minutes, so that a constant sample sputter current of $I_{sample}=15 \mu A$ is achieved.
2. **Epolish:** Electropolishing for 2 minutes in H_2PO_3 (see section 3.1).
3. **Plasma:** Low pressure (250mTorr, 20W) oxygen plasma treatment (see section 3.4).

The morphological evolution of the samples upon exposure to these treatments has been followed with the help of *ex situ* AFM measurements since it has not been possible to resolve the plasma and epolished surfaces with STM due to an increased amount of oxygen and carbon species as well as an increased roughness. Similarly, the morphological evolution during CO_2RR has been followed by means of AFM. Nevertheless, the obtained AFM images on the different surfaces are summarized in Figures 5.4 and 5.5 for the Cu(100) and Cu(111) surface, respectively. These images also reflect the presence of large well-defined terraces on the UHV-prepared surfaces, Fig. 5.4 and 5.5 (a).

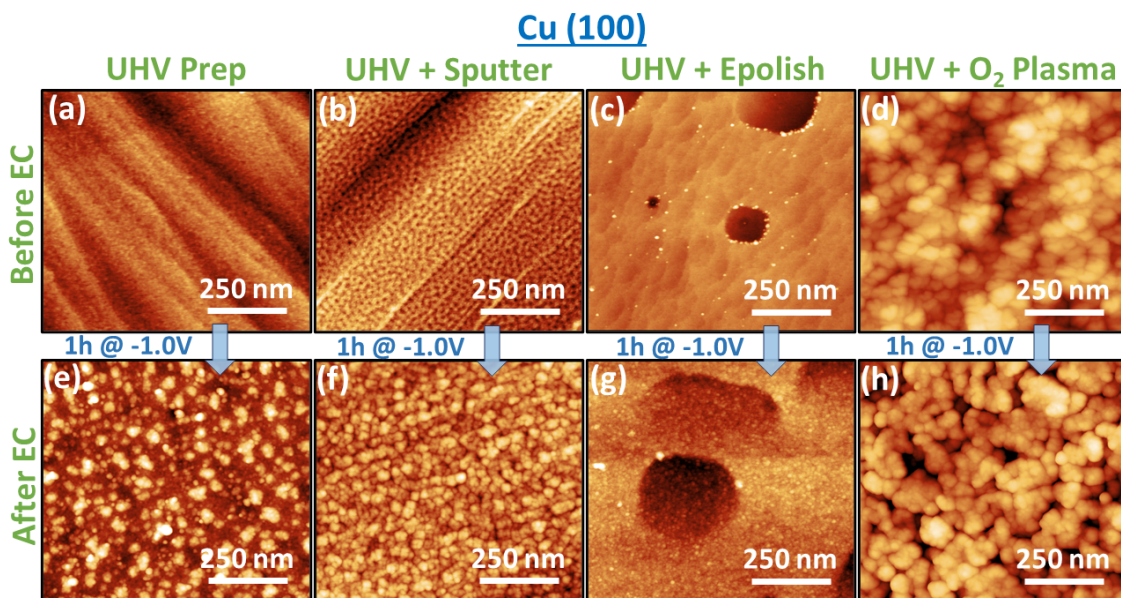


Figure 5.4: (a)-(d) AFM images of Cu(100) single crystals in their as prepared state before EC after different pre-treatments and (e)-(h) the respective images acquired after the samples have been exposed to CO_2RR conditions for 1h at -1.0V vs RHE in 0.1M $KHCO_3$. Colorscale: (a) 0-4nm, (b) 0-5 nm, (c, f, g) 0-12nm, (e) 0-20 nm and (d, h) 0-50 nm.

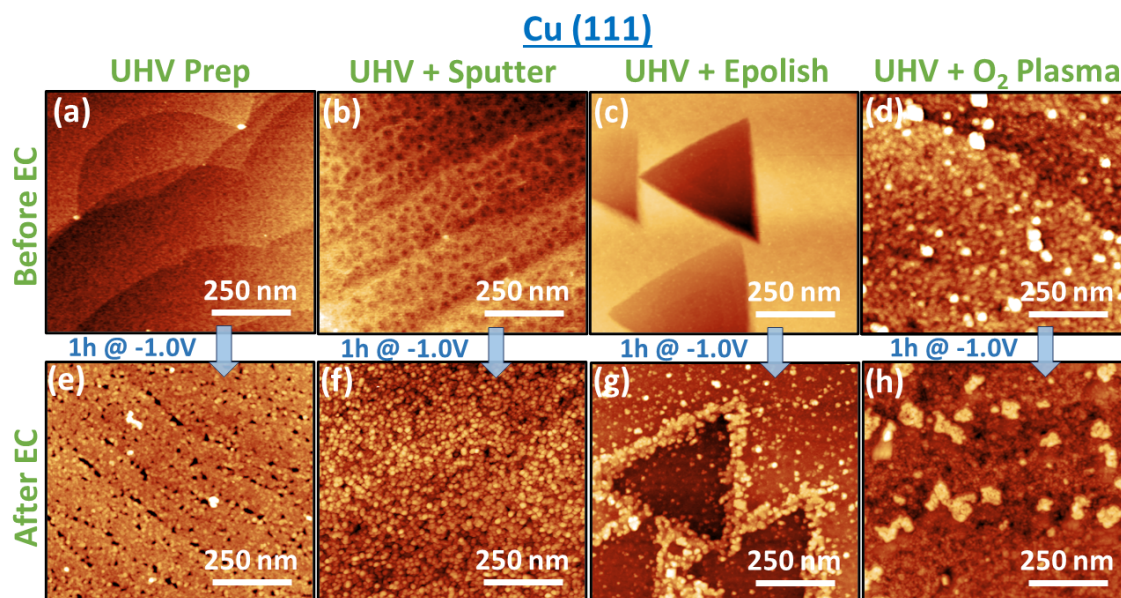


Figure 5.5: (a)-(d) AFM images of Cu(111) single crystals in their as prepared state before EC after different pre-treatments and (e)-(h) the respective images acquired after the samples have been exposed to CO₂RR conditions for 1h at -1.0V vs RHE in 0.1M KHCO₃. Colorscale: (a) 0-2 nm, (b) 0-4, (c-f, h) 0-12 nm, (g) 0-14nm.

Looking at the sputtered surfaces, both orientations behave differently. While on Cu(100) small holes (ca. 2 nm) across the terraces can be observed the Cu(111) surface shows a more disturbed network-like structure with bigger holes (ca. 5 nm) across the still persisting terraces. Upon epolishing the pristine UHV prepared samples, the large terraces previously observed are lost for both surfaces. In the case of Cu(100), a higher number of steps with seemingly rough and defective edges can be seen accompanied by large (< 50nm) etch pits whose geometry is determined by the surface crystal orientation. Similar etch pits are seen for the Cu(111) surface, which are triangular, following the crystal orientation. Those etch pits most likely originate from oxygen etching at the high anodic potentials applied [37]. Once O₂-plasma-treated, the Cu(111) sample still displays large terraces, pointing out the surprising morphological stability of the surfaces for all treatments but the electropolishing treatment. Interestingly, the overall roughness as probed by AFM of all but the plasma-treated samples seems to be similar, even though their morphology and local structure is significantly different.

After electrochemistry, all surfaces show the formation of particles, independent of the treatment. Surprisingly, the amount seen seems to be dependent on the surface orientation as well as the pre-treatment. While the Cu(100) surface shows a large number of particles the Cu(111) surface seems to remain cleaner, so that even terrace and step-related features on the UHV prepared samples can be seen after EC (Fig. 5.5 (e)). Alongside the former step edges, holes appear. Similarly, the epolished samples still show the presence of etch pits after EC, which are covered

by a high amount of particle agglomerations in the case of the triangular structures on the Cu(111) surface. Thus, the AFM images clearly highlight that the surfaces are to an extent resilient to all but the electropolishing treatment, since some of the original features (e.g. steps and terraces) are still observable. Surprisingly, these even persist through the CO₂ electroreduction.

To gain insight into the chemical state of the samples in their as prepared and after EC state, quasi *in situ* XPS measurements were conducted. The results for the Cu LMM, O1s and C1s regions are shown in Fig. 5.6 and 5.8. Since CO TPD experiments have also been conducted to probe the adsorption strength of CO on the different surfaces, the XPS data acquired after TPD are also shown hereby.

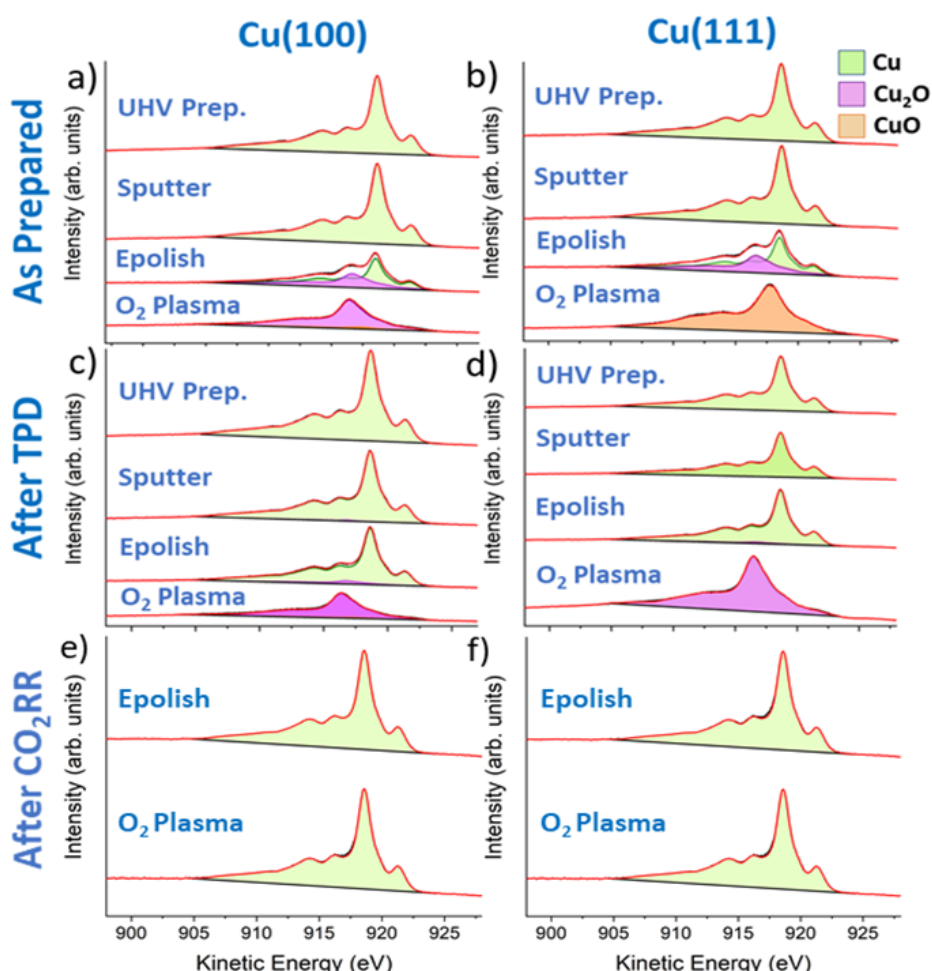


Figure 5.6: Cu LMM data on Cu single crystals after (a,b) different pre-treatments (c,d) CO TPD ramping up to $T=325\text{K}$ and (e,f) 1h of CO₂RR at -1.0V vs RHE in 0.1M KHCO₃.

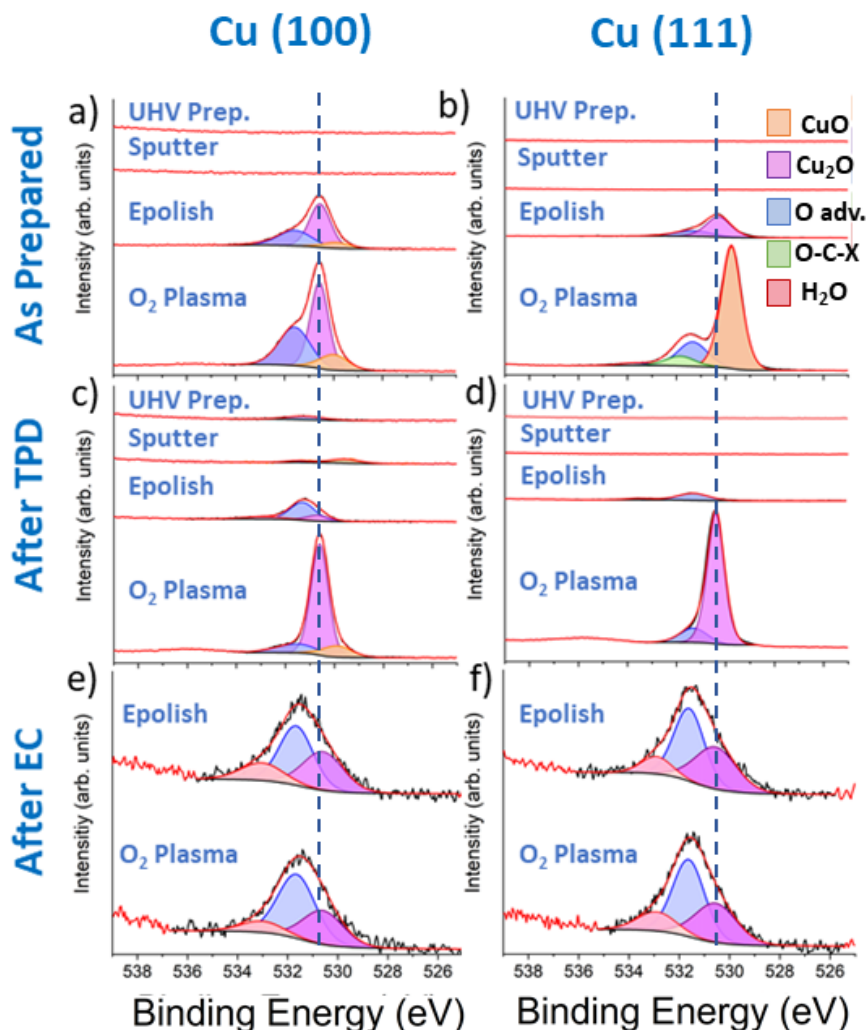


Figure 5.7: (a-f) O1s XPS data acquired on differently treated single crystals after different treatments in their (a,b) as prepared, (c,d) after CO TPD and (e,f) after EC state. (g-l) the corresponding C1s XPS data. EC samples are run for 1h at -1.0V vs RHE in 0.1M KHCO₃.

The XPS spectra confirm that the agglomerations and structures in AFM are related to Cu or Carbon species, as no other elements or contaminations have been detected. This also shows that the catalytic performance, which is discussed later on, is not affected by the presence of poisonous elements who are known to stifle the CO₂RR selectivity [89]. The Cu Auger spectra after electrochemistry reveal that copper is in its metallic state, independently of the pre-treatment and its initial chemical state which is summarized in Table 5.1. Thus, the selectivity trends observed on these samples are not affected by the presence of oxides during CO₂RR, but solely depend on the structural properties of the samples in this case which is important since it enables drawing conclusions about the structure-selectivity correlations.

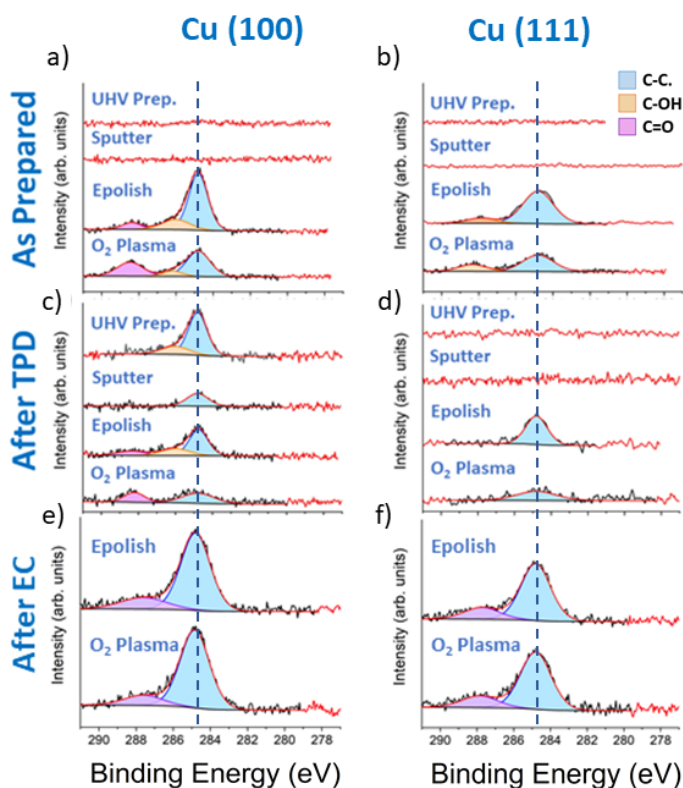


Figure 5.8: (a-f) O1s XPS data acquired on differently treated single crystals after different treatments in their (a,b) as prepared, (c,d) after CO TPD and (e,f) after EC state. (g-l) the corresponding C1s XPS data. EC samples are run for 1h at -1.0V vs RHE in 0.1M KHCO_3 .

Sample	Treatment	As prepared	After TPD	After EC
Cu(100)	UHV Prep	100% Cu	100% Cu	-
	Sputter	100% Cu	100% Cu	-
	Epolish	63.5% Cu, 36.5% Cu_2O	93% Cu, 3% Cu_2O	100% Cu
	Plasma	93% Cu_2O . 7% CuO	100% Cu_2O	100% Cu
Cu(111)	UHV Prep	100% Cu	100% Cu	-
	Sputter	100% Cu	100% Cu	-
	Epolish	62.5% Cu, 37.5% Cu_2O	99% Cu, 1% Cu_2O	100% Cu
	Plasma	100% CuO	100% Cu_2O	100% Cu

Table 5.1: Composition of differently treated Cu(100) and Cu(111) surfaces extracted by linear combination fitting of the Cu LMM spectra with the corresponding references.

To probe the binding strength of CO, one of the most important intermediates in CO₂RR, and gain additional information about the surface temperature programmed desorption measurements have been conducted. Similar measurements have already proven their value within the field of CO₂RR previously [65, 110] but have not been available on well-ordered single crystal surfaces up to now. The acquired data are summarized in Fig. 5.9.

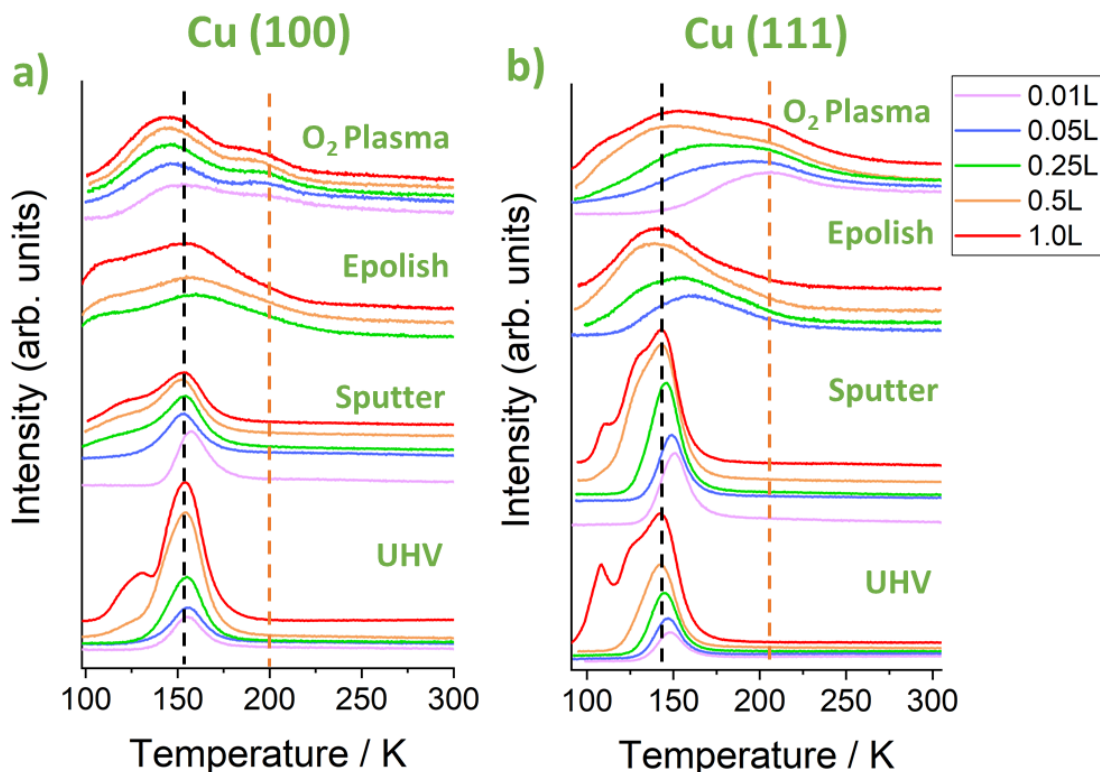


Figure 5.9: CO TPD at various dosing on (a) Cu(100) and (b) Cu(111) single crystal surfaces after different pre-treatments. Ramp rate is $R=2 \text{ K}^*\text{s}^{-1}$ up to a maximum temperature of $T=325\text{K}$. Black and orange dashed lines indicate terrace site binding and highest binding strength features, found on the epolished and plasma treated samples, respectively.

Consistent with the literature, the binding strength of CO at 1L dosing is found to be higher on the pristine atomically flat well-ordered (UHV prep) Cu(100) surface than on the Cu(111) surface [111], Figure 5.9, (black dashed line). Since the binding strength of CO at higher dosing and consequently higher coverages is weakened due to CO-CO interaction on the surface [111], the highest binding sites can be observed at the lower dosing. Using a dosing of 0.01L, the respective desorption temperatures were found to be $T_{100}=154\text{K}$ and $T_{111}=147\text{K}$. Assuming first order desorption and employing the Redhead model (chapter 2.5) the respective CO desorption energies are $39.5 \frac{\text{kJ}}{\text{mol}}$ for Cu(100) and $36.5 \frac{\text{kJ}}{\text{mol}}$ for Cu(111).

Cu (100)					Cu (111)				
<u>0.01L Dosing</u>	UHV	Sputter	Epolish	Plasma	<u>0.01L Dosing</u>	UHV	Sputter	Epolish	Plasma
T / K	154	157	-	199	T / K	147	150	-	206
BE / (kJ/mol)	39.5	40.3	-	51.4	BE / (kJ/mol)	37.6	38.4	-	53.3

<u>1.0L Dosing</u>	UHV	Sputter	Epolish	Plasma	<u>1.0L Dosing</u>	UHV	Sputter	Epolish	Plasma
T / K	156	153	185	188	T / K	142	142	198	206
BE / (kJ/mol)	40	39.2	47.7	48.5	BE / (kJ/mol)	36.2	36.2	51.2	53.3

Figure 5.10: Desorption temperature and binding strength of CO on differently pre-treated Cu single crystals.

Those peaks and features have been attributed to CO sitting linearly on top of terrace binding sites with the carbon atom bound to Cu [111, 159]. Thus, the fact that a dominant peak reflecting the presence of these binding sites can be observed in TPD is consistent with the AFM and STM analysis, showing that the UHV prepared surfaces consist of large pristine terraces. Looking at the spectra at a high dosage of 1 L additional peaks can be observed at $T=113\text{K}$ for Cu(111) and $T=121\text{K}$ at Cu(100). Those are related to the interaction of CO with itself lowering the adsorption strength on the surface and most likely multilayer adsorption, as indicated by the scalability of the peaks with increasing dosage [111, 160].

The features observed on the sputtered surfaces are found to be very similar to the ones of the UHV-prepared surfaces, indicating that even though AFM showed the surfaces to be different on a mesoscopic scale the atomic order and structure still remain intact on those surfaces. Only slightly higher desorption temperatures of $T_{100}=157\text{K}$ and $T_{111}=150\text{K}$ are found at low dosing. Furthermore, the binding features at low temperatures are found to be broader as compared to the pristine UHV-prepared cases, while at the same time the surface CO coverage seems to be reached faster, indicating the presence of defective binding sites on the terraces, which is consistent with the AFM imaging analysis showing holes within the terraces.

This picture changes significantly for the electropolished samples as the peaks attributed to terrace sites are significantly broader, indicating disorder and a disturbed surface containing defects within the atomic lattice. Furthermore, the peak maximum for low dosing is shifted towards higher desorption temperatures, supporting the idea defective lattice sites and step edges are present, since those are expected to exhibit a stronger binding for CO [111]. Even though carbon contamination residuals made the CO TPD challenging on these surfaces, especially for lower dosing, the presence of additional binding sites and tailing of the peaks was clearly observable. Looking at the highest dosing of 1 L those features are situated at $T_{100}=185\text{K}$ and $T_{111}=198\text{K}$ respectively. Comparison with the knowledge present

in the literature leads to the conclusion that those features are related CO binding to higher-index steps and/or defective highly under-coordinated surface sites [111]. Similarly, the O₂ plasma treated samples show well defined high temperature desorption features at T₁₀₀=199K and T₁₁₁=206K for low dosing, indicating the presence of a large amount of high-index stepped sites as well as defects within the atomic lattice [65, 111, 160]. Those findings are in agreement with CO TPD studies conducted on polycrystalline Cu surfaces, which also showed the presence of strong binding sites at oxidized and oxide-derived catalysts [65, 110].

This reveals that the sample pre-treatment and history has a significant impact on the surface structure with respect to its atomic order and flatness. This is especially important since additional morphological features are present for electropolished and oxide derived catalysts that are most commonly used and subject to studies in the field of CO₂RR. Those structures might significantly alter the CO and CO-like intermediate binding and thus, be the active sites facilitating the reduction of CO₂ toward hydrocarbons.

To put these findings in perspective, all samples have been run under CO₂RR conditions at a potential of -1.0V vs RHE, that is known to enable the production of hydrocarbons [37, 43, 45]. The data are summarized in Figure 5.11

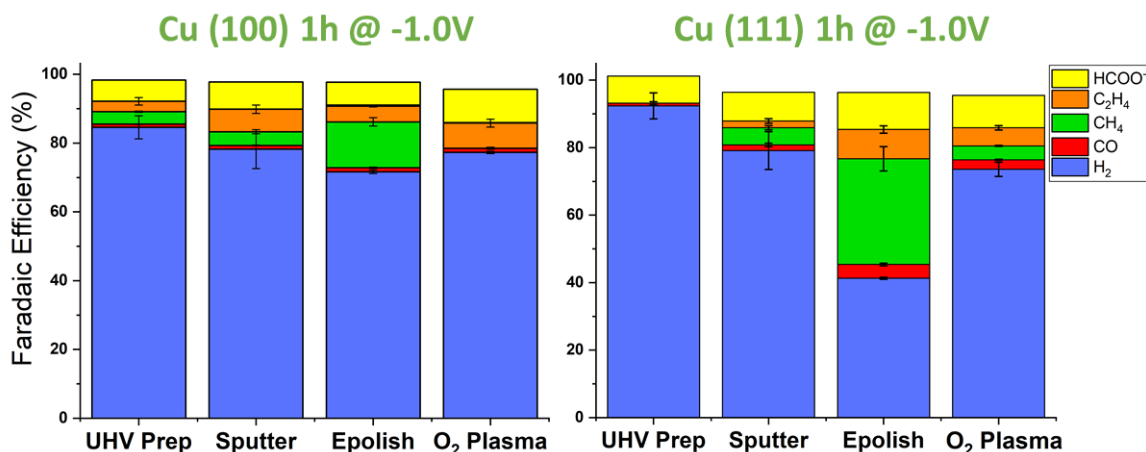


Figure 5.11: Faradaic efficiency of differently pre-treated Cu(100) and Cu(111) single crystals at -1.0V vs RHE in 0.1M KHCO₃.

Remarkably, the pristine well-ordered clean surfaces (UHV prep) do not show a high amount of hydrocarbons. In fact, the overall selectivity for CO₂RR is found to be lower than 16 % and HER is favoured, unlike expected from reports on similar oriented surfaces in the literature [37, 43]. The only exception to this trend of an unusual high hydrogen production are the electropolished surfaces who show selectivity trends that are to a good extent in agreement to previous reports [37, 43, 45]. Even though the addition of defects via Ar-sputtering results in an improvement of the hydrocarbon selectivity to a minor extent (5-8 %) for both orientations, the change is very small. This is, however, in agreement with the TPD data showing

those surfaces to be very similar with respect to their morphology and atomic structure to the pristine well-ordered UHV prepared surfaces. Interestingly, the small changes invoked by the addition of defects already result in a selective formation of specific products over both surfaces, as Cu(100) begins to favour ethylene and Cu(111) methane, which is in agreement with the expectations from previous studies [43].

As the AFM images showed both surfaces to evolve differently depending on their crystal orientation upon sputtering them, this suggests that the pristine crystal orientation is not determining the selectivity of a given Cu catalyst, but rather the presence of specific defects and structures, that are differently active for a given product. Those are most likely different on different crystal orientations, resulting in different coverages of reaction intermediates due to a different binding strength on the distinct geometries.

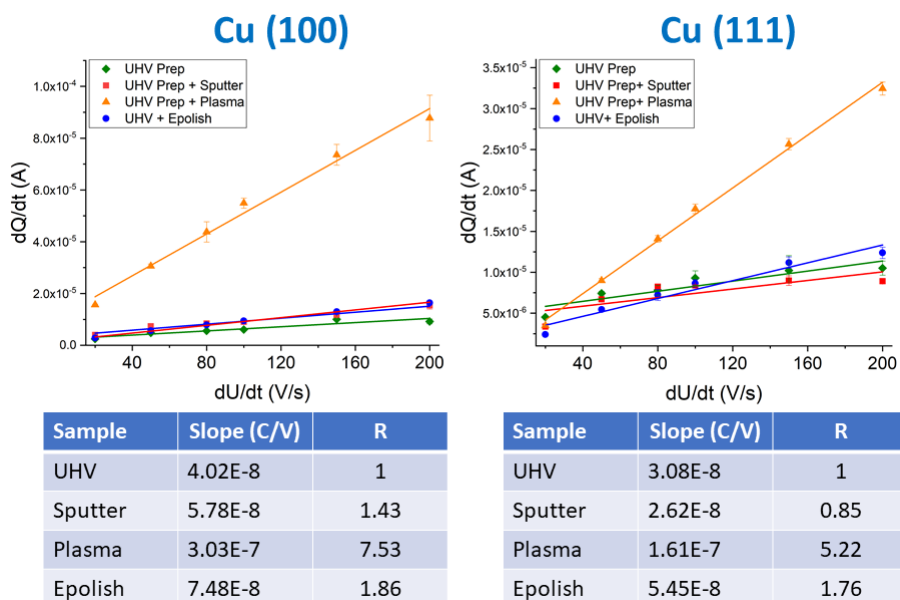


Figure 5.12: Electrochemical surface area measurements acquired after 1h of CO₂RR at -1.0V vs RHE in 0.1M KHCO₃.

In agreement with prior work on oxide derived Cu catalysts, the oxygen plasma pre-treated samples show a higher selectivity for C₂ products [68] further supporting the idea that the superior selectivity of oxide derived catalysts is not linked to the presence of specific crystal orientations but instead linked to specific active sites [79]. Nevertheless, the overall amount of hydrocarbons is low on the surfaces, and only trace amounts of alcohols (<1%) could be detected. Since the XPS data revealed that the samples are clean of any impurities that are known to stifle the hydrocarbon generation [89], this can be excluded as possible reason for the surprisingly high H₂ selectivity observed.

Looking also at the electrochemical surface area measurements (Fig. 5.12) after 1h of CO₂RR, the samples are consistent with the AFM analysis found to be almost the same roughness as the UHV-prepared ones. The only exception are the plasma pre-treated samples. Since the epolished samples have been found to be more selective for hydrocarbons, this supports the idea that the catalytic selectivity is not solely linked to the overall macro- and mesoscopic roughness but instead significantly dependent on the structure and morphology on the atomic scale.

The previously described data on atomically well ordered flat single crystals clearly point out the importance of the atomic structure with respect to the selectivity a given catalysts surface exhibits. Contrary to what is available and expected from the present literature, these samples favour the production of hydrogen over CO₂RR to a large extent. Consequently, theoretical considerations employing pristine surfaces cannot be used to model and explain experimental data that are based on electropolished single crystal surfaces. In fact, the study presented here also revealed that even the previously reported selectivity differences seen on differently oriented surfaces vanish without any defects and or higher index facets being present. Only upon introducing those surface features purposely on the hereby investigated surfaces the selectivity trends reported in the literature for electropolished samples are recovered. The different selectivity dependence on the surface orientation is thus not linked to the structure of those surfaces in their atomically well-ordered pristine state, but rather to the surface structure evolving from these pristine surfaces due to the impact of different treatments introducing different defective surface sites and higher index facets and step edges. Furthermore, the study points out the need of further developments of theoretical models as the major predicted product in such models should also be hydrogen instead of hydrocarbons on pristine atomically flat surfaces.

Moreover, since it was possible to demonstrate that atomically well ordered surfaces with large terraces favour hydrogen production, the previous idea that a high number of Cu(111) or Cu(100) facets are present for methane or ethylene producing catalysts has to be re-evaluated. Similarly, this also affects the understanding of nano-sized catalysts. Those type of systems are on the basis of the hereby presented experimental data more likely to exhibit specific active sites that consist of defective (under-coordinated) atomic sites and/or high index steps. A possible reason for the pristine and atomically clean samples being inert for CO₂RR could be that the crucial CO₂ activation step and the consequent reduction to CO is not happening at these surfaces. These findings are also in agreement with the previously discussed results on pulsed electropolished Cu(100) single crystals, where the selectivity for ethylene was also found to be affected by the presence of specific defects and high index facets.

6 Role of the Electrolyte on CO₂RR

This chapter of the scientific work focuses on the effect of the electrolyte composition on Cu based catalysts for CO₂RR, especially oxide derived ones. Previous studies on this subject using metallic Cu in combination with halides and alkaline metals reported an effect on the selectivity and activity of those type of catalysts [63, 67, 161] in particular, desirable suppression of HER. The electrolyte's influence on oxide-derived catalysts remains unknown up to this point but is of general interest since these type of catalyst outperform metallic ones by up to 36 % when it comes down to their selectivity for C₂ hydrocarbons [68]. As mentioned, this effect has been attributed to the presence of low coordinated sites, morphology, the presence of special crystalline facets such as Cu(100) and possibly the presence of Cu⁺ species [10, 68, 72]. Especially morphology and structure have been reported to be altered by halides on metallic Cu in the past, which was believed to invoke the change in the observed selectivity [61, 67]. Thus, studying the effect of halides on the morphology of oxide derived catalysts could lead to new insights. If there is no change in the selectivity while a change in morphology is observed, this would suggest that the changes in selectivity are rather linked to the chemical environment and/or state of the employed catalysts. If there is a change of the selectivity going alongside with a change in the morphology, this could provide insight into which structures are beneficial. If the morphology remains unaffected and at the same time the selectivity changes, this would also suggest a strong correlation of the catalysts performance and its chemical environment and/or state.

With these things in mind it is clear that the investigation of the electrolyte's impact on oxide-derived Cu is of special interest, since it could be a possible pathway to gain more insight into the role of key activity and selectivity determining parameters but also lead to further advancing the field from the technological point of view. The latter could be possible due to a stacking beneficial effect of the favourable trends displayed by oxide-derived catalysts, together with the ones from halides and alkaline cations leading to a higher overall performance for CO₂RR.

6.1 Chemical Effect of the electrolyte

6.1.1 Halides

The first part of the investigation focuses on the impact of halides being present during the reaction. Therefore, the presented study was designed around adding different halides (Cl, Br, I) into the commonly used aqueous 0.1 M KHCO₃ solution and O₂-plasma oxidized polycrystalline Cu foils were used as catalyst.

The employed Cu foils (Advent Research Materials Ltd., 99,995%) were first ultrasonicated in acetone and ultrapure water ($R = 18.2M\Omega$) and consequently electropolished for 5 min at 3V vs a Ti foil (see also chapter 3.1). Afterwards they were plasma treated using the setup described in chapter 3.4 using a pressure of 250mTorr and a plasma power of 20W for 2 min.

Employing a combination of SEM, XPS, EDX and gas chromatography based analysis the development of the morphology and the chemical state of the samples due to the exposure of halides during CO₂RR was followed.

Figure 6.1 shows SEM images of the plasma treated Cu foils after being immersed for 30 min in the 0.1M KHCO₃ + 0.3M KX (X= Cl, Br, I) solution before (a, b, c, d) and after electrochemistry (e, f, g, h).

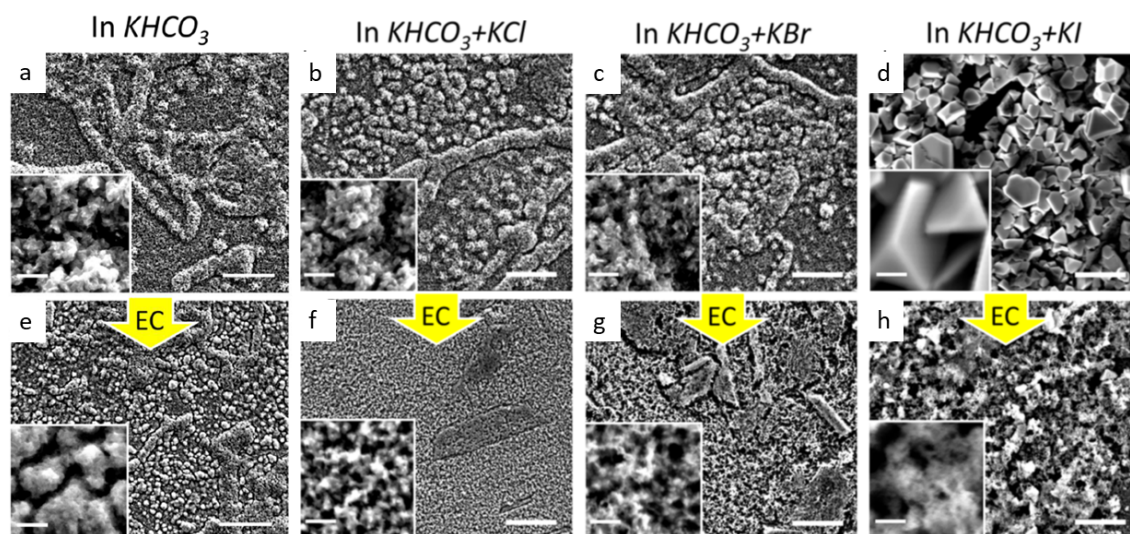


Figure 6.1: SEM images of oxygen plasma treated polycrystalline Cu foils before (a, b, c, d) and after (e, f, g, h) reaction at -1.0V vs RHE for 1 h in different electrolytes. Top row images represent the sample state after 30 min immersion into (a) 0.1 M KHCO₃ aqueous electrolyte additionally adding : (b) 0.3M KCl, (c) 0.3 M KBr and (d) 0.3M KI. The bottom row displays the corresponding samples after CO₂RR for 1h. Scale bars indicate 5 μ m and 500 nm for the inset image. Images taken by Dr. Dunfeng Gao. Reprinted with permission from [62]. Copyright 2017 American Chemical Society. Published in [62].

As it can be seen there is no significant change in the sample morphology from

the original plasma treated Cu foil showcased previously (Fig. 4.1) when being immersed into the 0.1M KHCO_3 electrolyte as well as for the KCl and KBr containing electrolytes. Within the iodide containing electrolyte the sample undergoes a significant change in its morphology as the formation of well defined crystals is observed. The formation of these most likely result from the strong interaction and affinity of Cu^+ to I^- species [162–164]. Comparing the non-halide and halide exposed samples (fig. 6.1, bottom row) after 1h at -1.0V vs RHE with each other, there is a clear difference. Even though KCl and KBr solutions did not show a significant impact on the sample morphology before electrochemistry, they affect it during CO_2RR conditions. Both invoke a further nanostructuring of the already rough plasma treated Cu, resulting in a higher surface roughness as compared to the non-halide exposed case. For the case of iodine, this behaviour seems to be enhanced even further, as the beforehand seen nanocrystals vanish and a porous, almost foam like, structure is seen in their place. In agreement to this, the EDX analysis shows only the iodine exposed samples to undergo a significant change in their chemical state from CuI in their immersed state to mainly metallic Cu after CO_2RR [62]. Thus, the strong morphological change seen for the iodine containing electrolytes is likely linked to a change in the chemical state of the pre-oxidized Cu foils, which is in agreement to what has been reported on metallic surfaces [67, 161].

To further investigate these changes in the chemical state in detail, quasi *in situ* XPS measurements were conducted. The XPS data shown within this section are aligned to the carbon 1s line ($E_B = 284.8\text{eV}$) [148, 165]. The underlying base samples being the electropolished and oxygen plasma treated foils have been discussed previously (see also chapter 4.1) and were metallic after 1h of EC at CO_2RR potentials (Fig. 4.3 and 4.4), which is an important result that has to be taken into account when studying the halide exposed samples.

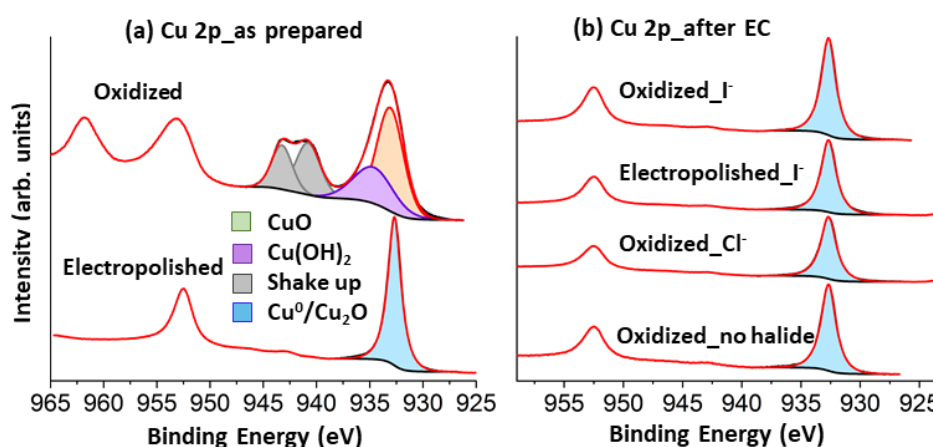


Figure 6.2: Quasi *in situ* Cu 2p spectra of (a) the as prepared samples and (b) the samples after 1h of CO_2RR in 0.1M KHCO_3 + 0.3M KI, KCl and no halides at all (top to bottom). Reprinted with permission from [62]. Copyright 2017 American Chemical Society. Published in [62].

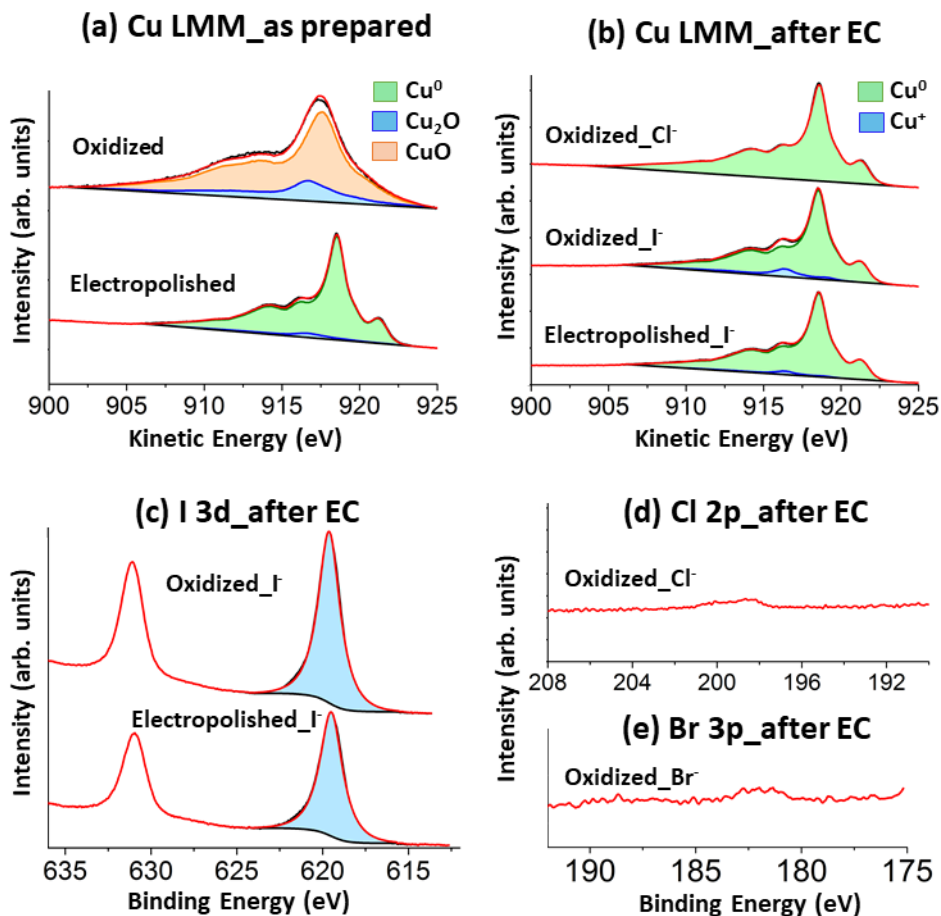


Figure 6.3: Quasi *in situ* Cu LMM Auger spectra for the (a) as prepared electropolished and plasma oxidized samples, (b) the samples after CO₂RR at -1.0V vs RHE for 1h in 0.1M KHCO₃ + 0.3M KCl/KI, (c) core level spectra for the I 3d region after electrochemistry, (d) and (e) corresponding core level spectra for the Cl 2p and Br 3p region after electrochemistry. Reprinted with permission from [62]. Copyright 2017 American Chemical Society. Published in [62].

Conducting similar measurements on the halide containing electrolyte cases yields the data shown in Figures 6.2 and 6.3. The "as prepared" denoted XPS datasets represent the initial states of the aforementioned samples. While the oxygen plasma treated sample (Fig. 6.3 (a)) is consistent with the previously highlighted dataset on a similar sample (compare Fig. 4.3) the electropolished shows less oxides to be present. This is due to the reason that all electropolished samples used for studying the halide effect have been transported in phosphoric acid (85 %) instead of air to further improve the experimental procedure. The goal was to lower the exposure time to air as much as possible after the electropolish treatment, so that the amount of oxide resulting from reoxidation in air is kept as small as possible. As the data suggests this procedure is working out very well as the amount of oxides detected in the as prepared state decreases by more than 40 % to almost zero. The presence of

the shake-up features in the Cu 2p spectra for the oxidized case proves that indeed as also suggested by the linear combination fitting of the Cu LMM data (see Fig. 6.3 (a)) the sample mainly consist of CuO (85%, atomic percentage from linear combination fitting) and Cu₂O (15%), while the electropolished foil is dominated by metallic Cu (95%). The obtained 5% of Cu₂O for the electropolished sample are most likely from short transfer time of the sample in air after taking it out of the protective acid environment, rinsing it with ultra pure water and mounting it in the UHV chamber loadlock.

After 1h of electrochemistry at a potential of -1.0V vs RHE in 0.1M KHCO₃ + 0.3M KI solution the oxygen plasma treated foil was, similar to the other samples, mostly reduced yielding 91% for the metallic species and 9% for Cu⁺ species judging from linear combination fitting with the corresponding references. In the case of conducting the CO₂RR in a KCl-containing solution, no sign of Cu⁺ species was found. Analysis of the corresponding O 1s spectra (Fig. 6.4) and the I 3d spectra (Fig. 6.3 (c)) for the iodine exposed samples yielded that the plasma treated foil contains some Cu₂O after EC as there is a clear feature towards lower binding energies. The corresponding peak within the fit is located at $E_B=530.2\text{eV}$, which is the characteristic binding energy for Cu₂O [104]. For the electropolished sample, no oxides were detected after electrochemistry within the O 1s spectra. Thus the respective Cu⁺ species within the Cu LMM spectra (Fig. 6.3 (b)) consist of CuI. This evidences that the Cu⁺ species detected for the plasma treated case is likely to be a mixture of Cu₂O and CuI, which is also supported by the higher amount of Cu⁺ detected as compared to the electropolished case.

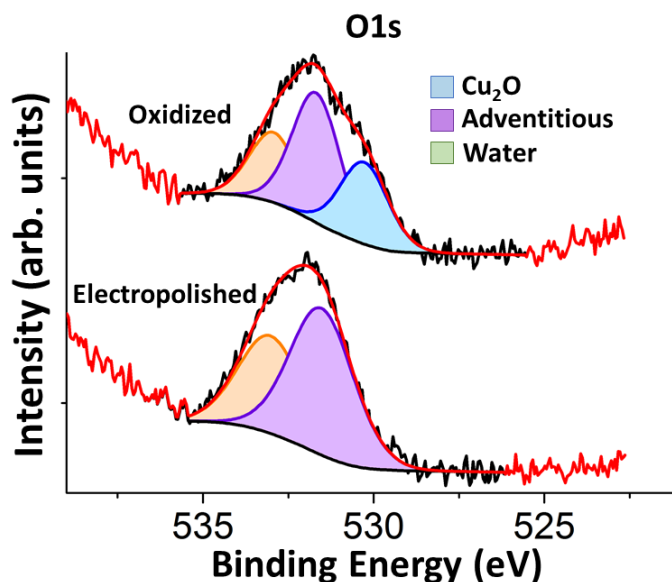


Figure 6.4: Quasi *in situ* O1s spectra of the oxidized and electropolished samples after 1h of reaction at -1.0V vs RHE in 0.1M KHCO₃ + 0.3M KI. Reprinted with permission from [62]. Copyright 2017 American Chemical Society. Published in [62].

Keeping the results in mind that no oxides have been present on the plasma-treated foils after EC run without iodine in the electrolyte solution (Fig. 4.3), the copper oxides do not possibly originate from the previously discussed systematic error of the experimental quasi *in situ* XPS setup and therefore, CuI is believed to be the major Cu⁺ species present. In the case of the KCl and KBr only trace amounts of the halides are detected after EC (see Fig. 6.3 (d, e)). In agreement the Cu LMM data reflects no presence of Cu⁺ species. Note that the dataset obtained on Br (Fig. 6.3 (d)) was based on an *ex situ* sample where CO₂RR was conducted in the H-type cell setup connected to the GC, which is also why no Cu LMM dataset are shown. Since the quasi *in situ* cell does not have a membrane separating both compartments, the Br within the solution is able to be oxidized towards Br₂ at the Pt mesh counter electrode. Since Br₂ is highly corrosive, toxic and at the same time gaseous, the experiment could not be run within a single compartment cell setup.

The electrochemical data obtained during 1h of chronoamperometry on the studied electropolished and plasma oxidized foils in 0.1M KHCO₃ + 0.3M KX (X = Cl, Br, I) as well as pure 0.1M KHCO₃ electrolyte solution for reference is shown in Figure 6.5 for the combined C₂ + C₃ Faradaic efficiency and the geometric current densities.

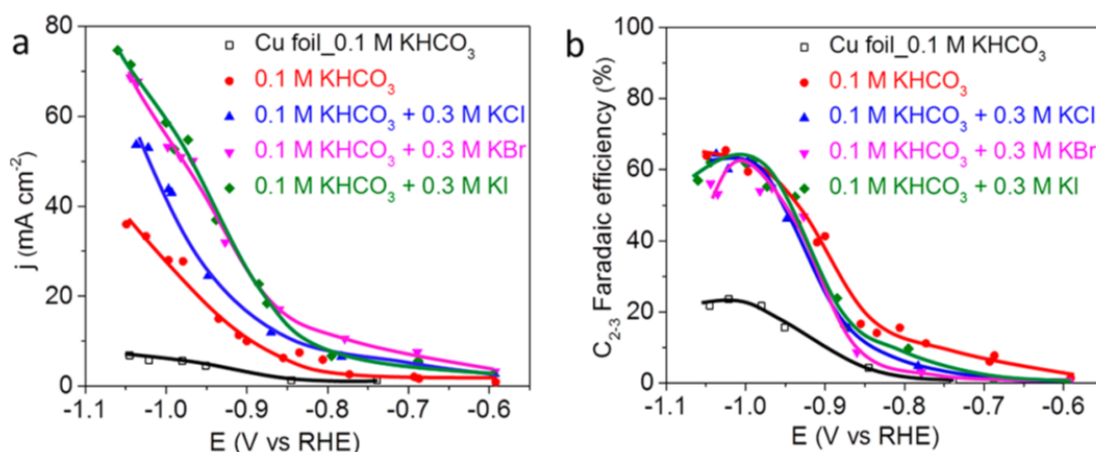


Figure 6.5: (a) Geometric current density ($A_{Geo.}=3 \text{ cm}^2$) and (b) the total Faradaic efficiency of C₂-C₃ products as a function of the applied potential for oxygen plasma-treated polycrystalline Cu foils in different electrolytes. Solid lines are guide for the eye. Data acquired by Dr. Dunfeng Gao. Reprinted with permission from [62]. Copyright 2017 American Chemical Society. Published in [62].

The obtained Faradaic efficiencies for the electropolished Cu foil in 0.1M KHCO₃ match the values reported in the literature [8, 12, 24, 122] also showing the characteristic high methane FE of up to 55% and the comparable low FE for ethylene of up to 23% [62]. Similarly oxygen plasma pre-treated foils also show the previously reported values for the pure bicarbonate solution [68]. Surprisingly the obtained Faradaic efficiency values for the samples measured in the halide containing electrolytes do not defer too much from the pre-oxidized Cu foils in pure 0.1M KHCO₃

(Fig. 6.5). The observed change in the selectivity that was reported on metallic Cu catalysts in combination with a halide-containing electrolyte is therefore not adding up to the already beneficial selectivity of oxide-derived catalysts [61, 67]). Significantly affected by the presence of halides is the overall activity of the catalyst though. Hereby the activity increase follows the trend: $\text{Cl}^- < \text{Br}^- < \text{I}^-$, clearly scaling with the size of the employed halide ion.

The only difference observed with respect to the selectivity is an increase of the H_2 Faradaic efficiency at low potentials (-0.6V to -0.8V vs RHE) at the expense of CO for the halide-exposed oxide-derived catalysts [62]. This might be due to halides lowering the overpotential for HER but also suggests that the binding properties and consequently the absorption strength of CO on the surface could be altered by the presence of halides on or in the vicinity of the electrode surface. Another possibility is that the binding and activation of CO_2 on the surface is affected. Both CO and the hydrogenated COOH originating from absorbed CO_2 on the surface are considered to be crucial intermediates for the C-C coupling step [37, 49, 52, 54]. Therefore, a possible influence of the halides due to their chemical nature has to be decoupled as much as possible from the changes in morphology, especially seen for the I-exposed sample (Fig. 6.1) and the general macroscopic roughness of the catalyst which is also considered to play a role towards the dimerization [54, 68].

To be able to gain insight into this electrochemical surface area measurements based on the double layer capacitance (compare chapter 2.1.4) have been conducted on the samples after being exposed to CO_2RR conditions for 1h at -1.0V vs RHE [62]. It was detected that the macroscopic overall surface area and roughness of the samples was significantly increased upon pre-treating the electropolished foils with an oxygen plasma. As also indicated by the SEM analysis (Fig. 6.1) the overall roughness does not increase that much when exposing the plasma treated samples to KCl- and KBr-containing electrolytes. In the case of the iodine-exposed samples the picture changes as the roughness increased by 1.6 as much as the bromine exposed sample [62]. Interestingly, both samples show a similar current density (Fig. 6.5(a)) despite of their difference in roughness and similar oxygen content after EC (Fig. 6.3). This finding suggests, that the enhanced catalytic performance cannot be attributed to the roughness of the samples alone.

This issue was addressed with the help of additional control experiments. First the samples used for CO_2RR at -1.0V vs RHE for 1h in halide containing media were rinsed with ultra pure water and reintroduced to CO_2RR conditions at -1.0V vs RHE for another hour this time in non halide-containing 0.1M KHCO_3 electrolyte. It has to be emphasized that for the case of iodine, the water rinsing is likely to not be able to remove all the iodine, as suggested by the obtained XPS data after EC (Fig. 6.3). The resulting current density and production rates of selected products are shown in Fig. 6.6.

Comparing the halide and non-halide containing electrolytes with each other, significant differences in the current density and production rates are observed. Both are lower without the presence of halides even though the samples exhibit a

similar morphology due to having been exposed to the halide induced morphology changes prior to the experiment.

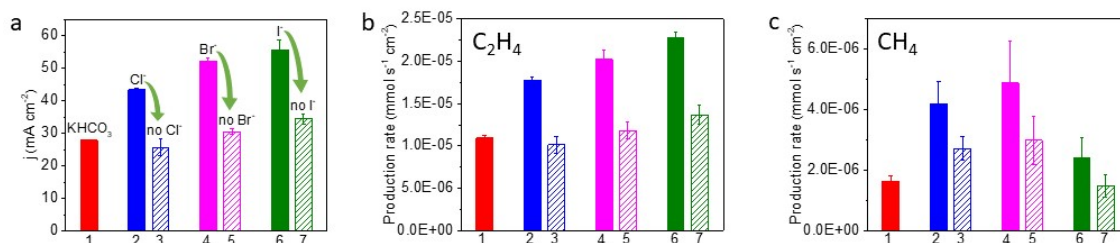


Figure 6.6: (a) Current density, (b) C₂H₄ and (c) CH₄ production rates of the oxygen plasma treated samples after 1h of CO₂RR at -1.0V vs RHE in (1) 0.1M KHCO₃, (2) 0.1M KHCO₃ + 0.3M KCl, (4) 0.1M KHCO₃ + 0.3M KBr, (6) 0.1M KHCO₃ + 0.3M KI and the same samples as in (2),(4),(6) in (3),(5),(7) run for and additional hour at -1.0V vs RHE in non-halide containing electrolyte (0.1M KHCO₃). Data acquired by Dr. Dunfeng Gao. Reprinted with permission from [62]. Copyright 2017 American Chemical Society. Published in [62].

From this it can be concluded that there is indeed a chemical effect of the halides during CO₂RR and the observed increase in the activity towards C₂₊ products is not solely dependent on the morphological structure of the employed catalyst. This is also supported by the fact that all samples show an increase in the current density even though the morphology does not change significantly from the one of the pre-oxidized foil measured in the absence of any halides, as seen in SEM (Fig. 6.1). Furthermore, this conclusion is indirectly supported by the fact that the overall roughness of the Br is lower than the one for the I-containing electrolyte case, yet both show a similar activity [62]. Thus, the roughness cannot be solely responsible for the changes observed as the I-exposed sample should exhibit a higher activity than the Br-exposed sample in this case.

In fact, the chemical nature of the halides and possible presence of Cu⁺ species seems to have a higher impact on the catalysts activity than the overall roughness which has also been suggested previously [68]. From the fact that the selectivity of oxide derived Cu foils exposed and not exposed to halides has proven to be very similar to each other and the fact that the XPS analysis of the just oxide derived did not show any oxides to be present after EC, it can be further concluded that the most dominant parameter affecting the catalysts performance in the halide exposed case are the halides themselves.

Comparing and linking the obtained conclusions within the presented study with the existing literature leads to a picture on how the proposed chemical effect could be understood. Generally halides are considered to participate in electrochemical reactions via their nature of strong adsorption on a given catalyst. Theoretical density functional theory (DFT) calculations carried out by Janik et. al. [166] suggested that the adsorption of halides on Cu(111), (100) and (211) surfaces occurs

within the potential ranges in which CO_2 electroreduction is typically carried out. Hereby the adsorption probability also follows the same trend of the observed activities within this study, which is $\text{Cl}^- < \text{Br}^- < \text{I}^-$. According to their theoretical investigation, this trend holds true for all Cu surfaces and is most dominant for Cu(100) [166]. To link the results within this study with this idea, the obtained current densities and production rates for ethanol and ethylene were plotted as a function of the adsorption potential on Cu(100), which is most favourable for C_2 products as predicted by Janik et. al.[166]. The result is shown in Figure 6.7.

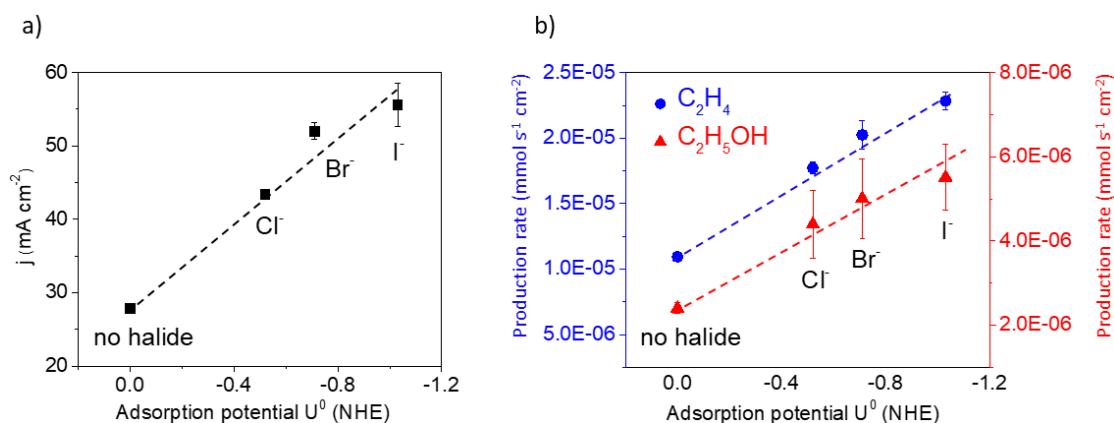


Figure 6.7: (a) Correlation of the current density and (b) production rates of ethanol and ethylene in different electrolytes operated at -1.0V vs RHE with the theoretically predicted values for the adsorption potential of halides on Cu(100) as predicted by McCrum et. al. Theoretical values extracted from [166]. Reprinted with permission from [62]. Copyright 2017 American Chemical Society. Published in [62].

A linear correlation between these two parameters can to a good extent be observed, which is in line with the conclusion that the chemical effects of the halides play the most important role in determining the presented sample activities. Here it is also important to note that the employed experimental H-type cell is not run in the CO_2RR transport limitations, yet. In that case an increase in the hydrogen selectivity should be observable for the halide exposed samples which is not the case. Therefore, from the fact that the activity increase is not selective towards a specific product [62], it can be concluded that the influence of the halides is linked to a common step of the CO_2RR .

A common step that was suggested by Koper et. al. [53] is the formation of the absorbed COOH intermediate on the surface from which CO is likely to originate. Hereby, the formation of the carboxyl (COOH) is considered to be the rate limiting step. Thus, a possible explanation of the observed trends could be that the halides facilitate the formation of the carboxyl intermediate on the surface.

This enhancement could take place by halides being present at the Cu surface donating their partial charge to the CO_2 molecules which form a covalent X^- -C bond leading to the transition from the linear to the bend CO_2 configuration of

the molecule on the surface [166]. Consequently, this bend structure CO₂, which is also considered to be the first activation step of the molecule, can be further converted to the COOH intermediate [53]. Since the donation of partial charge due to covalent bonding is equivalent to the idea that the binding strength of CO₂ and its intermediates is altered by the presence of halides, this conclusion goes in line with what has been previously discussed.

In conclusion, the effect of halides within the electrolyte on plasma oxidized polycrystalline Cu was studied within this section. A nanostructuring effect could be observed on halide exposed pre oxidized surfaces as compared to non-halide exposed ones. The observed morphological changes are most dominant for the case of iodine. This led to an increase of the overall roughness of the samples during the electrochemical reduction reaction. At the same, time an increased activity of all halide exposed samples could be observed, while the improved selectivity of oxide derived Cu that is typically high for higher chain hydrocarbons was preserved. Control experiments additionally provided valuable information about the fact that the roughness and structure of the samples even though altered, has a minor impact on the observed activity and selectivity as compared to the chemical effect of halides during reaction. These insights led to the proposed mechanism that the halides are likely to affect a common step among the CO₂RR towards hydrocarbons. A promising step is hereby the formation of the COOH intermediate on the surface that originates from the non-linear bend CO₂ molecule on the Cu surface. This bend structure formation is believed to be enhanced by the presence of halides on the surface donating partial charge to the CO₂ molecules, facilitating their adsorption. In line with this idea is the fact that the observed activity trends follow the strength of the adsorption of the halides (no halide < Cl⁻ < Br⁻ < I⁻) to Cu.

6.1.2 Cations

The second part of the chemical effect of the electrolyte focuses on the influence of cations present during the reaction on oxide derived Cu, as especially alkaline metal cations have shown to have a significant impact on the selectivity of electropolished foils in the past [63]. Hereby, the suppression of the parasitic HER in favour of the ethylene selectivity was reported. Furthermore, the magnitude was observed to be scaling with the employed cation size, which was explained by their respective hydration shell size, which is able to act as a buffer to stabilize the pH in the vicinity of the electrode surface to a certain extent [63]. Thus, the observed changes go back to the idea that the pH is affecting the reaction by giving rise to differences in the concentrations of H^+ and OH^- resulting in higher or lower probabilities for the hydration of a specific reaction intermediate as well as the availability of reactants in the electrode's vicinity [53, 57, 58].

With these things in mind, it can be seen why the influence of alkaline metals on oxide derived Cu is worth studying. Firstly if a local pH effect is responsible for the high selectivity towards ethylene of oxide-derived Cu [27, 68, 84], adding alkaline metal cations should either further enhance the selectivity or leave it unaltered. The latter would suggest that the local pH is already "saturated" on oxide derived Cu catalysts due to their higher overall roughness and structure meaning that there is no further increase of the pH in the electrode's vicinity possible, or that a further increase is not able to affect the reaction any more. Second, a beneficial effect on the selectivity towards C_{2+} hydrocarbons could be used to rationally design the employed electrolyte using the results obtained within the previous section on halide-enhanced CO_2RR . A possible synergetic effect of combining halides and cations could be the preservation of the higher current densities seen for halide exposed catalysts while further enhancing the selectivity.

To study these topics, oxygen plasma-treated polycrystalline Cu foils were also employed. The electrolyte was prepared by adding 0.1M $XHCO_3$ ($X = Li, Na, K, Cs$) to ultrapure water. For the investigation of a possible synergetic effect of halide and alkaline metal cations, the two best performing species were chosen. The employed electrolyte therefore consists of 0.1M $CsHCO_3 + 0.1M CsI$. The results on pure 0.1M $CsHCO_3$ are discussed in detail later on. The first approach was similar to the previous study, the characterization of the catalyst by SEM to gain insight into their structural properties under the influence of halides and/or cations within the electrolyte. Figure 6.8 shows the obtained SEM images on the cation exposed samples. The cases of 0.1M $KHCO_3$ and 0.1M $KHCO_3 + 0.3 M KI$ have not been reprinted here as the data previously shown is representative for those samples (see fig. 6.1).

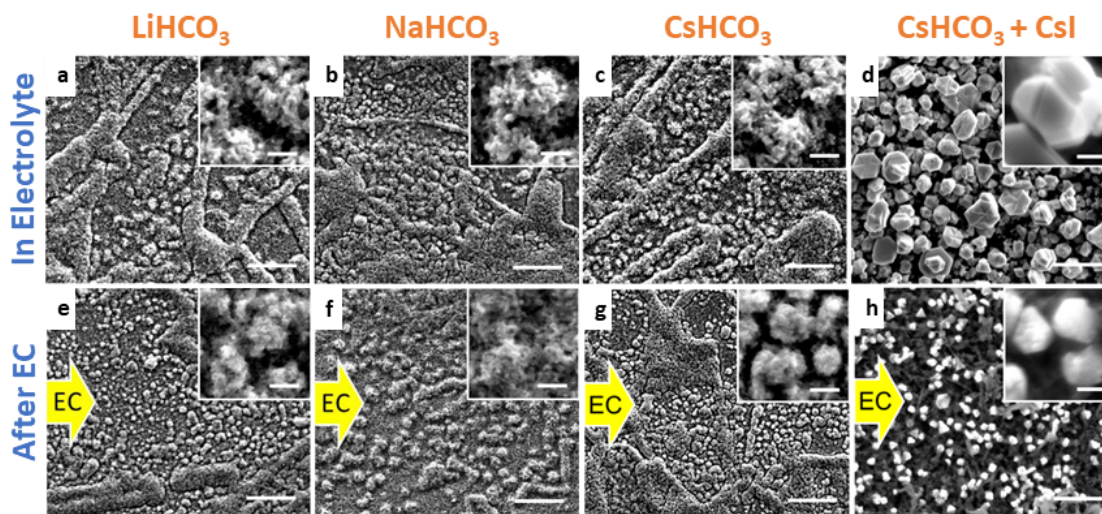


Figure 6.8: SEM images of the 2 minute oxygen plasma treated Cu foils after 30 min of immersion into (a) 0.1M LiHCO₃, (b) 0.1M NaHCO₃, (c) 0.1M CsHCO₃ and 0.1M CsHCO₃ + 0.1M CsI. Images (e)-(h) show the respective samples after 1h of CO₂RR at -1.0V vs RHE. Scale bars are 5 μ m and 500 nm in the main and inset image. Data acquired by Dr. Dunfeng Gao. Published in [65].

The first result from the SEM based data is that the presence of only the cations (Li, Na, K, Cs) does not result in a significant change of the samples morphology before and after reaction (Fig. 6.8 and 6.1). For the case of adding iodine to the 0.1M CsHCO₃ electrolyte a clear change in the overall sample morphology was observed, as again crystals in the range of 1-3 μ m are formed. Surprisingly the presence of Cs seems to stabilize the crystals during reaction, unlike it was the case for potassium (see Fig. 6.1) where the shaped NPs vanished during CO₂RR. This behaviour is also reflected by the elemental composition. Similar to the previous case of iodine exposure a change of the chemical state from CuO towards CuI is indicated by EDX data as there is almost 46 % iodine detected after immersion of the sample [65].

Different from the previous case of halides in 0.1M KHCO₃ but consistent with the SEM images obtained here, there is up to 27% I in elemental composition spectrum detected after 1h of CO₂RR at -1.0V vs RHE. The decrease of the signal is also going together with a change of the size of the observed crystals, as their size decreases from 1-3 μ m to 0.5-0.8 μ m. The surrounding of the crystals after EC was mainly metallic Cu. This finding already suggests that as compared to K, Cs seems to be able to stabilize the CuI species more, which could possibly result in the presence of Cu⁺ species during the reaction.

To address this topic in detail, again quasi *in situ* XPS measurements were carried out after 1h of CO₂RR. The quasi *in situ* XPS data obtained on the these samples after EC are similar to the previous case of just halide exposed samples and consistent with the reported EDX data [65].

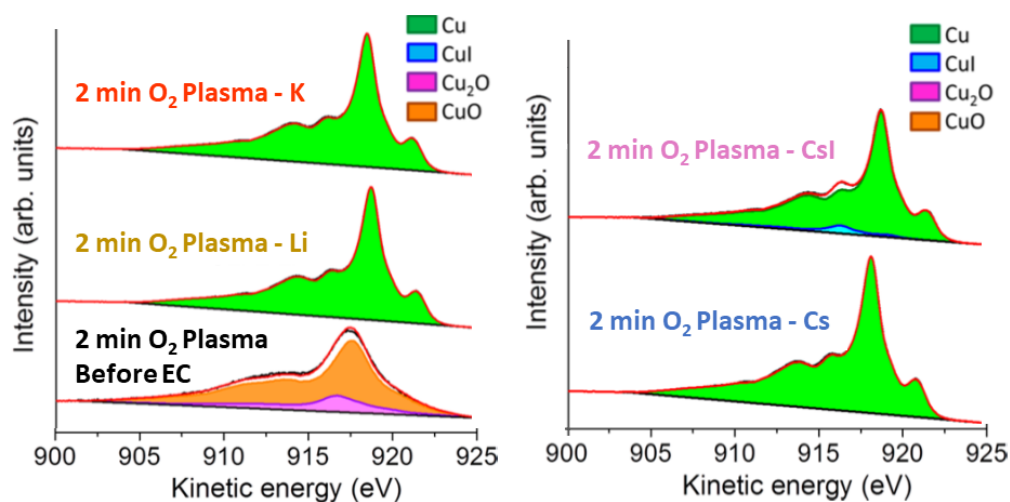


Figure 6.9: Quasi *in situ* Cu LMM Auger data obtained on the samples exposed to different cations within the electrolyte after 1h of electrochemistry at -1.0V vs RHE. Reprinted with permission from [65]. Copyright 2018 American Chemical Society. Published in [65].

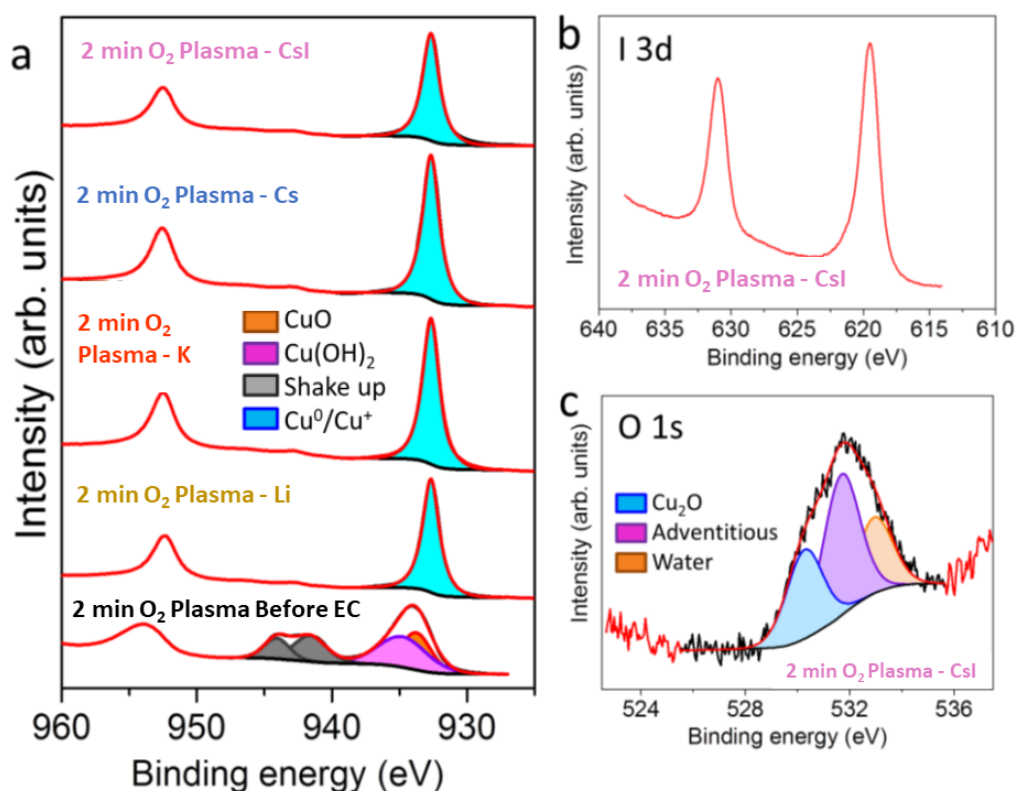


Figure 6.10: (a) Cu 2p quasi *in situ* XPS data on the cation exposed samples, (b) I 3d and (c) O1s on the CsI exposed sample after 1h of reaction at -1.0V vs RHE. Reprinted with permission from [65]. Copyright 2018 American Chemical Society. Published in [65].

The 2 minute oxygen plasma treated foil consists of a mixture of CuO (87%) and Cu₂O (13 %) before EC, which is almost the same as the previously obtained values supporting the reproducibility of the treatment (compare fig. 6.3). After electrochemistry is the different cation containing electrolytes, all the samples but the one exposed to iodine are metallic, judging from the linear combination fitting with the corresponding references. Again, the analysis of the I 3d and O 1s spectra (Fig. 6.10) suggests that the Cu⁺ obtained is a mixture of Cu₂O and CuI. Thus, the iodine supports and seems to stabilize the presence of Cu⁺ species since none of them are seen without iodine in the electrolyte. Furthermore, this also supports the strong interaction of iodide with Cu as previously discussed even in the presence of different cations. The presence of Cu²⁺ species can be excluded by looking at the Cu 2p data which again does not show the characteristic shake up peaks for Cu²⁺ species (Fig. 6.10).

The electrochemical behaviour was again probed with the help of the GC using 1 h long chronoamperometric runs. Figure 6.11 show the obtained values for the geometric current density and the combined C₂₊ Faradaic efficiencies after CO₂RR.

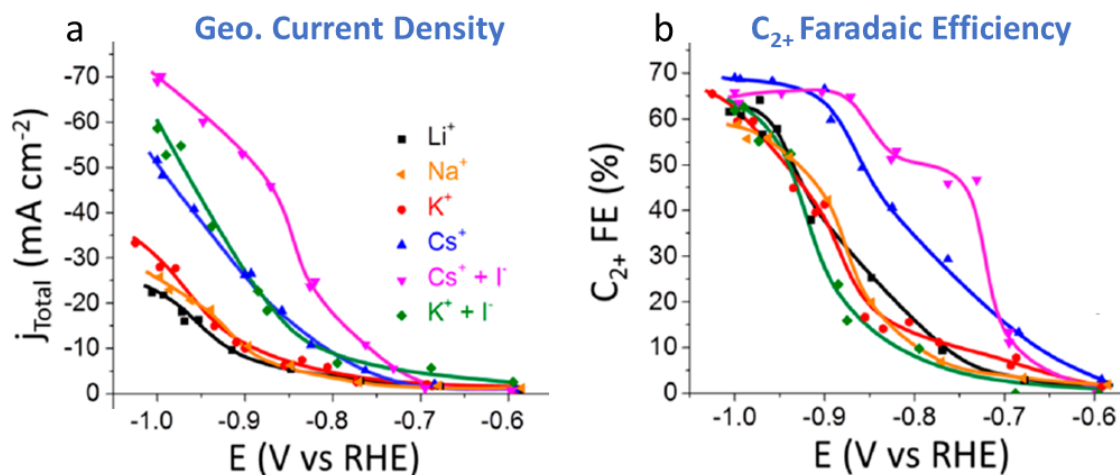


Figure 6.11: (a) Geometric current density ($A_{Geo} = 3\text{cm}^2$) and (b) combined C_{2+} Faradaic efficiency for oxide-derived Cu foils as a function of the applied CO₂RR potential measured in different electrolytes. Data acquired by Dr. Dungfeng Gao. Reprinted with permission from [65]. Copyright 2018 American Chemical Society. Published in [65].

Similar to what has been observed for the halide-containing electrolyte, in the case of iodide a decrease of the faradaic efficiency towards carbon monoxide was observed at low potentials (-0.6V vs RHE). Interestingly while this decreases benefits the selectivity towards HER for iodine in combination with potassium, Cs + I results in more formic acid.

The general trend of the current density observed is an increase with increasing cation size (Li < Na < K < Cs), similar to what has been reported for metallic foils [63]. In the case of the oxide-derived samples the obtained overall current density is

much higher, though due to the modified morphology. The double-layer capacitance data (Ref. [65]) indicate that the observed activity differences are not linked to the overall samples roughness, but rather to a chemical effect. The fact that the current density increase scales with the cation size supports the idea that the effect is linked to the size of the hydration shell, as previously suggested [63]. Adding iodine to the Cs containing electrolyte increased the overall activity even further (Fig. 6.11 (a)) and in addition, the Faradaic efficiency for higher chain hydrocarbons at lower potentials (Fig. 6.11 (b); -0.7V to -0.9V vs RHE).

This is attributed to the strong interaction of I with the Cu surface as discussed in the previous section (6.1.1). A clear trend towards higher chain hydrocarbons is also visible with increasing cation size, supporting the idea that cations facilitate the C-C coupling step. Furthermore, the obtained data suggests that it is possible to add the beneficial character of large sized cations namely Cs, with the production enhancing presence of iodine for higher chain hydrocarbons. The increased overall performance for the Cs + I samples is hereby most likely related to the stabilization of related nanostructures as well as the presence of Cu^+ species resulting in a superior partial current density for C_{2+} hydrocarbons of $J = 45.5 \frac{\text{mA}}{\text{cm}^2}$ as compared to other catalyst [65].

The discussed results have also been complemented by temperature programmed CO desorption experiments on these samples [65]. Similar to the previously described experiments on well-ordered Cu single crystal surfaces (see chapter 5) and in agreement with the interpretation the best performing samples with respect to their hydrocarbon selectivity also showed the presence of higher binding energy peaks around 172 to 213K even though the samples are polycrystalline [65]. As discussed those features can be assigned to the presence of defects and high index facets on the catalysts surface [110–112].

Interestingly the plasma-treatment time, which has reported to be a significant parameter with respect to the C_{2+} selectivity [68], is also affecting the presence of those higher binding energy features in the TPD spectra, whereas the best performing samples show them [65]. A possible explanation for this behaviour was previously suggested to be the presence of specific active sites on the catalyst which are only formed if the sample is electrochemically reduced/oxide-derived from the right starting conditions [68, 110], as also pointed out by pulsed electrolysis in the previous chapter (4.3). Recent studies also support this idea as it was shown that there is a significant difference in the selectivity when starting from Cu_2O vs CuO which was, however, believed to be linked to the poisoning by carbon species for the case of CuO derived catalysts [76]. Furthermore, it has to be kept in mind that the presented TPD data and studies in the literature [110] are only capable of grasping the nature of the sample before EC and after the samples have been exposed to the respective electrolyte. Naturally the sample surface state will not be precisely the same after being reduced under CO_2RR conditions.

Regarding the samples exposed to Cs and Cs + I, the high binding strength

feature is lost whereas it was found when exposing the sample to KI electrolyte [65]. This finding goes together with the different behaviour seen in SEM as the crystals seem to be stabilized by the presence of Cs as compared to K, and thus less defective and high index facets are present. Furthermore, this reveals that those Cu crystals seem to play a crucial role for the binding strength properties for CO on the catalysts surface. This is an important finding, especially since the crystals have shown to be stable under CO₂RR conditions when Cs is present even though decreasing in size.

In order to further investigate the the role of the cation size and their adsorption on the surface with respect to their influence on the C-C coupling step, density functional theory (DFT) calculations have been carried out by Michael J. Janik and his co workers on different Cu single crystal model surfaces. Hereby a Cu(100) surface was considered in the presence of cations at low and high coverages as well as the presence of water and subsurface oxygen to model the experimental oxide-derived Cu surfaces. Details about the nature and parameters of the used calculations can be found in Ref. [65]. The obtained results on Cu(100) are shown in Fig. 6.12.

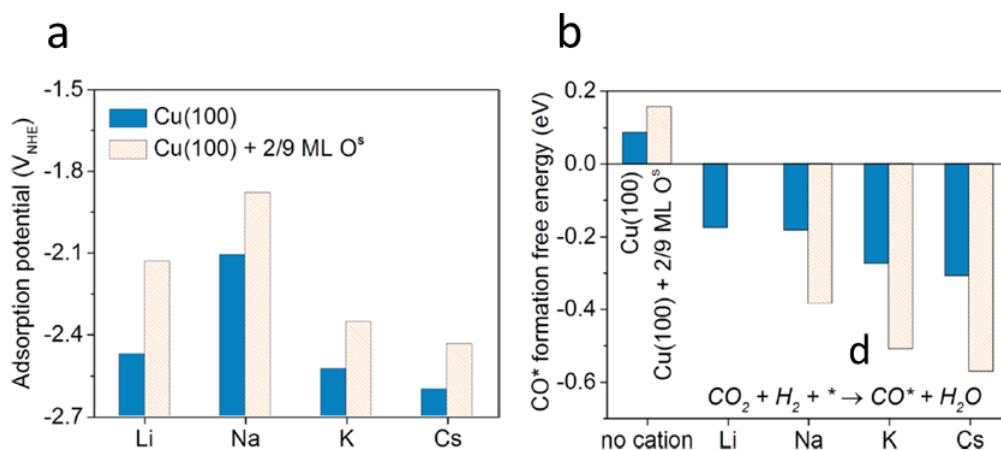


Figure 6.12: (a) Adsorption potential of Li, Na, K and Cs at 1/9 ML Water on Cu(100) in the absence and presence of subsurface oxygen (2/9 ML). (c) CO formation free energy calculated in the presence and absence of Li, Na, K and Cs on Cu(100) and Cu(100) with 2/9 ML subsurface oxygen. Calculations conducted by J. Janik. Published in [65].

The first result is that all cations adsorb favourably on all considered surfaces in the presence of water and subsurface oxygen at potentials below -1.0V vs NHE [65].

Examining the behaviour in the presence of the proposed reaction intermediates like CO, OCCO and OCCOH with emphasis on the Cu(100) low index surface, which has been reported experimentally to be the most beneficial for ethylene [37, 43] it was demonstrated that the presence of cations promotes the formation of these intermediates, as their free energy is more negative in the presence of adsorbed cations on the surface [65]. The promoting effect on polar and polarizable reaction

intermediates is hereby likely to be linked to the presence of a near-surface electric field. Reasons for such a field-enhancing the stability of reaction intermediates could be the presence of solvated alkali-metal cations in the outer Helmholtz plane or adsorbed on the catalysts surface [49, 52, 64]. The stronger binding of especially CO should in theory lead to a higher coverage of this crucial intermediate on the catalyst surface, which should lead to a greater C-C coupling and consequently lead to more C_{2+} products [37].

In contrast to what was previously reported in the literature where only the outer Helmholtz plane was populated with cations [64] the studies carried out hereby suggest that the effect of adsorbed cations on the formation of CO, OCCO and OCCOH is dependent on the cation identity. A possible explanation could be the change in distance of the intermediates with respect to each other on the catalyst surfaces when cations are not only present within the outer Helmholtz plane but also adsorbed on the surface which is favourable in the presence of oxygen. The magnitude of the interaction between intermediates and surface cations correlates with the surface normal dipole moment generated, whereas Cs generates the strongest one. These trends match the experimental trend of C_{2+} formation. Additionally the obtained result is consistent with the fact that in the presence of Cs CO formation is more favourable at low potentials, since Cs has also been found to be the strongest adsorbing cation [65].

To address the question if subsurface oxygen species generated by the plasma treatment might have an effect on the catalytic performance of the hereby employed catalysts, additional DFT calculations adding 2/9 ML of subsurface oxygen to the Cu(100) surface were carried out. Again the cation adsorption potential as well as the CO formation free energy was calculated. Looking at the results shown in fig. 6.12 (b, c) a promoting effect of 0.1-0.3 eV for the cation adsorption on the presence of subsurface oxygen is visible. This is independent of the applied potential and would further increase the cation coverage on the surface, thus resulting in a higher cation-linked promotion of the C-C coupling step and facilitate the production of C_{2+} products further. Additionally, the CO formation free energy calculated on the oxygen and non-oxygen containing surfaces in the presence of cations suggests that there is a further enhancement of the CO formation since the energy is even lower for the case of subsurface oxygen present. Even though the calculation have been carried out on pristine single crystalline surfaces and not on the experimentally employed polycrystalline Cu surfaces, the results indicate that if oxygen is present during the CO_2RR , it would be likely to further facilitate the performance towards higher chain hydrocarbons.

In summary the effect of cations within the electrolyte on oxide-derived plasma treated polycrystalline Cu was investigated and presented within this section. Similar to the case of halides, a clear trend in the performance of the employed catalyst with respect to its selectivity and activity for C_{2+} products could be observed that correlates with the size of the cations, namely (no cations < Li < Na < K < Cs). Furthermore, it was possible to enhance the partial current density for high chain

hydrocarbons by adding iodine to the best performing case of Cs, resulting in a partial current density of $J_{C_{2+}} = -45.5 \frac{mA}{cm^2}$, while maintaining a faradaic efficiency of 69% for those products. The observed enhancement is likely to be linked to the presence of shaped particles which maintain their morphology even under reaction conditions if Cs is present. The obtained TPD and ECSA results further indicated that even though the overall morphology and roughness is important, it is not the only crucial parameter in determining the catalysts behaviour. Hereby, the roughest sample, also showing the highest binding energy peaks in TPD, was not the best performing one. While the faradaic efficiency for ethylene and ethanol was similar at higher potentials independent of the differences in roughness for all samples (i.e. -1.0V vs RHE) the selectivity towards CO at lower potentials was found to be significantly different for lower potentials (-0.7V to -0.9V vs RHE), depending on the cation employed, demonstrating that their chemical nature plays a crucial role. The fact that the efficiencies at higher potentials are similar is likely linked to their oxide derived nature, resulting in specific active sites and possibly residual Cu⁺ species as indicated by quasi *in situ* XPS measurements. DFT calculations further supported these conclusions by pointing out that there is an increased cation surface absorption tendency, especially in the presence of subsurface oxygen species, resulting in a lower free formation energy and thus a higher coverage of crucial reaction intermediates on the surface, especially CO. The latter matches the experimentally observed fact of higher CO Faradaic efficiencies at lower potentials.

6.2 Electrolyte Driven Nanostructuring

The third part of the electrolyte effect related investigation focuses on the importance of morphological effects, since the previous experiments have always been in the presence of halide or alkaline ions, thus making it difficult to look at the sole effect of the catalyst's morphology. Consequently, to look at the effect of the catalyst's morphology while excluding the chemical effect due to the presence of halide ions in the electrolyte. All samples within this section were measured in pure 0.1M KHCO_3 after being restructured in the halide containing solutions via electrochemical cycling. As described in the experimental section, cycling is a powerful tool to analyse the presence of specific adsorption sites as well as to permanently change the morphology of a given surface due to oxidation and reduction. The latter is utilized hereby to invoke and stabilize the same changes that are seen when halides are present in the electrolyte. To also exclude the effect of the catalyst being oxide-derived as much as possible, electropolished metallic Cu foils have been chosen as working electrode.

The preparation was as mentioned based on cycling the Cu foils in 0.1 M KX (X=Cl, Br, I) and 0.1M K_2CO_3 aqueous solutions. The potential was hereby ramped up from E_1 to E_2 with a rate of $500 \frac{\text{mV}}{\text{s}}$ holding the potential at E_1 for 5s and at E_2 for 10s during each cycle. The chosen potentials and number of cycles are summarized in tabular form in tab. 6.1.

Sample	Electrolyte	E_1 / V vs RHE	E_2 / V vs RHE	Number of cycles
CuCl	0.1M KCl	0.4	2.0	5
CuBr	0.1M KBr	0.4	2.0	5
CuI	0.1M KI	0.4	0.8	3
CuCO_3	0.1M K_2CO_3	0.3	2.2	10

Table 6.1: Cyclic voltammety parameters for the employed sample preparation. Data acquired by Dr. Dunfeng Gao. Published in [66].

The SEM images after preparation, immersion and measuring the samples in CO_2 electroreduction at -1.0V vs RHE can be found in Figure 6.13. Similar to what has been reported previously [72, 86], the Cl-exposed samples show well defined Cu nanocubes, here with an edge size of 250-300nm. For the case of Br and I the morphology is drastically different, as faceted crystalline structures are observed for both cases. The Br-exposed samples show an overall flatter structure as compared to the case of I, where sharp needle-like structures can be seen, which is a clear difference to the case of plasma-oxidized Cu exposed to halides, where in the case of Br of crystalline structures formed, but only a roughening of the samples was observed. This can be explained by the fact that the copper oxides in the plasma treated case have been proven to be stable upon exposure to Br, resulting in the oxide facilitated structure to remain mostly intact as discussed in the previous sections.

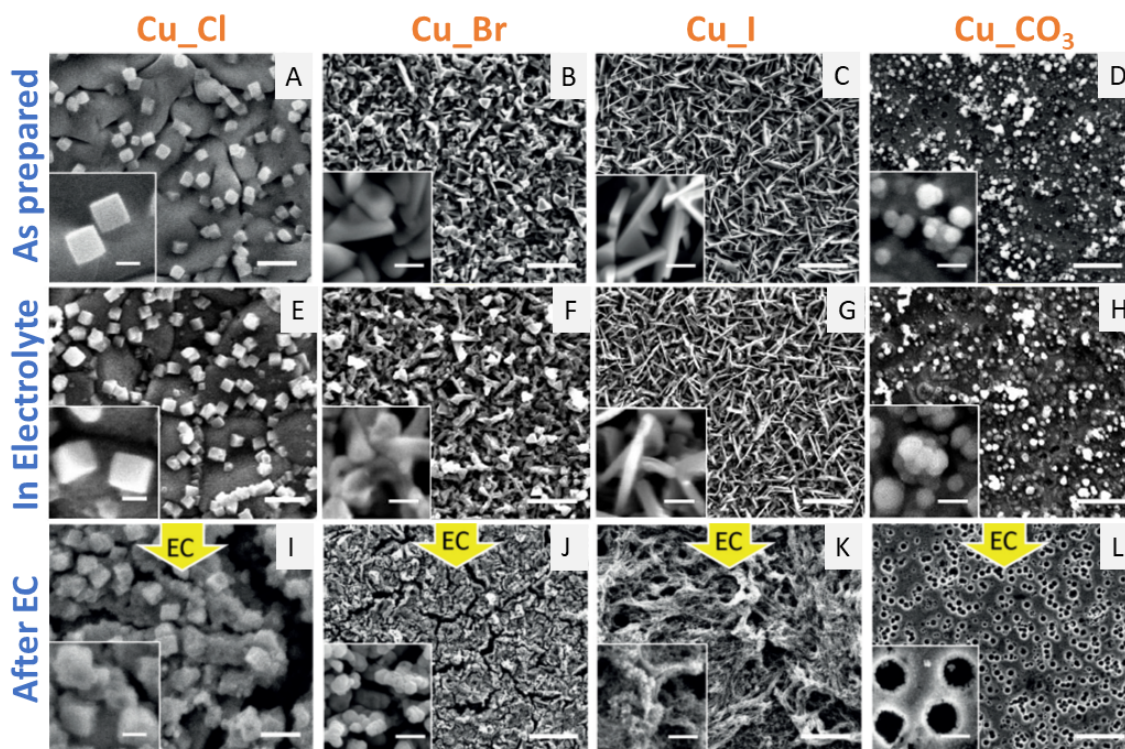


Figure 6.13: SEM images of Cu_Cl, Cu_Br, Cu_I, Cu_CO₃ as prepared (A-D), after 30 min of immersion into 0.1M KHCO₃ (E-H) and after 1 h of CO₂RR at -1.0V vs RHE in 0.1M KHCO₃ solution. The scale bars reflect 1 μ m and 200 nm for the inset for the Cu_Cl sample (A,E,I) and 5 μ m and 500nm for the inset for the Cu_Br (B,F,J), Cu_I (C,G,K) and Cu_CO₃ (D,H,L) sample. Data acquired by Dr. Dunfeng Gao. Published in [66].

As revealed by the XPS and EDX data obtained (Fig. 6.14 and Ref. [66]) the Br-exposed samples clearly undergo a change in their chemical composition resulting in restructuring. Comparing the case of the iodide cycled samples to the previous ones the EDX again shows a significant change in the chemical composition of the sample towards CuI, this time from an electropolished Cu foil instead of a pre-plasma oxidized one(Ref. [66]). The difference in the precursor state is therefore most likely responsible for the difference in the observed structures of well defined faceted crystals vs needle like structures. Since cycling is known to also electrochemically flatten samples, it might also affect the evolving structures [167]. The change in morphology, being most dominant for the iodine-cycled sample, is attributed to the high stability of CuI as previously discussed. In the case of the carbonate solution cycled sample, the formation of small particles as large as several 100 nm is observed, that are dispersed across the whole surface. Looking at the resulting structures by firstly exposing the samples to the employed 0.1M KHCO₃ electrolyte after cycling and carefully washing them with ultra pure water, no significant change of the overall morphology is observed. The edges of the cubes, as well as crystalline structures

for the Br and I cases become slightly roughened and truncated. Furthermore, a change towards a higher oxygen content is observed in EDX for all but the CuI samples after immersion into the electrolyte. This suggests that the halides within the samples are leaching into the electrolyte, with the halides then being replaced by oxygen.

Upon applying a potential of -1.0V vs RHE for 1h and running CO₂ electroreduction, the samples show drastically different morphologies from each other. While the cubes behave similar to previously reported studies on those type of samples [72, 86], showing a roughening of their surface but still mostly maintaining their cubic shape, the bromine and iodine cycled samples behave differently. The bromine cycled sample shows the appearance of particles with an average size of 220 ± 60 nm. The iodine cycled sample shows a significant roughening of the surface as also observed by electrochemical surface area measurements based on the capacitance of the Helmholtz layer (Ref. [66]). The needle like crystals seem to agglomerate forming a porous network-like surface. Regarding the case of the K₂CO₃ cycled samples, the particles observed prior to CO₂RR vanish, and pits with an average pore size of 430 ± 130 nm show up. As mentioned, the slight change in the morphology and chemical state when immersing the samples into the electrolyte already indicated leaching of the halides and the change of the chemical composition.

To be able to follow these chemical changes again, quasi *in situ* XPS measurements have been conducted. The obtained Cu LMM, Br 3p, I 3d and Cu 2p spectra are shown in Fig. 6.14, 6.15 and 6.16.

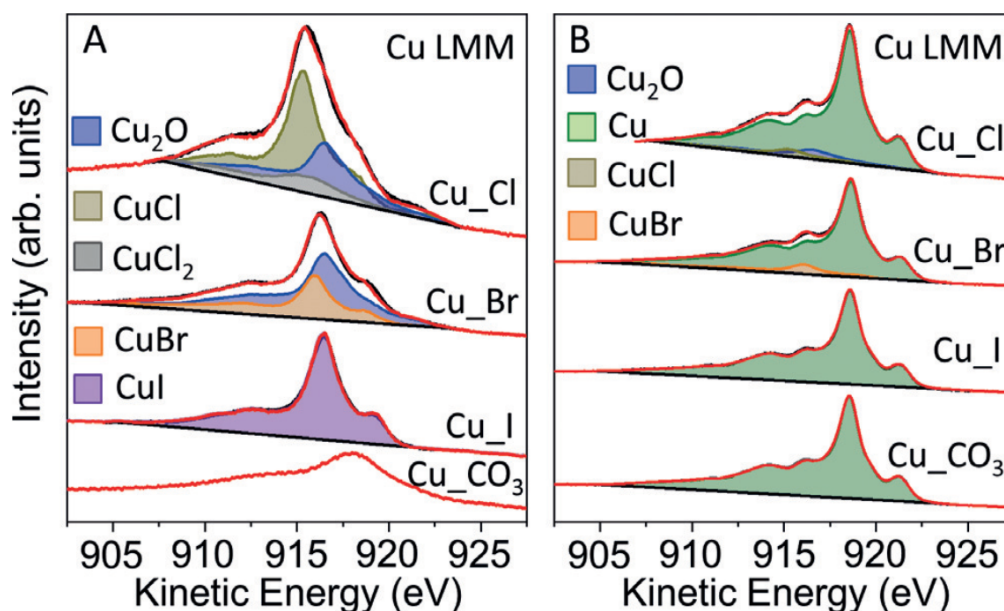


Figure 6.14: Quasi *in situ* Cu Auger LMM XPS spectra of the Cu_CO₃, Cu_Cl, Cu_Br and Cu_I samples before (A) and after (B) electrochemistry under CO₂RR conditions for 1h at -1.0V vs RHE in 0.1M KHCO₃ solution. Published in [66].

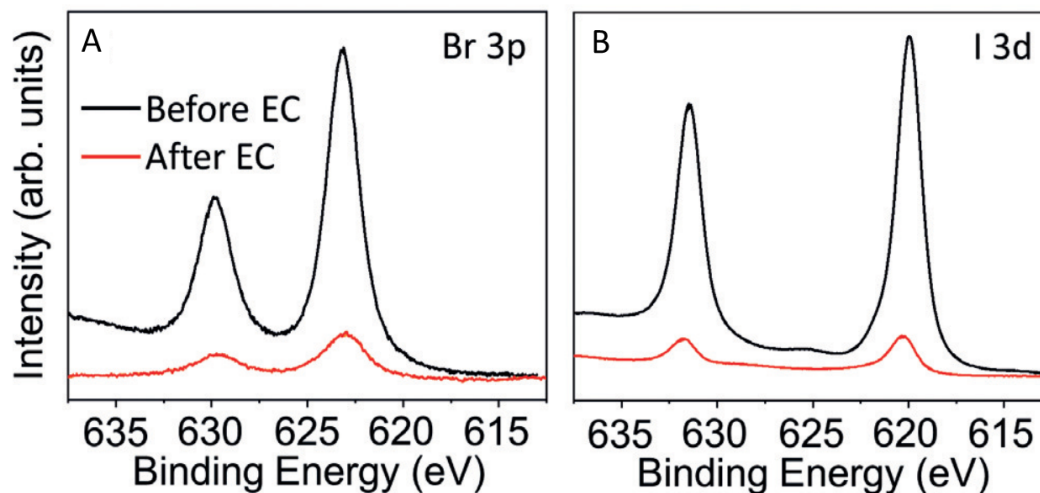


Figure 6.15: Quasi *in situ* Cu Auger LMM XPS spectra of the Cu_CO₃, Cu_Cl, Cu_Br and Cu_I samples before (A) and after (B) electrochemistry under CO₂RR conditions for 1h at -1.0V vs RHE in 0.1M KHCO₃ solution. Obtained Br 3p (A) and I 3d (B) spectra before and after electrochemistry under CO₂RR conditions for 1h at -1.0V vs RHE in 0.1M KHCO₃ solution. Published in [66].

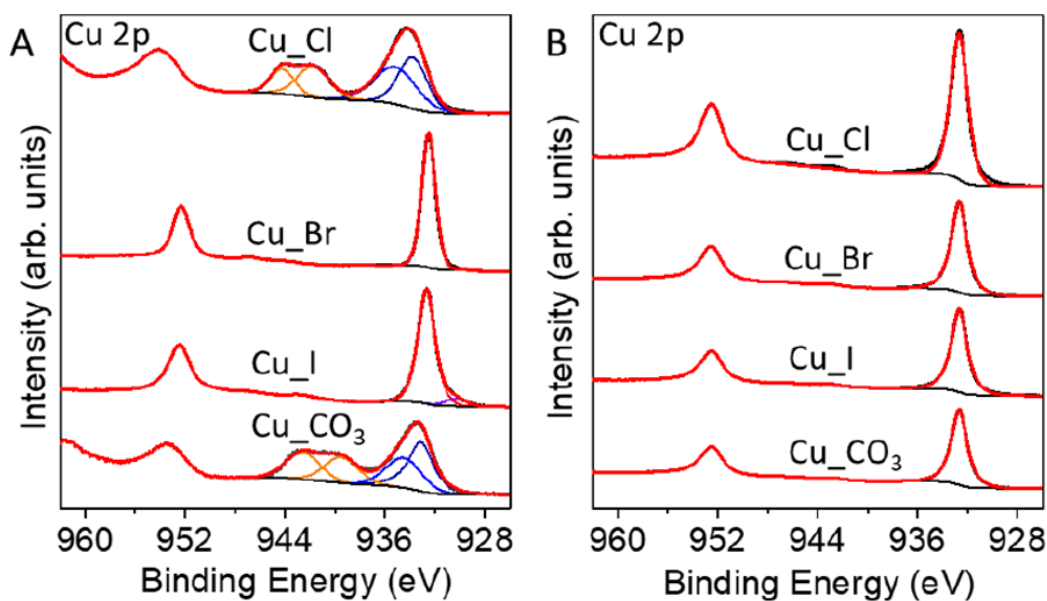


Figure 6.16: Acquired Cu 2p XPS spectra before (A) and after (B) CO₂RR for 1h at -1.0V vs RHE in 0.1M KHCO₃ solution. Published in [66].

Looking at the as prepared sample states, the Cu LMM Auger data show that the iodine-cycled samples contain the highest amount of halides bound to copper, as 100 % CuI is present. This is attributed to the fact that iodine exhibits the

strongest interaction with Cu, as discussed in the previous sections. The bromine cycled samples are composed of Cu₂O (65 at %) and CuBr (35 at %) and the Cl-cycled ones contain Cu₂O (31 at %), CuCl (56 at %) and CuCl₂ (12 at %) species. These differences in the compositions reflect the relative stability of copper halides with respect to each other, as discussed in previous sections.

The carbonate sample is in the 2+ oxidation state as it is a mixture of CuCO₃ and CuO, which is also supported by the presence of the typical shake up peaks in the Cu 2p spectra (fig. 6.16). The CuCO₃ reflecting component sits at $E_B=934.9\text{eV}$ and the CuO reflecting one at $E_B=933.5\text{eV}$ which is very close to the values reported in the literature [105].

After CO₂RR for 1h at -1.0V vs RHE in 0.1M KHCO₃ solution, all samples appear to be mostly in their metallic state even though residual halides could be detected on the surfaces by looking at the corresponding main intensity core level regions of Br and I. For Cl none was found after EC. Again, this reduction goes in line with the structural changes observed in SEM, as the surface roughness for all of them increases, which is also observed by the complementing ECSA analysis (Ref. [66]). This increase is strongest for the halides interaction the strongest with the surface (Br, I). Remarkably, the XPS analysis of the Cu LMM Auger and corresponding Cu 2p spectra also revealed that those surfaces do not undergo the transition to Cu²⁺ but instead, the Cu surface remains in its Cu⁺ state. Consequently, the increase in roughness and the development of the sample morphology as seen by SEM is dependent on the initial oxidation state, whereas Cu⁺ is, consistent with conclusion from previous chapters, the most beneficial.

Regarding the stability on the surface of these species, the Cu LMM Auger data suggest that the surface is mostly metallic, which was also seen by complementing operando XANES measurements (Ref. [66]). Nevertheless, the underlying linear combination as well as EXAFS fitting analysis also showed, unlike XPS, that CuI species are present under CO₂RR conditions. Combining these two spectroscopic results provides the information that these Cu⁺ species are within the subsurface region, since XANES is bulk and XPS surface-sensitive. The small amounts detected in both techniques (Ref. [66]) for the CuCl and CuBr samples are considered to be within the error of the experiments. Regarding the XPS measurements, the amount most likely originates from the fact that the samples are exposed to the electrolyte after CO₂RR and even though they were rinsed with ultra pure water immediately, residual species form post electrochemistry. This interpretation is supported by the fact that the interaction strength was found to be Cl < Br < I previously. Thus, there should also be CuI species present after EC if Cu⁺ on the surface would be stable, which is not the case.

Looking at the catalytic activity (Fig. 6.17 (a)) and the Faradaic efficiency of the joint C₂₊ products (Fig. 6.17 (b)), which have been obtained in chronoamperometric measurements for 1h in 0.1M KHCO₃ applying different potentials, it can be seen that all cycled samples show a significantly higher activity as the non-treated electropolished Cu foil, which is also shown again for reference purposes.

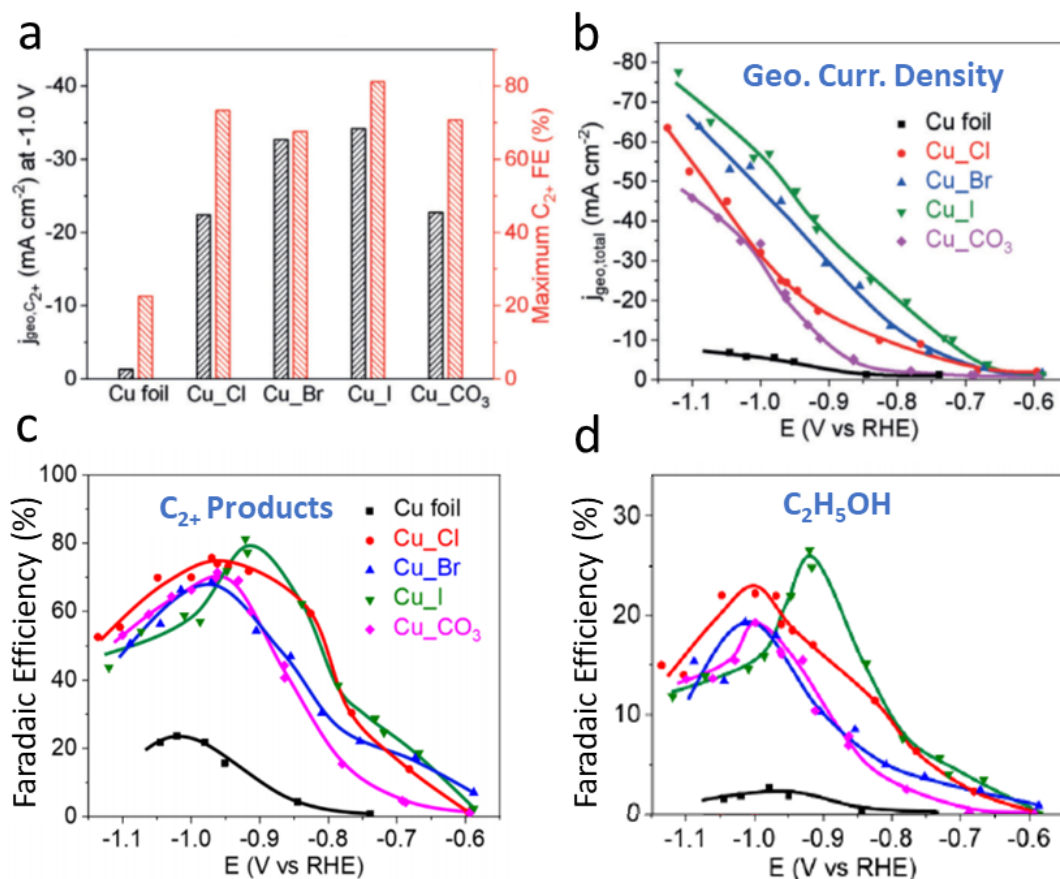


Figure 6.17: (a) Joint C₂₊ Faradaic efficiency and partial current density for the employed samples at -1.0V vs RHE and potential dependent (b) total geometric current density, (c) joint C₂₊ product Faradaic efficiency and (d) ethanol Faradaic efficiency.. Data acquired by Dr. Dunfeng Gao. Published in [66].

The highest joint Faradaic efficiency achieved for the C₂₊ products is seen for the iodine cycled samples up to 80 % at -0.9V vs RHE, which is remarkable considering the existing literature comparison [66]. The Cl and Br-cycled samples show a lower Faradaic efficiency for the joint C₂₊ products of 66-73 % at -1.0V vs RHE. Generally the behaviour with respect to the Faradaic efficiency is similar to oxide-derived polycrystalline Cu, while the obtained activities are different.

A special case, which is different to oxide-derived catalysts and also the other halide- and carbonate-cycled samples is the case of iodine cycling. Here a shift from -1.0V to -0.9V vs RHE for oxygenates such as ethanol and n-propanol can be observed, which was not observed for oxide derived catalysts [68]. Furthermore, an increase of the ethanol Faradaic efficiency by almost twice as much towards 30 % is observed for the cycled samples as compared to the oxide-derived ones (Fig. 6.5). Since the iodine samples are the only one showing Cu⁺ species to be present subsurface at the same time, a possible effect of Cu⁺ species linked to iodine or

oxygen is likely to influence to the selectivity and activity of oxygenates rather than ethylene, in agreement with the results from pulsed electrolysis experiments (chapter 4.3).

The reported Faradaic efficiency for ethylene on oxide-derived Cu with halides and/or alkaline metals (Fig. 6.5 and 6.11) show a similar behaviour to the halide cycled samples (Fig. 6.17), which have not been pre-oxidized. Thus, the selectivity for ethylene is consistent with previous results indicating that it is related to the catalysts structure and not to chemical state effects or the chemical influence of the electrolyte. From the presented TPD studies on single crystalline surfaces, those structural features that are likely also present in the halide-cycled nanostructures are undercoordinates sites, grain boundaries and defects within the lattice. Without knowing precisely how do these favourable structures look like the data acquired hereby evidence that they are invoked by the in situ reduction of the samples. All samples are either reduced towards metallic Cu from the oxide or the respective halide precursor state (see Fig. 6.14). These show, at the same time, an increase in the performance with respect to their selectivity towards ethylene and other C_{2+} products even when no halides are present. Since the morphology probed by SEM of all samples within this chapter (Fig. 6.1, 6.8 and 6.13) is different from each other the data also suggest that the most important factor for the ethylene selectivity is related to near atomic scale features. This idea of specific active sites being present after the reduction of Cu-based catalysts is also evidenced by other studies [73, 75, 76, 79, 129, 130].

In summary, by electrochemically restructuring metallic Cu samples in different solutions it was possible to synthesize highly selective and active catalyst for CO_2RR . By only running the obtained catalysts in a 0.1M $KHCO_3$ solution without any halides it was possible to narrow down the influence of structure and Cu^+ species on the selectivity. The iodine-modified samples showed the highest faradaic efficiency for C_{2+} products, which was about 80 % at a potential of -0.9V vs RHE, with a partial geometrical current density of $31.2 \frac{mA}{cm^2}$. The superior performance of the halide-cycled sample was possible to be attributed to the presence of Cu^+ species in combination with a high surface area, which was further nanostructured by the electro-reduction of the catalysts under reaction conditions, which is likely to be beneficial for the hydrocarbon selectivity.

6.3 Summary: Electrolyte Effects

In summary the last three sections focused on the effect of the electrolyte composition especially, halides and alkaline cations on the electrochemical reduction of carbon dioxide. Hereby, while leaving the pH of the employed 0.1M KHCO₃ solution mainly unaltered it was possible to significantly change the selectivity of the used copper based catalyst towards the desired reaction products while additionally improving the activity of the catalysts.

While in the first two sections the electrolyte was directly changed by adding either halides and/or alkaline cations to the solution and using oxide-derived plasma treated polycrystalline Cu foils as the catalyst of choice, the last section employed halide cycled electropolished foils in pure 0.1M KHCO₃ solution. Interestingly, a similar trend of the selectivity of all catalysts has been observed independent on the pretreatment or the electrolyte composition, which is an increase towards the desired C₂₊ hydrocarbons with the halide-cycled samples actually showing the highest combined C₂₊ Faradaic efficiency of up to 80 %. By careful comparison it was possible to further understand the role of the initial oxidation state and the role of oxides or rather anodic Cu⁺ species present during the reaction. Furthermore, it was possible to shed light on the interplay of structural properties and the chemical environment, including the presence of anions and cations in the electrolyte solution and their influence on the catalytic selectivity.

Importance of structural parameters

The obtained results suggested that the selectivity towards ethylene is to a large extent based on structural parameters such as overall macroscopic morphology and roughness as well as the microscopic structures. Thus, these findings based on the design of the electrolyte are in line with the previously discussed results on plasma oxidized dendritic Cu and single crystal Cu surfaces [27, 45].

This conclusion is based on the fact that all employed catalysts showed a similar increase in the ethylene selectivity independent on the electrolyte used. The spectroscopic analysis of the employed samples has shown that all catalysts, even though oxidized by either an oxygen plasma treatment and/or exposing them to halides tend to be reduced in the course of CO₂RR, since these Cu⁺ species suffer from low stability. This leads to the conclusion that similar to the cases discussed in the previous chapter 4.2, the presence of cationic Cu species during CO₂RR is less important for the ethylene selectivity than the actual structural properties evolving as a consequence of the reduction of the samples.

The accompanying SEM analysis (fig. 6.1, 6.8, 6.13) of the investigated samples has shown that all catalysts go through an increase in their overall roughness. The majority showed a high porosity and network-like structure on the catalyst surface in the size of several μm , with the Cs-exposed samples being the only exception. Here, well defined shaped and faceted crystals have been observed. For the case

of combining Cs and I on the O₂ plasma treated foils, faceted Cu crystals their structure under CO₂RR conditions even though shrinking in size. Especially those samples showed a slightly different ethylene selectivity with respect to the applied potential, as they have been able to produce a higher amount at lower potentials. This goes in line with the idea and experimental evidence that specific crystalline sites and facets lower the C-C activation barrier and thus significantly affect the catalytic selectivity [37, 43, 52]. Therefore, the evolving sites as a consequence of the pre-oxidation and consecutive reduction, together with the interaction of the surface with halides and/or alkaline cations, are believed to contribute to the observed catalytic trends.

Regarding the overall roughness all samples show a similar trend towards higher ethylene selectivity up to 50 %, instead of the 13-20 % obtained for an electropolished Cu foil in 0.1M KHCO₃ once a specific threshold roughness of approximately eight times as rough as the electropolished foil is reached. Even though it was possible to increase the the obtained roughness factors up to 60 times larger than the electropolished Cu foil there, was no significant impact on the selectivity observed with increasing roughness. A possible explanation for this behaviour could be the previously discussed local pH effect. Due to the higher surface area, a higher amount of the reaction educts are consumed resulting in the accumulation of OH⁻ species in the electrode vicinity. As discussed in the introduction, this leads to a suppression of the methane selectivity and consequently to a relative increase of the ethylene selectivity. Nevertheless, this effect cannot be accounted solely for the increased selectivity. The previously discussed results on oxide-derived dendrites have proven that a higher local pH is not enough to explain the catalytic behaviour of oxide derived catalysts. This was also evidenced previously but attributed to the presence of oxides during the reaction [68], which could be ruled out for the dendritic Cu catalysts. The most dominant parameter in determining the selectivity is the surface structure, which facilitates the coupling of carbon monoxide with each other.

Chemical effect

Unlike the Faradaic selectivity for ethylene, the activity of the samples was significantly different from each other depending on the electrolyte composition used, suggesting a chemical effect of the electrolyte on the reaction. In the case of halides, the increase in the activity was found to scale with the strength of the interaction of the employed halide with the surface and its corresponding adsorption properties on the surface. Especially iodine, which interacts strongly with the Cu surface, was found to increase the overall activity, while maintaining a high C₂ Faradaic efficiency. This is in part due to electrolyte-driven reconstructions but not solely. The data suggest that a common step of the CO₂RR is enhanced in the presence of halides. On the background of the available literature, this step is believed to be the formation of the activated bent CO₂ molecule on the surface and the hy-

drogenated COOH species, whose stability on the catalysts surface is increased by adsorbed halide ions. For the case of alkaline cations within the electrolyte, the findings were in line with what has been reported in the literature. The novelty being here is that the effect of an increasingly larger hydration shell with increasing cations size is also transferable to pre-oxidized Cu catalyst on which surface the cations appear to interact more strongly. Surprisingly, the effect was even enhanced on Cu_xO surfaces. DFT calculations and control experiments carried out supported the conclusion that the presence of Cu⁺ species and the overall high roughness of oxide derived catalysts leads to an emphasized interaction of the halides and/or cations present in the electrolyte solution and the catalyst surface resulting in a higher surface stability of crucial reaction intermediates like COOH.

Presence of cationic copper species

The obtained data also reflect a dependence of the selectivity towards oxygenates such as ethanol and n-propanol and the presence of Cu⁺ species which was also visible in the conducted pulsed electrolysis experiments [45]. The samples showing the biggest increase for oxygenates were also the ones that showed the highest content of Cu⁺ species either in the form of the respective copper halide (i.e. CuI) or Cu₂O. This clearly indicates a possible interaction of the cationic Cu species with the reaction intermediates, especially the C-C bonded intermediates. The binding strength and/or structure of the molecules could thereby be altered by the presence of Cu⁺ species, resulting in oxygenate production instead of ethylene.

7 Role of the Nanoparticle Size

Nanosized catalysts are a topic of their own within the field of CO₂ electroreduction. The interest directed towards these type of catalyst is based on the idea that quantum size effects could play a crucial role in determining and changing the surface properties of a given nano-sized system as compared to a bulk one. Thus, the interaction of the surface with CO₂ and its reaction intermediates along the pathway to hydrocarbons could be affected, and the hydrocarbon generation enhanced. Another beneficial feature of nanosized catalysts is that they offer a better surface to volume ratio, especially when employing spherical particles [168]. Achieving a similar or even better catalytic performance with the help of such systems as compared to bulk ones would therefore additionally reduce the amount of material needed. Even though this is of general interest for all material systems, it is of special importance for cases where rare metals such as Pt, Pd or Au are employed for example in bimetallic copper systems.

Even though the utilization of nanosized systems for CO₂RR on a large scale remained elusive up to now, recent scientific progress offers a route towards employing such systems. For instance, parameters such as the size and structure on the nano scale have been found to significantly affect the catalytic behaviour [81, 129, 169, 170]. Also, the importance of the presence of specific active sites in the form of low coordinated atoms and their effect on the catalysis has been pointed out [77, 156, 171]. Additionally studies employing bimetallic systems containing Cu highlighted that the catalytic performance can be enhanced using these type of nano scaled systems [38, 39, 172–174].

A promising one among them is the combination of CuZn not only because of its low cost and non-toxicity, but especially because of their catalytic behaviour. Recent studies pointed out that the catalytic performance on this system can be tailored to a large extent depending of the ratio of Cu to Zn and the pretreatment. For instance, it has been shown that the faradaic efficiency for CO and HCOOH can be improved significantly by employing nano-porous CuZn as compared to bare bulk CuZn alloyed systems [175]. Other studies also reported a possible enhancement of the hydrocarbons yield depending on the ratio of Cu to Zn, reaching from a higher amount of CH₄ on Zn-coated Cu [176] up to a more selective generation of ethylene and ethanol on oxide-derived bimetallic CuZn systems [187].

Nevertheless, even though these results point out the advantages of using nano-sized and structured systems, especially CuZn ones, insight into the role of different parameters on the electrocatalytic behaviour is missing. The reason for this is mainly the complexity of CO₂RR itself and the accompanying difficulties in control-

ling and stabilizing such systems with respect to their size, shape and composition, especially during reaction conditions [86, 156, 177]. Therefore model systems that allow to study the impact of a given parameter are of great interest.

This motivates the work presented within this chapter. By employing a polymer based synthesis, well defined size and composition controlled nanoparticles (NPs) are made to study the impact of their size and CuZn composition in CO₂RR activity and selectivity.

7.1 Zn Particles: Size and Oxidation State Effect

The first step was to understand the impact of the size and oxidation state on the monometallic particles system before starting to investigate bimetallic ones. Studies carried out on Cu monometallic NPs demonstrated that a decrease in size results in an increase of the overall activity at the cost of the desired selectivity, as the NPs only produced hydrogen below a threshold size [81]. Similar behaviour has also been observed for mono- and bimetallic Au and CuAu NPs [169, 170]. Even though these results suggest the effect to be independent on the metal system used, it has not been demonstrated for Zn.

Using the inverse micellar encapsulation synthesis method (see chapter 3.5), Zn NPs of different sizes were synthesised. The structural characterisation of the resulting NPs has been carried by means of AFM measurements to determine their size. The obtained AFM images can be found in Figure 7.1.

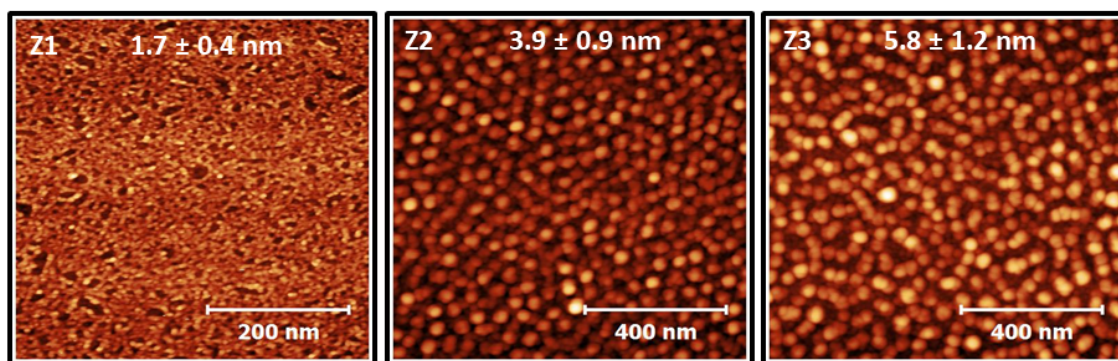


Figure 7.1: AFM images of differently sized Zn NPs produced using the parameters summarized in Table 7.1. Top right: average sizes extracted from the histographic analysis. Particles are supported on $\text{SiO}_2/\text{Si}(111)$. Data acquired and by Dr. Hyo Sang Jeon. Reprinted with permission from [29]. Copyright 2018 American Chemical Society. Published in [29].

Sample	Polymer	Loading	Particle Size (nm)
Z1	PS(26000)-P2VP(4800)	0.2	1.7 ± 0.4
Z2	PS(48500)-P2VP(70000)	0.1	3.9 ± 0.9
Z3	PS(26000)-P2VP(4800)	0.4	5.8 ± 1.2

Table 7.1: Synthesis parameters for the micellar NPs and the extracted sizes based on the AFM characterization. Reprinted with permission from [29]. Copyright 2018 American Chemical Society. Published in [29].

To test the electrocatalytic behaviour of the Zn NPs they have been supported on glassy carbon and run under CO₂RR conditions at -1.1V vs RHE in 0.1M KHCO₃ for 1h. The results are summarized in Figure 7.2. The normalization of the current density is done by subtraction of the bare glassy carbon geometric current density and normalizing the obtained remaining current density to the geometric surface area of the Zn NPs extracted from the AFM images assuming spherical particles.

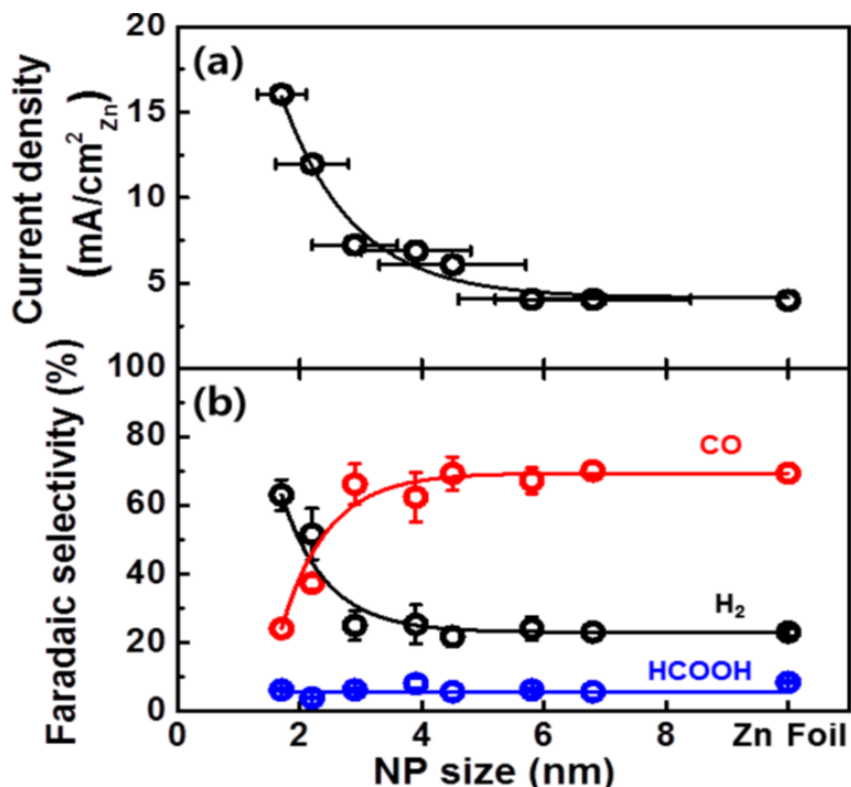


Figure 7.2: (a) Current density normalized to the Zn NP surface area and (b) Faradaic efficiency in dependence of the particle size. Data acquired and analysed by Dr. Hyo Sang Jeon. Reprinted with permission from [29]. Copyright 2018 American Chemical Society. Published in [29].

As it can be seen, the overall activity of the samples increases with decreasing particle size, starting to be different from the bulk Zn foil. The detected major products for all samples are hydrogen and carbon monoxide, which is expected for Zn [24]. Interestingly, the selectivity shows a strong dependence on the particle size as the obtained values for the CO and hydrogen Faradaic efficiencies change significantly below 3nm NP size. For the smaller sized particles, the major product detected is hydrogen, making up almost 70 % of the total Faradaic efficiency, whereas for the bigger ones CO is found to be the major product with almost 70 % Faradaic efficiency. Thus, these findings are in line with previous work on nano-sized particles that attributed the higher selectivity for HER to the increased presence of low-

coordinated sites on small particles as compared to bigger ones. DFT calculations suggested that those sites lead to a higher coverage of hydrogen and consequently explain the decreased CO₂RR towards CO [170].

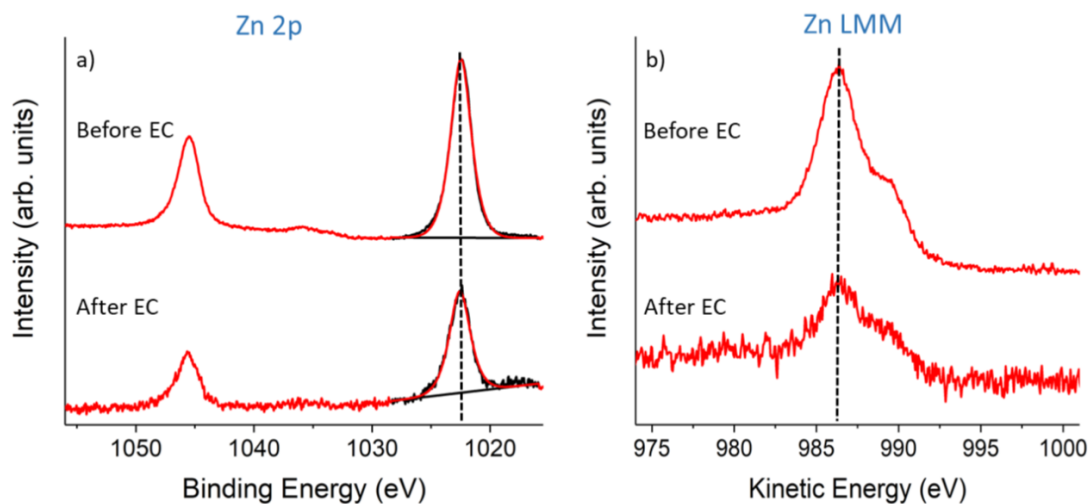


Figure 7.3: Quasi *in situ* XPS spectra of the (a) Zn 2p and (b) Zn LMM region for the 1.7 nm Zn NPs before and after EC. CO₂RR was carried out at -1.1V vs RHE for 1 h in 0.1M KHCO₃ solution. Reprinted with permission from [29]. Copyright 2018 American Chemical Society. Published in [29].

Species (Peak)	Before EC (eV)	After EC (eV)	Literature (eV)
Zn(OH) ₂ (Zn 2p _{3/2})	1022.5	1022.5	1023.4
Zn(OH) ₂ (Zn LMM)	987.4	986.5	986.6
ZnO (Zn 2p _{3/2})	–	–	1022.1 [180]
ZnO (Zn LMM)	–	–	988.2 [180]
Zn (Zn 2p _{3/2})	–	–	1021.8 [181]
Zn (Zn 2p _{3/2})	–	–	992.1 [181]

Table 7.2: Binding- and kinetic energy values for different Zn species for the NP samples and as reported in the literature [180, 181]. Reprinted with permission from [29]. Copyright 2018 American Chemical Society. Published in [29].

Quasi *in situ* XPS measurements were carried out on the smallest particle size sample since XPS is able to penetrate the 1.7 nm thickness, thus providing meaningful data about the whole particle. The acquired XPS data for the Zn 2p and Zn LMM Auger spectra are shown in Figure 7.3. The obtained results confirm the presence of Zn(OH)₂ species in the as prepared state of the samples as well as after

electrochemistry. The binding and kinetic energy values summarized in Table 7.2 reflect also the reported ones for $\text{Zn}(\text{OH})_2$ in the literature. It has to be pointed out that due to the way reported the quasi *in situ* XPS experiments are conducted, water cannot be completely prevented from being on the sample surface during the transfer from the electrochemical cell towards the UHV XPS setup. This can result in a rehydroxylation of the sample. Nevertheless, my XPS data are in agreement with XAS data measured for these samples [29], in particular, that $\text{Zn}(\text{OH})_2$ is present under CO_2RR conditions despite the negative applied potential.

These results point out that there is a size dependence resulting in a favoured H_2 production once the particles are small enough. Since this trend has been reported for other metal systems, such as Cu and Au [81, 170], the presented data also support the hypothesis that it is solely dependent on the size and not on the material system used. Furthermore, the demonstration of the presence of $\text{Zn}(\text{OH})_2$ species under reaction conditions is of importance since previous studies carried out on Zn catalysts have not been able to demonstrate it but suggested the catalytic activity and possibly the selectivity to be dependent on the presence of oxidized species [182].

7.2 Role of the Nanoparticle Composition

Knowing that the size dependent selectivity of nanoparticle catalysts is negligible when employing bigger particles (beyond 4 nm, see last chapter) those can be used to explore the effect of the composition on the nanoscale. Hereby, Cu and Zn have been combined to explore a potential synergetic behaviour, using again the polymer based encapsulation method for the NP synthesis. The characterization of the particle size was again done with the help of AFM measurements on Si-wafer supported particles. Figure 7.4 shows example AFM images from which the particle size distribution is determined. As it can, be seen the particles have an average size of 5 nm (see also Tab. 7.3) and are homogeneously spread across the surface.

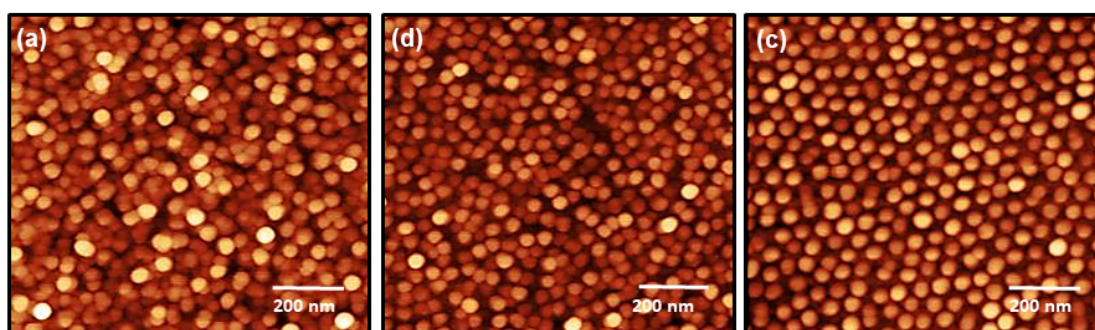


Figure 7.4: AFM images of (a) Cu_{100} , (b) $\text{Cu}_{50}\text{Zn}_{50}$ and (c) Zn_{100} composed particles deposited on Si-wafers ($\text{SiO}_2/\text{Si}(111)$). Data acquired and analysed by Dr. Hyo Sang Jeon. Reprinted with permission from [39]. Copyright 2019 American Chemical Society. Published in [39].

Sample	Polymer	Loading	Particle Size (nm)
Cu_{100}	PS(48500)-P2VP(70000)	0.2	5.2 ± 0.6
$\text{Cu}_{50}\text{Zn}_{50}$	PS(48500)-P2VP(70000)	0.2	4.9 ± 0.7
Zn_{100}	PS(48500)-P2VP(70000)	0.15	5.4 ± 0.7

Table 7.3: Synthesis parameters for the obtained $\text{Cu}_x\text{Zn}_{100-x}$ NPs and the extracted sizes based on the AFM characterisation. Reprinted with permission from [39]. Copyright 2019 American Chemical Society. Published in [39].

To ensure that the targeted nominal values from the synthesis for the composition are indeed real, XPS measurements of the samples supported on glassy carbon have been carried out. In addition the same samples have been characterized employing quasi *in situ* XPS after electrochemistry. This is of particular importance since previous studies on similar CuCo NPs have shown that a strong segregation of the metals can occur within bimetallic systems during CO_2RR [38]. If this was the case for the $\text{Cu}_x\text{Zn}_{100-x}$ particles the presence of only one metal at the surface could

dominate the catalytic behaviour to a large extent. The results obtained from the XPS data analysis are shown in Figure 7.5 and 7.6

As it can be seen, the targeted nominal composition values are very close to the real ones found when comparing the integrated area of the Cu 2p_{3/2} and Zn 2p_{3/2} peaks with each other. Surprisingly, the XPS data after CO₂RR also show that the initial composition of the particles remains intact under reaction conditions, as the values obtained from the integrated area are close to the ones before the reaction (Fig. 7.6). Thus, the CuZn bimetallic NP catalyst is stable under reaction conditions with respect to the surface content of Cu vs Zn and no significant segregation of the metals is observed.

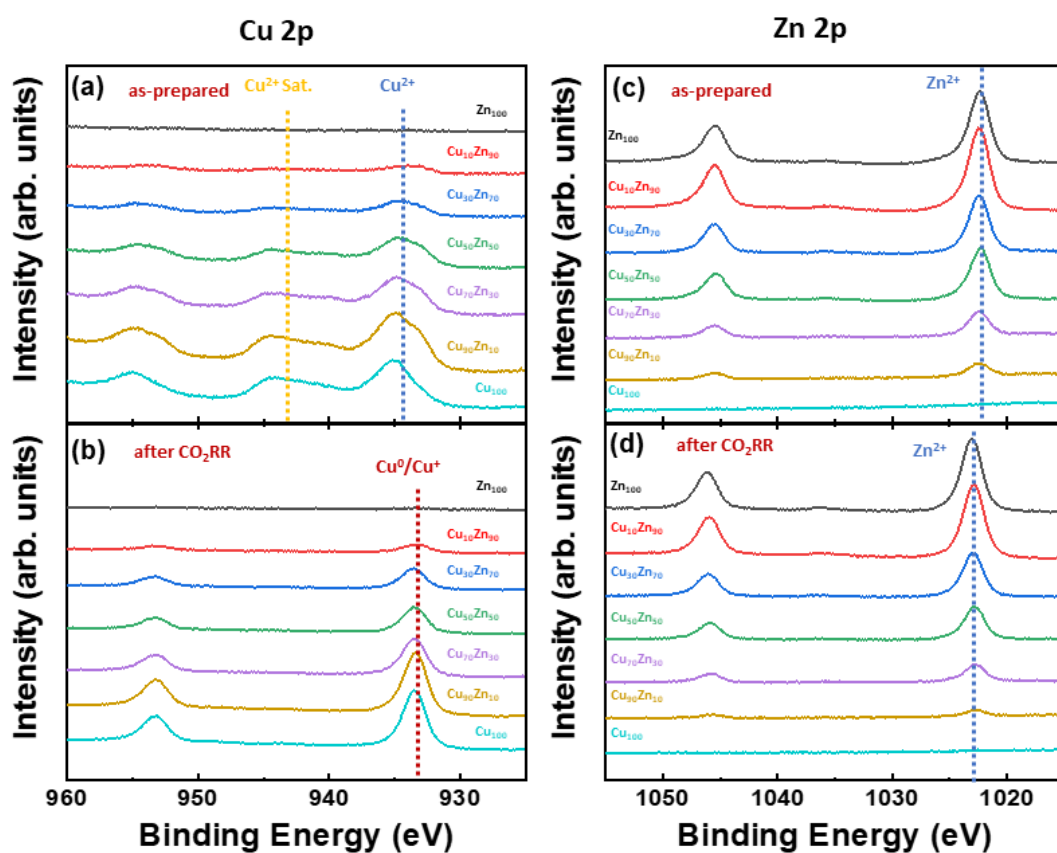


Figure 7.5: Quasi *in situ* Cu 2p and Zn 2p XPS data of CuZn NPs with different composition in their as prepared state (a,c) and after CO₂RR (b,d). Data acquired and analyzed with the help of Dr. Hyo Sang Jeon. Reprinted with permission from [39]. Copyright 2019 American Chemical Society. Published in [39].

Regarding the chemical state of the catalyst and its evolution during the reaction, open question still remain. It was attempted to acquire Zn and Cu LMM data, however, the signal intensity was too low for the nanoparticles samples due to the small amount of metals. Therefore, only the Cu and Zn 2p spectra could be acquired

and analysed. Since all samples behaved, according to XPS, similar to each other under reaction conditions only, the detailed analysis of the $\text{Cu}_{50}\text{Zn}_{50}$ composed sample is shown in Figure 7.7. Both metals are oxidized in their as prepared state. Judging from the characteristic shake-up peaks, copper is in its 2^+ state. Similarly, Zn is according to the binding energy also in its 2^+ state. Most likely both metals, judging from the binding energies, are a mix of oxide and hydroxide species in their as prepared state.

Upon exposure to CO_2RR conditions, the chemical state of Zn is, in agreement with previous results on pure Zn NPs, changing to $\text{Zn}(\text{OH})_2$. Copper does reduce, and is likely to be in its metallic state, even though the difference to Cu_2O can not be told due to the lack of access to the Cu LMM in this case (low intensity).

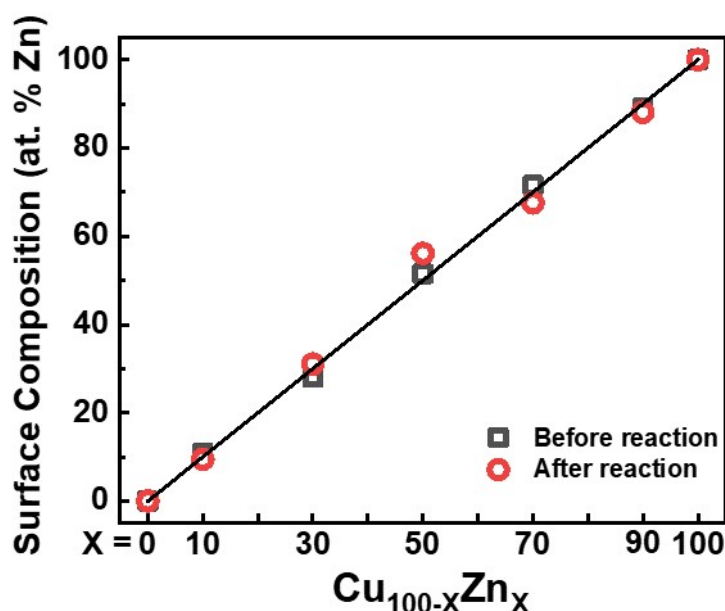


Figure 7.6: Surface composition before and after electrochemistry as extracted from the relative comparison of the integrated Cu 2p and Zn 2p peak areas. X-axis denotes the nominal composition as targeted during the synthesis. Data acquired and analyzed with the help of Dr. Hyo Sang Jeon Reprinted with permission from [39]. Copyright 2019 American Chemical Society. Published in [39].

It is important to note that all sample spectra have been aligned and corrected with help of the C 1s line spectrum ($E_B=284.8\text{eV}$). The fact that the Cu $2p_{3/2}$ peak energy is still differing from the reference values for Cu/ Cu_2O by almost 0.8eV is assigned to charging effects that have previously been discussed and are known to affect the binding energy as seen in XPS for NP systems [38]. Thus, this is also considered to account for the differences from the literature values for all of the obtained spectra and makes it difficult to judge whether or not the samples are in their oxide or hydroxide state before electrochemistry.

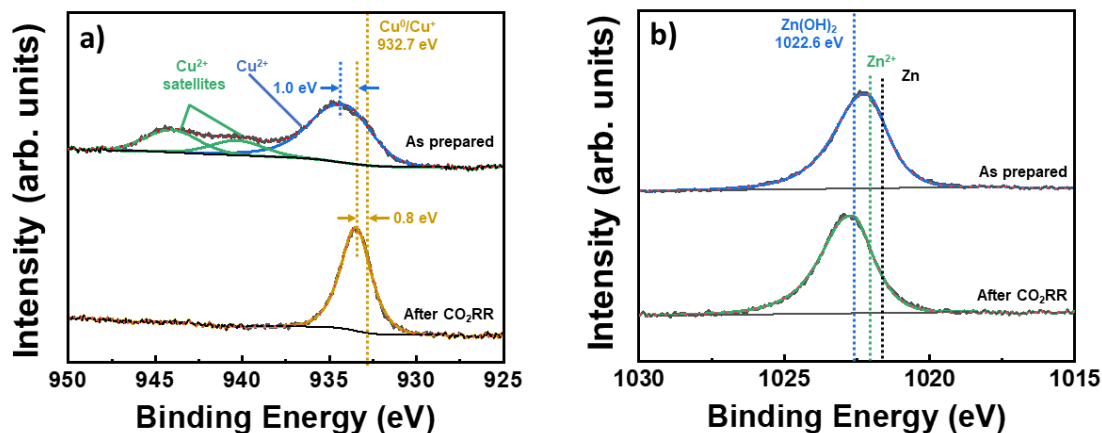


Figure 7.7: Fitted quasi *in situ* XPS data of the (a) Cu 2p and (b) Zn 2p region. Vertical lines mark binding energies for different chemical species of the two metals. Data acquired and analyzed with the help of Dr. Hyo Sang Jeon Reprinted with permission from [39]. Copyright 2019 American Chemical Society. Published in [39].

Looking at the catalytic performance at a potential of -1.35V vs RHE, a strong dependence of the Faradaic efficiency on the composition is visible, Fig. 7.8. Upon increasing the copper content within the NPs the selectivity changes from H_2 and CO , which is characteristic for Zn, towards methane. Remarkable is that even though copper is known to be able to produce also higher chain hydrocarbons like ethylene and ethanol, none of these are detected. Instead, the faradaic efficiency is almost 70 % for methane on $\text{Cu}_{50}\text{Zn}_{50}$. Once the particles are monometallic Cu, the hydrogen Faradaic efficiency is increased to 60 % again at the expense of methane, which is with 40 % similar to that of bulk electropolished Cu. Nevertheless, the amount of hydrogen seen is significantly higher than that obtained to the one bulk Cu at these potentials. The latter is attributed to particles size effects resulting in an altered CO vs H binding strength on the metal surface favouring hydrogen production [81]. The fact that the increased methane selectivity is only seen for bimetallic particles suggests a synergistic effect in between the catalytic sites of Cu and Zn that is dependent on the presence of sufficient Cu sites since it is not seen for Cu contents smaller than 50 %. Possibly due to the different binding properties of both metals for CO and H the hydrogenation of CO bound to Cu is enhanced on these particles.

To gain further information about the stability, chemical state and structure of the particles under CO_2RR conditions for different times, *operando* XAFS measurements were carried out [39]. From the qualitative comparison of the XAS NP sample spectra with the corresponding reference spectra for Cu and Zn, both metals are oxidized in their as prepared state and reduce under *operando* CO_2RR conditions [39]. Interestingly, the reduction speed appears to be different for both metals. While the Cu spectra for different reaction times do not differ much from each other and are similar to the one for metallic Cu, after a first initial fast reduction, the

Zn spectra change takes place slowly over time. Thus, Zn appears to reduce slower than Cu within the particles.

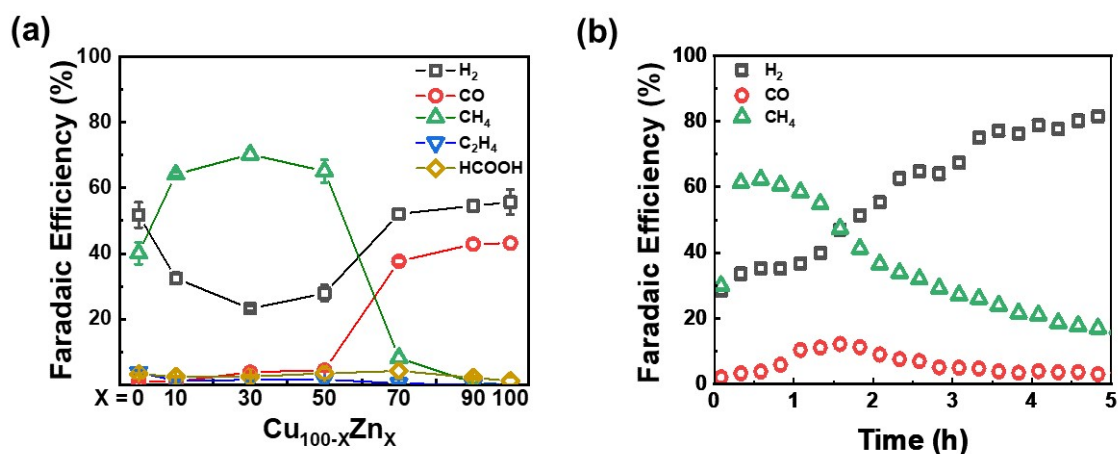


Figure 7.8: (a) Faradaic efficiency of differently composed CuZn NPs measured during 1h of CO_2RR and (b) long time test of $\text{Cu}_{50}\text{Zn}_{50}$ NPs at -1.35V vs RHE in 0.1M KHCO_3 solution. Data acquired and analyzed by Dr. Hyo Sang Jeon. Reprinted with permission from [39]. Copyright 2019 American Chemical Society. Published in [39].

In order to quantify these findings, linear combination fitting of the XAS spectra acquired after different times was done using the as prepared and final spectra which was obtained after 7h of CO_2 electrolysis. The oxides related to Cu are quickly reduced, independent of the Cu to Zn ratio within the particles. For the case of Zn, the reduction speed depends on the particle composition with the pure Zn particles being reduced the fastest and the bimetallic reducing on longer time scales, whereas the Cu rich need longer to be reduced.

Thus, the mixed particles are, consistent with XPS, found to contain Zn^{2+} species after extended periods of time (3h), despite the reducing conditions. The observed selectivity changes over the course of several hours are therefore likely linked to the presence of those species. Since the reduction of the Cu oxide species is happening at much smaller time scales (minutes), it can be ruled out that they are the reason for the catalytic trends observed.

Furthermore, analysis of the EXAFS data revealed that the formation of the brass alloy is invoked under CO_2RR conditions once the Zn species are reduced in the NPs. Since the catalytic behaviour of the particles is observed to change over the same time scale it can be concluded that the changes seen are linked to the alloy formation. Furthermore, the initial composition and oxidation state plays a crucial role in determining the rate of the alloy formation. The Zn rich particles favour the production of CO and H_2 and reduce significantly faster, while the alloy is present after already 1h of CO_2RR . The 1:1 CuZn particles initially show methane as major product which is changing in favour of CO and H_2 over the course of several hours

during which the ZnO reduction and the concomitant brass alloy formation take place.

Generally within NP systems, especially bimetallic ones, the lattice of a given metal can be disturbed invoking strain. This can be enhanced by the alloy formation in these cases since it is going alongside with a geometric change of the lattice structure. For the case of Cu, previous studies suggested that especially expansive strain on the Cu lattice could lead to an enhanced binding strength of CO and its stabilization on the surface. Consequently, the formation of products beyond CO is possible on these surfaces [38]. This expansive strain could explain the initial high formation of methane observed for Cu₅₀Zn₅₀ NPs and possibly the Cu rich particles. On the other hand, the alloy formation also results in changes of the electronic structure which is affecting the binding properties of the surface for CO as well. It is known that such a ligand effect invoked by the alloying is for instance changing the d-band center of metal atoms [183, 184], which is shifted away from the Fermi level due to the reduction of Zn and the formation of the CuZn alloy [185]. This shift is associated with the weakening of CO on the surface due to occupancy of states by the alloy [172, 186]. Thus, the product selectivity of the hereby investigated bimetallic NPs seems to be determined by the changes in the electronic structure whereas lattice strain effects appear to play an inferior role.

In summary, it was possible to determine and understand the catalytic behaviour of size selected and composition controlled Zn and CuZn nano-particles within the work presented in this section. In the case of pure Zn particles, it was found that their size plays a crucial role, as particles smaller than 4 nm do not exhibit the Zn-characteristic CO production. Instead, they generate hydrogen. This was attributed to the higher amount of under-coordinated sites that is increased for small NP systems. Additionally it was possible to observe a remarkable stability of Zn(OH)₂ species under CO₂RR conditions, which may possibly affect the catalytic activity in a beneficial way for Zn based systems.

In the case of CuZn composed NPs large enough not to suffer from an artificially increased hydrogen selectivity, as described previously, the composition was found to play a crucial role in determining the catalyst selectivity for specific products. While the Cu-rich NPs show a high initial selectivity for methane which was attributed to strain effects within the bimetallic system. Zn-rich particles favour H₂ and CO. Both selectivities were found to be linked to the presence and formation of the CuZn alloy within the particles. The rate of the alloy formation which is gradually evolving under reaction conditions and depends on how fast the reduction of the Zn species proceeds, which was found to be significantly faster for Zn-rich NPs than for Cu-rich cases. Consequently Cu rich particles exhibit a high methane production for longer times, which degrades over several hours due to the alloy formation. The fact that the methane formation on the alloy is stifled has been attributed to the weaker CO binding on the surface resulting from the antibonding properties of the electronic structure within the alloy which consequently leads to a higher amount of CO over methane being produced. These findings are also of importance

beyond the model nano-particle system since the obtained results clearly highlight the negative effect on the selectivity once the CuZn alloy is formed. This could also lead to a lower amount of C₂ hydrocarbons for bulk materials, especially ethanol which has been reported to be favoured on oxide derived CuZn systems [176, 187]. Thus, these results point out that it is crucial to design CuZn systems where the alloy formation can be prevented though, especially for longer reaction times. A possible route towards designing such catalysts was also pointed out hereby, as the presence of Zn²⁺ species was found to prevent the alloy formation. Consequently, the stabilization of those species is an important parameter to consider when rationally designing new catalysts for CO₂RR towards hydrocarbons.

8 Outlook and Conclusion

8.1 Conclusion

The scientific results presented in this work address several open questions within the field of CO₂RR by providing crucial insights and valuable information about the influence of specific parameters on this reaction.

The first parameter influencing CO₂RR being the presence of copper oxides and their presence under reaction conditions in oxide-derived catalysts. The combination of quasi *in situ* XPS and *operando* XANES techniques showed that polycrystalline electropolished Cu foils are in their metallic state under CO₂RR conditions, even when being pre-oxidized. The same was true for oxygen plasma-treated dendrites, whose selectivity for the desirable ethylene and ethanol products was further improved by the roughening plasma treatment even though the surface remained reduced under CO₂RR. Additionally, by combining these high surface area catalysts with different substrates, a further C₂ product selectivity improvement due to a synergetic effect could be highlighted. Both results are crucial since dendritic and other nano-structured catalysts are promising for industrial applications due to their high surface area, allowing them to be operated at high current densities. Furthermore, the investigation of oxide-derived catalyst, also when exposed to halides and/or cations, provided insight into the role of the local pH which can not be solely responsible for the increase in the C₂ selectivity of those catalysts.

Instead, structural properties have been found to be the major key factors determining the selectivity, which was also seen when going beyond the general case of polycrystalline catalysts. Employing pulsed electrolysis on single crystal surfaces it was possible to generate and maintain Cu oxide species during CO₂RR, allowing to investigate their role in addition to the modified structural properties of the pulsed surface, decoupling of their influence from structural properties. The results show that the combination of Cu(100) domains with defects is the key factor in enhancing the C₂ selectivity, especially for ethylene, while the presence of oxide species and Cu(I)/Cu(0) interfaces is found to increase the oxygenate selectivity. This fundamental understanding of the influence of those parameters and their interplay is of remarkable value when rationally designing electrochemical interfaces and catalyst to selectively produce specific C₂ products.

Following up on these results, surface sensitive characterizations employing UHV-based techniques such as TPD and STM revealed that structural properties on the atomic scale determine the reaction outcome drastically. Their influence on the

reaction was studied on well-ordered atomically flat single crystal surfaces. Surprisingly, unlike theoretically predicted, those surfaces consisting of large well-ordered terraces do not manage to catalyse the reduction of CO_2 , but instead favour the hydrogen evolution reaction. Only upon introducing defects, a large number of steps and high index surface sites, the CO_2RR activity previously reported on electropolished surfaces is regained. This sheds light onto crucial key structural parameters that are believed to be the active sites of the reaction, based on studies on electropolished surfaces reporting a dependence of the selectivity on the specific crystal orientation.

The findings presented here rather suggest that those pristine large-scale terraces are not the active sites but, rather high index and defective sites on the catalysts surface. In this framework this work shows that the crystal orientation-dependent selectivity has rather to be understood on the basis of differently evolving defects and stepped sites upon treatments, such as electropolishing, in dependence of the initial crystal orientation. Furthermore, carbon monoxide, which is considered the most important CO_2RR intermediate, was found to bind more strongly to surfaces with high index facets, a large number of steps and a high density of defect sites, As those surfaces have also been found to be the most selective for C_2 products, the results presented in this work suggest a link in between both.

The second part of this work focuses on the influence of the chemical environment, especially when exposing oxide-derived catalyst to different electrolytes containing halides and/or alkaline cations. The results show that a significant increase in the current density can be obtained while maintaining the intrinsic high C_2 product selectivity of oxide-derived catalysts when adding halides, especially Iodine, which also invokes a strong structural and chemical state change of the underlying catalyst. The results show that the interaction of the surface with those halides provide a chemical environment which enhances the stabilization of the common possible CO_2RR intermediate COOH on the catalyst surface, which is responsible for the observed activity increase.

8.2 Outlook

The insights on the electrochemical reduction of CO_2 provided by this work are to a large extend based on also developing and pushing the limits of the field on the experimental basis. While surface science techniques and approaches are traditionally employed on the basis of UHV environments, this work highlights the benefit in rethinking this approach.

Combining surface sensitive UHV-based techniques with electrochemical environments and carefully designing and employing well controlled and characterized surfaces in electrochemical environments, new fundamental insights could be gained, even though the precision and control that comes along with UHV environments had to be partially sacrificed. Advancing the technical development to close this

pressure gap as well as the scientific creative combination of techniques in new ways is crucial to generate new fundamental knowledge within the field. Furthermore, the further development and improvement of *operando* microscopy and spectroscopy techniques is of great importance since those experiments allow to extract information while the reaction is running in real time which is of great value when it comes to the understanding of the role of specific key parameters.

Combining those two approaches in the future, employing precise *operando* techniques on well controlled and characterized surfaces on the atomic scale could lead to understanding the reaction mechanisms underlying CO₂RR towards hydrocarbons in the future and even beyond serve for the understanding of other important reactions that might turn out to be key role for building a future society that is not based on a one way resource consumption but instead on a sustainable energy and resource cycle.

Literature

- (1) Boretto, A.; Rosa, L. Reassessing the projections of the world water development report. *NPJ Clean Water* **2019**, *2*, 1–6.
- (2) Abas, N.; Kalair, A. R.; Khan, N. Review of fossil fuels and future energy technologies. *Futures* **2015**, *69*, 31–49.
- (3) Ahmad, T.; Zhang, D. A critical review of comparative global historical energy consumption and future demand: The story told so far. *Energy Reports* **2020**, *6*, 1973–1991.
- (4) Nitopi, S.; Bertheussen, E.; Scott, S. B.; Liu, X.; Engstfeld, A. K.; Horch, S.; Seger, B.; Stephens, I. E.; Chan, K.; Hahn, C., et al. Progress and perspectives of electrochemical CO₂ reduction on copper in aqueous electrolyte. *Chemical reviews* **2019**, *119*, 7610–7672.
- (5) Bereiter, B.; Eggleston, S.; Schmitt, J.; Nehrbass-Ahles, C.; Stocker, T. F.; Fischer, H.; Kipfstuhl, S.; Chappellaz, J. Revision of the EPICA Dome C CO₂ record from 800 to 600 kyr before present. *Geophysical Research Letters* **2015**, *42*, 542–549.
- (6) Friedlingstein, P.; Jones, M.; O’sullivan, M.; Andrew, R.; Hauck, J.; Peters, G.; Peters, W.; Pongratz, J.; Sitch, S.; Le Quéré, C., et al. Global carbon budget 2019. *Earth System Science Data* **2019**, *11*, 1783–1838.
- (7) Breitkopf, C.; Swider-Lyons, K. In *Springer Handbook of Electrochemical Energy*; Springer: 2017, pp 1–9.
- (8) Hori, Y.; Murata, A.; Takahashi, R. Formation of hydrocarbons in the electrochemical reduction of carbon dioxide at a copper electrode in aqueous solution. *Journal of the Chemical Society, Faraday Transactions 1: Physical Chemistry in Condensed Phases* **1989**, *85*, 2309–2326.
- (9) Hori, Y. In *Modern aspects of electrochemistry*; Springer: 2008, pp 89–189.
- (10) Zhao, J.; Xue, S.; Barber, J.; Zhou, Y.; Meng, J.; Ke, X. An overview of Cu-based heterogeneous electrocatalysts for CO₂ reduction. *Journal of Materials Chemistry A* **2020**, *8*, 4700–4734.
- (11) Arán-Ais, R. M.; Gao, D.; Roldan Cuenya, B. Structure-and electrolyte-sensitivity in CO₂ electroreduction. *Accounts of chemical research* **2018**, *51*, 2906–2917.

- (12) Gattrell, M.; Gupta, N.; Co, A. C. A review of the aqueous electrochemical reduction of CO₂ to hydrocarbons at copper. *Journal of electroanalytical Chemistry* **2006**, *594*, 1–19.
- (13) Resasco, J.; Bell, A. T. Electrocatalytic CO₂ reduction to fuels: progress and opportunities. *Trends in Chemistry* **2020**.
- (14) Zegkinoglou, I.; Pielsticker, L.; Han, Z.-K.; Divins, N. J.; Kordus, D.; Chen, Y.-T.; Escudero, C.; Pérez-Dieste, V.; Zhu, B.; Gao, Y., et al. Surface segregation in CuNi nanoparticle catalysts during CO₂ hydrogenation: the role of CO in the reactant mixture. *The Journal of Physical Chemistry C* **2019**, *123*, 8421–8428.
- (15) Bell, A. T. In *Studies in Surface Science and Catalysis*; Elsevier: 2001; Vol. 136, pp 13–19.
- (16) Grabow, L.; Mavrikakis, M. Mechanism of methanol synthesis on Cu through CO₂ and CO hydrogenation. *Acs Catalysis* **2011**, *1*, 365–384.
- (17) Kang, Y.; Ye, X.; Murray, C. B. Size- and Shape-Selective Synthesis of Metal Nanocrystals and Nanowires Using CO as a Reducing Agent. *Angewandte Chemie* **2010**, *122*, 6292–6295.
- (18) Chen, C.-L.; Weng, H.-S. Nanosized CeO₂-supported metal oxide catalysts for catalytic reduction of SO₂ with CO as a reducing agent. *Applied Catalysis B: Environmental* **2005**, *55*, 115–122.
- (19) Hori, Y.; Wakebe, H.; Tsukamoto, T.; Koga, O. Electrocatalytic process of CO selectivity in electrochemical reduction of CO₂ at metal electrodes in aqueous media. *Electrochimica Acta* **1994**, *39*, 1833–1839.
- (20) Jenck, J. F.; Agterberg, F.; Droescher, M. J. Products and processes for a sustainable chemical industry: a review of achievements and prospects. *Green Chemistry* **2004**, *6*, 544–556.
- (21) McDaniel, M. P. In *Advances in catalysis*; Elsevier: 2010; Vol. 53, pp 123–606.
- (22) Walter, A.; Rosillo-Calle, F.; Dolzan, P.; Piacente, E.; da Cunha, K. B. Perspectives on fuel ethanol consumption and trade. *Biomass and Bioenergy* **2008**, *32*, 730–748.
- (23) Balat, M.; Balat, H. Recent trends in global production and utilization of bio-ethanol fuel. *Applied energy* **2009**, *86*, 2273–2282.
- (24) Azuma, M.; Hashimoto, K.; Hiramoto, M.; Watanabe, M.; Sakata, T. Electrochemical reduction of carbon dioxide on various metal electrodes in low-temperature aqueous KHCO₃ media. *Journal of the Electrochemical Society* **1990**, *137*, 1772–1778.

-
- (25) Chernyshova, I. V.; Somasundaran, P.; Ponnurangam, S. On the origin of the elusive first intermediate of CO₂ electroreduction. *Proceedings of the National Academy of Sciences* **2018**, *115*, E9261–E9270.
- (26) Mistry, H.; Choi, Y.-W.; Bagger, A.; Scholten, F.; Bonifacio, C. S.; Sinev, I.; Divins, N. J.; Zegkinoglou, I.; Jeon, H. S.; Kisslinger, K., et al. Enhanced carbon dioxide electroreduction to carbon monoxide over defect-rich plasma-activated silver catalysts. *Angewandte Chemie* **2017**, *129*, 11552–11556.
- (27) Scholten, F.; Sinev, I.; Bernal, M.; Roldan Cuenya, B. Plasma-modified dendritic Cu catalyst for CO₂ electroreduction. *ACS catalysis* **2019**, *9*, 5496–5502.
- (28) Won, D. H.; Shin, H.; Koh, J.; Chung, J.; Lee, H. S.; Kim, H.; Woo, S. I. Highly efficient, selective, and stable CO₂ electroreduction on a hexagonal Zn catalyst. *Angewandte Chemie International Edition* **2016**, *55*, 9297–9300.
- (29) Jeon, H. S.; Sinev, I.; Scholten, F.; Divins, N. J.; Zegkinoglou, I.; Pielsticker, L.; Cuenya, B. R. Operando evolution of the structure and oxidation state of size-controlled Zn nanoparticles during CO₂ electroreduction. *Journal of the American Chemical Society* **2018**, *140*, 9383–9386.
- (30) Tian, Z.; Priest, C.; Chen, L. Recent progress in the theoretical investigation of electrocatalytic reduction of CO₂. *Advanced Theory and Simulations* **2018**, *1*, 1800004.
- (31) Peterson, A. A.; Abild-Pedersen, F.; Studt, F.; Rossmeisl, J.; Nørskov, J. K. How copper catalyzes the electroreduction of carbon dioxide into hydrocarbon fuels. *Energy & Environmental Science* **2010**, *3*, 1311–1315.
- (32) Feaster, J. T.; Shi, C.; Cave, E. R.; Hatsukade, T.; Abram, D. N.; Kuhl, K. P.; Hahn, C.; Nørskov, J. K.; Jaramillo, T. F. Understanding selectivity for the electrochemical reduction of carbon dioxide to formic acid and carbon monoxide on metal electrodes. *Acs Catalysis* **2017**, *7*, 4822–4827.
- (33) Bohra, D.; Ledezma-Yanez, I.; Li, G.; De Jong, W.; Pidko, E. A.; Smith, W. A. Lateral Adsorbate Interactions Inhibit HCOO-While Promoting CO Selectivity for CO₂ Electrocatalysis on Ag. **2018**.
- (34) Chung, D. Y.; Kim, H.-i.; Chung, Y.-H.; Lee, M. J.; Yoo, S. J.; Bokare, A. D.; Choi, W.; Sung, Y.-E. Inhibition of CO poisoning on Pt catalyst coupled with the reduction of toxic hexavalent chromium in a dual-functional fuel cell. *Scientific reports* **2014**, *4*, 7450.
- (35) Hansen, H. A.; Varley, J. B.; Peterson, A. A.; Nørskov, J. K. Understanding trends in the electrocatalytic activity of metals and enzymes for CO₂ reduction to CO. *The journal of physical chemistry letters* **2013**, *4*, 388–392.

- (36) Liu, X.; Xiao, J.; Peng, H.; Hong, X.; Chan, K.; Nørskov, J. K. Understanding trends in electrochemical carbon dioxide reduction rates. *Nature communications* **2017**, *8*, 1–7.
- (37) Huang, Y.; Handoko, A. D.; Hirunsit, P.; Yeo, B. S. Electrochemical reduction of CO₂ using copper single-crystal surfaces: effects of CO* coverage on the selective formation of ethylene. *ACS catalysis* **2017**, *7*, 1749–1756.
- (38) Bernal, M.; Bagger, A.; Scholten, F.; Sinev, I.; Bergmann, A.; Ahmadi, M.; Rossmesl, J.; Cuenya, B. R. CO₂ electroreduction on copper-cobalt nanoparticles: Size and composition effect. *Nano Energy* **2018**, *53*, 27–36.
- (39) Jeon, H. S.; Timoshenko, J.; Scholten, F.; Sinev, I.; Herzog, A.; Haase, F. T.; Roldan Cuenya, B. Operando Insight into the Correlation between the Structure and Composition of CuZn Nanoparticles and their Selectivity for the Electrochemical CO₂ Reduction. *Journal of the American Chemical Society* **2019**, *141*, 19879–19887.
- (40) Choi, Y.-W.; Scholten, F.; Sinev, I.; Roldan Cuenya, B. Enhanced Stability and CO/Formate Selectivity of Plasma-Treated SnO_x/AgO_x Catalysts during CO₂ Electroreduction. *Journal of the American Chemical Society* **2019**, *141*, 5261–5266.
- (41) Kottakkat, T.; Klingan, K.; Jiang, S.; Jovanov, Z. P.; Davies, V. H.; El-Nagar, G. A.; Dau, H.; Roth, C. Electrodeposited AgCu foam catalysts for enhanced reduction of CO₂ to CO. *ACS applied materials & interfaces* **2019**, *11*, 14734–14744.
- (42) Lee, H.; Kim, S.-K.; Ahn, S. H. Electrochemical preparation of Ag/Cu and Au/Cu foams for electrochemical conversion of CO₂ to CO. *Journal of industrial and engineering chemistry* **2017**, *54*, 218–225.
- (43) Hori, Y.; Takahashi, I.; Koga, O.; Hoshi, N. Electrochemical reduction of carbon dioxide at various series of copper single crystal electrodes. *Journal of Molecular Catalysis A: Chemical* **2003**, *199*, 39–47.
- (44) Hori, Y.; Takahashi, I.; Koga, O.; Hoshi, N. Selective formation of C₂ compounds from electrochemical reduction of CO₂ at a series of copper single crystal electrodes. *The Journal of Physical Chemistry B* **2002**, *106*, 15–17.
- (45) Arán-Ais, R. M.; Scholten, F.; Kunze, S.; Rizo, R.; Cuenya, B. R. The role of in situ generated morphological motifs and Cu (i) species in C₂+ product selectivity during CO₂ pulsed electroreduction. *Nature Energy* **2020**, *5*, 317–325.
- (46) Durand, W. J.; Peterson, A. A.; Studt, F.; Abild-Pedersen, F.; Nørskov, J. K. Structure effects on the energetics of the electrochemical reduction of CO₂ by copper surfaces. *Surface Science* **2011**, *605*, 1354–1359.
- (47) Bagger, A.; Ju, W.; Varela, A. S.; Strasser, P.; Rossmesl, J. Electrochemical CO₂ reduction: classifying Cu facets. *Acs Catalysis* **2019**, *9*, 7894–7899.

- (48) Hagman, B.; Posada-Borbón, A.; Schaefer, A.; Shipilin, M.; Zhang, C.; Merte, L. R.; Hellman, A.; Lundgren, E.; Grönbeck, H.; Gustafson, J. Steps control the dissociation of CO₂ on Cu (100). *Journal of the American Chemical Society* **2018**, *140*, 12974–12979.
- (49) Pérez-Gallent, E.; Figueiredo, M. C.; Calle-Vallejo, F.; Koper, M. T. Spectroscopic observation of a hydrogenated CO dimer intermediate during CO reduction on Cu (100) electrodes. *Angewandte Chemie* **2017**, *129*, 3675–3678.
- (50) Zheng, Y.; Vasileff, A.; Zhou, X.; Jiao, Y.; Jaroniec, M.; Qiao, S.-Z. Understanding the roadmap for electrochemical reduction of CO₂ to multi-carbon oxygenates and hydrocarbons on copper-based catalysts. *Journal of the American Chemical Society* **2019**, *141*, 7646–7659.
- (51) Garza, A. J.; Bell, A. T.; Head-Gordon, M. Mechanism of CO₂ reduction at copper surfaces: pathways to C₂ products. *ACS Catalysis* **2018**, *8*, 1490–1499.
- (52) Pérez-Gallent, E.; Marcandalli, G.; Figueiredo, M. C.; Calle-Vallejo, F.; Koper, M. T. Structure-and potential-dependent cation effects on CO reduction at copper single-crystal electrodes. *Journal of the American Chemical Society* **2017**, *139*, 16412–16419.
- (53) Kortlever, R.; Shen, J.; Schouten, K. J. P.; Calle-Vallejo, F.; Koper, M. T. Catalysts and reaction pathways for the electrochemical reduction of carbon dioxide. *The journal of physical chemistry letters* **2015**, *6*, 4073–4082.
- (54) Montoya, J. H.; Shi, C.; Chan, K.; Nørskov, J. K. Theoretical insights into a CO dimerization mechanism in CO₂ electroreduction. *The journal of physical chemistry letters* **2015**, *6*, 2032–2037.
- (55) Xiao, H.; Cheng, T.; Goddard III, W. A. Atomistic mechanisms underlying selectivities in C1 and C2 products from electrochemical reduction of CO on Cu (111). *Journal of the American Chemical Society* **2017**, *139*, 130–136.
- (56) Bard, A. J.; Faulkner, L. R., et al. Fundamentals and applications. *Electrochemical Methods* **2001**, *2*, 580–632.
- (57) Varela, A. S.; Kroschel, M.; Reier, T.; Strasser, P. Controlling the selectivity of CO₂ electroreduction on copper: The effect of the electrolyte concentration and the importance of the local pH. *Catalysis Today* **2016**, *260*, 8–13.
- (58) Resasco, J.; Lum, Y.; Clark, E.; Zeledon, J. Z.; Bell, A. T. Effects of anion identity and concentration on electrochemical reduction of CO₂. *ChemElectroChem* **2018**, *5*, 1064–1072.
- (59) Xiao, H.; Cheng, T.; Goddard III, W. A.; Sundararaman, R. Mechanistic explanation of the pH dependence and onset potentials for hydrocarbon products from electrochemical reduction of CO on Cu (111). *Journal of the American Chemical Society* **2016**, *138*, 483–486.

- (60) Klingan, K.; Kottakkat, T.; Jovanov, Z. P.; Jiang, S.; Pasquini, C.; Scholten, F.; Kubella, P.; Bergmann, A.; Cuenya, B. R.; Roth, C., et al. Reactivity determinants in electrodeposited Cu foams for electrochemical CO₂ reduction. *ChemSusChem* **2018**, *11*, 3449–3459.
- (61) Reller, C.; Krause, R.; Volkova, E.; Schmid, B.; Neubauer, S.; Rucki, A.; Schuster, M.; Schmid, G. Selective electroreduction of CO₂ toward ethylene on nano dendritic copper catalysts at high current density. *Advanced Energy Materials* **2017**, *7*, 1602114.
- (62) Gao, D.; Scholten, F.; Roldan Cuenya, B. Improved CO₂ electroreduction performance on plasma-activated Cu catalysts via electrolyte design: halide effect. *ACS Catalysis* **2017**, *7*, 5112–5120.
- (63) Singh, M. R.; Kwon, Y.; Lum, Y.; Ager III, J. W.; Bell, A. T. Hydrolysis of electrolyte cations enhances the electrochemical reduction of CO₂ over Ag and Cu. *Journal of the American chemical society* **2016**, *138*, 13006–13012.
- (64) Resasco, J.; Chen, L. D.; Clark, E.; Tsai, C.; Hahn, C.; Jaramillo, T. F.; Chan, K.; Bell, A. T. Promoter effects of alkali metal cations on the electrochemical reduction of carbon dioxide. *Journal of the American Chemical Society* **2017**, *139*, 11277–11287.
- (65) Gao, D.; McCrum, I. T.; Deo, S.; Choi, Y.-W.; Scholten, F.; Wan, W.; Chen, J. G.; Janik, M. J.; Roldan Cuenya, B. Activity and Selectivity Control in CO₂ Electroreduction to Multicarbon Products over Cu_xO Catalysts via Electrolyte Design. *Acs catalysis* **2018**, *8*, 10012–10020.
- (66) Gao, D.; Sinev, I.; Scholten, F.; Arán-Ais, R. M.; Divins, N. J.; Kvashnina, K.; Timoshenko, J.; Roldan Cuenya, B. Selective CO₂ Electroreduction to Ethylene and Multicarbon Alcohols via Electrolyte-Driven Nanostructuring. *Angewandte Chemie International Edition* **2019**, *58*, 17047–17053.
- (67) Varela, A. S.; Ju, W.; Reier, T.; Strasser, P. Tuning the catalytic activity and selectivity of Cu for CO₂ electroreduction in the presence of halides. *ACS Catalysis* **2016**, *6*, 2136–2144.
- (68) Mistry, H.; Varela, A. S.; Bonifacio, C. S.; Zegkinoglou, I.; Sinev, I.; Choi, Y.-W.; Kisslinger, K.; Stach, E. A.; Yang, J. C.; Strasser, P., et al. Highly selective plasma-activated copper catalysts for carbon dioxide reduction to ethylene. *Nature communications* **2016**, *7*, 12123.
- (69) Liu, C.; Lourenço, M. P.; Hedström, S.; Cavalca, F.; Diaz-Morales, O.; Duarte, H. A.; Nilsson, A.; Pettersson, L. G. Stability and effects of sub-surface oxygen in oxide-derived Cu catalyst for CO₂ reduction. *The Journal of Physical Chemistry C* **2017**, *121*, 25010–25017.

- (70) Cavalca, F.; Ferragut, R.; Aghion, S.; Eilert, A.; Diaz-Morales, O.; Liu, C.; Koh, A. L.; Hansen, T. W.; Pettersson, L. G.; Nilsson, A. Nature and distribution of stable subsurface oxygen in copper electrodes during electrochemical CO₂ reduction. *The Journal of Physical Chemistry C* **2017**, *121*, 25003–25009.
- (71) Xiao, H.; Goddard, W. A.; Cheng, T.; Liu, Y. Cu metal embedded in oxidized matrix catalyst to promote CO₂ activation and CO dimerization for electrochemical reduction of CO₂. *Proceedings of the National Academy of Sciences* **2017**, *114*, 6685–6688.
- (72) Gao, D.; Zegkinoglou, I.; Divins, N. J.; Scholten, F.; Sinev, I.; Grosse, P.; Roldan Cuenya, B. Plasma-activated copper nanocube catalysts for efficient carbon dioxide electroreduction to hydrocarbons and alcohols. *ACS nano* **2017**, *11*, 4825–4831.
- (73) Lum, Y.; Ager, J. W. Stability of residual oxides in oxide-derived copper catalysts for electrochemical CO₂ reduction investigated with 18O labeling. *Angewandte Chemie International Edition* **2018**, *57*, 551–554.
- (74) Eilert, A.; Cavalca, F.; Roberts, F. S.; Osterwalder, J.; Liu, C.; Favaro, M.; Crumlin, E. J.; Ogasawara, H.; Friebel, D.; Pettersson, L. G., et al. Subsurface oxygen in oxide-derived copper electrocatalysts for carbon dioxide reduction. *The journal of physical chemistry letters* **2017**, *8*, 285–290.
- (75) Mandal, L.; Yang, K. R.; Motapothula, M. R.; Ren, D.; Lobaccaro, P.; Patra, A.; Sherburne, M.; Batista, V. S.; Yeo, B. S.; Ager, J. W., et al. Investigating the role of copper oxide in electrochemical CO₂ reduction in real time. *ACS applied materials & interfaces* **2018**, *10*, 8574–8584.
- (76) Velasco-Vélez, J.-J.; Jones, T.; Gao, D.; Carbonio, E.; Arrigo, R.; Hsu, C.-J.; Huang, Y.-C.; Dong, C.-L.; Chen, J.-M.; Lee, J.-F., et al. The role of the copper oxidation state in the electrocatalytic reduction of CO₂ into valuable hydrocarbons. *ACS Sustainable Chemistry & Engineering* **2018**, *7*, 1485–1492.
- (77) Loiudice, A.; Lobaccaro, P.; Kamali, E. A.; Thao, T.; Huang, B. H.; Ager, J. W.; Buonsanti, R. Tailoring copper nanocrystals towards C₂ products in electrochemical CO₂ reduction. *Angewandte Chemie International Edition* **2016**, *55*, 5789–5792.
- (78) Lum, Y.; Yue, B.; Lobaccaro, P.; Bell, A. T.; Ager, J. W. Optimizing C–C coupling on oxide-derived copper catalysts for electrochemical CO₂ reduction. *The Journal of Physical Chemistry C* **2017**, *121*, 14191–14203.
- (79) Lum, Y.; Ager, J. W. Evidence for product-specific active sites on oxide-derived Cu catalysts for electrochemical CO₂ reduction. *Nature Catalysis* **2019**, *2*, 86–93.

- (80) Weng, Z.; Wu, Y.; Wang, M.; Jiang, J.; Yang, K.; Huo, S.; Wang, X.-F.; Ma, Q.; Brudvig, G. W.; Batista, V. S., et al. Active sites of copper-complex catalytic materials for electrochemical carbon dioxide reduction. *Nature communications* **2018**, *9*, 1–9.
- (81) Reske, R.; Mistry, H.; Behafarid, F.; Roldan Cuenya, B.; Strasser, P. Particle size effects in the catalytic electroreduction of CO₂ on Cu nanoparticles. *Journal of the American Chemical Society* **2014**, *136*, 6978–6986.
- (82) Wang, J.; Zhang, F.; Kang, X.; Chen, S. Organic functionalization of metal catalysts: Enhanced activity towards electroreduction of carbon dioxide. *Current Opinion in Electrochemistry* **2019**, *13*, 40–46.
- (83) Luo, M.; Wang, Z.; Li, Y. C.; Li, J.; Li, F.; Lum, Y.; Nam, D.-H.; Chen, B.; Wicks, J.; Xu, A., et al. Hydroxide promotes carbon dioxide electroreduction to ethanol on copper via tuning of adsorbed hydrogen. *Nature communications* **2019**, *10*, 1–7.
- (84) Kim, J.; Choi, W.; Park, J. W.; Kim, C.; Kim, M.; Song, H. Branched copper oxide nanoparticles induce highly selective ethylene production by electrochemical carbon dioxide reduction. *Journal of the American Chemical Society* **2019**, *141*, 6986–6994.
- (85) Dinh, C.-T.; Burdyny, T.; Kibria, M. G.; Seifitokaldani, A.; Gabardo, C. M.; De Arquer, F. P. G.; Kiani, A.; Edwards, J. P.; De Luna, P.; Bushuyev, O. S., et al. CO₂ electroreduction to ethylene via hydroxide-mediated copper catalysis at an abrupt interface. *Science* **2018**, *360*, 783–787.
- (86) Grosse, P.; Gao, D.; Scholten, F.; Sinev, I.; Mistry, H.; Roldan Cuenya, B. Dynamic changes in the structure, chemical state and catalytic selectivity of Cu nanocubes during CO₂ electroreduction: size and support effects. *Angewandte Chemie International Edition* **2018**, *57*, 6192–6197.
- (87) Zhang, B.; Zhang, J.; Hua, M.; Wan, Q.; Su, Z.; Tan, X.; Liu, L.; Zhang, F.; Chen, G.; Tan, D., et al. Highly electrocatalytic ethylene production from CO₂ on nanodeficient Cu nanosheets. *Journal of the American Chemical Society* **2020**, *142*, 13606–13613.
- (88) Ma, W.; Xie, S.; Liu, T.; Fan, Q.; Ye, J.; Sun, F.; Jiang, Z.; Zhang, Q.; Cheng, J.; Wang, Y. Electrocatalytic reduction of CO₂ to ethylene and ethanol through hydrogen-assisted C–C coupling over fluorine-modified copper. *Nature Catalysis* **2020**, 1–10.
- (89) Hori, Y.; Konishi, H.; Futamura, T.; Murata, A.; Koga, O.; Sakurai, H.; Oguma, K. "Deactivation of copper" electrode in electrochemical reduction of CO₂. *Electrochimica acta* **2005**, *50*, 5354–5369.
- (90) Wuttig, A.; Surendranath, Y. Impurity ion complexation enhances carbon dioxide reduction catalysis. *ACS Catalysis* **2015**, *5*, 4479–4484.

-
- (91) Hall, A. S.; Yoon, Y.; Wuttig, A.; Surendranath, Y. Mesostructure-induced selectivity in CO₂ reduction catalysis. *Journal of the American Chemical Society* **2015**, *137*, 14834–14837.
- (92) Ciapina, E. G.; Santos, S. F.; Gonzalez, E. R. Electrochemical CO stripping on nanosized Pt surfaces in acid media: A review on the issue of peak multiplicity. *Journal of Electroanalytical Chemistry* **2018**, *815*, 47–60.
- (93) Farias, M. J.; Herrero, E.; Feliu, J. M. Site selectivity for CO adsorption and stripping on stepped and kinked platinum surfaces in alkaline medium. *The Journal of Physical Chemistry C* **2013**, *117*, 2903–2913.
- (94) Schouten, K. J. P.; Gallent, E. P.; Koper, M. T. The electrochemical characterization of copper single-crystal electrodes in alkaline media. *Journal of Electroanalytical Chemistry* **2013**, *699*, 6–9.
- (95) Meyer, E.; Hug, H. J.; Bennewitz, R., *Scanning probe microscopy: the lab on a tip*; Springer Science & Business Media: 2003.
- (96) Voigtländer, B., *Scanning probe microscopy: Atomic force microscopy and scanning tunneling microscopy*; Springer: 2015.
- (97) Sakurai, J. J.; Napolitano, J., *Modern Quantum Mechanics*, 2nd ed.; Cambridge University Press: 2017.
- (98) Chen, C. J., *Introduction to scanning tunneling microscopy*; Oxford University Press on Demand: 1993; Vol. 4.
- (99) Güntherodt, H.-J.; Wiesendanger, R., *Scanning tunneling microscopy I: general principles and applications to clean and adsorbate-covered surfaces*; Springer: 1992.
- (100) Reimer, L. *Scanning electron microscopy: physics of image formation and microanalysis*, 2000.
- (101) In *Spectroscopy in Catalysis*; John Wiley and Sons, Ltd: 2007; Chapter 3, pp 39–83.
- (102) Levine, I., *Quantum Chemistry*; Pearson advanced chemistry series; Pearson: 2014.
- (103) Somorjai, G., *Chemistry in Two Dimensions Surfaces*; Pearson advanced chemistry series; Cornell University Press: 1981.
- (104) Biesinger, M. C.; Lau, L. W.; Gerson, A. R.; Smart, R. S. C. Resolving surface chemical states in XPS analysis of first row transition metals, oxides and hydroxides: Sc, Ti, V, Cu and Zn. *Applied surface science* **2010**, *257*, 887–898.
- (105) Biesinger, M. C. Advanced analysis of copper X-ray photoelectron spectra. *Surface and Interface Analysis* **2017**, *49*, 1325–1334.

- (106) Koningsberger, D.; Mojet, B.; Van Dorssen, G.; Ramaker, D. XAFS spectroscopy; fundamental principles and data analysis. *Topics in catalysis* **2000**, *10*, 143–155.
- (107) Calvin, S., *XAFS for Everyone*; CRC press: 2013.
- (108) Ravel, B.; Newville, M. ATHENA, ARTEMIS, HEPHAESTUS: data analysis for X-ray absorption spectroscopy using IFEFFIT. *Journal of synchrotron radiation* **2005**, *12*, 537–541.
- (109) Booth, C.; Bridges, F. Improved self-absorption correction for fluorescence measurements of extended X-ray absorption fine-structure. *Physica Scripta* **2005**, *2005*, 202.
- (110) Verdaguer-Casadevall, A.; Li, C. W.; Johansson, T. P.; Scott, S. B.; McKewon, J. T.; Kumar, M.; Stephens, I. E.; Kanan, M. W.; Chorkendorff, I. Probing the active surface sites for CO reduction on oxide-derived copper electrocatalysts. *Journal of the American Chemical Society* **2015**, *137*, 9808–9811.
- (111) Vollmer, S.; Witte, G.; Wöll, C. Determination of site specific adsorption energies of CO on copper. *Catalysis letters* **2001**, *77*, 97–101.
- (112) Fu, S. S.; Somorjai, G. A. Interactions of O₂, CO, CO₂, and D₂ with the stepped Cu (311) crystal face: Comparison to Cu (110). *Surface science* **1992**, *262*, 68–76.
- (113) Hensley, A. J.; Therrien, A. J.; Zhang, R.; Marcinkowski, M. D.; Lucci, F. R.; Sykes, E. C. H.; McEwen, J.-S. CO Adsorption on the “29” Cu x O/Cu (111) Surface: An Integrated DFT, STM, and TPD Study. *The Journal of Physical Chemistry C* **2016**, *120*, 25387–25394.
- (114) De Jong, A.; Niemantsverdriet, J. Thermal desorption analysis: Comparative test of ten commonly applied procedures. *Surface Science* **1990**, *233*, 355–365.
- (115) Niemantsverdriet, J.; Markert, K.; Wandelt, K. The compensation effect and the manifestation of lateral interactions in thermal desorption spectroscopy. *Applied surface science* **1988**, *31*, 211–219.
- (116) Niemantsverdriet, J. W., *Spectroscopy in catalysis: an introduction*; John Wiley & Sons: 2007.
- (117) Redhead, P. Thermal desorption of gases. *vacuum* **1962**, *12*, 203–211.
- (118) Habenschaden, E.; Küppers, J. Evaluation of flash desorption spectra. *Surface science letters* **1984**, *138*, L147–L150.
- (119) King, D. A. Thermal desorption from metal surfaces: A review. *Surface Science* **1975**, *47*, 384–402.
- (120) Miller, P. E.; Denton, M. B. The quadrupole mass filter: basic operating concepts. *Journal of chemical education* **1986**, *63*, 617.

-
- (121) Kononkov, N.; Cousins, L.; Baranov, V.; Sudakov, M. Y. Quadrupole mass filter operation with auxiliary quadrupolar excitation: theory and experiment. *International journal of mass spectrometry* **2001**, *208*, 17–27.
- (122) Kuhl, K. P.; Cave, E. R.; Abram, D. N.; Jaramillo, T. F. New insights into the electrochemical reduction of carbon dioxide on metallic copper surfaces. *Energy & Environmental Science* **2012**, *5*, 7050–7059.
- (123) Li, Y.; Jia, W.-Z.; Song, Y.-Y.; Xia, X.-H. Superhydrophobicity of 3D porous copper films prepared using the hydrogen bubble dynamic template. *Chemistry of Materials* **2007**, *19*, 5758–5764.
- (124) Popov, K. I.; Živković, P. M.; Nikolić, N. Electrochemical aspects of formation of dendrites. *Zaštita materijala* **2016**, *57*, 55–62.
- (125) Dutta, A.; Rahaman, M.; Mohos, M.; Zanetti, A.; Broekmann, P. Electrochemical CO₂ conversion using skeleton (sponge) type of Cu catalysts. *ACS Catalysis* **2017**, *7*, 5431–5437.
- (126) Hao, M.; Charbonneau, V.; Fomena, N.; Gaudet, J.; Bruce, D.; Garbarino, S.; Harrington, D. A.; Guay, D. Hydrogen Bubble Templating of Fractal Ni Catalysts for Water Oxidation in Alkaline Media. *ACS Applied Energy Materials* **2019**, *2*, 5734–5743.
- (127) Kelly, P. J.; Arnell, R. D. Magnetron sputtering: a review of recent developments and applications. *Vacuum* **2000**, *56*, 159–172.
- (128) Handoko, A. D.; Ong, C. W.; Huang, Y.; Lee, Z. G.; Lin, L.; Panetti, G. B.; Yeo, B. S. Mechanistic insights into the selective electroreduction of carbon dioxide to ethylene on Cu₂O-derived copper catalysts. *The Journal of Physical Chemistry C* **2016**, *120*, 20058–20067.
- (129) Kim, D.; Kley, C. S.; Li, Y.; Yang, P. Copper nanoparticle ensembles for selective electroreduction of CO₂ to C₂–C₃ products. *Proceedings of the National Academy of Sciences* **2017**, *114*, 10560–10565.
- (130) Fields, M.; Hong, X.; Nørskov, J. K.; Chan, K. Role of subsurface oxygen on Cu surfaces for CO₂ electrochemical reduction. *The Journal of Physical Chemistry C* **2018**, *122*, 16209–16215.
- (131) De Luna, P.; Quintero-Bermudez, R.; Dinh, C.-T.; Ross, M. B.; Bushuyev, O. S.; Todorović, P.; Regier, T.; Kelley, S. O.; Yang, P.; Sargent, E. H. Catalyst electro-redeposition controls morphology and oxidation state for selective carbon dioxide reduction. *Nature Catalysis* **2018**, *1*, 103–110.
- (132) Zhou, Y.; Che, F.; Liu, M.; Zou, C.; Liang, Z.; De Luna, P.; Yuan, H.; Li, J.; Wang, Z.; Xie, H., et al. Dopant-induced electron localization drives CO₂ reduction to C₂ hydrocarbons. *Nature chemistry* **2018**, *10*, 974–980.

- (133) Lee, S.; Park, G.; Lee, J. Importance of Ag–Cu biphasic boundaries for selective electrochemical reduction of CO₂ to ethanol. *Acs Catalysis* **2017**, *7*, 8594–8604.
- (134) Ripatti, D. S.; Veltman, T. R.; Kanan, M. W. Carbon monoxide gas diffusion electrolysis that produces concentrated C₂ products with high single-pass conversion. *Joule* **2019**, *3*, 240–256.
- (135) Le Duff, C. S.; Lawrence, M. J.; Rodriguez, P. Role of the adsorbed oxygen species in the selective electrochemical reduction of CO₂ to alcohols and carbonyls on copper electrodes. *Angewandte Chemie* **2017**, *129*, 13099–13104.
- (136) Dinh, C.-T.; Burdyny, T.; Kibria, M. G.; Seifitokaldani, A.; Gabardo, C. M.; De Arquer, F. P. G.; Kiani, A.; Edwards, J. P.; De Luna, P.; Bushuyev, O. S., et al. CO₂ electroreduction to ethylene via hydroxide-mediated copper catalysis at an abrupt interface. *Science* **2018**, *360*, 783–787.
- (137) Dutta, A.; Rahaman, M.; Luedi, N. C.; Mohos, M.; Broekmann, P. Morphology matters: tuning the product distribution of CO₂ electroreduction on oxide-derived Cu foam catalysts. *ACS Catalysis* **2016**, *6*, 3804–3814.
- (138) Ferraria, A. M.; Carapeto, A. P.; do Rego, A. M. B. X-ray photoelectron spectroscopy: silver salts revisited. *Vacuum* **2012**, *86*, 1988–1991.
- (139) Wagner, C. D.; Naumkin, A. V.; Kraut-Vass, A.; Allison, J. W.; Powell, C. J.; Rumble Jr, J. R. NIST standard reference database 20. *NIST XPS Database Version* **2003**, *3*, 251–252.
- (140) Kaspar, T. C.; Droubay, T.; Chambers, S. A.; Bagus, P. S. Spectroscopic evidence for Ag (III) in highly oxidized silver films by X-ray photoelectron spectroscopy. *The Journal of Physical Chemistry C* **2010**, *114*, 21562–21571.
- (141) Munoz, M.; Argoul, P.; Farges, F. Continuous Cauchy wavelet transform analyses of EXAFS spectra: A qualitative approach. *American mineralogist* **2003**, *88*, 694–700.
- (142) Timoshenko, J.; Kuzmin, A. Wavelet data analysis of EXAFS spectra. *Computer Physics Communications* **2009**, *180*, 920–925.
- (143) Savinelli, R. O.; Scott, S. L. Wavelet transform EXAFS analysis of mono- and dimolybdate model compounds and a Mo/HZSM-5 dehydroaromatization catalyst. *Physical Chemistry Chemical Physics* **2010**, *12*, 5660–5667.
- (144) Calle-Vallejo, F.; Koper, M. T. Theoretical considerations on the electroreduction of CO to C₂ species on Cu (100) electrodes. *Angewandte Chemie* **2013**, *125*, 7423–7426.
- (145) Yano, J.; Yamasaki, S. Pulse-mode electrochemical reduction of carbon dioxide using copper and copper oxide electrodes for selective ethylene formation. *Journal of applied electrochemistry* **2008**, *38*, 1721.

-
- (146) Shiratsuchi, R.; Aikoh, Y.; Nogami, G. Pulsed Electroreduction of CO₂ on Copper Electrodes. *Journal of The Electrochemical Society* **1993**, *140*, 3479.
- (147) Kumar, B.; Brian, J. P.; Atla, V.; Kumari, S.; Bertram, K. A.; White, R. T.; Spurgeon, J. M. Controlling the product syngas H₂: CO ratio through pulsed-bias electrochemical reduction of CO₂ on copper. *ACS Catalysis* **2016**, *6*, 4739–4745.
- (148) Miller, D.; Biesinger, M.; McIntyre, N. Interactions of CO₂ and CO at fractional atmosphere pressures with iron and iron oxide surfaces: one possible mechanism for surface contamination? *Surface and Interface Analysis: An International Journal devoted to the development and application of techniques for the analysis of surfaces, interfaces and thin films* **2002**, *33*, 299–305.
- (149) Jović, V.; Jović, B. EIS and differential capacitance measurements onto single crystal faces in different solutions: Part II: Cu (111) and Cu (100) in 0.1M NaOH. *Journal of Electroanalytical Chemistry* **2003**, *541*, 13–21.
- (150) Kunze, J.; Maurice, V.; Klein, L. H.; Strehblow, H.-H.; Marcus, P. In situ STM study of the effect of chlorides on the initial stages of anodic oxidation of Cu (111) in alkaline solutions. *Electrochimica Acta* **2003**, *48*, 1157–1167.
- (151) Vidal-Iglesias, F. J.; Arán-Ais, R. M.; Solla-Gullón, J.; Herrero, E.; Feliu, J. M. Electrochemical characterization of shape-controlled Pt nanoparticles in different supporting electrolytes. *ACS Catalysis* **2012**, *2*, 901–910.
- (152) Protopopoff, E.; Marcus, P. Potential–pH diagrams for hydroxyl and hydrogen adsorbed on a copper surface. *Electrochimica Acta* **2005**, *51*, 408–417.
- (153) Hahn, C.; Hatsukade, T.; Kim, Y.-G.; Vailionis, A.; Baricuatro, J. H.; Higgins, D. C.; Nitopi, S. A.; Soriaga, M. P.; Jaramillo, T. F. Engineering Cu surfaces for the electrocatalytic conversion of CO₂: Controlling selectivity toward oxygenates and hydrocarbons. *Proceedings of the National Academy of Sciences* **2017**, *114*, 5918–5923.
- (154) Todorova, T. K.; Schreiber, M. W.; Fontecave, M. Mechanistic understanding of CO₂ reduction reaction (CO₂RR) toward multicarbon products by heterogeneous copper-based catalysts. *ACS Catalysis* **2019**, *10*, 1754–1768.
- (155) Schouten, K.; Kwon, Y.; Van der Ham, C.; Qin, Z.; Koper, M. A new mechanism for the selectivity to C 1 and C 2 species in the electrochemical reduction of carbon dioxide on copper electrodes. *Chemical Science* **2011**, *2*, 1902–1909.
- (156) Roberts, F. S.; Kuhl, K. P.; Nilsson, A. High selectivity for ethylene from carbon dioxide reduction over copper nanocube electrocatalysts. *Angewandte Chemie* **2015**, *127*, 5268–5271.

- (157) Simon, G. H.; Kley, C. S.; Roldan Cuenya, B. Potential-dependent Morphology of Copper Catalysts During CO₂ Electroreduction Revealed by In Situ Atomic Force Microscopy. *Angewandte Chemie International Edition* **2020**.
- (158) Pritchard, J. On the structure of CO adlayers on Cu (100) and Cu (111). *Surface Science* **1979**, *79*, 231–244.
- (159) Roiaz, M.; Falivene, L.; Rameshan, C.; Cavallo, L.; Kozlov, S. M.; Rupprechter, G. Roughening of Copper (100) at Elevated CO Pressure: Cu Adatom and Cluster Formation Enable CO Dissociation. *The Journal of Physical Chemistry C* **2018**, *123*, 8112–8121.
- (160) Makino, T.; Okada, M. CO adsorption on regularly stepped Cu (410) surface. *Surface science* **2014**, *628*, 36–40.
- (161) Hsieh, Y.-C.; Senanayake, S. D.; Zhang, Y.; Xu, W.; Polyansky, D. E. Effect of chloride anions on the synthesis and enhanced catalytic activity of silver nanocoral electrodes for CO₂ electroreduction. *ACS Catalysis* **2015**, *5*, 5349–5356.
- (162) Hsiao, G.; Anderson, M.; Gorer, S.; Harris, D.; Penner, R. Hybrid electrochemical/chemical synthesis of supported, luminescent semiconductor nanocrystallites with size selectivity: copper (I) iodide. *Journal of the American Chemical Society* **1997**, *119*, 1439–1448.
- (163) Lefevre, G.; Walcarius, A.; Ehrhardt, J.-J.; Bessière, J. Sorption of iodide on cuprite (Cu₂O). *Langmuir* **2000**, *16*, 4519–4527.
- (164) Ng, C. H. B.; Fan, W. Y. Shape evolution of Cu₂O nanostructures via kinetic and thermodynamic controlled growth. *The Journal of Physical Chemistry B* **2006**, *110*, 20801–20807.
- (165) Swift, P. Adventitious carbon—the panacea for energy referencing? *Surface and Interface Analysis* **1982**, *4*, 47–51.
- (166) McCrum, I. T.; Akhade, S. A.; Janik, M. J. Electrochemical specific adsorption of halides on Cu 111, 100, and 211: A Density Functional Theory study. *Electrochimica Acta* **2015**, *173*, 302–309.
- (167) Huemann, S.; Nguyen, T. M. H.; Broekmann, P.; Wandelt, K.; Zajonz, H.; Dosch, H.; Renner, F. X-ray Diffraction and STM Study of Reactive Surfaces under Electrochemical Control: Cl and I on Cu(100). *The Journal of Physical Chemistry B* **2006**, *110*, 24955–24963.
- (168) Moshfegh, A. Nanoparticle catalysts. *Journal of Physics D: Applied Physics* **2009**, *42*, 233001.
- (169) Mistry, H.; Reske, R.; Strasser, P.; Cuenya, B. R. Size-dependent reactivity of gold-copper bimetallic nanoparticles during CO₂ electroreduction. *Catalysis Today* **2017**, *288*, 30–36.

- (170) Mistry, H.; Reske, R.; Zeng, Z.; Zhao, Z.-J.; Greeley, J.; Strasser, P.; Cuenya, B. R. Exceptional size-dependent activity enhancement in the electroreduction of CO₂ over Au nanoparticles. *Journal of the American Chemical Society* **2014**, *136*, 16473–16476.
- (171) Feng, X.; Jiang, K.; Fan, S.; Kanan, M. W. Grain-boundary-dependent CO₂ electroreduction activity. *Journal of the American Chemical Society* **2015**, *137*, 4606–4609.
- (172) Kim, D.; Resasco, J.; Yu, Y.; Asiri, A. M.; Yang, P. Synergistic geometric and electronic effects for electrochemical reduction of carbon dioxide using gold–copper bimetallic nanoparticles. *Nature communications* **2014**, *5*, 1–8.
- (173) Rasul, S.; Anjum, D. H.; Jedidi, A.; Minenkov, Y.; Cavallo, L.; Takanebe, K. A highly selective copper–indium bimetallic electrocatalyst for the electrochemical reduction of aqueous CO₂ to CO. *Angewandte Chemie* **2015**, *127*, 2174–2178.
- (174) Clark, E. L.; Hahn, C.; Jaramillo, T. F.; Bell, A. T. Electrochemical CO₂ reduction over compressively strained CuAg surface alloys with enhanced multi-carbon oxygenate selectivity. *Journal of the American Chemical Society* **2017**, *139*, 15848–15857.
- (175) Hu, H.; Tang, Y.; Hu, Q.; Wan, P.; Dai, L.; Yang, X. J. In-situ grown nanoporous Zn-Cu catalysts on brass foils for enhanced electrochemical reduction of carbon dioxide. *Applied Surface Science* **2018**, *445*, 281–286.
- (176) Keerthiga, G.; Chetty, R. Electrochemical reduction of carbon dioxide on zinc-modified copper electrodes. *Journal of the Electrochemical Society* **2017**, *164*, H164.
- (177) Luo, W.; Zhang, Q.; Zhang, J.; Moioli, E.; Zhao, K.; Züttel, A. Electrochemical reconstruction of ZnO for selective reduction of CO₂ to CO. *Applied Catalysis B: Environmental* **2020**, *273*, 119060.
- (178) Ankudinov, A.; Ravel, B.; Rehr, J.; Conradson, S. Real-space multiple-scattering calculation and interpretation of x-ray-absorption near-edge structure. *Physical Review B* **1998**, *58*, 7565.
- (179) Pan, H.; Knapp, G.; Cooper, S. L. EXAFS and XANES studies of Zn²⁺ and Rb⁺ neutralized perfluorinated ionomers. *Colloid and Polymer Science* **1984**, *262*, 734–746.
- (180) Dake, L.; Baer, D.; Zachara, J. Auger parameter measurements of zinc compounds relevant to zinc transport in the environment. *Surface and Interface analysis* **1989**, *14*, 71–75.
- (181) Gaarenstroom, S.; Winograd, N. Initial and final state effects in the ESCA spectra of cadmium and silver oxides. *The Journal of chemical physics* **1977**, *67*, 3500–3506.

- (182) Nguyen, D.; Jee, M.; Won, D.; Jung, H.; Oh, H.; Min, B.; Hwang, Y. *ACS Sustainable Chem. Eng* **2017**, *5*, 11377–11386.
- (183) Gao, D.; Arán-Ais, R. M.; Jeon, H. S.; Cuenya, B. R. Rational catalyst and electrolyte design for CO₂ electroreduction towards multicarbon products. *Nature Catalysis* **2019**, *2*, 198–210.
- (184) Mistry, H.; Varela, A. S.; Kühn, S.; Strasser, P.; Cuenya, B. R. Nanostructured electrocatalysts with tunable activity and selectivity. *Nature Reviews Materials* **2016**, *1*, 1–14.
- (185) Andrews, P.; Hisscott, L. X-ray photoelectron spectroscopy of some Cu-Zn alloys. *Journal of Physics F: Metal Physics* **1975**, *5*, 1568.
- (186) Liu, K.; Ma, M.; Wu, L.; Valenti, M.; Cardenas-Morcoso, D.; Hofmann, J. P.; Bisquert, J.; Gimenez, S.; Smith, W. A. Electronic effects determine the selectivity of planar Au–Cu bimetallic thin films for electrochemical CO₂ reduction. *ACS applied materials & interfaces* **2019**, *11*, 16546–16555.
- (187) Ren, D.; Ang, B. S.-H.; Yeo, B. S. Tuning the selectivity of carbon dioxide electroreduction toward ethanol on oxide-derived Cu_xZn catalysts. *Acs Catalysis* **2016**, *6*, 8239–8247.

Curriculum Vitae

Personal Information

First Name	Fabian
Surname	Scholten
Date of Birth	02.12.1989
Place of Birth	Schwelm, Germany

Work Experience

Civilian Service	AWO-EN: 45549 Sprockhövel (2009-2010)
Scientific Assistant	Ruhr University Bochum Theoretical Physics II (2013-2014)
Scientific Assistant	Ruhr University Bochum Theoretical chemistry (2015-2016)
Scientific Assistant	Ruhr University Bochum Experimental Physics IV (2017-2019)
Scientific Assistant	Fritz Haber Institute of the Max Planck Society (2019-2021))

Education

School	Grundschule Haßlinghausen (1996-2000) Gymnasium Gevelsberg (2000-2009)
Bachelor of Science Physics	Ruhr University Bochum (2010-2014)
Master of Science Physics	Ruhr University Bochum (2014-2017)
PhD Student	Ruhr University Bochum (2017-present)